Akademiya Nauk SSSR

OPTICAL INSTABILITY

OF THE EARTH'S ATMOSPHERE

Edited by N. I. Kucherov

Translated from Russian

Optical Instability

of the Earth's Atmosphere

(Opticheskaya neustoichivost' zemnoi atmosfery)

Edited by N.I. Kucherov

Translated from Russian

Published Pursuant to an Agreement with
THE NATIONAL AERONAUTICS AND SPACE ADMINISTRATION, U.S.A.
and
THE NATIONAL SCIENCE FOUNDATION, WASHINGTON, D.C.

Translated by Z. Lerman

Price: $5.00

Available from the
U.S. DEPARTMENT OF COMMERCE
Clearinghouse for Federal Scientific and Technical Information
Springfield, Va. 22151

xii/13/5

Table of Contents

TRANSLATOR'S FOREWORD

There is a regrettable lack of uniformity in the terminology used in the literature in all that concerns "astroclimate", or the phenomena of astronomical seeing in the broad sense. A few words of explanation on the usage adopted in this volume are therefore in order.

Seeing and image quality are used interchangeably for the Russian "kachestvo izobrazheniya" in the general sense: these terms thus constitute a qualitative optical characteristic of the atmosphere and also describe the state of the finite telescopic image. The term shimmer disk is sometimes preferred when the Russian "kachestvo izobrazheniya" refers (as it often does) to the actual telescopic diffraction pattern. Shimmer angle has been adopted as a translation of the Russian term "ugol turbulentnosti" (literally, turbulence angle), which is a quantitative measure of "boil", the blurring of the diffraction disk.

Image pulsation ("drozhanie izobrazheniya" in Russian) denotes position fluctuations or "dancing" of stars, while scintillation is invariably taken to mean brightness fluctuation ("mertsanie" in Russian).

A useful classification of the various phenomena will be found in the table on page 41.

EXPLANATORY LIST OF ABBREVIATIONS OF USSR PERIODICALS
APPEARING IN THIS BOOK

Abbreviation	Full name (transliterated)	Translation
ATs	Astronomicheskii Tsirkulyar	Astronomical Circular
AZh	Astronomicheskii Zhurnal	Astronomical Journal [Soviet Astronomy — AJ]
DAN SSSR	Doklady Akademii Nauk SSSR	Proceedings of the USSR Academy of Sciences [Soviet Physics — Doklady]
Izv. AN AzSSR	Izvestiya Akademii Nauk Azerbaidzhanskoi SSR	Bulletin of the Azerbaidzhan Academy of Sciences
Izv. AN SSSR	Izvestiya Akademii Nauk SSSR	Bulletin of the USSR Academy of Sciences
Izv. GAO	Izvestiya Glavnoi Astronomicheskoi Observatorii	Bulletin of the Main Astronomical Observatory [Pulkovo]
Izv. GAO AN UkrSSR	Izvestiya Glavnoi Astronomicheskoi Observatorii Akademii Nauk Ukrainskoi SSR	Bulletin of the Main Astronomical Observatory of the Ukrainian Academy of Sciences
Izv. KAO	Izvestiya Krymskoi Astrofizicheskoi Observatorii	Bulletin of the Crimea Astrophysical Observatory
Trudy GGO	Trudy Glavnoi Geofizicheskoi Observatorii	Transactions of the Main Geophysical Observatory
Trudy TsAO	Trudy Tsentral'noi Aeronomicheskoi Observatorii	Transactions of the Central Aeronomical Observatory
Vestnik AN KazSSR	Vestnik Akademii Nauk Kazakhskoi SSR	Bulletin of the Kazakh Academy of Sciences
Vestnik MGU	Vestnik Moskovskogo Gosudarstvennogo Universiteta	Bulletin of the Moscow State University

INTRODUCTION

The atmosphere is not stationary: it changes continuously and its optical properties are inherently unstable. This optical instability of the air medium is of considerable significance in various fields of research and observation where light transmission through the atmosphere plays a basic role. Under the category of optical instabilities we mainly have the different atmospheric perturbations whose integrated effect constitutes the astroclimate: these are image pulsation, scintillation, and the blurring of the diffraction disk. The interest of various researchers in optical instability of the atmosphere increased to such an extent that the Astronomical Council of the USSR Academy of Sciences set up a special committee devoted entirely to the study of this subject. Moreover, three All-Union Conferences were held: the first in 1955 in Moscow, the second in 1958 again in Moscow, and the third in 1962 in Kiev.

The outburst of international scientific activity in the field of optical instability of the atmosphere which was felt in 1954—1959 somewhat subsided in subsequent years, but in 1962 a new upward trend was registered. The artificial satellites and space probes collected a great amount of new data on the upper atmosphere and on the outer space environment. New interesting and important problems arose, which attracted the attention of many geophysicists and astronomers. This shift in the center of gravity of scientific interests and efforts is observed mainly among scientists specializing in atmospheric physics. Recently, scientific organizations engaged on optical instability research switched to astroclimatic topics. Twelve scientific organizations were represented at the Third All-Union Conference on Optical Instability of the Atmosphere, held in Kiev in July 1962, and the number of papers devoted to astroclimate was 12 out of the total 28, i.e., 43%.

Soviet astronomers have recently been charged with a very difficult and responsible task: to select suitable sites for the erection of new observatories, including an astrophysical observatory with the largest telescope in the USSR. A considerable number of research groups were dispatched into various areas of the Soviet Union, and many astronomical observatories took part in the astroclimatic survey. The work of these expeditions remains unparalleled by any other country in the world. On the other hand, these researches aroused a definite interest in astroclimate in Soviet astronomical observatories.

International astronomical circles pay an ever growing attention to the problems of astroclimate. In October 1962, the International Astronomical Union held a symposium in Rome on observatory site selection and related astroclimatic topics. The subject of astroclimatic surveys in various parts of the world occupied a significant portion of the symposium agenda. Not only astronomers took part in the discussions, but also

geophysicists and meteorologists. The question of close cooperation between meteorologists and astronomers in connection with observatory site selection and the study of interrelationships between meteorological conditions and astronomical seeing was raised in unambiguous terms. The participants emphasized that telescopes must be erected at a certain height above the ground, to improve image quality. It was also stressed that the future specialization of the projected observatory should be taken into consideration in assessing the relative merits of alternative sites, since different purpose observations have different seeing requirements. This symposium has proved unequivocally that the level of astroclimatic research in the USSR is much higher than in all other countries.

The present collection mainly includes the proceedings of the Third All-Union Conference held in Kiev in July 1962. The proceedings of the Second All-Union Conference were published by the USSR Academy of Sciences in 1962 under the title of "Trudy soveshchaniya po mertsaniyu i drozhaniyu zvezd" (Proceedings of the Conference on Scintillation and Pulsation of Stars).

The papers in this volume deal with chromatic refraction, image pulsation and scintillation, and astroclimate. Some papers are devoted to problems of automation of observational techniques used in the study of optical instability of the atmosphere.

N. I. Kucherov

O. A. Mel'nikov, G. G. Lengauer, and N. F. Kuprevich

CHROMATIC REFRACTION AND ITS RELATION
TO LARGE-TELESCOPE GUIDING

1. Chromatic refraction is hardly encountered in work with short-focus telescopes, whereas for telescopes with focal distances in excess of 3 m this phenomenon must be taken into consideration mainly in high-precision astrophotographic projects, e.g., determination of stellar parallaxes and proper motions (particularly when the objects are close to the horizon). Modern reflectors give a very large image at the fixed focus, which is equivalent to focal distances of tens and hundreds of meters. Chromatic refraction in this case is a considerable obstacle to effective guiding, especially if the guiding telescope and the recording devices are set to operate at frequencies in different regions of the spectrum.

Refraction at any wavelength, expressed in seconds of arc, can be written in the following form for quite arbitrary meteorological conditions:

$$R_\lambda'' = r_\lambda'' F(z') = a \frac{(n_\lambda - 1)}{\sin 1''} F(z').$$

Here n_λ is the refractive index of the ground air at the given wavelength for the given meteorological conditions, $a = 0.99875$ is a constant derived in the theory of refraction, and $F(z')$ is a known function of the apparent zenith distance z'. For moderately large z', we may approximately take $F(z') \approx \operatorname{tg} z'$.

Let $n_{0\lambda}$ be the refractive index of the so-called "standard air", i.e., air at $p_0 = 760$ mm Hg (at 0 °C and for $g_0 = 980.665$ cm/sec^2), $t_0 = +15$ °C, relative humidity $f = 0$, and CO_2 content of 0.03% (by volume). The refraction $R_{0\lambda}''$ for the standard air is written as

$$R_{0\lambda}'' = a \frac{(n_{0\lambda} - 1)}{\sin 1''} F(z')$$

so that

$$R_\lambda'' = R_{0\lambda}'' \frac{(n_\lambda - 1)}{(n_{0\lambda} - 1)}.$$

The refractive index n_λ is related to $n_{0\lambda}$ by the approximate expression

$$(n_\lambda - 1) = (n_{0\lambda} - 1)\left[\frac{1.0550}{1 + 0.00367t}\right]\frac{p}{760};$$

1

(a more exact formula takes account of air humidity and changes in CO_2 content). The refraction at any particular wavelength — "chromatic refraction" — is therefore a function of $n_{0\lambda}$, the refractive index of standard air. The determination of $n_{0\lambda}$, however, is a fairly complex problem. It has been treated in sufficient detail by Edlen /1/ in 1952—1953. Among more recent researches we have the publications of Koronkevich /2/, Rank et al. /3/, Svenson /4/, Peck and Kanna /5/, and Erickson /6/. The results of some experimental determinations of the standard-air refractive index are plotted in Figure 1 as difference $\Delta n_{0\lambda} \cdot 10^8$ between
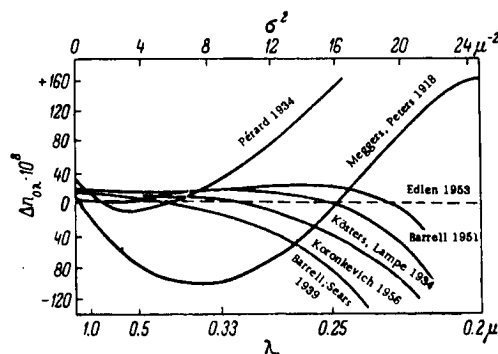
FIGURE 1.

the determinations of various authors and the data of Edlen /1/. (Figure 1 is based on Edlen's résumé, with the inclusion of the data from /2/.) We see that the discrepancies in $n_{0\lambda}$ according to the various authors are as large as -100 and $+160$ in the units of the figure (i.e., to eighth significant digit) at the farthest region of the spectrum. For $z' = 60°$, this corresponds to several tens of angular seconds in the calculated value of monochromatic refraction.

2. The refraction of any particular heavenly body is a function of the energy distribution $J(T, \lambda)$ in its spectrum and of the spectral sensitivity $s(\lambda)$ of the "receiver" (the guider, the photographic plate, etc.). In refraction calculations, one preferably assumes the index n_λ corresponding to the isophote wavelength λ_i, which is easily determined according to established rules /7/. The isophote wavelengths ensure the best approximation of the monochromatic stellar magnitudes to the actual magnitude measurements for the given energy distribution in the spectrum of the body and the particular colorimetric system employed. The B, V system is commonly used, and it is in this system that we carry out our calculations.

The isophote temperatures calculated (approximately) for some wavelengths are listed in Table 1 with the corresponding spectrophotometric gradients Φ. The spectrophotometric gradients are highly useful in chromatic refraction calculations, since they are included in many stellar catalogs and are approximately linear functions of the color indices.

2

These gradients are also convenient in calculating the various distortions introduced by atmospheric effects into the spectral energy distribution of the luminary. For example, the stars are rendered redder by atmospheric

TABLE 1

$T°$	B		V	
	$\lambda_i(B)$, Å	Φ_B	$\lambda_i(V)$, Å	Φ_V
2000	4571	7.19	5593	7.19
6000	4414	2.41	5486	2.43
15000	4369	1.08	5465	1.16
50000	4354	0.60	5458	0.70

dispersion and absorption, and their apparent refraction therefore decreases. The corresponding change in spectrophotometric gradient can be found from the relation

$$\Phi_\lambda(T_g) = \Phi_\lambda(T) + \Delta\Phi_\lambda + \nabla\Phi_\lambda.$$

Here T is the temperature of the star, which is related to the spectro-photometric gradient $\Phi_\lambda(T)$ by the well-known expression

$$\Phi_\lambda(T) = \frac{C_2}{T}\left(1 - e^{-\frac{C_2}{\lambda T}}\right)^{-1},$$

T_g the temperature corresponding to the distorted energy distribution in the spectrum, $\Delta\Phi_\lambda$ the correction for atmospheric absorption, and $\nabla\Phi_\lambda$ the correction for atmospheric dispersion. These corrections are given by

$$\Delta\Phi_\lambda = -2.30 \sec z' \frac{d}{d\frac{1}{\lambda}} \lg p_\lambda,$$

$$\nabla\Phi_\lambda = +2.30 \frac{d}{d\frac{1}{\lambda}} \lg\left|\frac{dn_\lambda}{d\lambda}\right|,$$

where p_λ is the absorption coefficient of the Earth's atmosphere. Calculations show that, in the mean, we may take in the entire working range of wavelengths in the B, V system $\nabla\Phi \approx +1.5$, and also $\Delta\Phi \approx +0.4 \sec z'$ and $\Delta\Phi \approx +0.8 \sec z'$ for high and poor seeing conditions, respectively.

If the distortions of spectrophotometric gradients are known, a table similar to Table 1 can be applied to calculate the distorted isophote wavelengths λ_i, and hence the corresponding n_λ, and finally the chromatic refractions.

Table 2 reflects the qualitative aspect of the procedure. It lists the chromatic refraction coefficients $r''_{0\lambda}$ in seconds of arc (standard air) for some values of the spectrophotometric gradient Φ in the B, V systems.

It is remarkable that $r''_{0\lambda}$ is nearly a linear function of Φ. Table 3 gives the corresponding differential refraction for stars of various Φ

3

in relation to stars with $\Phi = 4.0$ for several zenith distances z'; the differential refraction is calculated in millimeters, for a focal distance $F = 100$ m. The differential refraction for larger focal distances is proportionately greater.

TABLE 2

Φ	$r_{0\lambda}''$	
	$\lambda_i(B)$	$\lambda_i(V)$
15	57''542	57''120
10	57.666	57.171
5	57.793	57.218
1	57.894	57.250

TABLE 3

Φ	$\lambda_i(B)$			$\lambda_i(V)$		
	$z'=40°$	$z'=60°$	$z'=75°$	$z'=40°$	$z'=60°$	$z'=75°$
15	—0.11	—0.23	—0.50	—0.04	—0.09	—0.19
10	—0.06	—0.13	—0.28	—0.02	—0.05	—0.10
5	—0.01	—0.02	—0.05	0.00	—0.01	—0.02
1	+0.03	+0.06	+0.13	+0.01	+0.02	+0.04

The corrections for the combined effect of selective absorption and atmospheric dispersion are listed in Table 4. We see that in the V system these corrections are negligible.

TABLE 4

Transparency	$\lambda_i(B)$			$\lambda_i(V)$		
	$z'=40°$	$z'=60°$	$z'=75°$	$z'=40°$	$z'=60°$	$z'=75°$
Poor	—0''00	—0''03	—0''23	0''00	—0''01	—0''07
Good.	0.00	—0.02	—0.10	0.00	—0.01	—0.03

The length of atmospheric spectra between, say, 0.3 and 0.7μ is $\sim 1''.52$ for $z' = 25°$ and $\sim 12''.2$ for $z' = 75°$, which corresponds to 0.74 and 5.9 mm for a focal distance $F = 100$ m.

It is also interesting to consider the rate of change in the length of the atmospheric spectrum in seconds of arc per hour or in millimeters per hour, for $F = 100$ m. (This question arises, in particular, when the guiding telescope and the "receiver" have different spectral sensitivity

4

' bands, e.g., visual and infrared.) The corresponding rates of change are listed in Table 5 for the $0.56 - 2.0\mu$ region for the latitude 44°, three azimuths A, and three zenith distances z'.

FIGURE 2.

TABLE 5

A	z'		
	40°	60°	75°
0°	0.00 sec of arc/hr	0.00 sec of arc/hr	0.00 sec of arc/hr
45	0.22	0.51	1.80
90	0.31	0.71	2.56
0°	0.00 mm/hr	0.00 mm/hr	0.00 mm/hr
45	0.10	0.24	0.88
90	0.15	0.35	1.24

From the numerical data above we see that differential chromatic refraction may reach substantial magnitudes and it therefore must be taken into consideration in problems connected with the guiding of long-focus telescopes.

3. The experimental aspect of the problem was studied by taking photographs of binaries with 0.04 sec exposure through the Pulkovo 285-mm television telescope (equivalent focal distance 56 m), with subsequent 8.3-fold enlargement on the kinescope screen /8/. As an example, Figure 2 gives a somewhat enlarged print showing a succession of images of γ Leonis, with 3".9 component separation. The double-star structure is actually distinguishable in one case only — the third image from the bottom; the other images are highly blurred. This is attributable to the unsatisfactory location of the telescope (on the balcony of a public building). These first experimental photographs are unfortunately inadequate for reaching any definite conclusions concerning differential chromatic refraction, the more so since the components of γ Leonis belong to close spectral and luminosity classes, gKOp and gG5. A special television telescope is now being mounted in a new isolated building. Experimental investigations of differential chromatic refraction, whose applied significance is self-evident, will be repeated with this new telescope, for more suitable objects belonging to radically different spectral classes.

Bibliography

1. Edlen, B. —JOSA, **43** : 339. 1953.

2. Koronkevich, V. P. Dissertation.— Institut Metrologii im. D. I. Mendeleeva. Leningrad. 1956.

3. Rank, D.H., G.D.Sakcena, and T.K.McCobin. — JOSA, **48** : 455. 1958.

4. Svenson, K. — Ark. Fys., **16** : 361. 1960.

5. Peck, E.R. and B.N.Kanna. —JOSA, **52** : 416. 1962.

6. Erickson, K.E. —JOSA, **52** : 777. 1962.

7. Martynov, D.Ya. Prakticheskaya astrofizika (Applied Astrophysics).— Moskva, Fizmatgiz. 1961.

8. Kuprevich, N.F. —Izv. GAO, No.163 : 133. 1960.

I. G. Kolchinskii

CORRELATION BETWEEN IMAGE PULSATIONS OF STARS AT A SMALL ANGULAR DISTANCE FROM EACH OTHER

1. CALCULATION OF CORRELATIONS

Examination of the trails of double stars photographed with a fixed astrograph will reveal a fairly close correlation between the deviations from the mean line for each of the two components. For example, an almost perfect correlation is observed for the trails of the brighter components of the β Scorpii system (some 14" separation) photographed with the 400-mm astrograph at our observatory. If fairly many trails of sufficiently bright stars from a dense cluster (e.g., the Pleiades) are photographed on one plate, the correlation between the fluctuations is seen to diminish as the angular separation between the stars increases. This trend was observed by Schlesinger /1/ as early as 1912. While comparing the trail fluctuations for the brighter stars of the Pleiades, he noticed that all correlation vanished already at distances of some 20'.

According to Bugoslavskaya /2/, who examined some plates taken with the wide-angle astrograph of the Shternberg Astronomical Institute ($d = 230$ mm, $f = 2.3$ m), the principal minima and maxima recur for trails separated by 0°.5, whereas at a distance of 1° the entire scintillation pattern changes. No other estimates have been made to the best of our knowledge. And yet the determination of the exact angular separation between close stars at which the image pulsations become uncorrelated is of considerable interest in astrometry. In this paper, proceeding from some simplifying assumptions, we calculate the correlation function R_{12} for the pulsation of two stars at a small angular distance from each other. R_{12} is also determined from the results of measurements of Pleiades trails photographed with the 400-mm astrograph of the Ukrainian Academy of Sciences' Main Astronomical Observatory. By comparing the theoretical and the observational results, we estimate the effective thickness of the atmosphere, whose influence on image pulsation is decisive.

The pulsation of a star viewed through a telescope is the result of phase fluctuations on the front of the light wave reaching the objective. If we consider the simple case of an objective covered by a diaphragm with two narrow parallel slits, distant D from each other (this separation is approximately equal to the objective diameter), the difference of phase fluctuations $\Delta\varphi$ at this distance is related to the image pulsation δa by the following expression:

$$\Delta\varphi = \frac{2\pi D}{\lambda}\,\delta a. \qquad (1)$$

Here it is assumed that the mean position of the plane wave front traveling from the star is parallel to the plane of the objective (diaphragm). Relation (1) can be assumed to apply for each of two close stars (separated by a small angular distance), so

$$\Delta\varphi_1 = \frac{2\pi D}{\lambda}\,\delta\alpha_1,$$

$$\Delta\varphi_2 = \frac{2\pi D}{\lambda}\,\delta\alpha_2, \tag{2}$$

where $\Delta\varphi_1$, $\Delta\varphi_2$, $\delta\alpha_1$, $\delta\alpha_2$ are the corresponding differences of phase fluctuations at the distance D and the corresponding image pulsations. For simplicity, the plane through the lines from the center of the objective to the two stars is taken as perpendicular to the diaphragm slits.
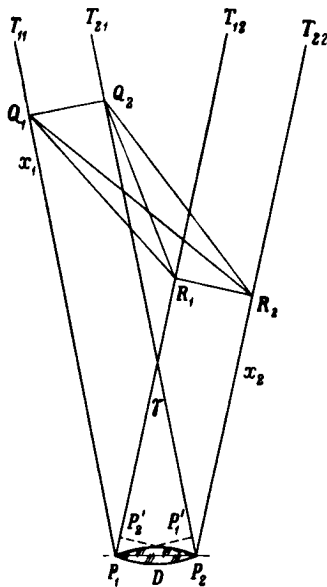
FIGURE 1.

The correlation functions for the pulsations of the light wave traveling from the two stars is given by

$$R_{\alpha_1\alpha_2} = \frac{\overline{\delta\alpha_1\delta\alpha_2}}{\sqrt{\overline{(\delta\alpha_1)^2}}\,\sqrt{\overline{(\delta\alpha_2)^2}}}\,. \tag{3}$$

This expression is clearly identical to

$$R_{\varphi_1\varphi_2} = \frac{\overline{\Delta\varphi_1\Delta\varphi_2}}{\sqrt{\overline{(\Delta\varphi_1)^2}}\,\sqrt{\overline{(\Delta\varphi_2)^2}}}\,. \tag{4}$$

The problem thus reduces to the computation of the correlation coefficient between the difference of phase fluctuations in two pairs of parallel beams which make a small angle with the telescope objective. Let this small angle

be γ (Figure 1). Let D be the diameter of the objective. Take the rays Q_1P_1, Q_2P_2 and R_1P_1, R_2P_2. Let L be the path of the rays in the atmosphere, and let

$$\frac{D}{L} \ll 1.$$

We assume that the refractive index n' fluctuates mainly due to fluctuations of temperature T'. Then, in the geometrical optics approximations, assuming small fluctuations in n', the difference in phase fluctuations at the points P_1 and P_2 for the rays Q_1P_1 and Q_2P_2 is given by (see /3/)

$$(\varphi_{P_1} - \varphi_{P_2})_1 = \frac{\omega}{2c} \frac{pK}{(\bar{T})^2} \int_0^L (T_1' - T_2')_1 \, dx_1. \tag{5}$$

Here ω is the circular frequency, c the velocity of light, p atmospheric pressure in millimeters, K a constant coefficient, $\bar{T}$ the absolute temperature (mean value), x_1 an integration constant reckoned along the line P_1Q_1 or P_2Q_2.

In this integral we neglect the comparatively small phase tailing on the small segment $P_2P_1' \sim D\gamma$, which is justified for small n' and for n' correlation lengths comparable with D (as the case is in practice).

For the rays R_1P_1, R_2P_2 we similarly have

$$(\varphi_{P_1} - \varphi_{P_2})_2 = \frac{\omega}{2c} \frac{pK}{(\bar{T})^2} \int_0^L (T_1' - T_2')_2 \, dx_2. \tag{6}$$

The mean value of the product of these differences is

$$\overline{(\varphi_{P_1} - \varphi_{P_2})_1 (\varphi_{P_1} - \varphi_{P_2})_2} = \left(\frac{\omega}{2c}\right)^2 \frac{p^2K^2}{(\bar{T})^4} \int_0^L \int_0^L \overline{(T_1' - T_2')_1 (T_1' - T_2')_2} \, dx_1 dx_2. \tag{7}$$

The integrand may be written as

$$(T_1' - T_2')_1 (T_1' - T_2')_2 = \overline{T_{11}' T_{12}'} - \overline{T_{21}' T_{12}'} + \overline{T_{21}' T_{22}'} - \overline{T_{11}' T_{22}'}. \tag{8}$$

We introduce a Gaussian correlation function for the fluctuations in T'. Then

$$\overline{T_{11}' T_{12}'} = \overline{(T')^2} e^{-\frac{(Q_1R_1)^2}{a^2}}, \tag{9}$$

where Q_1R_1 is the distance between two points on the corresponding rays, a the correlation length. Similarly,

$$\overline{T_{21}' T_{12}'} = \overline{(T')^2} e^{-\frac{(Q_2R_1)^2}{a^2}}, \tag{10}$$

$$\overline{T_{21}' T_{22}'} = \overline{(T')^2} e^{-\frac{(Q_1R_2)^2}{a^2}}, \tag{11}$$

$$\overline{T_{11}' T_{22}'} = \overline{(T')^2} e^{-\frac{(Q_1R_2)^2}{a^2}}. \tag{12}$$

Substituting (9)—(12) in (8), we find

$$\overline{(T_1' - T_2')_1 (T_1' - T_2')_2} = \overline{(T')^2} \left(e^{-\frac{(Q_1R_1)^2}{a^2}} - e^{-\frac{(Q_2R_1)^2}{a_1}} + e^{-\frac{(Q_2R_2)^2}{a^2}} - e^{-\frac{(Q_1R_2)^2}{a^2}} \right). \quad (13)$$

From Figure 1 we see that

$$\left. \begin{aligned}
(Q_1R_1)^2 &= x_1^2 + \left(x_2 + D \sin \tfrac{\gamma}{2} \right)^2 - 2x_1 \left(x_2 + D \sin \tfrac{\gamma}{2} \right) \cos \gamma, \\
(Q_2R_2)^2 &= x_2^2 + \left(x_1 + D \sin \tfrac{\gamma}{2} \right)^2 - 2x_2 \left(x_1 + D \sin \tfrac{\gamma}{2} \right) \cos \gamma, \\
(Q_1R_2)^2 &= (x_1 - x_2)^2 + \left(D + 2x_2 \sin \tfrac{\gamma}{2} \right)^2 - \\
&\quad - 2(x_1 - x_2)\left(D + 2x_2 \sin \tfrac{\gamma}{2} \right) \cos \left(90° + \tfrac{\gamma}{2} \right), \\
(Q_2R_1)^2 &= \left(x_1 + D \sin \tfrac{\gamma}{2} - \frac{D}{2 \sin \tfrac{\gamma}{2}} \right)^2 + \left(x_2 + D \sin \tfrac{\gamma}{2} - \right. \\
&\quad \left. - \frac{D}{2 \sin \tfrac{\gamma}{2}} \right)^2 - 2 \left(x_1 + D \sin \tfrac{\gamma}{2} - \frac{D}{2 \sin \tfrac{\gamma}{2}} \right) \times \\
&\quad \times \left(x_2 + D \sin \tfrac{\gamma}{2} - \frac{D}{2 \sin \tfrac{\gamma}{2}} \right) \cos \gamma.
\end{aligned} \right\} \quad (14)$$

Here $P_1Q_1 = x_1$ and $P_2R_2 = x_2$. For small $\gamma (\gamma \ll 1)$, we have

$$\left. \begin{aligned}
(Q_1R_1)^2 &= (x_1 - x_2)^2 + D\gamma (x_2 - x_1), \\
(Q_2R_2)^2 &= (x_1 - x_2)^2 + D\gamma (x_1 - x_2), \\
(Q_1R_2)^2 &= (x_1 - x_2)^2 + D^2 + D\gamma (x_1 + x_2), \\
(Q_2R_1)^2 &= (x_2 - x_1)^2 + D^2 - D\gamma (x_1 + x_2).
\end{aligned} \right\} \quad (15)$$

Substituting (15) in (13), we find

$$\overline{(T_1' - T_2')_1 (T_1' - T_2')_2} = \overline{(T')^2} \left[e^{-\frac{(x_1-x_2)^2 + D\gamma(x_2-x_1)}{a^2}} + e^{-\frac{(x_1-x_2)^2 - D\gamma(x_2-x_1)}{a^2}} - \right.$$
$$\left. - e^{-\frac{(x_2-x_1)^2 + D^2 - D\gamma(x_1+x_2)}{a^2}} - e^{-\frac{(x_1-x_2)^2 + D^2 + D\gamma(x_1+x_2)}{a^2}} \right]. \quad (16)$$

Substituting the above expression in (7), we obtain a sum of four double integrals

$$I = I_1 + I_2 - I_3 - I_4, \quad (17)$$

where

$$I_1 = \int_0^L \int_0^L e^{-\frac{(x_1-x_2)^2 + D\gamma(x_2-x_1)}{a^2}} dx_1 dx_2,$$

$$I_2 = \int_0^L \int_0^L e^{-\frac{(x_1-x_2)^2 - D\gamma(x_2-x_1)}{a^2}} dx_1 dx_2,$$

$$I_3 = \int_0^L \int_0^L e^{-\frac{(x_2-x_1)^2 + D^2 - D\gamma(x_1+x_2)}{a^2}} dx_1 dx_2,$$

$$I_4 = \int_0^L \int_0^L e^{-\frac{(x_1-x_2)^2 + D^2 + D\gamma(x_1+x_2)}{a^2}} dx_1 dx_2.$$

10

It is easily seen that $I_1 = I_2$. Therefore,

$$I = 2I_1 - (I_3 + I_4). \tag{18}$$

For I_1 we find

$$I_1 = \frac{a^2}{2}\left(e^{-\frac{L^2 - D\gamma L}{a^2}} - 1\right) + \frac{\sqrt{\pi}}{2}\, e^{p^2} \cdot a\left[\Phi\left(\frac{L}{a} - p\right) + \Phi(p)\right]\left(L - \frac{D\gamma}{2}\right) +$$
$$+ \frac{a^2}{2}\left(e^{-\frac{L^2 + D\gamma L}{a^2}} - 1\right) + \frac{\sqrt{\pi}}{2}\, e^{p^2} \cdot a\left[\Phi\left(\frac{L}{a} + p\right) - \Phi(p)\right]\left(L + \frac{D\gamma}{2}\right), \tag{19}$$

where $p = \frac{D\gamma}{2a}$. Seeing that $\Phi(x) = \frac{2}{\sqrt{\pi}}\int_0^x e^{-s^2} ds$ (Kramp's function), we write

$$I_3 + I_4 = \frac{a^2 \sqrt{\pi}}{4p}\, e^{-\frac{D^2}{a^2} + p^2}\left\{ e^{\frac{4Lp}{a}}\left[\Phi\left(\frac{L}{a} + p\right) - \Phi(p)\right] - \right.$$
$$- e^{-\frac{4Lp}{a}}\left[\Phi\left(\frac{L}{a} - p\right) - \Phi(-p)\right] + \left[\Phi\left(\frac{L}{a} + p\right) - \Phi(p)\right] -$$
$$\left. - \left[\Phi\left(\frac{L}{a} - p\right) - \Phi(-p)\right]\right\}. \tag{20}$$

Substituting (19) and (20) in (18), we obtain an expression for $I(p) = I\left(\frac{D\gamma}{2a}\right)$. Putting $p = 0$, we have

$$I(0) = 2a^2\left(e^{-\frac{L^2}{a^2}} - 1\right) + 2\sqrt{\pi}a\Phi\left(\frac{L}{a}\right)\cdot L -$$
$$- a^2\sqrt{\pi}e^{-\frac{D^2}{a^2}}\left[2\frac{L}{a}\Phi\left(\frac{L}{a}\right) + \frac{2}{\sqrt{\pi}}\left(e^{-\frac{L^2}{a^2}} - 1\right)\right]. \tag{21}$$

For $\frac{L}{a} \gg 1$ and $\gamma = 0$,

$$I\left(\gamma = 0,\ \frac{L}{a} \gg 1\right) = 2\sqrt{\pi}aL\left(1 - e^{-\frac{D^2}{a^2}}\right). \tag{22}$$

Multiplying this expression by $\left(\frac{\omega}{2c}\right)^2 \frac{p^2 K^2}{(T)^4}$, we obtain the mean square of the difference of phase fluctuations for two parallel rays.

If $\frac{L}{a}$ is large and p is small, we omit terms of higher orders of smallness in (19) and (20) to obtain

$$I(p) \cong 2\sqrt{\pi}\left[aL - \frac{a^2}{8p}\, e^{-\frac{D^2}{a^2}}\left(e^{\frac{4Lp}{a}} - e^{-\frac{4Lp}{a}}\right)\right]. \tag{23}$$

The normalized cross-correlation function is

$$R(\gamma) = \frac{\overline{(\varphi_{p_1} - \varphi_{p_2})_1 (\varphi_{p_1} - \varphi_{p_2})_2}}{\overline{(\varphi_{p_1} - \varphi_{p_2})^2}} = \frac{aL - \frac{a^2}{8p}\, e^{-\frac{D^2}{a^2}}\left(e^{\frac{4Lp}{a}} - e^{-\frac{4Lp}{a}}\right)}{aL\left(1 - e^{-\frac{D^2}{a^2}}\right)}, \tag{24}$$

and $R(\gamma)_{\gamma\to 0}=1$. Here of necessity $\dfrac{L}{a}\gg 1$ and $p=\dfrac{D\gamma}{2a}\ll 1$. We write (24) as

$$R\left(\frac{D}{a},\ \frac{L\gamma}{2a}\right)=\frac{1}{1-e^{-\frac{D^2}{a^2}}}\left[1-\frac{e^{-\frac{D^2}{a^2}}\left(e^{2\frac{D}{a}\left(\frac{L\gamma}{a}\right)}-e^{-\frac{D}{a}\left(\frac{L\gamma}{a}\right)}\right)}{4\frac{D}{a}\left(\frac{L\gamma}{a}\right)}\right]. \tag{25}$$

Figure 2 plots the function $R\left(\dfrac{D}{a},\ \dfrac{L\gamma}{a}\right)$ for various $\dfrac{D}{a}$ and $\dfrac{L\gamma}{a}$. The graphs are plotted for $R>0$ only. For large γ, the function R calculated from (25) may assume large negative values. This is a consequence of our underlying assumption. For our problem, it is significant that already for $\dfrac{L\gamma}{a}\sim 1$ and $\dfrac{D}{a}\sim 1$, the function R is substantially less than unity.
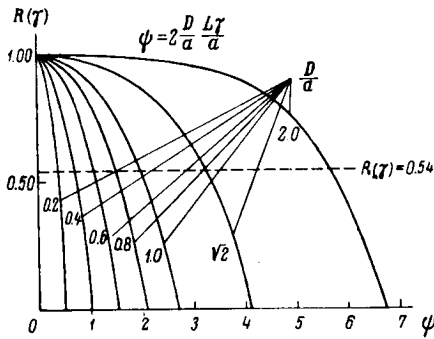
FIGURE 2.
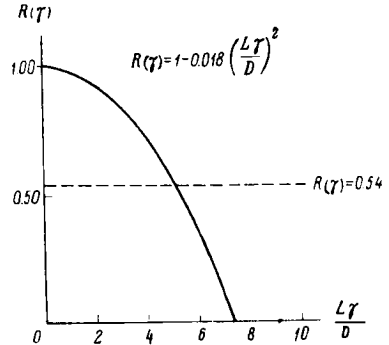
FIGURE 3.

If terms of higher order in γ are retained, the final estimate is obviously not affected.

Note that correlation coefficients of the same form were derived by Krasil'nikov /3/ for the fluctuations of the signal level in two receivers at a certain distance from each other (Gaussian correlation between the fluctuations in n' was assumed). For the case of telescopic image pulsation, we may take $\dfrac{D}{a}\sim 1$, since the correlation length is of the same order as the objective diameter D. Here

$$R\left(\frac{D}{a}=1,\ \frac{L\gamma}{D}\right)=1.582-0.582\frac{e^{2\frac{L\gamma}{D}}-e^{-\frac{2L\gamma}{D}}}{4\frac{L\gamma}{D}}=$$

$$=1.582-0.582\frac{\operatorname{sh}\frac{2L\gamma}{D}}{2\frac{L\gamma}{D}}. \tag{26}$$

We now proceed with the evaluation of (7), assuming that the fluctuations in n' at points 1 and 2 are functionally related by

$$\overline{(n_1' - n_2')^2} = B^2 \rho_{12}^{2/3}. \tag{27}$$

Here ρ_{12} is the distance between the two points, B^2 is a constant. Then

$$\overline{(T_1' - T_2')_1 (T_1' - T_2')_2} = \frac{1}{2} B^2 [(Q_2 R_1)^{1/3} - (Q_1 R_1)^{1/3} - (Q_2 R_2)^{1/3} + (Q_1 R_2)^{1/3}]. \tag{28}$$

Substituting (28) in (7), and retaining terms of the lowest order in γ, we finally obtain

$$I \approx \left[4\left(\frac{D}{L}\right)^{5/3} L^{8/3} - 0.072 L^3 \gamma^2 D^{-1/3} \right]. \tag{29}$$

Moreover,

$$I(L, D, 0) = 2 \int_0^L \int_0^L \{ [(x_2 - x_1)^2 + D^2]^{1/3} - (x_2 - x_1)^{2/3} \} dx_1 dx_2 \approx 4 D^{5/3} L. \tag{30}$$

In accordance with our assumptions, $\frac{D}{L} \ll 1$, $\gamma \ll 1$. Therefore,

$$R(\gamma) = \frac{I(L, D, \gamma)}{I(L, D, 0)} \cong 1 - 0.018 \left(\frac{L\gamma}{D}\right)^2. \tag{31}$$

If γ is expressed in minutes of arc, we have

$$R(\gamma) = 1 - 1.51 \cdot 10^{-9} \left(\frac{L}{D}\right)^2 \cdot \gamma^2. \tag{32}$$

The function (31) is plotted in Figure 3.

The correlation between the image pulsations thus essentially diminishes at the angular distance $\gamma = \frac{a}{L}$ (if Gaussian correlation function is adopted for n') or $\gamma = \frac{D}{L}$ (if the 2/3 law is assumed).

To sum up, the larger the air mass L, the smaller the angular distance at which the pulsations become uncorrelated. For example, the correlation between the image pulsations of the two components of a binary separated by an angle γ is higher for small zenith distances (when L is small) than for large zenith distances. This also applies to any two points of a planetary disk separated by a small angle γ. This phenomenon is responsible for the rapid deterioration of the resolving power at large z.

For large a or D, the correlation starts diminishing at progressively larger γ. The applied significance of this effect in astrophotography can be illustrated by the following example. The moon or some planet are being photographed for the purpose of figure determination; the exposure is a fraction of a second. If the pulsations of the lower and the upper edges of the image are uncorrelated, the figure of the planet may be distorted. A diaphragm will not help in this case, since for a smaller aperture the image pulsations become uncorrelated at a smaller angular distance between the extreme points of the image. Full-aperture observations are therefore

more accurate in this case. That the correlation decreases sharply for $L_\gamma \sim a$ (or D) is physically obvious. L_γ is the distance between the two beams at a distance L from the objective. If L_γ is comparable with the characteristic size of the refractional inhomogeneities, the correlation between phase fluctuations for two pairs of rays radically diminishes.

2. COMPARISON WITH OBSERVATIONS

The correlation between image pulsations of two close stars can be estimated from observations. We examined two plates with trails of the Pleiades cluster. The relevant data are summarized in Table 1.

TABLE 1

Date	Plate	$\varkappa$	Standard deviation
20 Feb. 1957	A	73°	0".52
25 Dec. 1961	B	30	0.32

The photographs were made through a full aperture, 40 cm. On plate A, 10 trails were measured, on plate B, 12 trails. These trails are listed in Table 2.

TABLE 2

Trail number	Star	Magnitude
1	+24°546	5.6
2	Asterope I	5.6
3	Taygete	4.1
4	Maia	3.7
5	+23°505	5.3
6	Pleione	5.1
7	Electra	3.5
8	Alcyone	2.7
9	Atlas	3.5
10	Merope	4.0
11	+23°563	6.1
12	+22°563	5.5

The plates were measured on the MIR-12 instrument equipped with a special micrometer. A section 50 mm long was measured in each trail, which corresponded to a period of some 2 min. The deviations from the mean line were measured at intervals of 0.1 mm. The measurements on plate A were treated so as to yield the coefficients of the straight lines providing the best approximation to 5-mm long sections of the trail, and the deviations were calculated relative to these lines.

14

• Plate B was treated graphically. A smooth curve was passed through the averaged results of measurements, and the deviations were taken relative to this curve. In practice, both techniques give the same result. For each trail a succession of 500 deviations Δ_i was compiled: $\Sigma \, \Delta_i$ was close to zero.

The correlation coefficients between pairs of trails were calculated from

$$R_{kl} = \frac{\sum_i \Delta_{ik}\Delta_{il}}{\sqrt{\sum_i \Delta_{ik}^2}\ \sqrt{\sum_i \Delta_{il}^2}}\,. \tag{33}$$

Here k and l are the trail numbers. All the trails were measured from east to west at equal intervals, so that the Λ_i having the same i on different trails corresponded to the same instants. The coefficients R_{kl} were then matched with the angular distances γ between the stars. Our R_{kl} fall into four groups in this respect: $\gamma \leqslant 12.5;\ 12.5 < \gamma \leqslant 25';\ 25' < \gamma \leqslant 50';\ \gamma > 50'$. They are listed in Table 3.

TABLE 3

Star pairs	Angular distance γ	Mean γ for the group	R_{kl}		Mean $R(\gamma)$
			Plate A	Plate B	
5—7	10.6		0.48		
6—9	5.6	10.1	0.50	0.54	0.54
3—4	10.6		0.46	0.68	
3—5	11.9		0.47		
2—3	11.2			0.63	
4—5	15.0		0.32	0.72	
1—2	20.0			0.76	
7—10	21.9	20.9	0.41		0.36
8—9	21.9		0.24	0.11	
4—7	20.0		0.31		
6—8	24.4		0.11		
8—10	18.8		0.31		
3—7	21.8		0.33		
11—12	25.0			0.33	
7—8	35.6	38.4	0.28	0.62	0.29
5—10	28.1		0.33		
4—8	26.9		0.35		
4—10	25.6		0.46		
9—10	38.1		0.11	0.14	
4—9	48.1		0.12		
3—8	48.8		0.53		
4—6	49.4		0.04		
5—8	38.1		0.38		
10—11	48.8			0.10	
5—6	61.2		0.07	0.08	
6—7	59.4	59.7	0.20	0.05	0.08
3—6	58.8		0.06		
5—9	60.0		0.01		
7—9	57.5		0.06		

The mean correlation coefficient for each group and the individual R_{kl} are plotted in Figure 4 as a function of γ, where dots mark the data of plate A, circles the data of plate B, and dotted circles the mean values. From

Table 3 and Figure 4 we come to the following conclusions:
1) All R_{hl} are positive.
2) $R(\gamma)$ decreases with increasing γ.
3) If a "correlation radius" $\gamma*$ is defined as the angle γ such that $R(\gamma*) = 0.5$, we find that its value is 10', which is in good agreement with previous crude estimates.
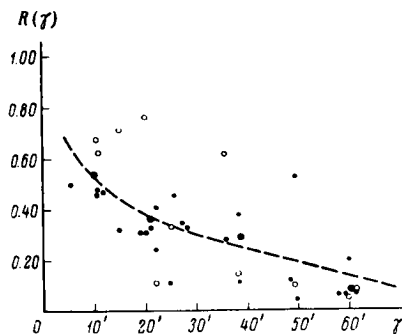
FIGURE 4.

Comparison of theoretical formulas (24) and (32) with $R(\gamma)$ can be carried out only to a certain approximation, since strictly speaking, these formulas apply to an objective screened by a diaphragm with two slits. For an ordinary circular aperture, the image pulsation is an integrated effect. We may assume, however, that the mean square difference in phase fluctuations and the mean square angle pulsations are described by the same formula as for the slitted diaphragm, provided a certain effective diameter is substituted for the distance between the slits. In comparing formula (32) with observations, we shall use the diameter of the photographic objective of our astrograph, i.e., $D = 40$ cm.

Let us first consider relation (24). We take $R(\gamma) = 0.54$ for $\gamma = 10'$. Marking $R(\gamma) = 0.54$ on the graphs with various $\dfrac{D}{a}$ (see Figure 2), we obtain the values of $\dfrac{L}{D}$ and L listed in Table 4.

TABLE 4

$\dfrac{D}{a}$	$\dfrac{L\gamma}{D}$	$\dfrac{L}{D} (\gamma = 10')$	$L (D = 40 \text{ cm})$
0.2	4.40	$1.5 \cdot 10^3$	605 m
0.4	2.18	$7.5 \cdot 10^2$	300
0.6	1.41	$4.9 \cdot 10^2$	195
0.8	1.13	$3.9 \cdot 10^2$	155
1.0	0.98	$3.4 \cdot 10^2$	135
$\sqrt{2}$	0.80	$2.8 \cdot 10^2$	110
2.0	0.72	$2.5 \cdot 10^2$	100

We now proceed with an analysis of relation (31). Here, for $\gamma = 10'$ and $R(\gamma) = 0.54$, we have $\frac{L}{D} = 1.76 \cdot 10^3$.
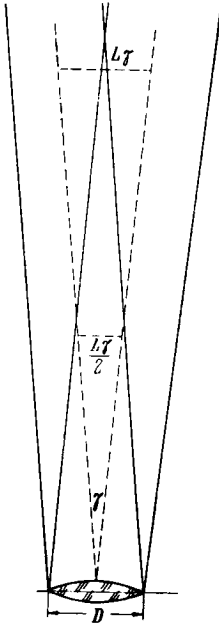
FIGURE 5.

For $D = 40$ cm, we have $L \sim 700$ m. But $L = L_0 \sec z$, where L_0 is the layer thickness. Identifying this thickness with $z = 52°$ (the mean z for the two plates), we find $L_0 \sim 400$ m. From (24) and (32) it thus follows that the layer thickness L_0 is a few hundred meters. This estimate of L_0 is in good agreement with other estimates. Relations (24) and (32) lead to a rapid reduction in R: if, as it follows from out data, $R(\gamma) = 0.54$ for $\gamma = 10'$, $R(\gamma)$ is zero already for $\gamma = 15'$. In reality, however, $R(\gamma)$ does not vanish even when $\gamma \sim 60'$. The fact that the correlation coefficient in the foregoing formulas does not decrease at infinity is a consequence of our approximation. An expression can be written for $R(\gamma)$ which will drop to zero at infinity. Indeed, for small γ and $L \gg D$, $R(\gamma)$ approximately corresponds to the correlation coefficient between the differences in phase fluctuations for two pairs of parallel beams displaced by parallel translation to a distance $S = \frac{L\gamma}{2}$ (Figure 5). The corresponding correlation function in the case of the $\frac{2}{3}$ law can be derived from expression (20) in /4/, by substituting $\frac{L\gamma}{2}$ for the original translation distance $v\tau$. Then

$$R(\gamma) = \frac{\left(1 + \frac{L\gamma}{2D}\right)^{5/3} + \left(\left|1 - \frac{L\gamma}{2D}\right|\right)^{5/3}}{2} - \left(\frac{L\gamma}{2D}\right)^{5/3}. \qquad (34)$$

The graph of this function is plotted in Figure 6; the dotted circles mark the observed values. Clearly, $\lim_{\gamma \to \infty} R(\gamma) = 0$. For $R(\gamma) = 0.54$, we have $\frac{L\gamma}{2D} = 1.42$. For $\gamma = 10'$, which corresponds to 0.00291 radians, we have

FIGURE 6.

17
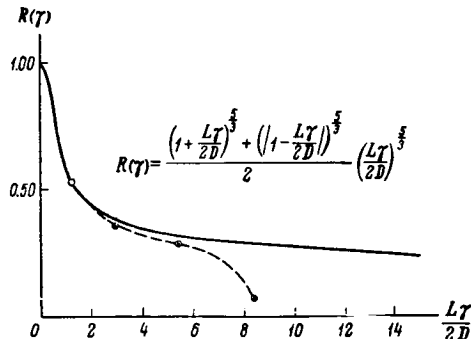
$\frac{L}{2D} \cong 4.9 \cdot 10^2$. for $D = 40\,\text{cm}$, we obtain $L \sim 380\,\text{m}$. Table 5 lists the values of $R(\gamma)$ recovered from the graph for various angular distances, assuming this $\frac{L}{D}$ ratio.

The fit between the observed and the calculated values is satisfactory. The observed curve displays a tendency to depart from the theoretical line in the direction of lower $R(\gamma)$. This aspect is apparently attributable to the omission of the low-frequency pulsations. The latter should raise the correlation radius. Indeed, suppose that the hypothesis of "frozen turbulence" applies. Then,

$$\frac{a}{v} \cong \tau, \tag{35}$$

where a is the correlation scale, v the corresponding wind velocity component, and τ the period of fluctuation. On the other hand, the correlation radius γ is given by

$$L\gamma \sim a. \tag{36}$$

From the last two relations we have

$$\gamma \sim \frac{v\tau}{L} = \frac{v}{\nu L}, \tag{37}$$

where $\nu = \frac{1}{\tau}$ is the frequency of fluctuations. From (36) it follows that low-frequency fluctuations produce a larger correlation radius γ^* than the high-frequency fluctuations do. For example, for fluctuations with a period of $10\,\text{sec}$, i.e., $\nu = 0.1\,\text{c/s}$, the correlation radius γ^* is 10 times as large as for $\nu = 1\,\text{c/s}$. If the latter frequencies correspond to γ^* of some $10'$, then frequencies of $0.1\,\text{c/s}$ correspond to γ^* of some $100'$, i.e., the γ^* is comparable with the diameter of the plate field $(\sim 2°)$.

TABLE 5

γ	$\frac{L\gamma}{2D}$	$R(\gamma)_{calc.}$	$R(\gamma)_{obs.}$
$21'$	2.94	0.38	0.36
38.4	5.40	0.32	0.29
59.7	8.40	0.29	0.08

In our opinion, $R(\gamma)$ should be determined with various instruments as a function of z, meteorological conditions, and locality. This will provide a basis for estimation of the effective thickness of the atmospheric layer responsible for the pulsation of stellar images.

Bibliography

1. Schlesinger, F. —Publ. Allegheny Obs., 3, No.1. 1912.

2. Bugoslavskaya, E.Ya. —AZh, 15:450. 1938.

3. Krasil'nikov, V.A. —Izv. AN SSSR, geogr. and geophys. series, No.13:33. 1949.

4. Kolchinskii, I.G. —Izv. GAO AN UkrSSR, 4:13. 1961.

I. G. Kolchinskii

BEADING OF STAR TRAILS

The trails of moving stars photographed through a fixed tube of an astrograph often reveal so-called beading. The trail density is not uniform, and the trail seems to be made up from individual nodules which are much darker than the rest of the image. The distance between these nodules (beads) is approximately constant along the trail. The beads are mostly set against a continuous background of the principal trail, but in some cases the trail may break into isolated beads, the gaps showing hardly any perceptible darkening.

Trail beading was often commented upon by observers of double stars, e. g., Hertzsprung /1/, since in photographic observations of binaries the trails are applied to improve plate setting.

Bugoslavskaya /2/ also investigated trail beading. Measurements of trails taken with the Moscow Observatory large astrograph gave $\tau = 0\overset{s}{.}3$ as the mean time interval between successive beads. For the wide-angle astrograph this interval was $0\overset{s}{.}37$, and for the coronograph $0\overset{s}{.}34$.

BEADING IN TRAILS TAKEN AT THE MAIN
ASTRONOMICAL OBSERVATORY OF THE
UKRAINIAN ACADEMY OF SCIENCES

To elucidate the exact nature of beading, we inspected 157 plates with trails photographed on the 400-mm astrograph of the Main Astronomical Observatory in the period from January 1955 to December 1956. The observations had been carried out during 79 nights. Each plate showed from one to five trails. Examination of the plates indicated that all the trails could be divided into five groups.

1) Trails without beading.
2) Trails with faint, hardly noticeable beads.
3) Trails with distinct beads which have no sharp outline.
4) Trails with very distinct, equally spaced beads.
5) Trails with highly pronounced beading, the individual beads placed at approximately equal intervals.

From the 157 plates inspected, 60 plates (37%) revealed distinct trail beading. Two of these plates (Nos. 159 and 161), both taken during the night of 29/30 December 1956, displayed 10 trails for various z from 51

to 81°. All these trails are distinctly beaded. The distribution of beaded plates in z is given in Table 1.

TABLE 1

	$z < 60°$	$60° \leqslant z < 70°$	$70° \leqslant z < 80°$	$z > 80°$
Percent of the total number of beaded plates	12	32	36	20
Percent of the total number of plates	21	39	30	10

We see from Table 1 that trail beading prevails at high zenith distances. All plates taken at $z > 80°$ present distinctly beaded tails. Of the total of 79 nights, beading was observed during 34 nights, i.e., in 43% of the cases.

In certain nights, the beading seems to be particularly distinct. The amplitude of luminosity variation, which corresponds to the change in photographic density from bead to gap, could not be determined with satisfactory photometric precision, since the plates had been originally intended for image pulsation measurements and therefore did not carry an imprinted photometric scale. A crude estimate was obtained by studying the variation of trail width as a function of stellar magnitude. This dependence for our plates (Ilford Ordinary, No. 30) was derived by measuring
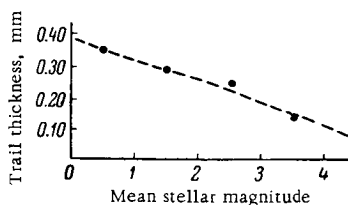
FIGURE 1.

the widths of 34 selected trails. All stars were divided into four groups corresponding to the magnitudes $0-1$, $1-2$, $2-3$, $3-4$. The mean effective exposure, i.e., the time during which the star image moved over the plate by a distance equal to its diameter, was approximately constant for the four groups. The average results are plotted in Figure 1. As a crude estimate, an increase by one stellar magnitude corresponds to trail broadening by 0.07 mm. The amplitude of brightness variation in beaded trails is estimated in the following.

IMAGE PULSATION AND TRAIL BEADING

Examination of the plates showed that the beads were in no way connected with image pulsation, at least not with pulsations in the region of 1 c/s.

21

In many cases, several beads were accommodated in a single pulsation wave.

Figure 2 plots the deviation from the mean line (the trail direction) for one of our plates (No. 150). The measurements were made at intervals of 0.1 mm. No correction was introduced for the trail slant relative to the axis of the measuring instrument. Black dots mark the abscissas corresponding to interbead gaps. We see that several beads are accommodated by a single pulsation wave. Image pulsation and trail beading are thus two independent phenomena.
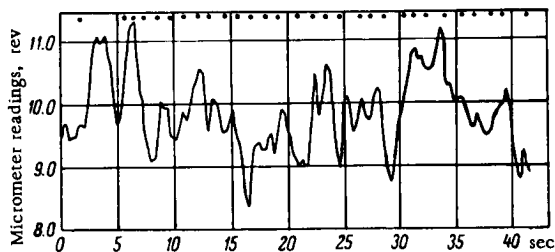
FIGURE 2.

No definite conclusions can be reached concerning the shape of the beads. Some beads appear as characteristic nodules against the trail background, while other beads are nearly circular. In some cases, the beads are distinctly elongated in the direction of the zenith, which is apparently due to atmospheric dispersion.

"BEADING PERIOD"

To determine the mean time between successive beads ("beading period"), we selected 14 plates with 35 trails, characterized by regular beaded structure. The gap-to-gap distances were measured, since the cross hairs could be set more easily to the relatively light gaps: the cross hairs are difficult to distinguish against the high-density beads. A length of 20 mm was measured in each trail. The results of the measurements are given in Table 2. The mean distance between the gaps, which in the case of a regular beaded structure is equal to the distance between the beads, is 0.20 mm. It fluctuates from 0.13 mm to 30 mm for individual trails. Allowing for the velocity of the star across the plate, we find that the bead separation ranges from $0^{s}33$ to $0^{s}86$. The mean time between successive gaps is $0^{s}53$. The bead separation variance for a single trail is $1/3 - 1/4$ of the mean. Our τ is comparable with the analogous values ($0^{s}3$ and $0^{s}37$) obtained by E. Ya. Bugoslavskaya in Moscow with the large and the wide-angle astrographs of the Shternberg Astronomical Institute.

TABLE 2

Plate number	Trail number	Date	Star	z	τ
11	1	16 II 1955	η CMa	80°.3	0^s.75
11	2	16 II 1955	»	79.8	58
11	3	16 I 1955	»	79.7	69
11	4	16 II 1955	»	79.7	75
11	5	16 II 1955	»	79.6	58
12	1	17 II 1955	ε CMa	82.3	57
12	2	17 II 1955	»	82.8	54
12	3	17 II 1955	»	83.4	68
12	4	17 II 1955	»	84.2	86
12	5	17 II 1955	»	84.7	83
16	1	27 II 1955	α Vir	70.1	43
16	2	27 II 1955	»	69.2	41
16	3	27 II 1955	»	68.4	36
20	1	2 III 1955	α Hyd	60.4	45
20	2	2 III 1955	»	61.2	45
20	3	2 III 1955	»	62.1	53
20	4	2 III 1955	»	63.0	53
20	5	2 III 1955	»	64.0	48
23	1	29 III 1955	σ Sgr	82.9	42
23	2	29 III 1955	»	82.3	50
23	3	29 III 1955	»	81.6	42
24	1	7 IV 1955	α CMa	76.5	36
24	2	7 IV 1955	»	77.5	39
24	3	7 IV 1955	»	78.5	36
25	1	14 IV 1955	ζ Ori	80.4	42
26	1	19 IV 1955	α Hyd	60.6	33
26	2	19 IV 1955	»	61.3	33
30	1	22 IV 1955	»	63.3	45
32	1	28 IV 1955	α CMi	72.5	40
33	1	24 V 1955	σ Sgr	81.9	67
33	2	24 V 1955	»	81.0	64
35	1	13—14 VI 1955	α Sco	76.9	73
37	1	10 VII 1955	α Oph	39.9	54
41	1	11 VII 1955	α Boo	64.9	48
41	2	11 VII 1955	»	66.4	53

If the τ values from Table 2 are plotted as a function of z, the bead separation is seen to increase with z. For $z = 60°$, it is 0^s.4, and for $z = 80°$, close to 0^s.6 (Figure 3).
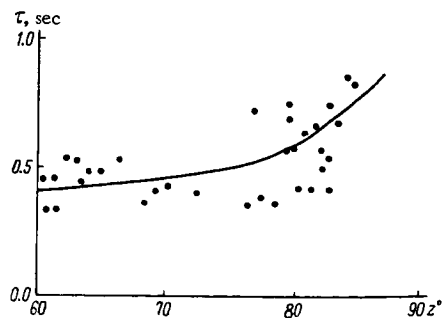

FIGURE 3.

23

Table 3 presents some data on the relation of bead size to gap size. We see that a bead is on the average 1.5 times as large as a gap. The comparatively large diameter of the beads is attributable to photographic effects: in the bead region, the quantity of light hitting the plate is higher

TABLE 3

Plate and trail number	Bead and gap size, mm		Bead/gap ratio	Bead — gap difference
	bead	gap		
16, тр. 3	0.10	0.05	2.0	0.05
35, тр. 1	0.17	0.14	1.2	0.03
12, тр. 3	0.16	0.10	1.6	0.06
33, тр. 1	0.15	0.13	1.2	0.02
24, тр. 1	0.10	0.07	1.4	0.03
Average	0.13	0.09	1.5	0.04

and the image diameter increases. The mean difference in the bead and gap lengths is 0.04 mm. The trail thickness increases by 0.07 mm for each stellar magnitude, so the difference of 0.04 mm implies that the amplitude of brightness variation from bead to gap is close to 1^m.

CAUSES OF TRAIL BEADING

Some preliminary suggestions as to the nature of beading can be made. In our opinion, it is related to the low-frequency scintillation component. Indeed, the spectrum of scintillation has the following peculiar features.

1) Scintillation intensity increases from high to low frequencies. According to Siedentopf [3], the proportion of low frequencies in the r.m.s. scintillation intensity characteristic increases for large z (Table 4).

TABLE 4

γ, c/s	σ^2, %	
	$z = 0°$	$z = 60°$
> 10	65	40
$1 - 10$	30	50
< 1	5	10

2) The peak rise in scintillation intensity is due to frequencies less than 5 c/s.

3) The largest scintillation amplitudes are observed at frequencies of $3-15$ c/s.

We see that these properties of scintillation are in good agreement with the properties of trail beading that we have derived. For large z, when the low-frequency scintillation components prevail, intensity fluctuations in the luminous flux of a moving source apparently produce beading with a certain characteristic space frequency, which corresponds to the fluctuation frequency of the luminous flux. More detailed discussion of this topic is beyond the scope of the present paper.

Bibliography

1. Hertzsprung, E. —Publ. Astroph. Obs. Potsdam, No. 75. 1920.

2. Bugoslavskaya, E. Ya. —Trudy soveshchaniya po mertsaniyu zvezd, pp. 173—181. Moskva—Leningrad. Izdatel'stvo AN SSSR. 1959.

3. Siedentopf, H. —In: "Astronomical Optics and Related Subjects" (Zd. Kopal, editor), pp. 317—322. Amsterdam. 1956.

N 67-15465

N. I. Kozhevnikov

SOME RESULTS OF DIRECT OBSERVATIONS OF REFRACTIONAL FLUCTUATIONS IN THE GROUND LAYER AND THE DISTRIBUTION PARAMETERS OF THE FLUCTUATIONS

1. In /1/ we have described a method for visual (and photographic) observation of fluctuations in the refractive index of air in the ground layers of the atmosphere in daytime. An optical scheme of the instrument is shown in Figure 1. The objective O_1 throws the image S_1 of the solar disk on the screen M_1. The aperture O_2 (0.03 cm in diameter) is located outside the image S_1, not far from its edge. The size of O_2 is chosen so that, on the one hand, the diameter is as small as possible, and on the other, the diffraction of a convergent light beam by O_2 is negligible.
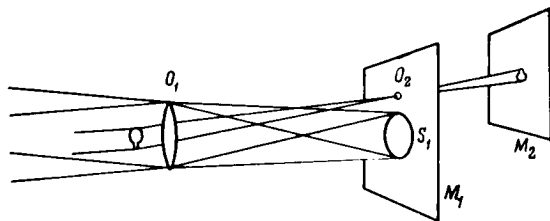
FIGURE 1.

If the air layers were perfectly homogeneous, the screen M_2 placed behind the screen M_1 would remain dark (the aperture O_2 being outside the solar disk). Fluctuations in the refractive index, however, cause a deflection of the sun rays from the initial direction (pulsation of the sun's limb). Sunlight therefore reaches the aperture O_2 and the screen M_2 is illuminated. In /1/ we have observed that the shape and the size of the light spots appearing on the screen M_2 when the atmosphere is turbulent (see Figure 1) correspond to a parallel projection of the atmospheric inhomogeneities on the objective O_1. By observing the light spots on M_2 we in fact observe the fluctuations in the refractive index of the air medium. The aperture O_2 is provided at a constant angular distance (as measured from the center of the objective O_1) from the mean position of the sun's disk edge in unperturbed atmosphere. To pass through O_2, the light rays must be deflected through a definite angle. They should therefore meet with an atmospheric inhomogeneity whose refractive index deviates by a definite amount from the mean refractive

index of air under the given conditions /2/. Since these deviations are small, the deflection angle can be taken as proportional to the amplitude of refractional fluctuations. The aperture O_2 thus automatically selects those rays which are deflected through a preset angle. M_2 therefore displays a distribution of light spots corresponding to the actual distribution of fluctuations (having equal refractive indices).

The principal results obtained for refractional inhomogeneities by this method are presented in /1, 3, 4/: we shall briefly consider the conclusions. Atmospheric inhomogeneities were found to be in the shape of bands extending in the direction of the wind; they are made up from individual round formations, appearing on the screen M_2 in the form of light spots. The projections of the inhomogeneities were also observed with the aperture O_2 provided inside the solar disk (not far from the limb or from the edge of some sunspot). The inhomogeneities register in this case as dark spots. With respect to their size, the inhomogeneities fall into two groups: in group I the mean size is 2.5 cm, and in group II, 10 cm. The number of group-I and group-II inhomogeneities decreases rapidly as the aperture O_2 is moved away from the disk edge. Group-II inhomogeneities are made up from group-I inhomogeneities.

2. For the structural function $D_n(r_1, r_2)$ of the refractive index, we have

$$D_n(r_1, r_2) = \overline{|n(r_1) - n(r_2)|^2} = c_n^2 |r_2 - r_1|^{1/3}, \quad l_0 \ll |r_2 - r_1| \ll L_0, \qquad (1)$$

$$D_n(r_1, r_2) = \overline{|n(r_1) - n(r_2)|^2} = c_n^2 |r_2 - r_1|^2, \quad l_0 \gg |r_2 - r_1|. \qquad (2)$$

Here $n(r)$ is the refractive index at the point r, c_n is a constant; L_0 external turbulence length, l_0 internal turbulence length /5/. Relations (1) and (2) follow from the theory of homogeneous isotropic turbulence /6, 7/. These relations can also be interpreted as expressions for the least mean distance between two regions of space having the refractive indices n and $n+\Delta n$, respectively. On the other hand, relations (1) and (2) also define the least mean distance between two regions of space having the same refractive index. Indeed, let n_1 be the refractive index at the point r_1. Then the region of space where n is equal to n_2 $(n_2 = n_1 + \Delta n)$ extends from the point r_1 to the least mean distance specified by (1) and (2). Let this distance be r. But the distance R (the least mean distance) between two regions of space having the same value n_2 cannot be less than r. Indeed, if $R < r$, the distance from the region n_2 to the region n_1 is less than r. Studying the distribution of equal-amplitude refractional fluctuations, we thus gain some insight into the structural function of the refractive index.

3. Let us apply the tools of Sec. 2 to the results concerning ground-air refractional fluctuations described in Sec. 1. We determine the mean distance Δr between two inhomogeneities having the same refractional fluctuation $n+\Delta n$. Since the refractive index fluctuations are comparatively small, the angle of deflection $\Delta \gamma$ of the rays passing through the atmospheric inhomogeneity can be taken as proportional to the fluctuation Δn. It is therefore the position fluctuation $\Delta \gamma$ which is adopted as the parameter of the turbulence field, and not the actual refractional fluctuation Δn (see also /2/). $\Delta \gamma$ depends on the distance of the aperture O_2 from the mean (unperturbed) position of the sun's limb; it is measured in seconds of arc. Δr was determined as a function of $\Delta \gamma$ for group I and group II separately. Since group-I inhomogeneities generally combine to form group-II

inhomogeneities, the distances between individual group-I inhomogeneities were measured within the corresponding group-II inhomogeneity.

The distance Δr was determined as follows. The screen M_2 was replaced with a camera whose objective has been removed; the film thus served as the screen M_2. The photographs were taken with 1/250 sec exposure. One of the inhomogeneities in each photograph was then selected, and the distances were measured from this inhomogeneity to other nearby inhomogeneities. The procedure was then repeated for other inhomogeneities. Since each photograph corresponds to a certain $\Delta\gamma$, the average of all the measured distances on one photograph gives Δr as a function of $\Delta\gamma$. Some photographs of atmospheric inhomogeneities are shown in Figures 2, 3, 4, 5.
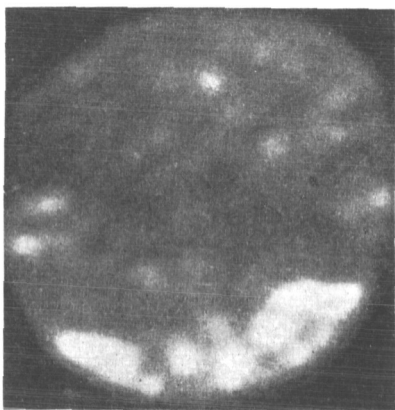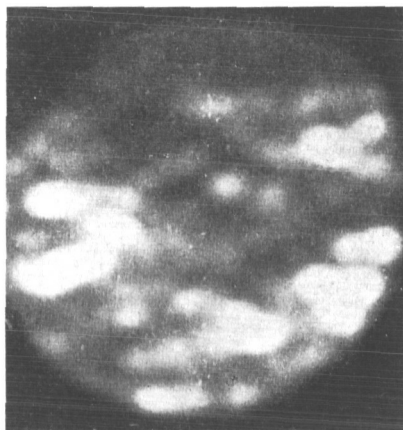

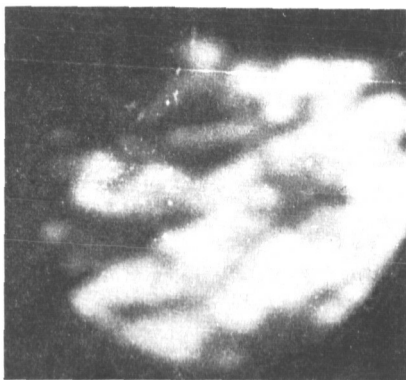FIGURE 2. $\Delta\gamma = 15''$.

FIGURE 3. $\Delta\gamma = 10''$.

FIGURE 4. $\Delta\gamma = 5''$.

FIGURE 5. $\Delta\gamma = 0''$.

.   Figures 6 and 7 plot Δr as a function of $\Delta\gamma$. Δr is in centimeters, $\Delta\gamma$ in seconds of arc.   The data in Figure 6 pertain to group-I inhomogeneities, and those in Figure 7 to group-II inhomogeneities.   Consider Figure 7: the dots are the results of measurements, the large circles are the mean Δr.   Curve a gives the dependence $\Delta r = a_1 (\Delta\gamma)^3 + \beta_1$ which has been plotted to ensure the best fit of the experimental points.   Curve b plots the dependence $\Delta r = a_2 (\Delta\gamma)^2 + \beta_2$, and curve c the dependence $\Delta r = a_3 (\Delta\gamma)^4 + \beta_3$. We see that curve a is the best approximation to the results of measurements. This dependence, however, should apply when $\Delta r > l_0$ (see relations (1) and (2)).
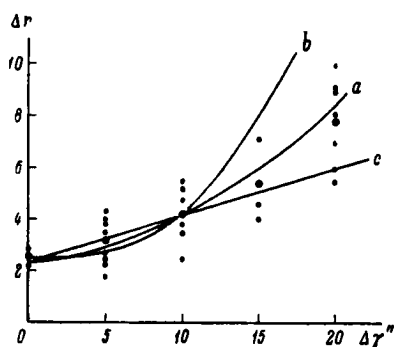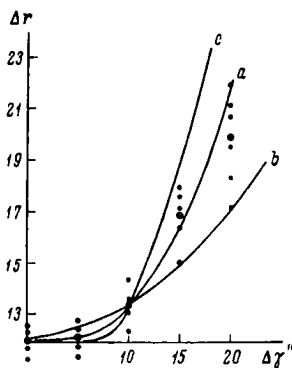
FIGURE 6.   FIGURE 7.

   The notations in Figure 6 are as in Figure 7.   Curve a plots the dependence $\Delta r = a_1 (\Delta\gamma)^2 + b_1$, curve b the dependence $\Delta r = a_2 (\Delta\gamma)^3 + b_2$, and curve c the dependence $\Delta r = a_3 \Delta\gamma + b_3$.   Curve a again provides the best approximation to the observation results.   Curve a in Figure 6 probably corresponds to a transition region, between $\Delta r > l_0$ and $\Delta r < l_0$.
   Group-II inhomogeneities (having a mean size of some 10 cm) are thus scattered at distances

$$\Delta r \sim (\Delta\gamma)^3, \tag{3}$$

while group-I inhomogeneities occur at distances

$$\Delta r \sim (\Delta\gamma)^2. \tag{4}$$

   The following conclusions can be drawn from the preceding.
   1) The assumption of a homogeneous isotropic field of refractional fluctuations is justified with fair accuracy for the ground air layers.
   2) The structural function of this fluctuation field is described (a) by relation (1) for distances $\Delta r > 10$ cm, and (b) by a relation of the form $\Delta r \sim (\Delta\gamma)^2$ for distance 2.5 cm $< \Delta r < 10$ cm.
   3) The internal turbulence length l_0 should satisfy the inequality $l_0 < 2.5$ cm, i.e., l_0 is comparable with the size of group-I inhomogeneities.   Indeed, the relation $\Delta r \sim (\Delta\gamma)^3$ is observed for $\Delta r > l_0$; in our case, it is satisfied for $\Delta r > 10$ cm.   Hence, $l_0 < 10$ cm.   But since group-II inhomogeneities break into group-I inhomogeneities, and l_0 represents the least eddy size, l_0 should not be greater than 2.5 cm.

29

Bibliography

1. Kozhevnikov, N.I. —Nauchnye Doklady Vysshei Shkoly,
        No.3:143. 1958.

2. Krasil'nikov, V.A. —DAN SSSR, 65:291. 1949.

3. Kozhevnikov, N.I. —Solnechnye Dannye, No.8:75. 1961.

4. Kozhevnikov, N.I. —Vestnik MGU, No.4:14. 1962.

5. Tatarskii, V.I. Teoriya fluktuatsionnykh yavlenii pri rasprostranenii
        voln v turbulentnoi atmosfere (The Theory of Fluctuational
        Phenomena for the Propagation of Waves in a Turbulent
        Atmosphere). —Moskva, Izdatel'stvo AN SSSR. 1959.

6. Kolmogorov, A.N. — DAN SSSR, 30:299. 1941.

7. Obukhov, A.M. —DAN SSSR, 32:22. 1941.

15466

N. V. Bystrova and A. N. Demidova

THE EFFECT OF ATMOSPHERIC TURBULENCE
ON IMAGES OF EXTENDED CELESTIAL SOURCES

In /1/ we proposed a method for the determination of the height of the
atmospheric layer responsible for edge distortion in the images of extended
celestial sources. Observations of the sun according to this method have
been carried out at Pulkovo since 1958, and of the moon since 1960. The
results of these observations, in conjunction with meteorological data on
wind speeds and directions at various altitudes in the troposphere, lead
to the following conclusions.

In daytime, the atmospheric layer responsible for edge distortion of
the solar disk extends at altitudes of from 0.3 to 2.5 km, the mean height
being 1.5 km. Observations of the lunar limb indicate that during the night
the corresponding inhomogeneities occur at a higher level — between 1.5
and 9 km, the mean height being 4.5 km /2/. In /3/ we have shown that in
daytime, in the presence of cumuliform clouds, the largest atmospheric
inhomogeneities occur at a certain level inside the cloud or slightly below
the base height. In a cloudless sky, the inhomogeneities are generally
observed at the same heights as on clouded days.

According to /4/, the daytime height of the atmospheric layer where
the refractive index of the visual spectrum undergoes an abrupt change
coincides (with a correlation coefficient of 0.92) with the upper limit of
the planetary boundary layer if the following conditions are satisfied:
(a) the layer actually exists at the time of observation, (b) there is one
highly active layer whose height is not greater than 3 km. These conditions
are generally satisfied in practice.

It is noteworthy that atmospheric inhomogeneities manifested in solar
limb observations occur at the same height as the lifted air layers with an
abruptly changing refractive index, which are of some significance in the
long-range tropospheric propagation of ultrashort radio waves. Some
other properties are apparently also common to these layers: their existence
is independent of the presence or the absence of cloudiness, they are both
probably related to inversion layers. Solar limb observations may therefore
prove useful in the study of propagation of ultrashort radio waves in the
troposphere /5/.

Simultaneous observations of lunar limb deformation and of the schlieren
pattern of stars were made. The results showed that the atmospheric
inhomogeneities responsible for both these phenomena were located at
the same altitude /6/. This implies that the scintillation of stars is
produced by the same atmospheric layer which causes directional
displacement of deformations in the image of the lunar limb.

Bibliography

1. Bystrova, N.V. and A.N.Demidova. —Solnechnye dannye, No. 11. 1960; Izv. GAO, No.169 : 89. 1961.

2. Demidova, A.N. and N.V.Bystrova. —ATs, No.231 : 26. 1962.

3. Bystrova, N.V. and A.N.Demidova. —Solnechnye dannye, No.3 : 73. 1961.

4. Bystrova, N.V., A.N.Demidova, and N.A.Lazareva. — Solnechnye Dannye, No.8 : 77. 1961.

5. Bystrova, N.V. and A.N.Demidova. —Solnechnye dannye, No. 12 : 77. 1962.

6. Demidova, A.N. and N.V.Bystrova. —ATs, No.232 : 12. 1962.

V. M. Bovsheverov, A. S. Gurvich, and M. A. Kallistratova

PULSATION OF AN ARTIFICIAL LIGHT SOURCE IN THE GROUND LAYER

Phase fluctuations of a light wave traveling through the atmosphere or, in other words, the pulsation of stars and the sun, are determined by fluctuations in the refractive index due to atmospheric turbulence. Image pulsation attracts not only astronomers and radiophysicists, but also geophysicists, since the fluctuation of light from extraterrestrial sources provides additional information on the turbulent state of the atmosphere, in particular, on the magnitude of the structural constant C_n of the refractive index in free atmosphere.

Measurements of image pulsation from star trails on photographic plates /1/ helped to establish several important rules governing this phenomenon (e. g., variation with zenith distance) and to determine the autocorrelation function /2/. However, irregularities in meteorological conditions along the path of light, which could not be investigated in due detail simultaneously with image pulsation, and the complex treatment of pulsation measurements, which of necessity limits the available volume of statistical data, make any detailed comparison of observational data with turbulent mixing intensity in the atmosphere all but impossible. Recently developed methods for the investigation of turbulence at heights of under 3 km and the data obtained on the spectrum of temperature fluctuations at these altitudes /3/ suggest that this comparison will be made in the near future.

To obtain a reliable relation between the observed data and the spectrum of phase fluctuations, on the one hand, and the intensity and the spectrum of eddy pulsations in certain atmospheric layers, on the other, we should first verify the theoretically predicted dependences /4/ for the ground air layer. The ground layer is a natural laboratory of fluctuational phenomena, since the structural function of the refractive index has been determined with sufficient accuracy in this region, and the relation of turbulence characteristics to mean meteorological parameters (vertical profiles of the mean wind velocity and temperature) is also known.

In the present paper, we investigate the pulsation intensity of the image of an artificial light source as a function of the distance traversed by the light beam in the ground layer and of the mean meteorological parameters. Application of frequency analysis enabled us to establish the energy frequency spectrum of image pulsations and to verify some conclusions of the theory /4/.

APPARATUS

Wave-front fluctuation pickup (WFP) described in /5/ was used as the receiver of light. WFP operates as follows: a beam of light focused by a lens with 800 mm focal distance is scanned harmonically (i.e., moved sinusoidally along a horizontal line) by the mirror of a high-frequency loop. The reflected light is directed to a narrow vertical slit, with a photomultiplier behind it. If the mean position of the light spot falls exactly on the slit midline, the signal picked up by the photomultiplier contains only the second harmonic of the scanning frequency (Figure 1). As the mean position of the spot is displaced, the first harmonic appears in the signal; its amplitude is proportional to image displacement, and it is in phase with mirror oscillations or displays a 180° phase shift, depending on the sense of deflection of the image relative to the slit.
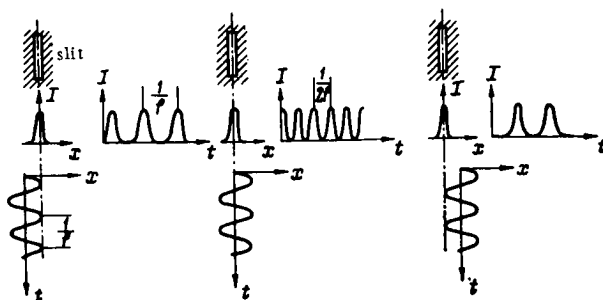
FIGURE 1. The appearance of the first harmonic in the photomultiplier current 1.

A tracking system tuned to the first harmonic focused the image on the slit by regulating the direct current through the loop. We measured the changes in direct current, since they were proportional to the angular deflection $\Delta\varphi$ of the ray at the outlet. The tracking system (its gain factor is fairly high) sharply reduces the influence of scintillation (fluctuations in light intensity) on the magnitude of the output signal. To ensure normal operating conditions of the tracking system under extreme amplitude scintillation, an additional feedback loop was introduced regulated by the mean photomultiplier current. On account of this double feedback, a 100-fold variation in luminous flux changes the current (which is proportional to $\Delta\varphi$) by no more than 10%. If the source image is blurred by the turbulent inhomogeneity of the medium, the instrument reacts to any displacement of the image's "center of gravity" on the slit. The instrument measures angular displacement in the horizontal plane, and it is insensitive to refraction in the vertical plane.

The mean square pulsations were measured with an electrodynamic multiplier, which is described in /6/. The scale of this instrument was calibrated in units of source position variance $\sigma_\varphi^2 = \overline{(\varphi - \bar{\varphi})^2}$. The energy frequency spectrum $W(f)$ of the random variable φ was measured with a frequency analyzer provided with 34 half-octave filters in the frequency range from 0.01 to 1000 c/s.

MEASUREMENTS

The measurements were made at night during August 1960 at the Tsimlyanskaya Research Station of the Institute of the Physics of the Atmosphere, on a plain stretch of open steppe. The light receiver was mounted on a reinforced concrete base under cover. A directional light source (a projector) was positioned at selected points, at distances $L = 125$, 250, 500, 1000, and 2000 m. The projector aperture was adjusted so as to provide a light source of some 2'' at all distances. Some 60 measurements of position variances and frequency spectra were made in all. In each session, the variances and the spectral densities were averaged over 10-min periods. The vertical profiles of the mean wind velocity and the mean temperature up to heights of 12 m were measured simultaneously with image pulsations from a mast along the ground track of the light source. Turbulence characteristics of the ground layer above the flat stretch of steppe were taken as constant along the track, which extended approximately at one height, $z = 1.5$ m.

IMAGE PULSATION VARIANCE

The graph in Figure 2 gives the variances σ_φ^2 measured for various distances L under different meteorological conditions. This graph illustrates the magnitudes of σ_φ^2, and also shows that there is a linear dependence of σ_φ^2 on L. It is also clear from the graph that the set noise σ_n converted to angular units is approximately 1''.

The theory of wave propagation in a locally isotropic turbulent medium /4/ gives the following expression for the mean square of the phase difference of electromagnetic oscillations at two points distant b from each other in a plane at right angles to the direction of propagation:

$$D_s(b) = \overline{[S_1 - S_2]^2} = 2.9 k^2 b^{5/3} \int_0^L C_n^2(r)\, dr, \tag{1}$$

where S is the phase, k the wave number, L the path length in the medium, C_n the structural constant of the refractive index n, which is determined from the Kolmogorov—Obukhov 2/3 law

$$D_n = \overline{[n(\bar{r}) - n(\bar{r} + \bar{\rho})]^2} = C_n^2(r)\rho^{2/3} \tag{2}$$

and characterizes the intensity of refractional fluctuations.

For light propagation in a homogeneous turbulent medium, the structural constant C_{n0} is independent of position. The source position variance σ_φ^2 is then given by

$$\sigma_\varphi^2 = \frac{D_s(b)}{k^2 b^2} = 2.9 b^{-1/3} L C_{n0}^2. \tag{3}$$

In our measurements, b is the diameter of the objective in the light receiver. The linear dependence of Figure 2 is consistent with relation (3).

To check the consistence between the measured and the theoretical results, we calculated the structural constants C_n for all the days of observation (excluding the data for $L = 125\,\text{m}$). Fluctuations of the refractive index in the visual spectrum are produced by air density pulsations, which are mainly conditioned by temperature fluctuations. C_n is related to the structural constant of temperature fluctuations C_T (C_T enters the 2/3 law of temperature fluctuation $\overline{[T(\vec{r}) - T(\vec{r} + \vec{\rho})]^2} = C_T^2 \rho^{2/3}$) by the expression

$$C_n = \frac{69 \cdot 10^{-6} p}{T^2} C_T, \tag{4}$$

where T is the temperature in °K, p the pressure in mb, C_T the structural constant in $°\text{K}/\text{cm}^{1/3}$
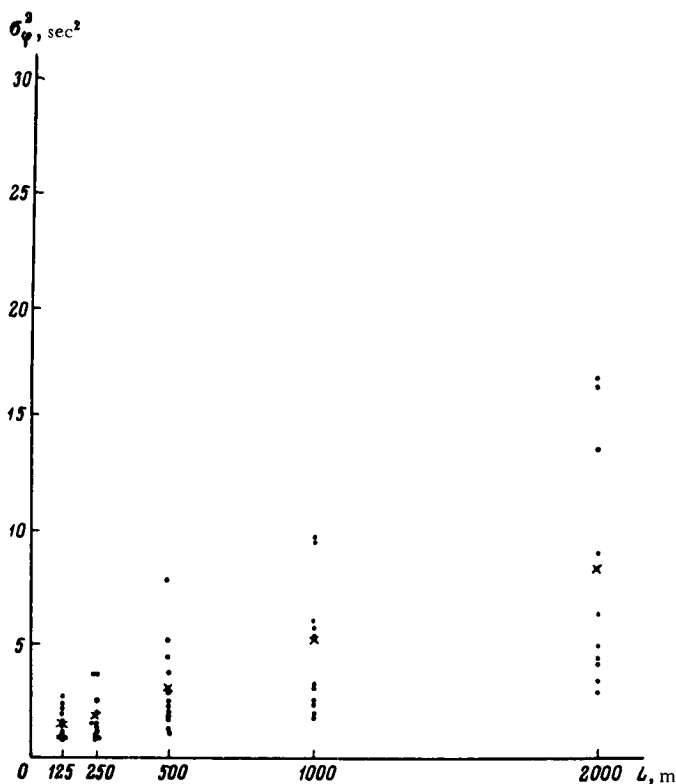
FIGURE 2. Image pulsation variance vs. distance:
Crosses mark the mean values of σ^2_φ.

C_T was determined from vertical profiles of mean wind velocity and temperature using the formula

$$C_T = \frac{0.54}{z^{1/3}} \frac{dT(z)}{d \ln z} a(\text{Ri}), \tag{5}$$

36

where $Ri = \dfrac{\dfrac{g}{T}\dfrac{dT(z)}{dz}}{\left(\dfrac{du}{dz}\right)^2}$ is the Richardson number characterizing atmospheric stability, $a(Ri)$ a dimensionless coefficient which has been derived experimentally in /7/; in the ground layer, $a = 2.4$ for $Ri < -1.0$; and $a = 0.5$ for $Ri > +0.3$; $T(z)$ and $u(z)$ are the mean temperature and wind speed at the height z. The gradients $\dfrac{dT(z)}{dz}$ and $\dfrac{du(z)}{dz}$ were measured at the height of 1.5 m — the mean track height.

Having found C_T and C_n, we calculated from (3) the theoretical values of $\sigma_{\varphi T}$ for each day of observation. These data are plotted in Figure 3, where the abscissa gives the theoretical values of $\sigma_{\varphi T}$ and the ordinate the experimentally determined image pulsation variances (with allowance for set noise).
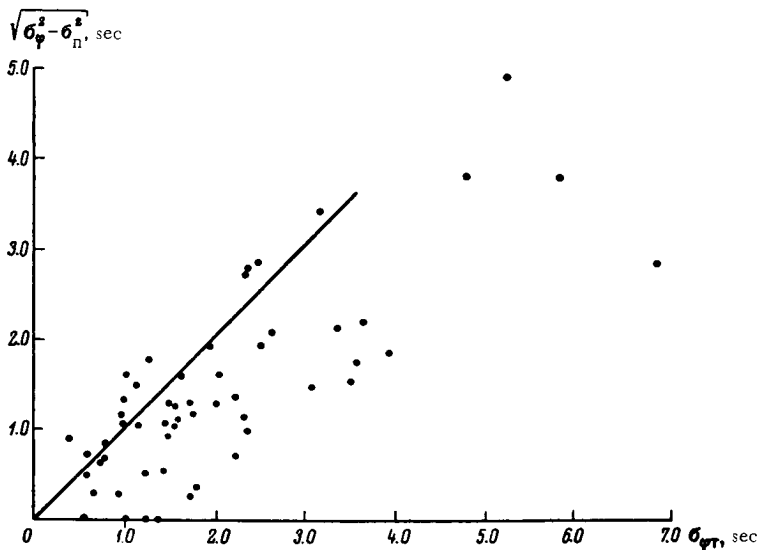
FIGURE 3. Experimental and theoretical image pulsation variances.

The straight line in Figure 3 represents perfect coincidence of experimental and theoretical data. We see from the graph that the experimental points fall close to this line. The regression coefficient is 0.97 in this case. The scatter of the experimental points is due not only to errors in the determination of pulsation variance, but also to inaccuracies in $\sigma_{\varphi T}$, which are calculated using C_n. This constant cannot be found with high accuracy, since it depends on experimentally determined vertical profiles of mean wind velocity and temperature.

In various applications the intensity of image pulsation is not enough: we want to know what frequency band carries the main proportion of energy of the random fluctuations. Energy spectra were obtained with a multichannel analyzer which had been appropriately calibrated to measure the spectral power density of phase fluctuations, $W(f)$. The spectral distribution of energy as a function of meteorological conditions, distances, etc., is more conveniently investigated using spectra which have been normalized to the total fluctuational power σ_φ^2. Clear notions of the spectrum and its peculiar features can be obtained by plotting the spectral function in logfrequencies (since the spectrum is very broad, occupying many octaves). The following identical transformation can be applied in the process:

$$\sigma_\varphi^2 \equiv \int W(f)\,df = \int fW(f)\,d\ln f = \int fW(f)\ln 2\,d(\log_2 f),$$

which shows that $fW(f) \cdot \ln 2$ is the fluctuational power in a frequency band of one octave. The dimensionless function $U = \dfrac{fW(f)\ln 2}{\sigma_\varphi^2}$ thus represents the relative contribution from fluctuational power in a frequency band of one octave.

In /4, 8/ it is shown that U is a function of the dimensionless parameter $\dfrac{fb}{v_\perp}$, where b is the diameter of the objective, $v_\perp$ the projection of wind velocity at right angles to the ray. The dependence of U on $\dfrac{fb}{v_\perp}$ is expressed as

$$U = 0.045 \sin^2 \frac{\pi bf}{v_\perp} \left(\frac{bf}{v_\perp}\right)^{-\frac{7}{3}}. \tag{6}$$

For $\dfrac{bf}{v_\perp} \ll 1$, i.e., in the low frequency region, this function has the form

$$U_{\Delta s} \sim \left(\frac{bf}{v_\perp}\right)^{\frac{1}{3}}. \tag{7}$$

For $\dfrac{bf}{v_\perp} \gg 1$, in the high-frequency region, the envelope function is

$$U_{\Delta s} \sim \left(\frac{bf}{v_\perp}\right)^{-\frac{5}{3}}. \tag{8}$$

The characteristic frequency f_1 for which the function $U_{\Delta s}$ reaches its maximum is determined by the base length and the wind velocity:

$$f_1 = 0.22\frac{v_\perp}{b}.$$

In the treatment of spectra obtained with the frequency analyzer, each spectrum was normalized, the dimensionless frequency $\dfrac{fb}{v_\perp}$ was calculated, and $U_{\Delta s}$ vs. $\dfrac{fb}{v_\perp}$ was then plotted. The individual spectra were then averaged.

The averaged spectrum is shown in Figure 4. For purposes of comparison with the theory, the figure also gives the asymptotic behavior of the theoretical function $U_{\Delta S}$ at low frequencies (from (7)) and at high frequencies* (from (8)).

The point $\dfrac{fb}{v_\perp} = 0.22$ corresponding to the maximum in the theoretical spectrum is also marked in the figure.
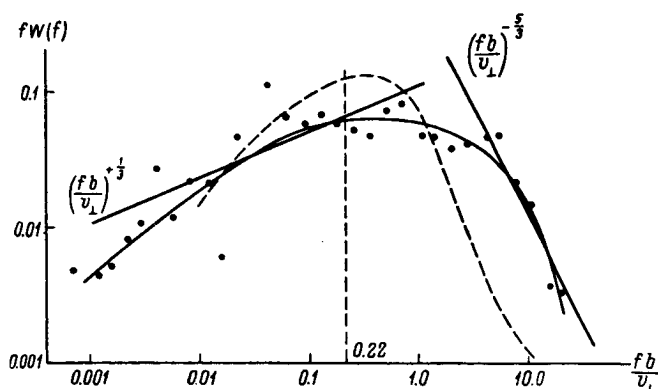
FIGURE 4. Nondimensional frequency spectrum of image pulsation.

We see from the graph that the experimental and the theoretical spectra follow the same trend. In the low-frequency region, the spectral function drops faster than the theoretical rate. This is apparently due to an increased deviation from the 2/3 law for the large-scale turbulence represented by the low-frequency region of the spectrum. The dashed curve in Figure 4 plots the spectrum of phase fluctuations for sound waves /8/, whose general trend is close to the spectrum of image pulsation.

CONCLUSIONS

Our results indicate that the magnitude of image pulsations in the ground layer can be calculated from the theory of /4/, if the vertical distribution of the mean wind velocity and temperature is known. Analogous calculations for a ray traversing the entire thickness of the atmosphere require not only knowledge of the vertical wind-velocity and temperature profiles, but also the dependence of C_n on $\dfrac{dT}{dz}$ and $\dfrac{du}{dz}$ in free atmosphere (some investigations of this dependence are under way now /3/).

---

* At high frequencies, $\sin^2\left(\dfrac{\pi fb}{v_\perp}\right)$ cannot be marked on the experimental spectrum: $v_\perp$ being variable, the zeros vanish in the mean. Moreover, the half-octave filter accommodates several maxima and minima at high frequencies, and we should therefore take the average value of 1/2 for $\sin^2\left(\dfrac{\pi fb}{v_\perp}\right)$.

The results of our measurements confirm the theoretical conclusion that the mean square fluctuation in source position is proportional to the distance traversed by light in the turbulent medium.

The spectrum of phase fluctuations is in satisfactory agreement with the theoretical calculations from the Kolmogorov—Obukhov theory of turbulence, adopting the hypothesis of "frozen turbulence". The non-dimensional phase fluctuation spectra of light and sound waves are fairly close to one another.

Bibliography

1. Kolchinskii, I.G. — AZh, **34**(4) : 638. 1957.

2. Kolchinskii, I.G. — Trudy soveshchaniya po issledovaniyu mertsaniya zvezd, p. 145. Izdatel'stvo AN SSSR. 1959.

3. Tsvang, L.R. — Izv. AN SSSR, geophys. series, No. 10. 1963.

4. Tatarskii, V.I. Teoriya flyuktuatsionnykh yavlenii pri rasprostranenii voln v turbulentnoi atmosfere (The Theory of Fluctuational Phenomena in the Propagation of Waves in Turbulent Atmosphere). — Moskva, Izdatel'stvo AN SSSR. 1959.

5. Bovsheverov, V.M., A.S.Gurvich, and M.A.Kallistratova. — Izvestiya vuzov, Radiofizika, **4**, No. 5. 1961.

6. Korn, G. and T.Korn. Elektronnye modeliruyushchie ustroistva (Electronic Analog Devices), p. 240. Moskva. 1955.

7. Tsvang, L.R. — Izv. AN SSSR, geophys. series, No. 8 : 1252. 1960.

8. Golitsyn, G.S., A.S.Gurvich, and V.I.Tatarskii. — Akusticheskii Zhurnal, **6**, No. 2. 1960.

O. B. Vasil' ev

IMAGE PULSATION AS A FUNCTION OF ZENITH DISTANCE

Several works have recently been published on the relation of image pulsation to zenith distance. We are reluctantly forced to return to this subject, since the published results are not quite satisfactory. Before proceeding with the discussion of image pulsation, we wish to define the field with some precision. This is particularly necessary since at present there is much confusion in terminology pertaining to various astroclimatic characteristics.

Optical inhomogeneities in the atmosphere, which are transformed by intrinsic local fluctuations, transported by wind, and displaced by the Earth's diurnal rotation, cause a certain instability of stellar images, which amounts to changes in the amplitude of the incident light wave and to changes in its phase. The apparent instability also depends on the size of the atmospheric inhomogeneities relative to the diameter of the telescope objective (if the atmospheric-optical disturbance is produced by inhomogeneities in the immediate vicinity of the objective) or on the size of the "schlieren pattern" moving across the objective (this applies to the scintillation of stars, when the inhomogeneities may be far from the objective and may have various sizes).

On the basis of the above characteristics, we propose the following classification of atmospheric-optical disturbances encountered in work with small telescopes (of the order of 10 inches).

Size of atmospheric inhomogeneities or size of "schlieren" relative to the objective diameter (D)	Nomenclature of atmospheric-optical disturbances produced by	
	wave amplitude fluctuations	wave phase fluctuations
Less than or equal to D		Blurring of diffraction pattern (shimmer disk)
Equal to or greater than D (by 2–3 orders of magnitude)	Scintillation of stars	Pulsation of stars
Greater than D (by from 2–3 to 4–5 orders of magnitude)	Seeing anomalies (random variations)	Refraction anomalies ("random refractions")
Much greater than D (by more than 4–5 orders of magnitude)	Fluctuations of atmospheric transparency	Fluctuations of normal refraction

Inhomogeneities or "schlieren" smaller than or equal to the diameter of the objective cannot produce a net displacement of the stellar image in the

telescope's focal plane as they drift across the objective: many small inhomogeneities occupying the field of sight are observed simultaneously, which is manifested in a certain blurring of the diffraction pattern of the star —"shimmer disk" — characterized by the shimmer angle t_z''. Elementary calculations will easily show that the diffraction pattern is blurred by amplitude and phase fluctuations at frequencies of 10 c/s and higher.

Scintillation is caused only by amplitude fluctuation of the incoming light waves. In this case, as we have remarked above, we should only deal with the size of the "schlieren". Therefore, if scintillation is defined as fluctuations in the apparent stellar brightness with frequencies of from 0.02 (50-sec period) to 1000 c/s, the "schlieren" responsible for this phenomenon are of the order of $10^2 - 10^3$ objective diameters (a few tens of meters) and less.

Image pulsation is produced by fluctuations in the path of the light wave due to inhomogeneities which are larger than the telescope objective (smaller inhomogeneities blur the diffraction pattern, as previously explained). Elementary calculations show that image pulsation is meaningful only at frequencies below 10 c/s. If, as in the case of scintillation, image pulsation is assumed to have the frequency of 0.02 c/s (50-sec period) as its lower bound, the corresponding inhomogeneities are of the order of from 1 to $10^2 - 10^3$ objective diameters, i.e., from tenths of a meter to tens of meters).

Path shifts with periods of from 1 min to 5 hrs (frequencies from 0.02 to 0.00005 c/s) are generally called "random refractions" or refraction anomalies. These phenomena are produced by inhomogeneities ranging in size from $10^2 - 10^3$ to $10^4 - 10^5$ objective diameters, i.e., from hundreds of meters to tens of kilometers.

Mixing of air masses (there is of course not much point in speaking of inhomogeneities which measure more than a few tens of kilometers) alters the atmospheric transparency and the normal refraction, but the variation of these parameters has a frequency below 0.00005 c/s.

The above classification of atmospheric-optical perturbations has its origin not only in geometrical characteristics of the inhomogeneities in the Earth's atmosphere and in external symptoms, but also in physical factors differentiating between the various disturbances. We are therefore faced with the problem of constructing appropriate theoretical models for each of the above groups.

In what follows, by image pulsation we mean position fluctuations of the photometric center of gravity of ̣ne stellar image in the telescope's focal plane, with frequencies of from 0.02 to 10 c/s, which are produced by atmospheric inhomogeneities greater than the telescope diameter, i.e., measuring from tenths of a meter to a few tens of meters. When speaking of image pulsation, we should always specify the position angle of star fluctuations. If image pulsation is inferred from photographic trails of stars, we obtain vertical pulsations (the trails are photogra ̣ied in the meridian), in the direction of the vertical at the given point of the sky.

One of the projects of the Main Astronomical Observatory of the USSR Academy of Sciences (Pulkovo) for 1960 — 1961 included treatment of a large volume of data on image pulsations collected by the Kuban' Expedition (photographic trails taken with AZT-7 telescope). More than 400 trails photographed on 45 nights (some 100 sessions) were reduced. This

enormous bulk of material was treated with special semiautomatic equipment designed and built by the author at the Pulkovo Observatory. The results of these measurements were applied to investigate the mean square amplitude of the star's deviation from its mean position (for brevity, we henceforth refer to this quantity as the "pulsation amplitude") as a function of the star's zenith distance.

In 1915, Banakhevich /1/ proposed the following empirical relation for this dependence:

$$\sigma_z'' = \sigma_0'' \sqrt{\sec z - 0.78}.\tag{1}$$

This relation, as later authors have commented, is in excellent agreement with observational data; it is often considerably more accurate than some more recent "improved" relations. Unfortunately, this relation did not attract due attention in its time, and in 1935 Danjon and Couder /2/ proposed the well-known empirical formula

$$\sigma_z'' = \sigma_0'' \sec z,\tag{2}$$

which however was at variance with the then available, as well as later observations.

In 1940, Ulrink /3/ published the empirical formula

$$\sigma_z'' = \sigma_0'' \sqrt{\sec z}.\tag{3}$$

An identical expression was derived by V. A. Krasil'nikov in 1949 /4, 5/ from the theory of propagation of acoustic and ultrashort radio waves in an atmosphere with highly developed dynamic turbulence. Krasil'nikov's calculations proceed from A. M. Obukhov's concepts of the temperature fluctuation field in turbulent flow.

In 1952, Kolchinskii /6/ analyzed the observations of various authors and came to the conclusion that they were in satisfactory agreement with Krasil'nikov's results. We are regretfully forced to call attention to the fact that Krasil'nikov's theory has absolutely no bearing on image pulsation, so that Kolchinskii erred in his conclusion that this theory provides a satisfactory approximation to the observed stellar pulsations. In theoretical calculations, the atmospheric inhomogeneities were assumed of the order of $10-20$ cm, which is generally less than the telescope diameter; these inhomogeneities therefore blur the diffraction pattern of the star, but do not cause image pulsation. In conclusion of his paper /5/, Krasil'nikov himself writes, "the frequencies of fluctuations in the star position according to observations are up to 100 per sec, which is fully consistent with our notions, since the field of temperature pulsations is characterized by frequencies of the same order. We note in conclusion that our reasoning does not apply to slow variations in star positions produced by large density inhomogeneities (the so-called "random refraction"), which can be observed with the astrograph cross hairs constantly trained on the star". Krasil'nikov thus stated explicitly that his results did not apply to the phenomenon of image pulsation.

Kolchinskii's other calculations based on Krasil'nikov's formula for the phase difference φ between opposite edges of the telescope objective are also in error.

Later observations showed that empirical relations of the type (3) provide an unsatisfactory approximation to experimental data. N.I. Kucherov proposed a new formula as an approximation to observations made at the Main Astronomical Observatory:

$$\sigma''_z = \sigma''_z \sec^k z, \tag{4}$$

k ranging from 0.16 to 1.53. I. G. Kolchinskii also applied formula (4) in his investigations, but k was found to range from 0.45 to 0.83, so that the mean value of 0.5 was assumed.

In 1960, Darchiya /7/ came to the conclusion that even (4) was inadequate for approximation to observations, and he introduced an even more general relation

$$\sigma''_z = \sigma''_0 \sec^k z + \sigma''_1. \tag{5}$$

The introduction of a third independent parameter, which is physically quite unsubstantiated, does not solve the problem, however; it only leads to an unnecessary complication of the empirical dependence.

The Kuban' Expedition findings thus could not be approximated with any of the empirical relations available at that time, since none fitted the actual data, as we easily verified. Proceeding from purely refractional considerations, we tested the dependence of σ''_z on tg z. Our attempt was quite successful /8/, and the great majority of observations closely fitted the line

$$\sigma''_z = \sigma''_0 + k \, \text{tg} \, z. \tag{6}$$

The values of k vary from session to session, ranging from 0.05 to 0.25. The graphs of σ''_z vs. tg z are plotted in Figure 1.

This dependence also provides a satisfactory approximation to averaged data in each range of zenith distances. Figure 2 a plots the mean pulsation amplitude as a function of tg z from Pulkovo observations carried out in different years at four different points. Figure 2 b plots the same dependence for the observational data used by Kolchinskii (with the exception of A. F. Subbotin's observations, which on account of their amplitudes — a few seconds — cannot be classified as image pulsations). Inspection of this figure proves beyond all doubt that the observations are in excellent agreement with the proposed empirical relation.

However, to tell the truth, averaged observational data are often adequately fitted with relations of the form (1) or (3), but in these cases some follow the former relation, while others follow the latter. This implies that under certain conditions relation (6) can be replaced either with relation (1) or relation (3). Let us establish the conditions for this substitution. We consider the variation with tg z of the functions

$$f_1(z) = (\sec z - 1)^{1/2}, \tag{7}$$
$$f_3(z) = \sec^{1/2} z - 1, \tag{8}$$

as well as the function

$$f_2(z) = (\sec z - 0.78)^{1/2} - 0.47, \tag{9}$$

44
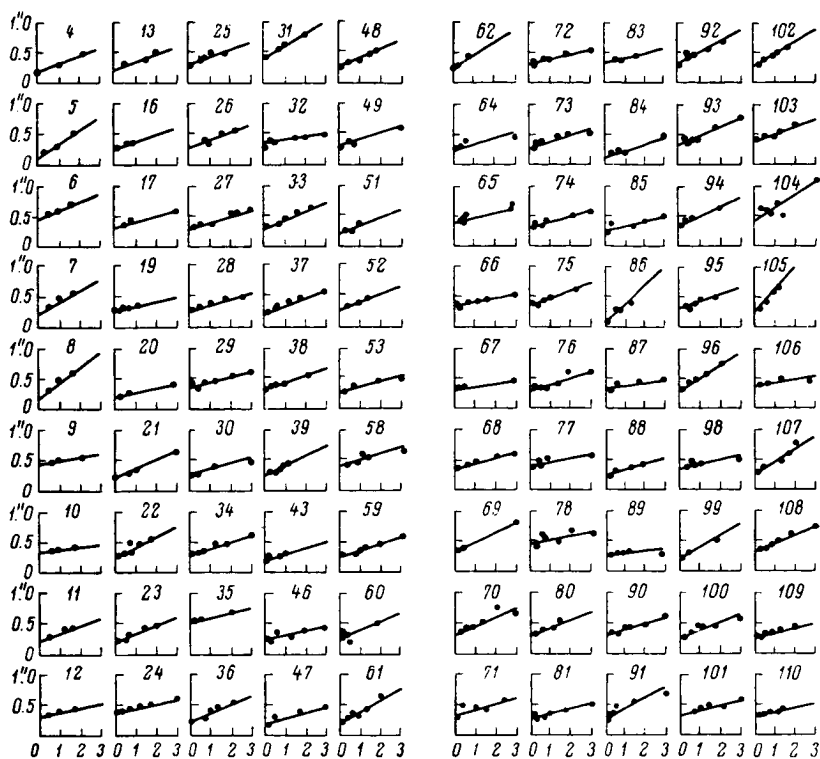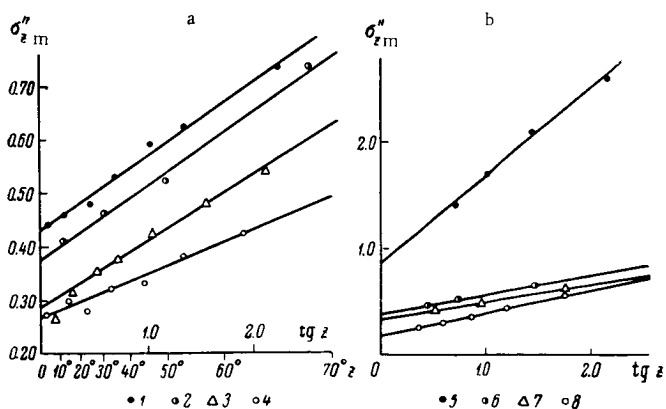
FIGURE 1.

FIGURE 2. $\sigma_{z\,m}$ vs. tg z.

a: 1) Suvorovskaya, 2) Anapa, 3) Kuban', 4) Mountain Astronomical Station of the Main Astronomical Observatory;

b: 5) Fesenkov, Alma-Ata, 1947, 6) Przybyllok, Königsberg, 1922—1929, 7) Bugoslavskaya, Moscow, 1903—1935, 8) Banakhevich, Kazan', 1906—1907.

which is clearly seen to occupy an intermediate position between $f_1(z)$ and $f_3(z)$. The corresponding curves are plotted in Figure 3. We see that $f_1(z)$ is roughly proportional to tg z for $0° \leq z \leq 40°$, and between these z limits we have the approximate relation

$$\text{tg } z \approx 1.51 (\sec z - 1)^{1/2}. \tag{10}$$

The function $f_3(z)$ is roughly proportional to tg z for $30° \leq z \leq 70°$, and between these z limits we have the approximate relation

$$\text{tg } z \approx 0.35 + 3.38 (\sec^{1/4} z - 1). \tag{11}$$

The function $f_2(z)$ is roughly proportional to tg z for $20° \leq z \leq 60°$, and between these z limits we have the approximate relation

$$\text{tg } z \approx 2.34 (\sec z - 0.78)^{1/4} - 0.97. \tag{12}$$

We see that under certain conditions expressions of the form (1) and (3) can indeed be substituted for the empirical relation (6). However, (6) is a two-parametric formula, while (1) and (3) are both one-parametric formulas, so that this substitution is permissible only for a certain relation
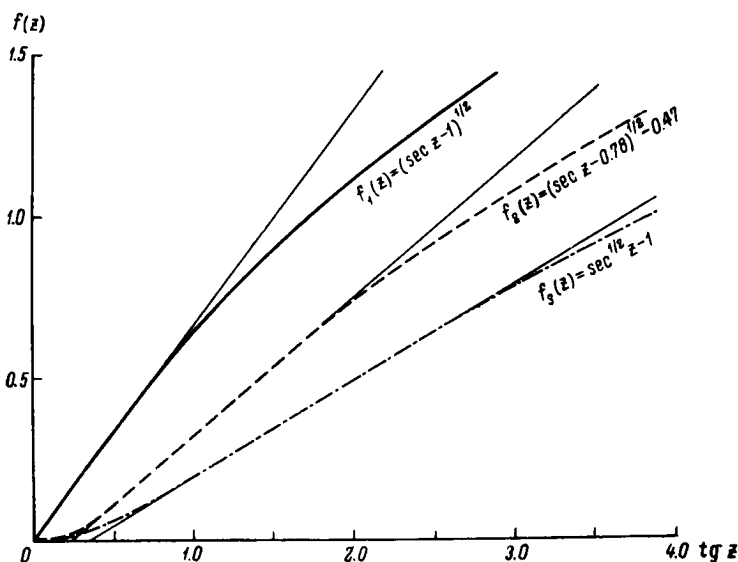
FIGURE 3.

between the parameters σ_0'' and k in (6). Relations (11) and (12) lead to the following conclusion: (a) formula (6) can be replaced with (3) when $\frac{\sigma_0''}{k} \approx 3$; (b) formula (6) can be replaced with (1) when $\frac{\sigma_0''}{k} \approx 1$. Our observations contain subsets which satisfy conditions (a) and (b), as well as the condition

46

$\frac{\sigma_0''}{k} \approx 2$, when neither substitution is admissible. The corresponding plots are given in Figure 4, which proves the validity of our conclusions.

a •1   ○2 ;   b •3   ○4 ;   c •5   ○6
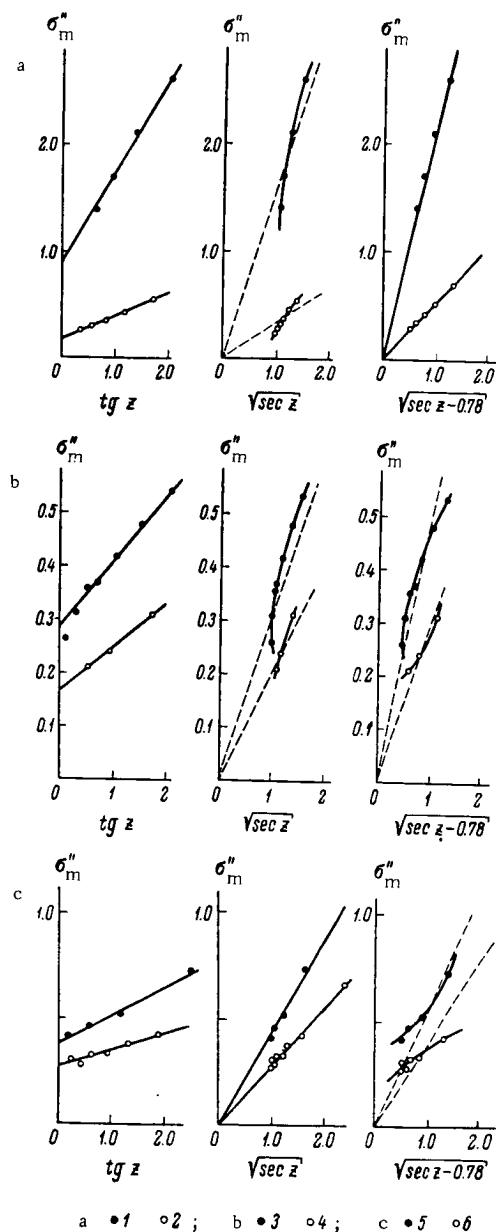
FIGURE 4. $\sigma_{z\,m}$ vs. z .
a: $k = 1$; 1) Fesenkov, 1947; 2) Banakhevich, 1906 − 1907;
b: $k = 2$; 3) Kuban', 4) Bugoslavskaya, 1903 − 1935;
c: $k = 3$; 5) Anapa; 6) Mountain Astronomical Station of the Main Astronomical Observatory.

47

The observations of V. G. Fesenkov and G. A. Banakhevich (Figure 4 a) are satisfactorily fitted with both (6) and (1); they do not agree with (3), however. Observations of the Kuban' Expedition and those of E. Ya. Bugoslavskaya (Figure 4 b) can be described by (6) only. Observations from Anapa and the Mountain Astronomical Station (Figure 4 c) are approximated with (6) and (3), but not with (1).

Figure 5 a is a graph of σ_z'' vs. z according to (3), the dots representing Fesenkov's observations; this graph is reproduced from Kolchinskii's paper, where it is presented as proof of the proportionality of σ_z'' to the square root of sec z. Examination of Figure 5 b shows that (6) provides a much better approximation to these observations than (3) does. A similar result is obtained in all the other cases.
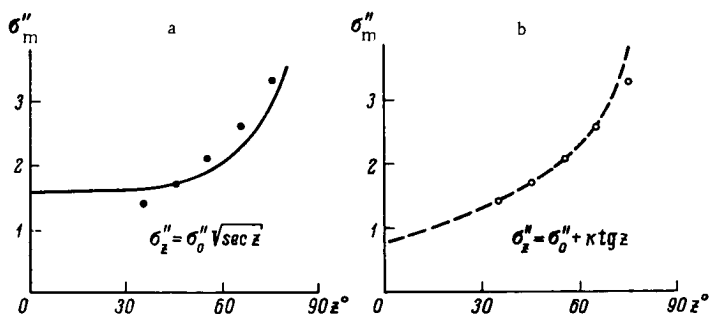
FIGURE 5.

We thus conclude that σ_z'' is always proportional to the tangent of z. In some cases, this proportionality can be replaced with expressions (3) and (1), but the original relation invariably ensures a better fit of the experimental points.

Back in 1956, Ellison /9/ suggested that the phenomenon of image pulsation is attributable to refraction in large inhomogeneities. This approach fully explains our empirical relation. Since nearly everybody will be acquainted with the refraction theory, we hardly need any mathematics. It should be noted, however, that the term with tg z is apparently introduced by refraction in inhomogeneities in the immediate vicinity of the objective. The constant term is contributed by inhomogeneities dispersed along the entire path of the ray.

Kolchinskii, making use of the law of large numbers, derives a proportionality of the pulsation amplitude to $\sqrt{N}$, where N is the number of inhomogeneities encountered by the ray in the atmosphere; this clearly leads to a proportionality to $\sqrt{\sec z}$. The law of large numbers, however, applies only if the inhomogeneities are small in comparison with the path length, i.e., if there is indeed a large number of inhomogeneities. This again holds true for the small inhomogeneities, which are smaller than the objective diameter. The main point, however, is that the law of large number can be applied in Kolchinskii's form only if the atmospheric inhomogeneities are spherically symmetric (interchangeability of $\sqrt{N}$ and $\sqrt{\sec z}$). If the large inhomogeneities are elongated parallel to the Earth's

·surface and actually form so-called "atmospheric lenses", the integrated effect is by no means proportional to $\sqrt{\sec z}$.

An interesting regularity emerged upon examining the results of Pulkovo observations (all observations were made by the same technique, using identical telescopes): k decreased with increasing elevation of the observation point above sea level, i.e., the straight line in our graph should gradually approach the abscissa axis with increasing elevation. This conclusion is supported by the recent observations of the Zelenchuk Expedition (1961). The results of these observations will be published when the treatment is completed.

In conclusion, we should note that direct experiments can be staged to prove or disprove the point of view advocated in this paper. By observing pressure micropulsations near the telescope objective or the fluctuations of density in a cell equal to the size of the objective and comparing the fluctuations of these parameters with the observed image pulsation, one will detect the correlation, or lack of such, between the different phenomena and thus settle the principal query raised in our paper. It would be interesting to observe image pulsations in the direction of the almucantar, i.e., at right angles to the direction of the pulsations measured from photographic trails. The results of these observations, if proved consistent with our notions, could serve as a basis for the development of a detailed refraction theory of image pulsation.

The valuable assistance of the late N.I. Kucherov in the preparation of this paper should not remain unmentioned.

Bibliography

1. Banakhevich, G.A. Tri etyuda po refraktsii (Three Essays on Refraction). Kazan. 1915.

2. Danjon, A. and A. Couder. Lunettes et Telescopes. Paris. 1935.

3. Ulrink, W. —Z. Vermessungswesen, 69:321. 1940.

4. Krasil'nikov, V.A. —Izv. AN SSSR, geography and geophysics series, No.13:33. 1949.

5. Krasil'nikov, V.A. —DAN SSSR, 65:291. 1949.

6. Kolchinskii, I.G. —AZh, 29:350. 1952; AZh, 34:638. 1957.

7. Darchiya, Sh.P. —Izv. GAO, No.165. 1960.

8. Vasil'ev, O.B. and V.V. Vyazov. —Izv. GAO, No.170. 1962.

9. Ellison, M.A. —In: "Astronomical Optics and Related Subjects" (Zd. Kopal, ed.). Amsterdam. 1956.

N. I. Kucherov

THE EFFECT OF SYNOPTIC FRONTS ON SEEING

Optical instability of the atmosphere can be described in terms of the shimmer angle t_0'' and the mean square amplitude of image pulsation σ_0, reduced to the zenith. The graph of nightly averages of these quantities plotted over a certain period can be regarded as a basic characteristic of the local astroclimate. Figure 1 plots the variation of t_0'' for the Mount Sanglok station, in the south of Tadzhikistan (bottom trace), and for the Bairam-Ali station — an oasis in the Kara-Kum Desert near the town of Mara (top trace). The shimmer angles for the various nights are marked by points in the graph, and observations carried out for several nights in succession are joined by a line. Comparison of the two plots distinctly brings out the difference in seeing conditions in the two places. In Mount Sanglok the atmosphere is calmer than in Bairam-Ali, and the seeing is therefore much better. In other words, the astronomical climate of Sanglok is more favorable for observations than that of Bairam-Ali.
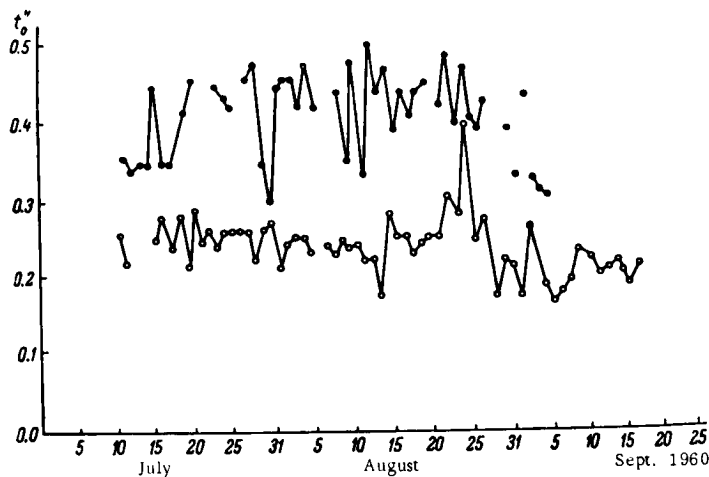
FIGURE 1.

Analysis of these graphs led to some interesting and important conclusions. Various authors have repeatedly tried to establish a relationship of seeing to various meteorological factors: humidity, wind, temperature, pressure, etc. Some formulas have been published which hold true for particular periods only, losing their validity for all other observations.

50

· For example, it is an observationally established fact that high atmospheric pressure generally, but not always, improves seeing. This also applies to relative humidity: an increase in this parameter will sometimes improve seeing, while in other times no change will occur /1 −4/. These facts suggest that seeing is not determined by a single meteorological factor: the reason for deterioration of seeing should be sought in the integrated action of several simultaneous meteorological factors, namely in synoptic processes. Physical characteristics within a single air mass are more or less uniform, but as we cross the boundary surface between two adjoining air masses of different geographic origin, many of the meteorological parameters change abruptly. Turbulent mixing of air at the interface is more vigorous than under ordinary conditions.

In analyzing the extensive observational material collected by the astroclimatic expedition of the Pulkovo Observatory in the years 1960 − 1962, we discovered that one of the main reasons for deterioration of seeing was the presence of synoptic fronts in the observer's sphere of action. Figures 2, 3, 4 plot the variation of the shimmer angle t_0'' and give the corresponding synoptic charts (copies of the Soviet Central Weather Institute maps); the various fronts are shown in the charts, and the observation points are marked with circles. When a front approaches the observation point, seeing deteriorates and t_0'' increases; once the front has passed by, the atmosphere

FIGURE 2.

51

29-VIII-1961

30-VIII-1961

31-VIII-1961

Semirodniki
VIII-1961

t_0''

0.30

0.20

0.10

29　30　31 Date

FIGURE 3.

10-VIII-1961

11-VIII-1961

12-VIII-1961

——— Chapal —·— Chinary — — — Dzhissa
VIII-1961

t_0''
0.40

0.30

0.20

0.10

10　11　12 Date

FIGURE 4.

FIGURE 5.

53

calms down and t_0'' diminishes. Different synoptic fronts produce different changes in t_0''. The frontal layer broadens with the age of the frontal system, since the extent of turbulent mixing grows with the time of contact between air masses of different origin. Sometimes, the atmosphere in a certain locality remains agitated for a comparatively long time. This happens when several synoptic fronts pass in succession, or when one front remains stationary for some time in the vicinity of the observation point.

Let us consider an interesting example which illustrates the effect of one highly extended synoptic front on astronomical seeing in various places which are fairly distant from one another. Take the synoptic situation over Caucasus and Pamir for the period of 24 — 26 September 1960 (Figure 5). An anticyclonic high extends over the European Part of the USSR and Western Siberia. At the southern edge of the anticyclone, a warm front extends through the low in the south of Europe; the warm front covers th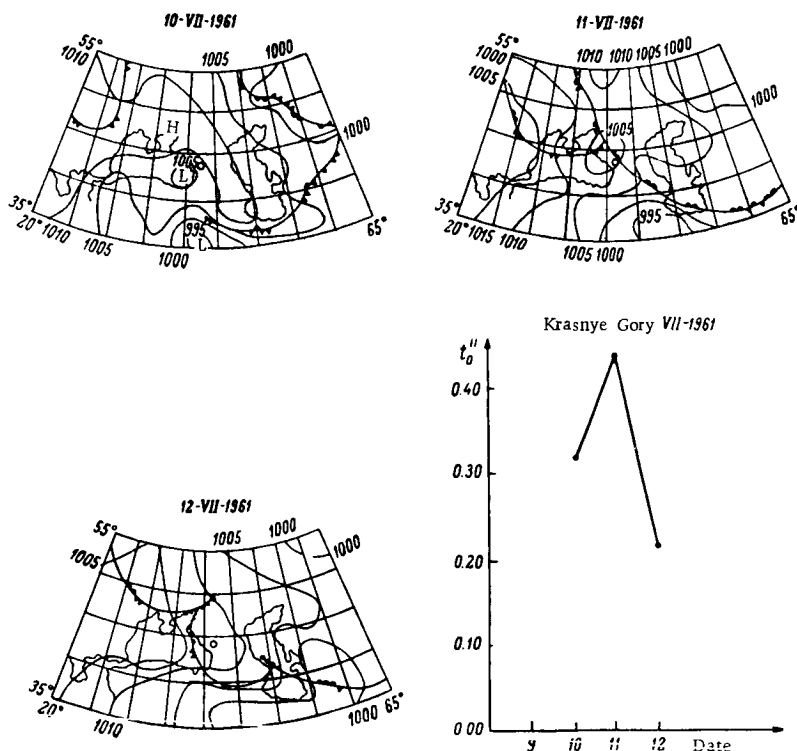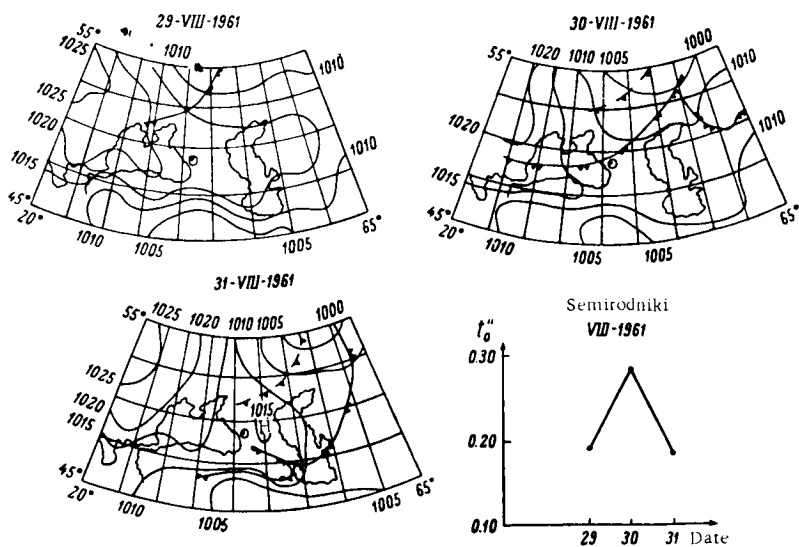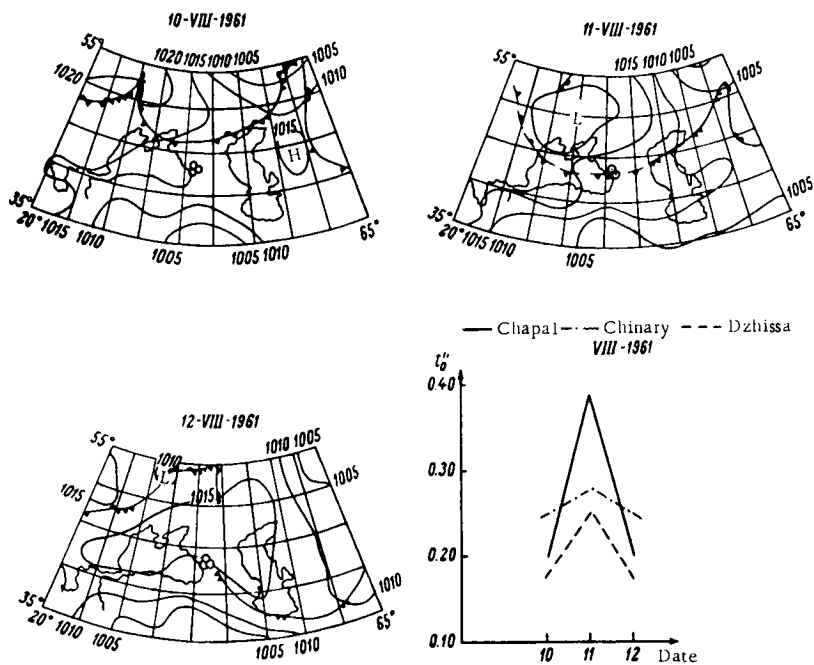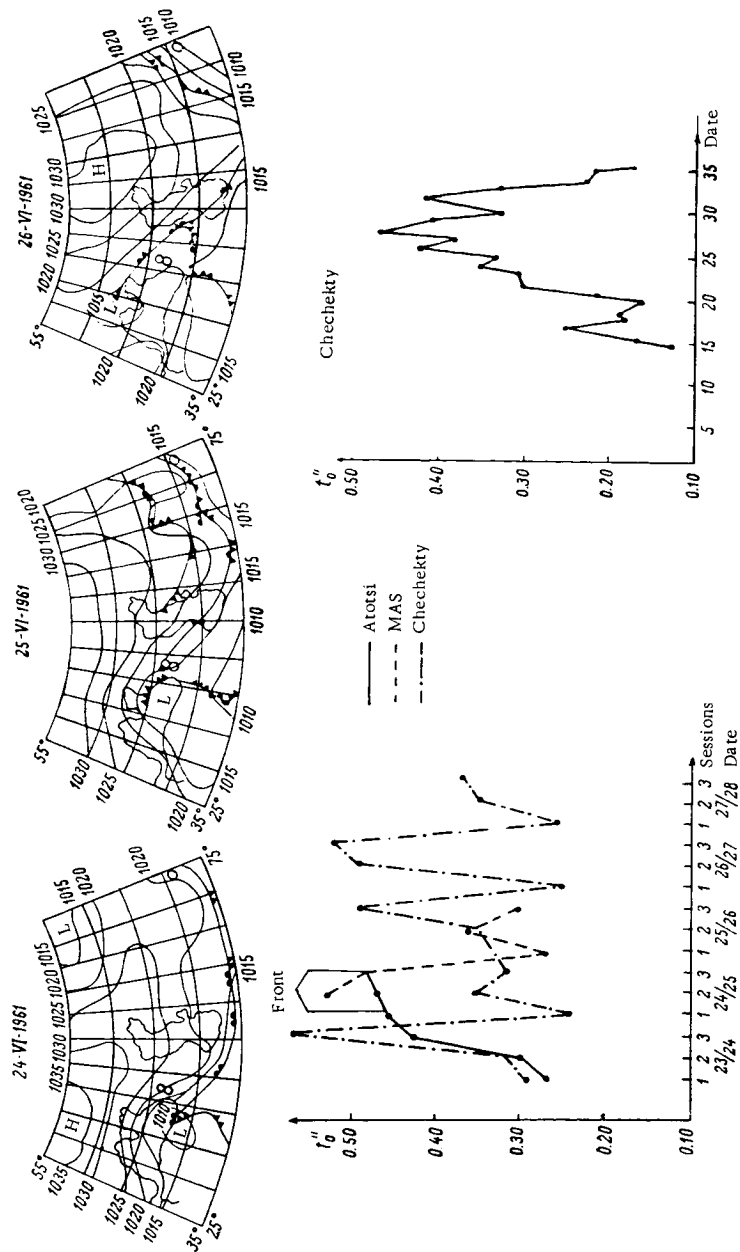e southern part of Caucasus, the south coast of the Caspian Sea, and South Pamir, where it reverses its sign. The frontal system is well formed in the ground layer and in the middle troposphere.

On the 500/1000-mb chart for 3 hours Moscow Time on 24 September this front is represented by a frontal high with a temperature gradient of 10 — 12° over 1000 km. Extensive cloudiness which strongly interferes with observations precedes the passage of the front. In the night between 23 and 24 September, the only sky window in Caucasus was at the Atotsi station (Georgian SSR).

On 25 September, the frontal system becomes sharper. The temperature gradient is as high as 11 — 13° in the 500/1000-mb layer. The front has advanced during the previous day, and it now extends simultaneously over two observation points distant thousands of kilometers from each other, causing sharp reduction in astronomical seeing. During the following night, the front passes over North Caucasus. The line of occlusion stretches far to the northeast, from Makhachkala to Rostov to Dnepropetrovsk. The seeing in Caucasian stations has improved, returning to the prefrontal level. In the Pamir region, the frontal system is trapped by the mountain chains for a comparatively long time, poor seeing persists for several Central Asian stations (e.g., Tyup, on the east coast of Issyk-Kul' Lake, and in Uzbekistan mountains).

We had to verify that the emerging dependence was not accidental, and we therefore undertook to analyze the entire volume of observational data from Mount Chapal and Krasnye Gory hamlet in North Caucasus in the area of the village Zelenchukskaya and from the village Privetnoe in Crimea in the Sudak area; these places sharply differ in their characteristic geographical conditions. Mount Chapal is one of the lateral peaks 50 km from the Caucasus main range, which obscures the southwestern horizon by up to 5°. In other directions, the horizon is plainly visible. The observation point near Krasnye Gory hamlet is situated in a steppe region at the foot of mountains. Hilly steppe extends to the north and to the west, while at a distance of 45 — 60 km to the south and to the east the steppe merges into the Caucasian foothills. The Privetnoe station in Crimea is located on seashore, 250 — 300 m above sea level.

The analysis was based on nighttime shimmer angles t_0'' (2 — 3 sessions every night), measured in four azimuths (north, south, west, and east) at various zenith distances, t_{20}'', t_{40}'' and t_{70}''. Ground layer maps and baric charts were employed in synoptic analysis.

Table 1 lists the nights used in analysis, each at least with two observation sessions. We see from Table 1 that the total number of these nights in the three places is 195, and they are spread over different seasons.

TABLE 1

Months	Chapal 1961—1962	Krasnye Gory 1961	Privetnoe 1962
April	—	—	11
May	—	5	16
June	16	18	10
July	11	12	13
August	15	17	15
September	13	—	8
January	15	—	—
	70	52	73

A case was regarded as positive in our analysis if the following three conditions were observed:

1) high seeing (small, stable shimmer angle) in the absence of frontal activity;

2) deterioration of seeing with the approach of a frontal zone;

3) improvement of seeing once the frontal zone has passed by.

The results of statistical analysis are arranged in Table 2, which lists the percentage of positive, negative, and undecided cases.

TABLE 2

Months	Chapal 1961—1962			Krasnye Gory 1961			Privetnoe 1962		
	positive, %	negative, %	undecided, %	positive, %	negative, %	undecided, %	positive, %	negative, %	undecided, %
April	—	—	—	—	—	—	73	20	7
May	—	—	—	80	0	20	62	19	19
June	100	0	0	72	20	8	80	20	0
July	91	9	0	84	8	8	77	16	7
August	66	8	26	65	35	0	66	27	7
September	55	15	30	—	—	—	87	13	0
January	73	20	7	—	—	—	—	—	—
Average	77	10	13	73	18	9	74	18	8

We see from Table 2 that the positive cases prevail in all the three observation areas (having an average frequency of 75%). This clearly confirms the relationship between synoptic fronts and astronomical seeing. We must keep in mind, however, that in some cases (25%) no such relationship is observed. This category includes an average of 15% negative cases, when a synoptic front undoubtedly passed but seeing remained high, or conversely seeing deteriorated without the passage of a synoptic front, and another 10% of undecided cases, when the synoptic analysis gave contradictory or inconclusive results. We should stress that most of the synoptic fronts were cold fronts.

Let us consider some additional cases for Krasnye Gory and Chapal stations.
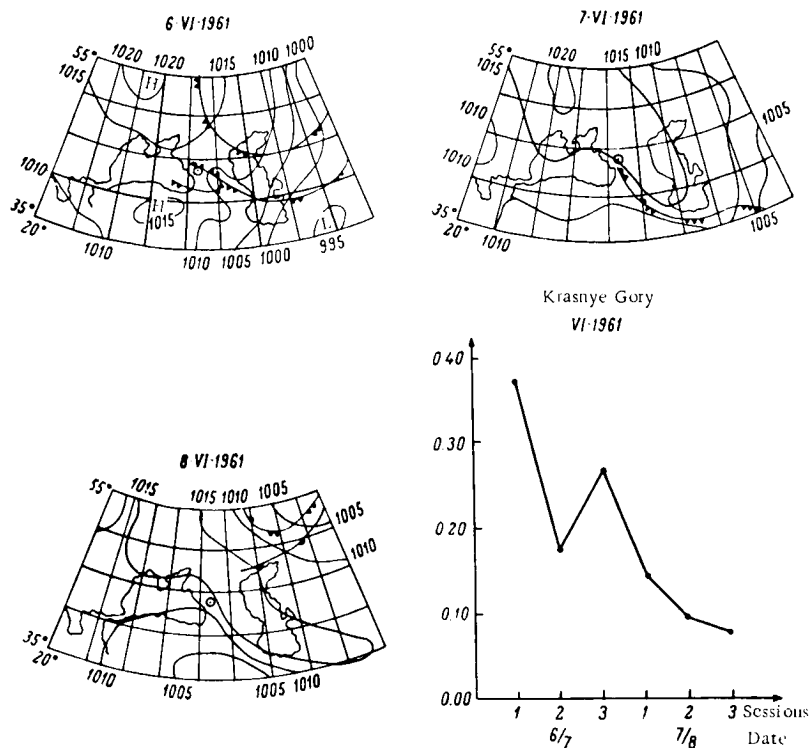
FIGURE 6.

1. The shimmer angle in Krasnye Gory dropped from an average of 0".37 to 0".8 between 6 and 8 June (Figure 6). The synoptic weather conditions for that period reveal the following: in the night between 4 and 5 June, a stable anticyclonic high was observed over the European Part of the USSR, centered in the Baltic area. North Caucasus was under the influence of the front which extended in the latitudinal direction at the southern edge of the anticyclone, along the north slopes of Caucasus. High temperature gradients are apparent in the 850 mb chart; the pressure

1822

field has not changed by 6 June: the front has been stopped by the mountains, hardly advancing in the southerly direction. Occlusion and orographic bending of the front are observed. By the evening of 6 June, the front moves slowly to the southeast, and at 3 hours on 7 June it has advanced fairly far. In the night between 7 and 8 June, the Caucasus area is free from frontal activity: stable anticyclone weather is established.

2. At 3 hours on 21 June, a blurred pressure field extends over North Caucasus. A cold front is approaching from the northwest. Seeing in Krasnye Gory high (Figure 7). At 3 hours on 22 June, the cold front is fairly near to Krasnye Gory, passing at a distance of less than 100 km from the observation point. In the 500/1000 mb chart, the frontal zone is manifested in the temperature gradient. Seeing poor, $t_0'' = 0''.4$.
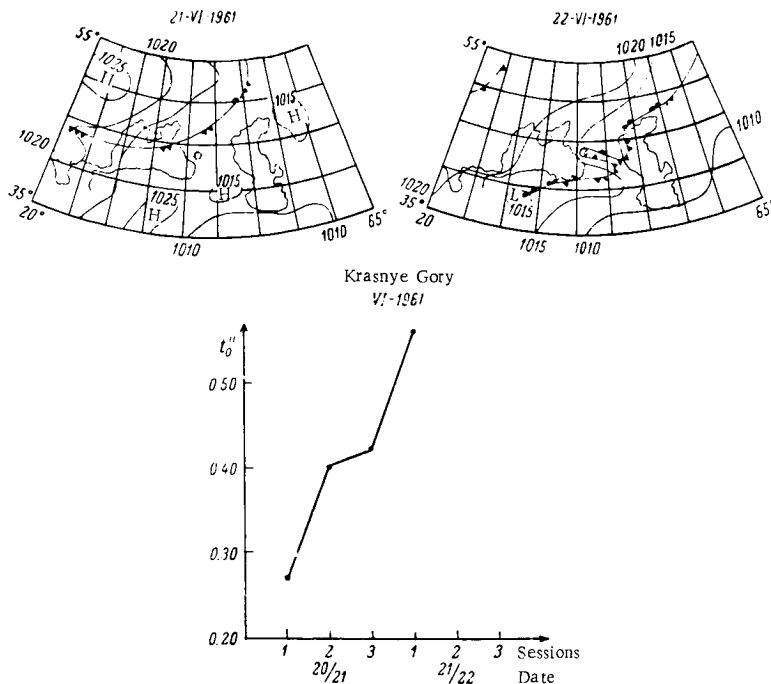
FIGURE 7.

We see from the last example that seeing deteriorates a long time before the actual passage of the front, which is possibly due to orographic disturbance of the air stream. The disturbing influence of the Caucasus range on a uniform air stream is observed only when the stream actually collides with the mountains, while in frontal processes the contribution of the mountains is felt already at distances of 400 — 500 km.

It is interesting to compare the processes responsible for the deterioration of seeing with those which cause the bumpy flight of airplanes. We can freely draw an analogy between the two phenomena, since in both cases we are dealing with eddy processes, with density variations. The relation between seeing and movement of synoptic fronts that we have established

is consistent with the dependence of "bumpy air" on the same factor.
Indeed, bumpy air is mostly encountered in regions where synoptic fronts
(generally cold) pass near the ground. In front-free areas, bumpy air was
reported in 33% of the cases only /5, 6/. The intensity of cold-front
turbulent mixing is considerable due to stream convergence, rising
temperature gradients, and "collapse" of cold air in the leading part of
the front. The cold air collapses due to frictional deceleration, on account
of which the bottom layers of cold air lag behind the summit masses as
the front advances. The upper layers are thus exposed to contact with
underlying warm air; the situation is characteristically unstable, and the
cold summit topples down.

Downward eddy motions are less pronounced in warm fronts, since they
are but slightly inclined and the horizontal temperature gradients are much
smaller than in cold fronts.

The relation discussed in this paper throws light on various properties
of the astroclimate and suggests a certain criterion for the selection of
future observatory sites.

In conclusion, my deepest thanks to L. K. Zinchenko for his help in
synoptic analysis.

Bibliography

1. Schmeidler, F. —AN, **281**:145. 1953

2. Bok, B. J. —AJ, **60**:29. 1955.

3. Thackeray, A. D. —Pretoria MN Astr. Soc. S. Africa, **15**:35. 1956.

4. Kucherov, N. I. —Trudy soveshchaniya po issledovaniyu mertsaniya
        zvezd. Moskva-Leningrad, Izdatel'stvo AN SSSR. 1959.

5. Pchelko, I. G. Aerosinopticheskie usloviya boltanki samoletov
        v verkhnikh sloyakh troposfery (Aerosynoptic Conditions for Air-
        craft Bumping in the Upper Troposphere). —Gidrometeoizdat. 1962.

6. Pinus, N. Z., editor. Atmosfernaya turbulentnost' vyzyvayushchaya
        boltanku samoletov (Atmospheric Turbulence and Aircraft
        Bumping). —Gidrometeoizdat. 1962.

L. K. Zinchenko

AN ESTIMATION OF ATMOSPHERIC TURBULENCE AFFECTING SEEING

N 67-15470

Astronomers often encounter various undesirable phenomena produced by atmospheric instability, such as image pulsation and blurring of the diffraction disk. The present paper analyzes these phenomena along the following line.

Optical inhomogeneities caused by atmospheric turbulence considerably lower the quality of the diffraction disk, since light waves propagating in a turbulent medium undergo phase and amplitude fluctuations due to changes in the refractive index of the medium. A relation should be established between the diffraction disk and the turbulent state of the atmosphere. A detailed analysis of this topic is complicated by unavailability of experimental turbulence parameters at various altitudes.

One of the principal problems of the modern turbulence theory is the choice of the criterion describing the state of agitated atmosphere. The Richardson number is the most convenient for applied purposes, as it only requires knowledge of vertical temperature gradients and of the wind velocity vector /1/. This number, as a physical quantity, takes its origin in the hypothesis on the existence of two predominant modes of energy conversion. The first of these two modes converts the kinetic energy of the mean flow into eddy energy. The second mode is a sink of eddy energy, which is expended as the work of vertical displacement of air particles in stable atmosphere. The equation of eddy energy balance is therefore

$$\frac{dE'}{dt} = \int \left[K_0 \beta - K_T \frac{g(\gamma_a - \gamma)}{T} \right] \rho dV,$$

where K_T is the eddy conductivity, K_0 eddy viscosity along the vertical, T the mean air temperature in the layer (the temperature at midlayer), ρ air density, V volume of unit air mass, g gravitational acceleration, β vertical wind-velocity gradient, γ_a, γ dry-adiabatic and actual vertical temperature gradients in the layer. The first term takes account of the gain in eddy energy per unit mass. The second represents the loss of energy per unit mass. If we take $\frac{K_0}{K_T} \sim 1$ and put $\mathrm{Ri} = \frac{g(\gamma_a - \gamma)}{T\beta^2}$, then for $\mathrm{Ri} < 1$, $\frac{dE'}{dt}$ is positive and the turbulence is conserved or grows, while for $\mathrm{Ri} > 1$ the turbulence decays.

A few words on the treatment of observations. Astronomical observations were made in June — July 1963 at the Main Geophysical Observatory (village Voeikovo, Leningrad Region); AZT-9 telescope was used, equipped with the

TABLE 1

	Good seeing								Poor seeing												Mean values			
	12 VI		28 VI		27 VI		28 VI		7 VI		8 VI		15 VI		19 VI		29 VI		6 VII		Good seeing		Poor seeing	
	н	в	н	в	н	в	н	в	н	в	н	в	н	в	н	в	н	в	н	в	н	в	н	в
	73	3.5	75	3.5	73	3.5	71	3–3.5	75	5.0	70	5.0	73	5.0	70	5.0	76	5.0	75	5.0	75	3.5	75	5.0
	45	2.5	45	2–2.5	45	2.0	45	2.5	45	3.0	57	4.0	55	3.5	42	3.5	44	3.5	45	3.5	45	2–2.5	40	3–3.5
	28	1.5–2.0	20	1.5	20	1.5	21	2.0	30	3.0	30	3.5	40	3.0	30	3.0	20	3.0	25	3.0	20	1.5–2.0	30	3–3.5

objective of a moon camera, aperture diameter, 140 mm, focal distance 5956 mm: the telescope was mounted near the site where the radio sondes were released. Random errors in the determination of wind speed and direction by radar were $0-3$, $1-2$ m/sec and $0-10$, $6-3°$, respectively. These errors are to be expected in the lower troposphere, up to heights of $3-5$ km. In the upper troposphere, larger errors are incurred.

Seeing was estimated according to the Danjon–Couder scale. Of the total of 17 nights, we selected nights with excellent or poor seeing. Medium-seeing nights were ignored. Excellent and poor seeing nights were picked out according to the following criteria:

	z	Seeing (Danjon-Couder scale)
Excellent	75°	3.5
	45	$2-2.5$
	$20-30$	1.5
Poor	75	5.0
	45	$3-3.5$
	$20-30$	$3-3.5$

A distribution of seeing in zenith distance for excellent- and poor-seeing nights is given in Table 1 (seeing is expressed in points of the Danjon–Couder scale).

The following characteristics were calculated for the sample nights: vertical temperature gradient, vertical wind-velocity gradient, and Richardson numbers for half-kilometer layers. In our calculations of Ri we made allowance for the dependence of its value, and of the critical magnitudes as well, on the thickness of the averaging layer. If the layer thickness is increased, the probability of detecting local high-turbulence regions diminishes: these pockets, according to experimental aircraft measurements, vary in thickness, but hardly ever exceed $300-600$ m, and in clear weather, according to American data, they are mostly less than 300 m /4/. The higher the turbulence, the thinner the atmospheric turbulent layer. Highest intensity (moderate and strong turbulence) is observed mainly in the lower 3-km layer of the

troposphere, and it is for these strata that our calculations are made. Half-kilometer intervals is thus a reasonable bet.

Turbulence can be expected to develop if the atmosphere is highly unstable. Thermal instability is connected with increased vertical temperature gradients, and dynamic instability is determined by the vertical wind-velocity gradients. However, the attempt to relate seeing to temperature and wind-velocity gradients separately (Figures 1, 2) gave inconclusive results. If, say, the stellar diffraction disk is blurred by
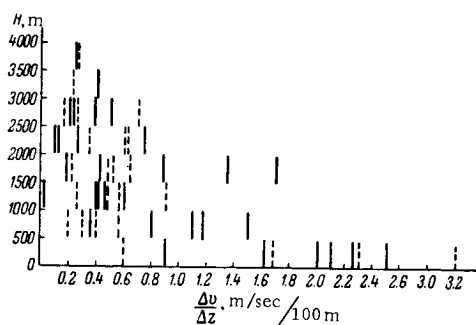
FIGURE 1. Distribution of wind-velocity gradients. Solid lines — poor-seeing nights; dashed lines — excellent-seeing nights.
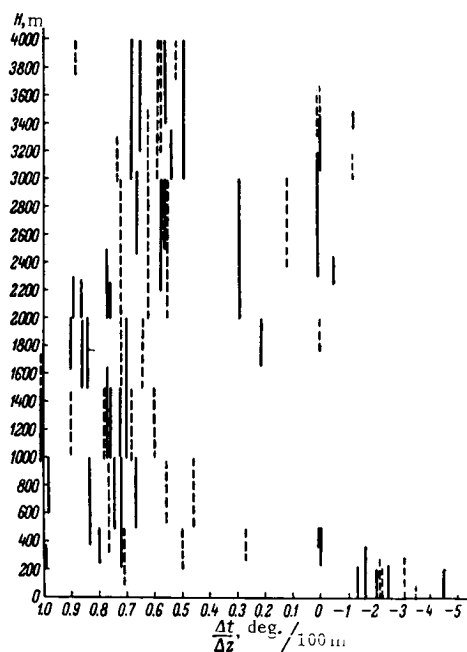
FIGURE 2. Distribution of air-temperature gradients. Solid lines — poor-seeing nights; dahsed lines — excellent-seeing nights.

61

large vertical temperature gradients, which lead to the onset of thermal
instability of air masses, the graph plotting the vertical distribution of
temperature gradients in nights of poor and excellent seeing will show
distinct concentration of points in the left- and the right-hand parts of the
plot. Nights with excellent seeing (dashed lines) should collect in the
right-hand part of the graph, where the temperature gradients are small.
This can also be argued for the relation to the vertical wind-velocity
gradient. No such pattern is observed in reality, however. Excellent-
and poor-seeing nights are dispersed at random. This is probably so
because the two gradients considered separately may mutually cancel
insofar as the onset of turbulence is concerned. Previous measurements
/2, 3/ show that the effect of wind-velocity gradient is often damped by
the stabilizing influence of temperature stratification in the atmosphere.
An increase in vertical temperature gradients obviously offsets the damping
influence of temperature stratification.
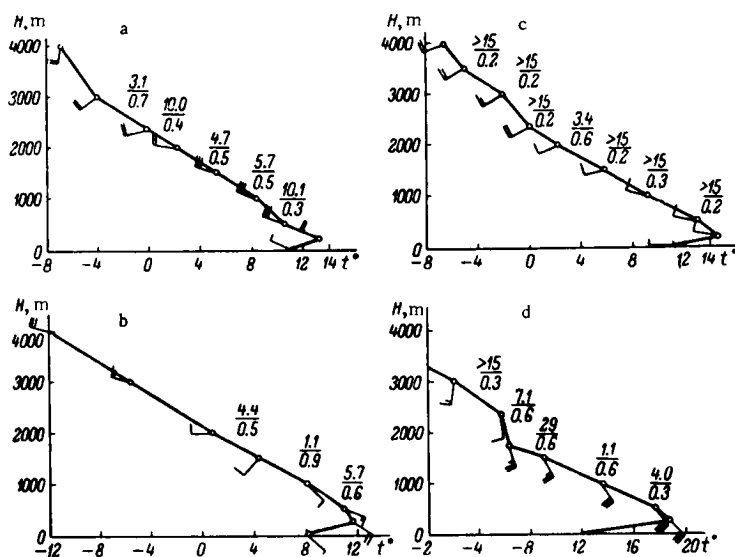
FIGURE 3. Distribution of Richardson numbers in nights with excellent seeing.

a) s	B	b) s	B	c) s	B	d) s	B
71	30 — 3.5	73	3.5	75	3.5	73	3.5
45	2.5	45	2.5	45	2.0 — 2.5	45	2.0
21	2.0	28	1.5 — 2.0	20	1.5	20	1.5

It follows from the preceding that an analysis based on separate treatment
of wind-velocity and temperature gradients may often lead to erroneous
results. The Richardson number incorporates both these disturbing forces
and provides a more accurate characteristic of the state of the atmosphere.
   The vertical distribution of Ri over any night is highly nonuniform, which
implies that the troposphere is stratified at various altitudes in relation to
the amount of eddy energy.
   Figures 3, 4 are the corresponding stratification curves of the atmosphere.
The fractional quantities to the right of the stratification curve express the

Richardson number ("numerator") and the vertical wind-velocity gradient ("denominator"). Cross hatching marks layers with Ri< 1, where turbulence sets in. Not a single case of turbulence was observed for nights with excellent seeing: Ri was invariably above the critical value, the atmosphere remained calm.
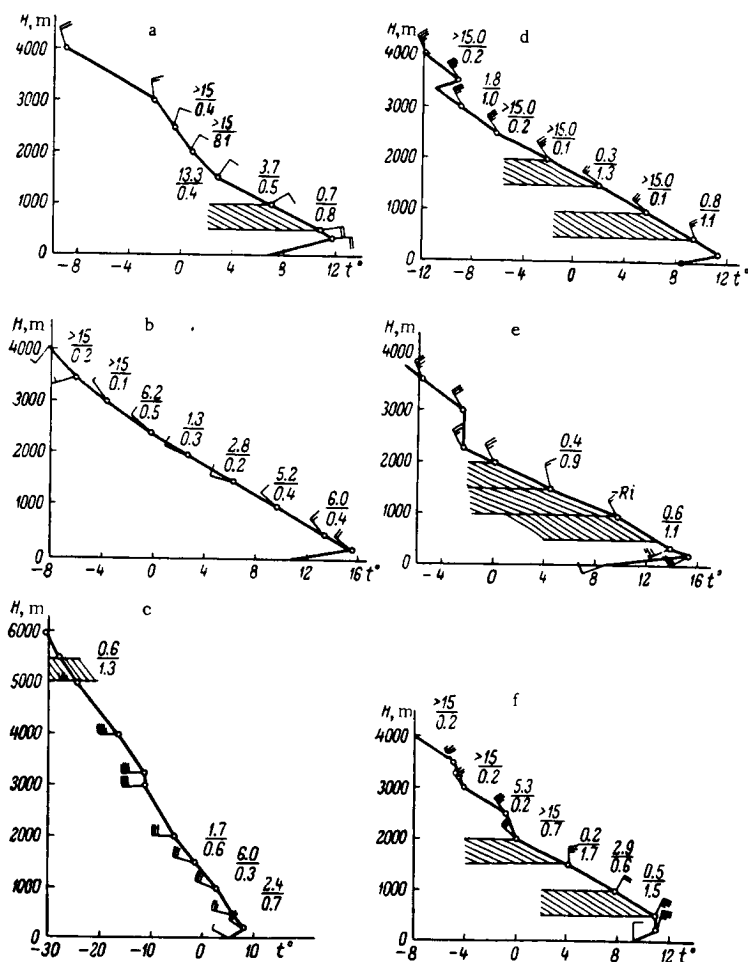
FIGURE 4. Distribution of Richardson numbers in nights with poor seeing.

a)	s	B	b)	s	B	c)	s	B	d)	s	B	e)	s	B	f)	s	B
	70	5.0		76	5.0		73	5.0		70	5.0		75	5.0		75	5.0
	42	3.5		44	3.5		55	3.5		57	4.0		45	3.0		45	3.0
	30	3.0		20	3.0		40	3.0		30	3.5		25	3.0		30	3.0

In nights with poor seeing, in addition to the generally diversified distribution of Richardson numbers (with the exception of the night between the 28 and the 29), there is always a layer, or even several layers, with

highly turbulent atmosphere (i.e., with $Ri < 1$). The height of these layers varies, ranging from 0.5 to 5.5 km (Table 2).

TABLE 2

| Date | Height of layer |
	0—0.5	0.5—1.0	1.0—1.5	1.5—2.0	2.0—2.5	2.5—3.0	3.0—3.5	3.5—4.0	4.0—4.5	4.5—5.0	5.0—5.5
6/7 7/8 14/15 18/19 5/6		$Ri < Ri_{cr.}$ $Ri < Ri_{cr.}$ $Ri < Ri_{cr.}$ $Ri < Ri_{cr.}$	$Ri < Ri_{cr.}$	$Ri < Ri_{cr.}$ $Ri < Ri_{cr.}$ $Ri < Ri_{cr.}$							$Ri < Ri_{cr.}$
Number of cases		4	1	3							1

We see from Table 2 that a high eddy energy is generally observed for the layer below 2 km; in four cases it is the $0.5 - 1$ km layer which is turbulent, and in three cases the $1.5 - 2$ km layer. A light wave propagating in these layers is deformed by refractional inhomogeneities, since in a layer where air masses move at random and there is incessant relative streaming in all directions, including vertical, air density changes every split second. If a star is viewed through this layer, a blurred diffraction disk is registered. Turbulent processes which distort the stellar images therefore apparently occur in the lower layers of the troposphere. If we draw an analogy with the turbulent processes responsible for aircraft bumping (which is inherently the same phenomenon, conditioned by changes in air density), we immediately notice an excellent correlation between the corresponding experimental data. An aircraft flying at a height of 5 km experiences as little as 10% of the overload on an aircraft at $1 - 1.5$ km /3/. It is apparently the lower-atmosphere turbulence which is of decisive significance in all that concerns seeing: a) optical inhomogeneities are most effective in the ground layer, where the air density is highest; b) the intensity of turbulence is greatest in this layer; c) eddies of minimum size occur in the ground layer.

In conclusion we should note that at present there are some contradictory results in connection with the applicability of the Richardson number as a criterion of high atmospheric turbulence.

The main reason for this undesirable development is that the intensity of turbulence is not a single-valued function of the Richardson number, although it clearly depends on this number. $Ri < 1$ provides us with a qualitative indication that, first, turbulence sets in and, second, the amount of accumulated eddy energy in steady-state conditions increases with the decrease in Ri. It must be stressed that the calculational turbulence parameters characterize this effect as a whole, without bringing out the particular region of the eddy spectrum which is responsible for the distortion of the stellar diffraction disk.

. Strict synchronization of aerological and astronomical observations in space and in time is highly important. If the time difference is large (2 — 2.5 hrs), the calculated Ri is distorted by local variations in temperature and wind velocity. If the distance between the point of observations and the site where the radio sonde is released is large (100 — 200 km), Ri is distorted by factors connected with the horizontal extent of the turbulent regions. In general, their sizes vary from a few kilometers to 400 — 500 km and more, although they seldom exceed 60 — 80 km /3/. In our investigations, astronomical observations were strictly synchronous with the meteorological probing. Time differences were as small as 20 — 40 min, and the telescope mount was practically at the site where the radio sondes were released. Our calculations were made for the lower troposphere (0 — 3 km), where the errors in wind measurements were minimal, so that the accuracy of Ri calculations could not be considerably affected by this factor. The calculated values of Ri thus provide an objective parameter for the energy reserve of the atmosphere.

The results of our measurements, which are highly tentative and must be further refined, point to a high correlation between astronomical seeing and the turbulence of the low troposphere (0 — 3 km), as estimated in terms of the Richardson number. Lack of data rules out a more exact definition of the seeing layer which is directly responsible for the blurring of the stellar diffraction disks. Turbulence, however, shows a tendency to be confined to the 0.5 — 2. 0 km layer.

The author is grateful to N. I. Kucherov for valuable suggestions.

Bibliography

1. Zavarina, M. V. — Tr. GGO, No. 123. 1961.

2. Pchelko, I. G. Aerosinopticheskie usloviya boltanki samoletov v verkhnikh sloyakh troposfery (Aerosynoptic Conditions of Aircraft Bumping in the Upper Troposphere). —Gidrometeoizdat. 1962.

3. Pinus, N. Z. — Tr. TsAO. 1948.

4. Pinus, N. Z., ed. Atmosfernaya turbulentnost', vyzyvayushchaya boltanku samoletov (Atmospheric Turbulence and Aircraft Bumping). —Gidrometeoizdat. 1962.

G. I. Bol' shakova and Sh. P. Darchiya

FLUCTUATIONS OF SHIMMER ANGLE

1. DIURNAL VARIATION OF SEEING

Nighttime observations reveal that seeing is not always constant. If the night is atmospherically unstable, sharp changes in seeing may occur during short observation sessions. The variation of t_0'' (shimmer angle reduced to the zenith), which characterizes the image quality or the astronomical seeing, does not always take the same course, either. For example, in Anapa, in the night between 19 and 20 December 1956, t_0'' monotonically decreased from $0''.55$ to $0''.25$, i.e., astronomical seeing improved, whereas between 28 and 29 April 1957 seeing deteriorated from $0''.18$ (in the evening) to $0''.48$ (the morning after). There are cases when seeing deteriorates rapidly and improves slowly, or vice versa.

These examples outline the nocturnal variation of seeing: t_0'' rises when the atmospheric inhomogeneity is high, while small t_0'' correspond to lower inhomogeneity with favorable observation conditions. The daytime atmospheric inhomogeneity is apparently also variable, which is mostly manifested in pulsation of the solar limb. It is therefore interesting to detect the relationship, if any, between the daytime and the nighttime seeing.

Daytime observations were made by projecting the sun's disk onto a screen with millimeter markings. When the image was in focus, distinct pulsations of the disk edge could be observed. These pulsations were measured in fractions of millimeter and then converted to angular dimensions. In Dagestan, the sun was observed by this technique every two hours from sunset to sunrise, during August and September 1959. In Pamir the observations were made from December 1959 through May 1960, in three daily sessions (9^h, 13^h, 15^h local standard time). The sun's disk in Dagestan measured 20 cm, and in Pamir 10 cm. The measurements were accurate to within 0.5 mm, which is on the average $20-30\%$ of the measured quantity for the given zenith distance of the sun. The method is obviously crude, but it nevertheless enabled us to trace with fair certainty the general trend of daytime astronomical seeing. In Figure 1 a, the abscissa gives the days and the hours of observation, the left-hand ordinate gives t_0'' (shimmer angle reduced to the zenith according to the secant law; it is marked by black dots in the graph), and the right-hand ordinate is the τ_0'' scale of solar limb pulsations in seconds of arc, also reduced to the zenith according to the secant law (white circles). Let us consider the observations for 15, 16, and 17 November 1959. In the night of 15 November, the seeing was poor, the zenith shimmer angle reaching $0''.9$; sharp improvement was observed by dawn, but seeing
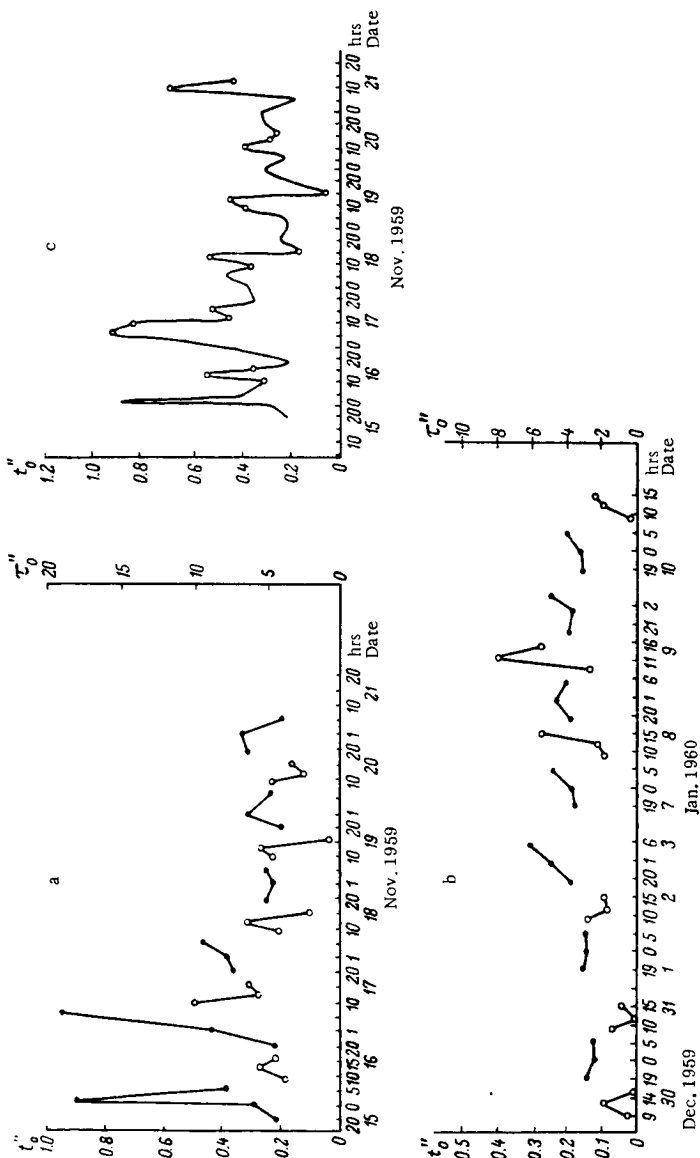
FIGURE 1. Variation of t_0'' in Pamir in 1959–1960

a variation of t_0'' and τ_0'' for 15 through 21 November 1959, b variation of t_0'' and τ_0'' for 30 December 1959 through 10 January 1960,
c variation of t_0'' for 15 through 21 November 1959.

67

remained middling. ($t_0'' = 0''.38$). Gradual improvement of atmospheric conditions persisted, and by 9 hours A.M., the edge of the solar disk oscillated by less then $4''$ of arc; the pulsations somewhat increased reaching $5''.5$ by noon; some improvement was registered toward sunset. The positive trend apparently did not subside, since during the first nighttime session (20^h) seeing was excellent. Improvement gave way to subsequent deterioration of seeing. By dawn, the sun was fairly "agitated" ($\tau_0'' = 10''$), i.e., astronomical seeing was unfavorable.

An interesting graph is reproduced in Figure 1 b. Here in the night between 30 and 31 December 1959 and between 31 December 1959 and 1 January 1960 astronomical seeing is excellent (t_0'' not greater than $0''.15$). The daytime values for 30 and 31 December and 2 January plotted in the same figure indicate that the daytime seeing was also satisfactory. Figures 1 a and 1 b thus lead to the conclusion that if the night is unstable, the nocturnal trend (whether improvement or deterioration of seeing) also persists during the day, and if the night is characterized by good and stable seeing, no deterioration is recorded during daytime. Comparison of t_z'' and τ_z'' for Dagestan (38 pairs) and Pamir (83 pairs) supports these conclusions.

The foregoing suggests that for simultaneously observed t'' and τ'' any deterioration in nocturnal astronomical seeing is accompanied by an increase in the magnitude of solar limb pulsations, and vice versa. Therefore, if we compare the t_z'' and τ_z'' values for early morning and late evening (this of course presupposes that the atmospheric inhomogeneities do not change much during the period between the observations of stars and the sun), t'' can be expressed in terms of τ'' and vice versa. Indeed, by examining pairs of t'' and τ'' measured in the morning and in the evening (the time between paired observations is on the average four hours), we arrive at the following results for Dagestan

$$\sum_{i=1}^{38} \frac{t_i''}{\tau_i''} = 0.22 \quad \text{or} \quad t'' = 0.22\tau'', \tag{1}$$

and for Pamir

$$\sum_{i=1}^{83} \frac{t_i''}{\tau_i''} = 0.085 \quad \text{or} \quad t'' = 0.085\tau''. \tag{2}$$

To avoid errors due to reduction to the zenith, the solar limb pulsations and the corresponding shimmer angles used in the derivation of (1) and (2) were measured for $z = 70°$ and $z = 75°$.

To verify the validity of (1) and (2), we calculated the correlation coefficient between t_0'' and τ_0'' /1/. For Pamir $r = 0.73 \pm 0.03$ with variance of $0''.04$.

The linear correlation equation is

$$t'' - \sum_{i=1}^{168} t_{0i}'' = r \frac{\sigma_y}{\sigma_x} \left(\tau'' - \sum_{i=1}^{108} \frac{\tau_{0i}''}{168} \right).$$

In our case,

$$t'' = 0.088\tau'' - 0''.0054.$$

Dropping 0''.0054, we obtain

$$t'' = 0.088\tau''. \qquad (3)$$

Expression (3) is very close to (2). Making use of expressions (1) and (2), we plotted the appropriate graphs for Pamir and Dagestan. We reproduce here one of the graphs for Pamir (Figure 1 c). In this graph, the abscissa gives the day and the hour of observation, the ordinate marks the shimmer angles t_0'' for daytime and nighttime observations. We see from the curve that the variation of t_0'' is reminiscent of random fluctuations.

Along the lines of Figure 1 c, we plotted graphs for the variation of t_0'' from night to night, from month to month, and from year to year. A comparison of these graphs has shown that while the diurnal variation of t_0'' follows a random fluctuation curve, the night-by-night variation of t_0'' is a much more regular oscillatory process, whereas the monthly and the yearly variations are nearly periodic fluctuations. The graphs $t = \begin{cases} f\,(\text{months}) \\ F\,(\text{years}) \end{cases}$ are understandably much smoother than the graph of Figure 1 c. If the graph is plotted for the nightly averages of t''_0, only the fluctuation component produced by comparatively long-lived atmospheric processes emerges, and the resulting curve is smoother than the detailed plot of Figure 1 c. In other words, in examining the night-by-night variation of t_0'', fluctuations produced by small-scale processes average out and only large-scale processes are evident. This argument also applies to month-by-month and year-by-year curves. The corresponding curves are even smoother, due to the progressive obliteration of microclimatic factors and accentuation of long-range climatic phenomena influencing astronomical seeing.

2. SHIMMER ANGLE FLUCTUATIONS OF DIFFERENT PERIODS

It would be interesting to establish the periods after which large (or small) shimmer angles start repeating. To this end, we proceeded with various continuous observations and calculated the time intervals (a) between two successive maxima (from numerous curves of the type shown in Figure 1 c) and (b) between two successive minima. The period in Pamir observations ranged from a low of 4 hours (one case) to a high of 33 hours (one case out of 102). The extrema mostly occurred each 10 – 20 hours (67 cases). On the average, large (small) shimmer angles should be expected to recur each 16 hours.

The variation within this time interval is the shimmer amplitude, $A'' = t''_{max} - t''_{min}$. The amplitude ranges from 0''.08 (one case) to 1''.65 (two cases), with a modal value of $A'' = 0''.20 - 0''.40$ and a mean $\bar{A}'' = 0''.40$.

Analogous calculations for Dagestan gave a mean period of 10 hours and a mean amplitude of 0''.49.

The shimmer periods and the amplitudes are thus different in Pamir and Dagestan, but both places have the following points in common.

1. The shimmer angle displays diurnal fluctuations with a maximum-to-maximum (or minimum-to-minimum) period which is much less than 24 hours.

2. The mean difference between the maximum and the minimum values of the shimmer angle is $0''.40 - 0''.60$, which is far beyond the margin of error (0.5 scale points is the permissible error of a single observation in zenith if the measured quantity is $2 - 2.5$ scale points; this corresponds to an error of $0''.08$, but for small shimmer angles estimates of $1 - 2$ scale points can be obtained with an error not exceeding $0''.02$).

If the time between two successive t''_{max} (t''_{min}) in Dagestan and Pamir — two places with very different climatic and geographical conditions — is less than a day, we can safely assume that this will also be true for other localities. Steppe and desert areas may prove an exception to the rule, but there is unfortunately a shortage of experimental data for these regions. For both places, we calculated $N = 153$ time intervals between successive $t''_{0\,max}$ ($t''_{0\,min}$); these periods and the corresponding amplitudes are listed in Tables 1 and 2. In Table 1, T_h is the period between the extrema in Figure 1 b, in hours, n_h the frequency of the corresponding T_h, v_h the relative frequency $\left(v_h = \dfrac{n_h}{N}\right)$. In Table 2, A''_h is the amplitude, n'_h the frequency, and v'_h the relative frequency $\left(v'_h = \dfrac{n'_h}{N}\right)$.

TABLE 1

T_h	$\leqslant 10$	$11-20$	$21-30$	> 30
n_h . .	62	55	32	4
v_h . .	0.40	0.36	0.21	0.03

TABLE 2

N = 153

A''_h	$\leqslant 0''.20$	$0.21-0''.30$	$0.31-0''.40$	$0.41-0''.50$	$0.51-0''.70$	$0.71-0''.90$	$> 0''.90$
n'_h . . .	36	35	24	19	18	11	9
v'_h . . .	0.24	0.23	0.16	0.12	0.12	0.07	0.06

The data of these tables are plotted as graphs in Figure 2. We see from the graphs that the frequency of occurrence diminishes as T_h and A_h increase. Note that T_h are calculated for different times of year. Moreover, the data used in the calculation of T_h and A_h did not undergo any previous selection.
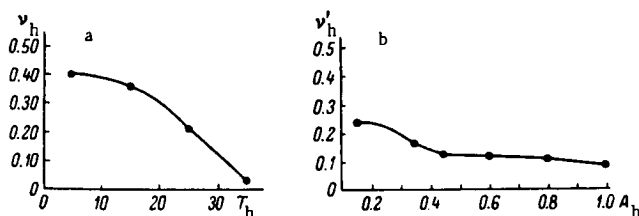

FIGURE 2. Frequency distribution of T_h and A_h.

We may therefore conclude that in our case T_h of some $10-20$ hours is the shortest, as well as the most probable ($P = 0.76$) period. The shimmer amplitude is $\leq 0''.50$ with a probability of $P = 0.75$.

The recurrence of large (small) t_0'' in night-by-night and month-by-month curves and the mean fluctuation amplitudes were calculated from the results of continuous observations in 13 different places (in the years $1954-1962$), and the data were tabulated as in Tables 1 and 2. Here we only give the summary table (Table 3). Like in Tables 1 and 2, T_h and v_h are the periods, in hours, and the relative frequencies, respectively. T_d and T_m are the periods measured in days and months, having the relative frequencies v_d and v_m. The left half of the table lists the amplitudes A_h, A_d, A_m, with their relative frequencies.

TABLE 3

$N = 153$		$N = 191$		$N = 49$		$N = 153$		$N = 191$		$N = 49$	
T_h	v_h	T_d	v_d	T_m	v_m	A_h	v_h	A_d	v_d	A_m	v_m
≤ 10	0.40	2	0.24	2—2.5	0.32	$\leq 0''.20$	0.24	$\leq 0''.15$	0.40	$\leq 0''.20$	0.69
11—20	0.36	3	0.23	3—4	0.29	0.21—0.30	0.23	0.16—0.25	0.29	0.21—0.30	0.26
21—30	0.21	4	0.20	5—6	0.24	0.31—0.40	0.16	0.26—0.35	0.13	0.31—0.40	0.025
> 30	0.03	5	0.13	7—8	0.15	0.41—0.50	0.12	0.36—0.45	0.10	0.41—0.50	0.025
		6—7	0.12			0.51—0.70	0.12	0.46—0.80	0.05		
		8—9	0.06			0.71—0.90	0.07	> 0.80	0.03		
		10—11	0.01			> 0.90	0.06				
		12—13	0.005								
		> 13	0.005								

We see from Table 3 that T_d varies from 2 to 13 days, but it hardly ever exceeds 10 days. Small (large) shimmer angles can be expected (with a probability of $P = 0.67$) to recur after $2-4$ days. The corresponding fluctuation amplitude is $\leq 0''.25$, with a probability of $P = 0.69$.

As regards the month-by-month variation of t_0'', we see from Table 3 that T_m is mostly in the range between two and four months ($P = 0.61$), with an amplitude of $\leq 0''.30$ ($P = 0.95$). The peak value of T_m (eight months) was observed in one out of 49 cases.

The above data on the expected fluctuation periods reveal the following general features:

1) the frequency of occurrence decreases with increasing T;
2) the frequency of occurrence decreases with increasing amplitude.

It is very important to find a period T which is longer than T_m. There are unfortunately no data covering a period of several years for one locality. Many-year data collected from various observation points can be applied to obtain at least an approximate solution for this problem.

In Figure 3, the ordinate gives the monthly averages for various observation points; the months are marked along the abscissa axis. It is obvious that the month-by-month variation of t_0'' follows the same trend in different localities. We therefore may average over the different sets

TABLE 4

No.	Observation point	Location	Observation period	Responsible organization
1	Pirkuli /2/	Azerbaidzhan SSR, Shemakha District	January–December 1954, May–September 1958	Shemakha Astrophysical Observatory of the Azerbaidzhan Acad. Sci.
2	Kardakh, Pirkuli	Ditto	May 1960 — April 1961	Ditto
3	Zar	Azerbaidzhan SSR, Kel'badzhar District	August–October 1960	Ditto
4	Pulkovo* /3/	Leningrad	April–November 1955, January–October 1956, February–July 1957 March–May 1958, September 1958— June 1959	GAO AN SSSR**
5	Anapa	Krasnodar Territory	August 1956 — July 1958	GAO AN SSSR**
6	Turchidag	Dagestan ASSR, Lakskii District	June–October 1957	GAO AN SSSR**
7	Mountain Station	Near Kislovodsk	December 1957 — October 1960, December 1960— September 1961, March—May 1962	GAO AN SSSR**
8	Susamyr	Kirgiz SSR	September 1958 — March 1959, May–June 1959, August–September 1959	GAO AN SSSR**
9	Chechekty	East Pamir, Badakhshan Mountain Observatory, Murgab District	November 1959 — October 1960	GAO AN SSSR**
10	Vikhli	Dagestan ASSR, Kulinskii District	November 1959— September 1960	GAO AN SSSR**
11	Chimgan	Uzbek SSR	July–October 1960	GAO AN SSSR**, TAO AN UzSSR***
12	Krasnye Gory	Krasnodar Territory, Otradnaya District	May–September 1961	GAO AN SSSR**
13	Chapal, Semirodniki	Karachaev–Cherkess Autonomous Region, Zelenchukskaya District	May 1961 — May 1962	GAO AN SSSR**
14	Volgograd	Volgograd	October 1955 — April 1956	Volgograd Planetarium
15	Suvorovskaya	Suvorovskaya, Essentuki District, Stavropol Territory	August–October 1956, February–April 1957	GAO AN SSSR**
16	Various places in Dagestan	Kumukh, Gunib, Kun-zakh, and Akhty Dis-tricts Dagestan ASSR	August–October 1958, July–September 1959	GAO AN SSSR**
17	Makhachkala	Makhachkala	July–August 1958	GAO AN SSSR**
18	Dzhissa, Marukha, Chinari, Pastukhova	Karachaev–Cherkess Autonomous Region, Zelenchukskaya District	May–September 1961	GAO AN SSSR**

* In /3/, no direct values are given for t_0'', which have been computed with the aid of Table 4 in that paper.
** [Glavnaya Astronomicheskaya Observatoriya — Main Astronomical Observatory of the USSR Academy of Sciences in Pulkovo.]
*** [Tashkentskaya Astronomicheskaya Observatoriya — Tashkent Astronomical Observatory of the Uzbek Academy of Sciences.]

72

of observations. The results of this averaging are plotted in Figure 4, where the dates are marked along the abscissa axis, and the ordinate gives the monthly averages of $\bar{t}_0''$ from all the observation points. The averaging was carried out for the observation points listed in Table 4. The dashed line in Figure 4 plots the month-by-month fluctuations of $\bar{t}_0''$, in seconds of arc, whereas the solid line traces the general trend.

FIGURE 3. Month-by-month variation of t_0'':
1) Suvorovskaya, 2) Anapa, 3) Turchidag, 4) Mountain Astronomical Station, 5) Chechekty, 6) Vikhli, 7) Pirkuli.

FIGURE 4.

The number of sources supplying observational data for each month is given in Table 5.
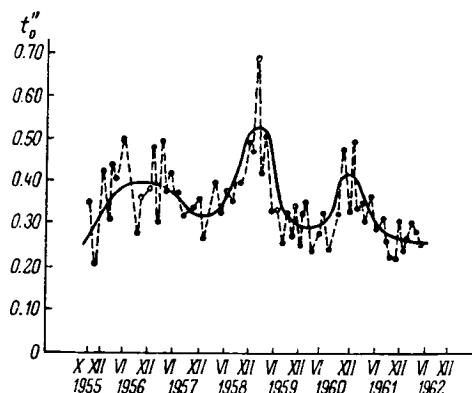
TABLE 5
Monthly numbers of observation points

years	I	II	III	IV	V	VI	VII	VIII	IX	X	XI	XII	total
Months													
1955										2	2	1	2
1956	2	2	2	2	1	1	2	3	3	3	1	1	4
1957	1	3	3	3	2	3	3	4	3	3	2	2	6
1958	3	3	3	3	4	3	3	4	5	5	4	4	7
1959	4	4	4	3	4	4	4	5	5	3	3	3	7
1960	3	3	3	3	4	4	5	6	6	5	1	2	6
1961	2	2	2	2	7	7	7	7	5	3	2	2	9
1962	2	3	4	5	4	2	7						5

73

Inspection of the curve in Figure 4 reveals a long-period fluctuation in t''_0, with a period of some two years. Winter is generally considered as a period of poorer astronomical seeing than summer. In reality, however, we see from the graph that poor-seeing winters may alternate with high-seeing winters. The astronomical seeing during the winter of 1957/58 was higher than during the winter of 1958/59, and the seeing during the winter of 1958/59 was much poorer than during the winter of 1959/60, etc.

To sum up, the following four periods T between successive maxima (or minima) of t''_0 on different time scales emerge from our data:

T_1 (hrs)			T_2 (days)			T_3 (months)			T_4 (years)		
min	max	av.	min	max	av.	min	max	av.	min	max	av.
4	34	14	2	17	4	2	8	4	—	—	2

The minimum T (in all three cases) is characteristic of the least stable seeing, and conversely the maximum T corresponds to high, stable seeing.

If larger series of observations were available, we could establish, first, the minimum and the maximum T for yearly variations of seeing and, second, the fluctuation period T on an even larger time scale; these long-range fluctuations are apparently due to solar activity, and in general they can be detected by careful inspection of curves like that in Figure 4.
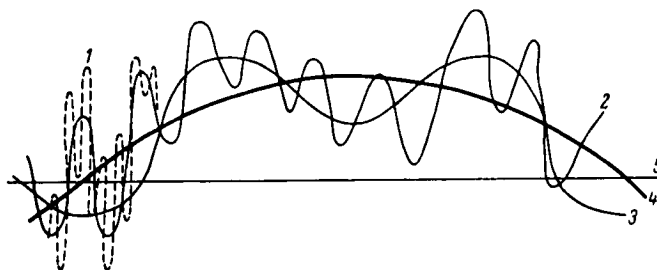
FIGURE 5. Fluctuations of shimmer angle with different periods between large (small) t''_0.
1) an average period of 14 hours, 2) 4 days, 3) 4 months, 4) 2 years, 5) mean level of t''_0.

The four classes of fluctuations are superimposed in Figure 5. Curve 1 is the short-period fluctuation T_1: we call it first-order fluctuation; curve 2 represents second-order fluctuations T_2, curve 3 third-order fluctuations T_3, and finally curve 4 plots fourth-order fluctuations with a period T_4. The straight line 5 indicates the mean value (the level) of the shimmer angle about which the long-period (biannual) fluctuations of t''_0 are described.

It follows from the preceding and from the curves in Figure 5 that even six to nine months of observation at a single point which give a consistently poor result cannot be regarded as proof of unfavorable astroclimatic conditions in the area: these six or nine months might coincide with the

downward trend of the biannual seeing curve. Conversely, high seeing persisting in some area for six or nine months is insufficient reason for expecting this situation to continue indefinitely. It is therefore obvious that two or three months of observations is far from being long enough to decide in favor, or otherwise, of any particular site.

3. WHAT CAUSES THE CHANGES IN SEEING ?

We did not try to establish the reasons for the existence of the four periods T_i ($i = 1, 2, 3, 4$) which govern the recurrence of $\bar{t}''_{0\,max}(\bar{t}''_{0\,min})$, since special meteorological investigations (in the ground layer, as well as at higher atltitudes) should be staged to this end. The underlying surface (soil cover, water bodies, ice, etc.) must not be ignored either, since heat transfer between surface formations and the ground air layer is of decisive significance in connection with atmospheric turbulence. Anyhow, all the processes which occur throughout the atmosphere, from the upmost reaches to the lowermost ground layers, are a consequence of Sun — Earth relationships.

This sketchy list of relevant factors is far from being complete, but here we shall consider only one of the probable candidates, namely the effect of synoptic fronts on astronomical seeing.* According to /4/,** synoptic fronts provide the main cause for deterioration of seeing.

The problem of the relation of atmospheric masses and fronts to astronomical seeing is of the greatest importance and, incidentally, it is not new. Back in 1950, Sokolova suggested /5/ that visual observations of stars at different azimuths provided an indication as to the intrusion of air masses. Regretfully, nobody in the USSR picked up this line of research, although at the end of her paper Sokolova had explicitly stated that it would be desirable to verify her conclusions, which had been based on scant data. This question is clearly of great significance not only for astronomers, but for other specialists as well. However, in our opinion, the conclusion that the passage of a synoptic front over the observation point lowers the astronomical seeing is unjustified. Synoptic fronts will of course affect the astronomical seeing, since they involve a substitution of air masses with new optical characteristics for the original air masses which may have had entirely different parameters. But it would be wrong to suggest that each and every front indiscriminately causes a deterioration in seeing. In some cases the atmospheric changes may improve the astronomical seeing, in other cases the seeing will remain unaffected. To settle the confusion, we turned to statistics.

We should first stress that of the four principal recurrence periods T, the first cannot be attributed to the influence of synoptic fronts, since in nature, at any given point, fronts cannot consistently succeed one another in periods of 14 hours on the average. Synoptic fronts apparently

---

* We analyzed only the ground-layer synoptic fronts, which pass very close to the surface.

** The effect of ground-layer synoptic fronts on astronomical seeing was first reported by N. I. Kucherov at the scientific meeting of the astrophysical departments of the Pulkovo Observatory in spring 1962.
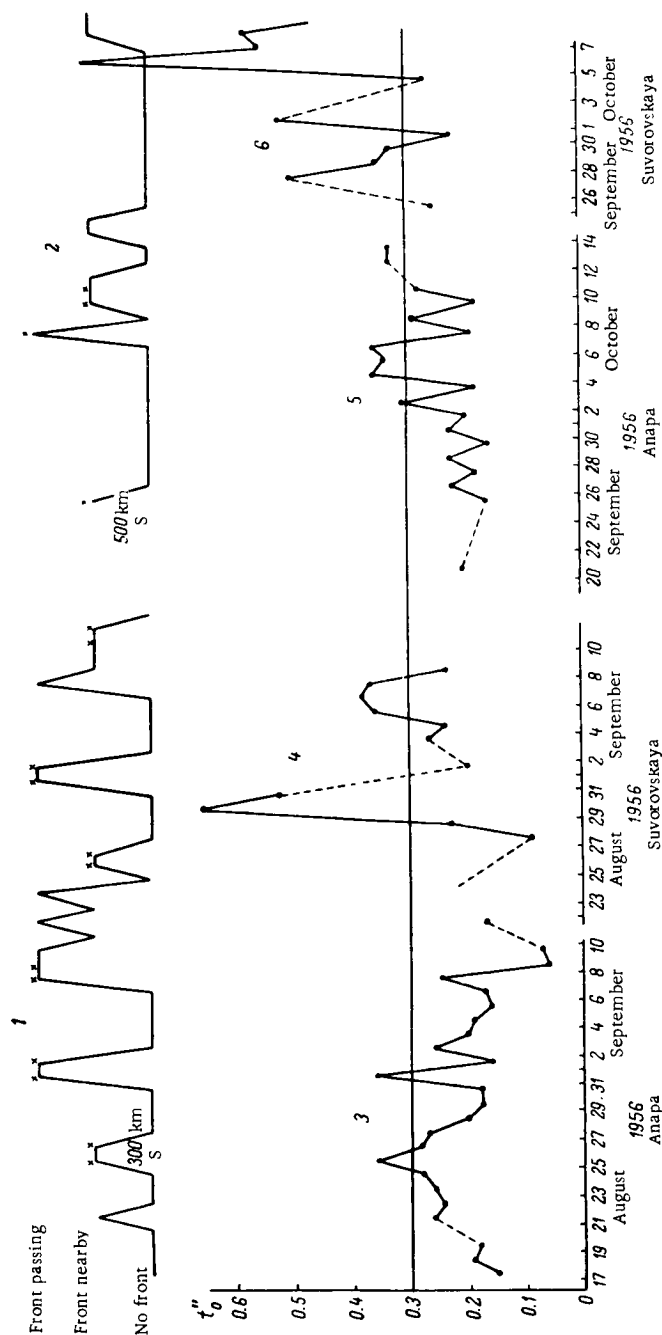
FIGURE 6. Synoptic fronts and seeing in 1956.
1, 2) position of fronts, 3) nighttime t''_0 measured in Anapa from 17 Aug. to 11 Sept., 4) Suvorovskaya, 24 Aug. to 10 Sept., 5) Anapa, 20 Sept. to 14 Oct., 6) Suvorovskaya, 25 Sept. to 9 Oct.

have direct bearing on second-order fluctuations in $\bar{t_0''}$, those with $T_2 \sim 4$ days, which is close to the recurrence time of weather fronts.

Having analyzed various synoptic charts /6/ and collated a great volume of observational data, we plotted the results in graphs (Figure 6). At this stage, (1) all observations were treated as equivalents, and (2) subjective bias was eliminated by considering the data for each and every night. The dates are marked along the abscissa axis, the ordinate gives the nightly average $\bar{t_0''}$. The ordinate is furthermore divided into three levels: the bottom level corresponds to the case when no fronts occur within a 100-km radius of the observation point; the second level corresponds to the case of a front passing within the 1000-km radius; the third level represents cases with the front passing directly over the observation point. The following hypotheses were adopted in the analysis of these graphs:

a) astronomical seeing deteriorates (i.e., $\bar{t_0''}$ is greater than 0".30, say) due to synoptic fronts;

b) seeing deteriorates gradually as the front advances, reaching a maximum when the front passes over the observation point; improvement is also gradual as the front moves on.

Graphs like those in Figure 6 were plotted for 1956 observational data (as described above). In 33 cases, seeing indeed deteriorated when synoptic fronts passed by, but in the remaining 34 cases seeing remained excellent despite the synoptic front, or else seeing deteriorated without any synoptic fronts in the area. Similar tests for other areas in 1957 — 1961 led to the conclusion that roughly in 50% of cases the passage or the approach of a synoptic front caused a deterioration in seeing, while in the other 50% of the cases this was not so. The same fifty-fifty ratio was recovered when deterioration in seeing to 0".40 (and not to 0".30 as in the previous tests) was adopted as a criterion for the influence of synoptic fronts.

The foregoing results are fully consistent with a further example: let us consider September 1960. Figure 7 gives two maps for 3 hours Moscow Time showing the observation points and the line of synoptic fronts (to
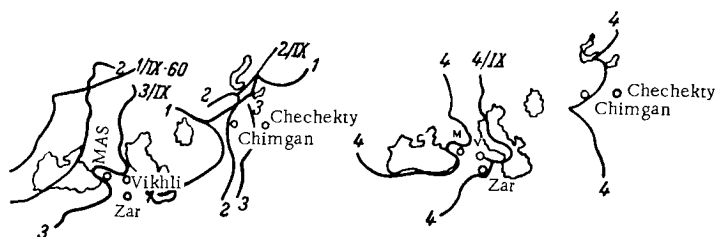

FIGURE 7. The position of synoptic fronts for 1 through 4 September 1960 at 3 hours Moscow Time.

avoid unnecessary details in the small drawings, the fronts are not identified as being cold, warm, etc.). The front numbers correspond to the dates in September, so front 1 is the front of 1 Sept., 2 the front of

2 Sept., etc. The following table lists the times of observation (Moscow Time) and the numerical value of the shimmer angle for each period.

	1 Sept.		2 Sept.		3 Sept.		4 Sept.	
	time	t_0''	time	t_0''	time	t_0''	time	t_0''
Mountain Astronomical Station	3	0.20	3	0.17	3	0.21	—	—
Vikhli	4	0.28	4	0.32	4	0.38	20	0.21
Zar.	3	0.14	5	0.60	1	0.22	1	0.75
Chimgan	0	0.36	—	—	1	0.24	2	0.30
Chechekty	2	0.09	2	0.13	—	—	2	0.24

An analysis of the chart in Figure 7 leads to the following conclusion. Let us first consider each point separately. At 3 hours on 1 Sept., when the front was more than 1000 km distant from the Mountain Astronomical Station, the zenith shimmer angle was $t_0'' = 0''.20$; on 2 Sept., when the front was close to the station, $t_0'' = 0''.17$, i.e., there was some improvement in seeing, and not deterioration, but on the whole the shimmer angle did not change significantly; on 3 Sept., with the front passing over the observation point, t_0'' was nearly the same ($0''.21$) as on 1 Sept., when the front had been more than a 1000 km away; unfortunately, no observations were made on 4 Sept. The data for the Mountain Astronomical Station thus show that t_0'' remained unaffected by the front.

Consider the observations in Vikhli (Dagestan). On 1 and 2 Sept., the shimmer angle was nearly constant, although on 2 Sept. the front was almost twice as close to Vikhli as on 1 Sept.; on 2 and 3 Sept., t_0'' also remained nearly constant, and yet on 3 Sept. the front passed very close to Vikhli; on 4 Sept., observations were only made at 20^h, but from the front configuration for 3 and 4 Sept., we see that by that time the front would have approached even closer to Vikhli (possibly passing over the observation point) than at 4 hours on 3 Sept., when $t_0'' = 0''.38$; and yet, the shimmer angle, instead of increasing, actually dropped to $0''.21$. Again, the advancing front instead of lowering the astronomical seeing, produced a certain improvement.

For Zar in Azerbaidzhan the seeing on 1 Sept. was excellent ($t_0'' = 0''.14$): the front located some $500 - 600$ km to the east moved away from the observation point at such an angle that only its flank was actually turned to Zar, so that it could not possibly affect the seeing, while the western front was too far from the observation point. Therefore the sudden deterioration in seeing (shimmer angle reaching $0''.60$) can hardly be attributed to the front approaching from the west, which at the relevant times was more than 1000 km away from the observation point. And yet, if we assume that the insignificant forward movement of the remote front did cause this change in seeing, we arrive at an obvious contradiction, when on 3 Sept. the front advances farther (to some 300 km from Zar) and the shimmer angle, instead of increasing further, drops to $t_0'' = 0''.22$. Only on 4 Sept., with the front actually passing over the observation point, did t_0'' rise to $0''.75$.

78

In Chimgan (Tashkent), no observations were made on 2 Sept. On 3 and 4 Sept., the shimmer angle remained nearly constant, although on 3 Sept. the front moved $300-400$ km to the east from Chimgan, while on 4 Sept. it actually passed over the observation point.

Finally, take Chechekty in East Pamir. On 1 and 2 Sept., the front remained at the same distance from Chechekty, and on 4 Sept., when the front advanced, t_0'' rose to $0''.24$. But we do not know what was the value of t_0'' on 3 Sept., when the front was even nearer than on 4 Sept., and the results are therefore inconclusive. In comparison with 2 Sept., however, the front was fairly near on 4 Sept.

Figure 7 and the corresponding tables therefore indicate that of the 12 values for t_0'' (the column under 1 Sept. is not included, since we have used it as reference), only two point to distinct deterioration in seeing with the approach of a synoptic front. If we take different observation points for one time, the conclusion is the same. We have so far discussed the data up to 4 Sept., but the situation does not change during the entire month of September.

If we assume that the variation in seeing is produced by synoptic fronts, the results of a statistical analysis for September 1960 are as shown in Table 6. Positive results in the table are those when t_0'' increased with the approach of a synoptic front. The data of Table 6 show that if we try to predict the variation of astronomical seeing on the basis of movement of synoptic fronts or to forecast the movement of synoptic fronts from measurements of t_0'', our forecasts will come true at most in 50% of the cases, which is obviously most unsatisfactory.

TABLE 6

Observation points	Total number of observations	Positive results, %	Negative results, %	Undecided, %
Mountain Astronomical Station	17	53	41	6
Vikhli	6	33	67	—
Zar.	14	28.5	50	21.5
Chimgan	23	52	30	18
Chechekty.	26	54	42	4
Total	86	47.5	42	10.5

To establish the true reasons for variation of seeing, the synoptic charts must be analyzed in much greater detail: the type of front (whether cold or warm, etc.) must be taken into consideration, as well as the inclination of the frontal plane and the azimuth of approach; we should also concentrate on other meteorological factors, both in the ground layer and in the upper atmosphere, which obtain before and after the passage of the front, taking account of topography and the composition of the underlying surface. In other words, we must consider the interaction of all the relevant factors. Some combinations of these factors may cause

a deterioration of seeing under frontal conditions, while other combinations will conversely produce a distinct improvement.

It is our opinion that ground-layer synoptic fronts are not the main factor responsible for variation of astronomical seeing.

CONCLUSIONS

1. There is a definite relationship between daytime and nighttime seeing: if nocturnal seeing is unstable, the instability persists during the day, while stable nocturnal seeing leads to stable daylight seeing. This conclusion is based on the results obtained at two observation points, high in the mountains of Pamir and Dagestan. The results should be verified for other areas with different topographic and climatic conditions (steppe and desert regions).

2. The recurrence of t_0'' with very long periods, which take a few months and even years, must be taken into consideration when examining the astroclimatic characteristics of an area. Systematic observations must be maintained for no less than two years to obtain a reliable estimate.

3. Statistical analysis of extensive experimental material, made in the first approximation, showed that synoptic fronts cause a deterioration in seeing, or alternatively, absence of synoptic fronts ensures high seeing approximately in 50% of the cases. In all other cases, a reverse phenomenon is observed. To obtain accurate results, the analysis must be repeated taking account of the inclination of the frontal plane, the type of the front, the direction of its motion, and many other detailed meteorological characteristics (in various atmospheric layers). In practice, the introduction of this multitude of different factors will complicate the problem of seeing forecasting beyond all hope, but they are clearly of considerable significance in theory.

The observations and the preliminary treatment of data were made with the participation of a large group of colleagues from the Main Astronomical Observatory and other organizations, as mentioned in /2, 7, 8/, to whom the author is deeply grateful.

Bibliography

1. Romanovskii, V. N. Primeneniya matematicheskoi statistiki v opytnom dele (Mathematical Statistics in Experiments). — Moskva-Leningrad, Gostekhizdat. 1947.

2. Akhundova, G. A. and Sh. P. Darchiya. —Izv. AN AzSSR, phys.-math. and engineering series, No. 1. 1961.

3. Demidova, A. N. and N. V. Bystrova. —Izv. GAO, No. 165. 1960.

4. Kucherov, N. I.—This volume, p. 50.

5. Sokolova, V. S. —Vestnik AN KazSSR, No. 1 (58). 1950.

6. Tsentral'nyi Institut Prognozov, Ezhednevnyi byulleten' pogody za 1954—1961 gg. (Central Forecasting Institute, Daily Weather Bulletin for the Period 1954—1961).

7. Darchiya, Sh.P. —Izv. GAO, No.169. 1961.

8. Bol'shakova, G.I. and Sh.P.Darchiya. —Izv. GAO, No.175:155. 1964.

Sh. P. Darchiya

SCINTILLATION OBSERVATIONS BY THE PULKOVO OBSERVATORY EXPEDITIONS IN THE YEARS 1956 — 1960

The paper presents some preliminary results of observations of the scintillation of stars carried out by various expeditions of the Pulkovo Observatory over a number of years. This is a descriptive work, and no attempt is made at theoretical generalizations. The results are nevertheless of considerable interest for the theoretician (the dependence of scintillation on the zenith distance z^0, the problem of monochromatic scintillation, etc.), since they represent a broad cross section of observation points at various elevations above sea level with diversified climatic and topographic conditions.

Scintillation of stars was observed through the AZT-7 telescope (objective aperture $D = 200$ mm), equipped with AFM-3 electrophotometer and N-10 oscillograph. The procedure of observation and treatment was described in detail in /1 — 3/, and we shall confine ourselves to the essentials.

The observations were made in the following places:

1. Village Suvorovskaya, Essentuki District, Stavropol Territory. Elevation $H \approx 300$ m above sea level (observation period August-October 1956 and February-April 1957). The stars were observed at various zenith distances and azimuths, at different times during the night. Observations were also made of the scintillation of a projector located to the east-southeast from Suvorovskaya, at a zenith distance of 88°.5. Distance between observation point and projector ~ 30 km, projector diameter 600 mm. The source of light was a 300 W filament bulb.

2. At the Mountain Astronomical Station (MAS) of the Main Astronomical Observatory ($H = 2100$ m) and in the Pamir mountains ($H = 3860$ m) scintillation was observed along the same lines as in Suvorovskaya. The observations at MAS were made from March to August 1958, and in Pamir during February and March 1960.

Stellar brightness fluctuations were recorded by moving the film in the oscillograph at a rate of 20 mm/sec, under constant gain conditions. Recordings of stars of first, second, and third magnitudes were selected, which ensured normal position of the extrema and of the mean level relative to zero.

Since various authors /1 — 4/ have established a proportionality between the mean square and the maximum amplitude of scintillation, with a coefficient of nearly 4.5, we shall only analyze the quantity

$$M = \frac{I_{max} - I_{min}}{I},$$

where M is the maximum scintillation amplitude in fractions of the mean recording level $\bar{I}$, I_{max} and I_{min} are the recording extrema (the maxima and the minima of the curve).

The scintillation frequency was determined by counting the intersection points of the scintillation recording with the mean level $\bar{I}$ in 5 seconds, and reducing the count N to 1 second. The results of the observations are presented in the following.

1. SCINTILLATION AS A FUNCTION OF OBJECTIVE DIAMETER

It is known that the scintillation amplitude increases for small objective apertures of telescopes. At Suvorovskaya observations which confirmed this fact were carried out with the projector. The projector is located almost at the horizon, so that high atmospheric layers (which are commonly held responsible for scintillation) are eliminated. The projector beam on its way to the telescope remained almost horizontal, traversing the ground air layer at a height of some $100-300$ m above the surface, but sometimes reaching a height of $700-800$ m (over surface depressions).
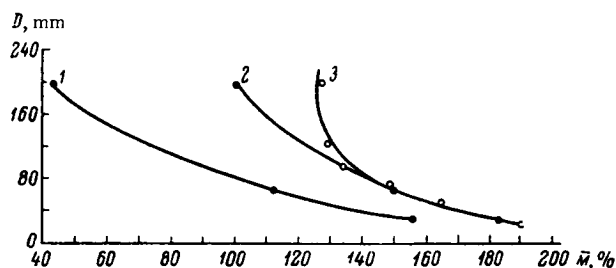

FIGURE 1. M vs. objective diameter.
1) Pulkovo, $z = 30°$, 2) Pulkovo, $z = 64°$ /5/, 3) Suvorovskaya, $z = 88°.5$. Observations in Pulkovo, February – March 1958.

The strong scintillation of the projector was due to the high turbulence in the ground layer, produced by heat transfer between soil and air.

Various maximum scintillation amplitudes were recorded by varying the objective aperture with a diaphragm. The results are in good agreement with the corresponding observations of other authors /1 –4/ for stars at different zenith distances. In particular, for comparison purposes Figure 1 gives not only Suvorovskaya (curve 3), but also Pulkovo (curves 1 and 2 /1/) observations. The abscissa marks the maximum amplitude M in percent, and the ordinate the objective diameter in millimeter.

We see from these curves that scintillation indeed diminishes as the objective aperture of the telescope is reduced, and also that the rate of change of M with D is higher at large zenith distances. Curve 2 (for $z = 64°$) is steeper than curve 1 (for $z = 30°$), and curve 3 (for $z = 88°.5$) is considerably steeper than both 1 and 2, particularly for $D > 80$ mm. For small objective apertures, curves 2 and 3, which represent observations at large zenith

distances, merge into one. Hence it follows that for large objectives the averaging out of scintillations is different at different zenith distances. For example, for $z = 30°$, on passing from $D = 200$ mm to $D = 65$ mm, M increases by a factor of 2.6 (from curve 1, $\frac{118}{43} = 2.6$), while for $z = 64°$, the same aperture reduction raises M by a factor of 1.5; for $z = 88°.5$ mere 10% increase is observed. The distortion of scintillation due to the averaging-out effect in large objectives is thus entirely different at different zenith distances, which is manifested in the peculiar shape of the M vs. z curves. Let us make use of the tabulated data from /5/.
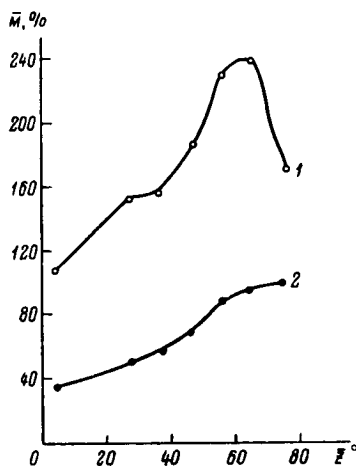
FIGURE 2. M vs. z.
1) $D = 30$ mm, 2) $D = 200$ mm.

Figure 2 plots M as a function of z. (The amplitudes M from /5/ were averaged over $z = 10°$ intervals.) The observations were made with AZT-7 telescope with various objective apertures. Curve 1 is for $D = 30$ mm, curve 2 for $D = 200$ mm. We see from Figure 2 that for small apertures (curve 1) "saturation" is reached near the horizon ("saturation" is a phenomenon when further increase in z beyond a certain limit does not intensify the scintillation, which sometimes even decreases), whereas for $D = 200$ mm, "saturation" is never reached. Anyhow, if there is "saturation" for large apertures, it is shifted to very high z and is not as distinct as for $D = 30$ mm. The causes of "saturation" are explained by monochromatic scintillation /6, 7/.

2. M VS. ZENITH DISTANCE AT VARIOUS OBSERVATION POINTS

Two very important considerations must always be borne in mind: first, it is impossible to make day-by-day observations under constant meteorological conditions (which may even change hour by hour during a

restless night), and second, the scintillation parameters are different for
-different objective diameters.

These two aspects are responsible for the variation of scintillation
amplitude with z. Let us consider this topic in some detail.

Scintillation (like the shimmer disk and image pulsation) is produced
by atmospheric inhomogeneities, which distort the plane wave front of
the light wave. On the other hand, the formation of the various atmospheric
inhomogeneities is governed by meteorological factors, such as air
temperature, pressure, wind speed and direction, air density, water
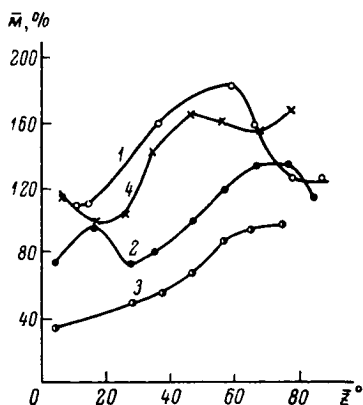vapor pressure, etc. Laikhtman /8/ has shown that a change in any of the
extrinsic factors (e.g., insolation,
turbulence, thermophysical parameters
of the soil, etc.) affects all the meteoro-
logical characteristics of the boundary
layer, at a height of some 2 km above
the surface. In our opinion, not only
the boundary layer is affected, but a
great part of the troposphere. These
changes will clearly alter the scintillation
amplitude and its distribution in z. Every
combination of intrinsic and extrinsic
meteorological factors therefore
corresponds to definite scintillation
parameters. Since the meteorological
characteristics change very rapidly,
the scintillation parameters, i.e.,
scintillation amplitude and the distribution
of M in z, will also fluctuate. Different
M vs. z curves can therefore be plotted
not only for each night, but even for each
hour, if the atmosphere is agitated. However, the meteorological
characteristics of the atmosphere at any observation point are more or
less stable on the average (constantly fluctuating about a mean level),
and so we come to the conclusion that the scintillation parameters will
fluctuate about some modal value. The modal value of the scintillation
parameters is therefore their mean value in a sufficiently large number
of observations. In comparing the data for different observation points,
we must take account of the distortion in the scintillation parameters due
to differences in objective diameters of the telescopes. The best course
in this case would be to make observations with identical instruments having
equal objective apertures, as was actually done in our observations.
Figure 3 plots the variation of M vs. z during the entire period of
observation at the following places: Suvorovskaya (curve 1), MAS (curve 2),
Pulkovo (curve 3) /5/, and Pamir (curve 4). The amplitudes M for these
four observation points were obtained using identical equipment with
200-mm objective aperture.

We see that the M vs. z curves for observation points which are close
to sea level and are located on flat ground are smooth, without any breaks
(with the exception of the inflexion at "saturation" point, as in curves 1
and 3). The corresponding curves for observation points at high altitudes
above sea level, in mountainous topography, show distinct breaks (curves 2

FIGURE 3. M vs. z at various observation points.
1) Suvorovskaya, 2) MAS, 3) Pulkovo, 4) Pamir.

and 4). Similar breaks near the zenith (Figure 4) are observed for curves which plot astronomical seeing (shimmer angle) vs. z for MAS /9/ and Pamir, whereas in Suvorovskaya no such phenomenon is observed. (The curves in Figure 4 are plotted for the same periods of observation as the scintillation curves.)

It therefore seems that seeing and scintillation near the zenith are both affected by the same factors; moreover, seeing and scintillation (and apparently image pulsation, too) are highly sensitive to the local topography: in flat areas, scintillation is observed in laminar atmosphere, where the layer thickness and the number of inhomogeneities increase smoothly, without any abrupt jumps, with increasing z. The curve $M=f(z)$ therefore shows no breaks, and it increases monotonically with increasing z (to "saturation" point). If the observation point is at great altitude above sea level, in a mountainous area, scintillation (as well as seeing) is determined by a highly distorted and turbulent layer: the light from stars at different z may be differently oriented relative to the scintillation-producing layer. Moreover, at some z, the light will intercept the crests of this layer, while at other zenith distances it will pass through the troughs, this creating differences in optical thickness. The combined influence of these factors is responsible for the break in the curves.

FIGURE 4. t_s vs. z at various observation points.
1) Suvorovskaya, 2) MAS, 3) Pamir.

Let us return to Figure 3 which shows that the "saturation" region is displaced in the direction of larger z for high elevations. In Suvorovskaya, for example, "saturation" is reached for $z = 55 - 60°$, scintillation subsequently decreasing; at MAS, the corresponding region is between 65 and 75°, while in Pamir no "saturation" is observed up to $z = 80°$: the scintillation amplitude M at $z = 77°$ is greater than for all other $z < 77°$. (The inflexion for $z = 45 - 70°$ is not a "saturation" region. It is apparently attributable to the same causes as the inflexion for $10 - 25°$, namely local topography.) The obscured horizon in Pamir unfortunately prevented scintillation observations at $z > 80°$.
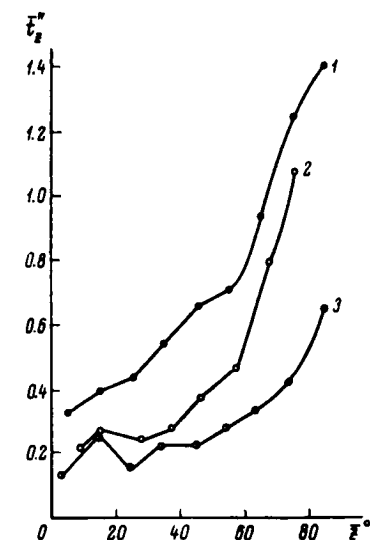
The effect of monochromatic scintillation explains the occasional absence of "saturation" and its displacement in the direction of higher z for high-altitude areas. Indeed, monochromatic scintillation distorts the shape of the curve $M=f(z)$ (inflexion appears) for $z = 55 - 60°$ and higher. To illustrate this point, Figure 5 shows a schematic section through four observation points A, B, C, D at different altitudes above sea level. We see from the diagram that the thickness of the dense ground layer, which is responsible for monochromatic scintillation, is different at the points A, B, C, and D. As the elevation increases, the thickness of this layer diminishes, and it may even vanish at particularly high altitudes (point D in our example). Let x in our scheme be the upper boundary of this layer.

86

Suppose that starting with z_1 (which corresponds to a layer thickness l_1) monochromatic layer is sufficient to produce "saturation". As the zenith distance increases further, the equivalent layer thickness rises to l_2, where a decrease in scintillation is observed. At the point A, "saturation" is thus reached for $z=z_1$; it persists up to $z=z_2$, and further increase in z produces a reduction in scintillation. At higher elevations (e.g., point B), "saturation" does not set in for $z=z_1$, since the atmospheric thickness is less than l_1 (which is necessary to produce "saturation"); the zenith distance z must additionally increase by an angle α if the dense atmospheric layer is to reach the required thickness l_1, i.e., at the point B "saturation" sets in for $z=z_1+\alpha=z_3$. The "saturation" region for B is thus displaced in the direction of higher z than for A (to simplify the drawing, we do not show the case when l_1 becomes equal to l_2 for points B, C, D). For point C, which is higher than point B, the "saturation" region (as we see from the drawing) is moved still farther from the zenith (i.e., closer to the horizon), so that $z_4 > z_3$, etc.; no "saturation" sets in at point D, since the dense layer producing this phenomenon is below the horizon and does not interfere with observations.
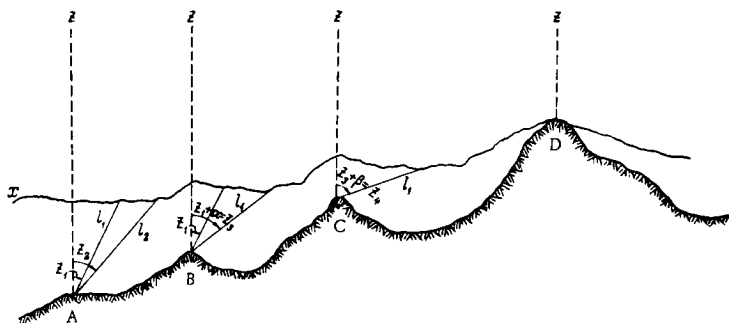
FIGURE 5.

The above scheme explains the relative shift in the "saturation" region for Suvorovskaya and MAS and its absence for Pamir. The departure from this general trend at Pulkovo, where "saturation" is indistinct and occurs for higher z than in Suvorovskaya, can be explained if we assume that the layer x during the observations in Pulkovo was much lower than in Suvorovskaya, which is quite probable.

3. SCINTILLATION FREQUENCY AS A FUNCTION OF OBJECTIVE DIAMETER

A projector was observed through a telescope with a variable objective diameter (the aperture was altered with the aid of diaphragms). A total of 32 observations were made. They were carried out during the first half of the night, under different meteorological conditions, so that the experimental points are widely spread in the corresponding graphs. If,

however, the observations are made under more or less similar meteoro-
logical conditions, limiting each session to no more than $1-1.5$ hours,
a distinct trend emerges (Figure 6): the number of intersection points
of the recording with the mean level, N, decreases as the objective diameter
increases. As we have previously remarked, the number of these inter-
section points is a measure of scintillation frequency. Various authors
point to a reduction in frequency with increasing diameter of the aperture.
Our results on the number of mean-level intersection points display the
same tendency.
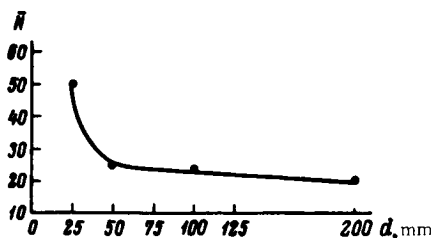
FIGURE 6.
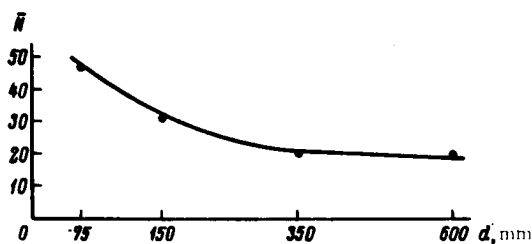
FIGURE 7.

Figure 7 also points to a reduction in the number of mean-level inter-
section points with increasing diameter of the projector. No diaphragms
were interposed in these measurements (i.e., the observations were made
with the full 200-mm aperture).

4. SCINTILLATION FREQUENCY AS A FUNCTION
OF ZENITH DISTANCE

The number of intersection points N was found to decrease with
increasing z. The $\bar{N}=\varphi(z)$ curves are of nearly identical shape (Figure 8,
solid lines). Breaks are again observed on the curves, particularly for
Pamir (Figure 8, dashed line); the breaks occur essentially for the same z

1822

88

as on $M = f(z)$ curves (Figure 3). It is noteworthy that no "saturation" is detected in these curves, and yet the breaks stand out distinctly. From the graphs $\bar{N} = \varphi(z)$ and $\bar{M} = f(z)$ it clearly follows that $\bar{M} = F(\bar{N})$, which is confirmed by the curve in Figure 9.
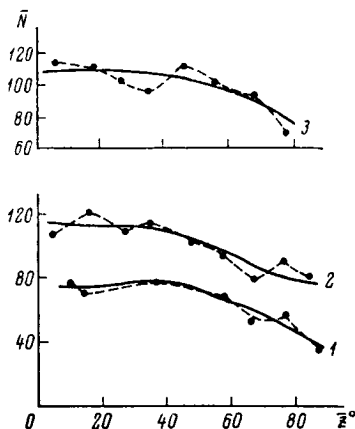
FIGURE 8. N vs. z for various observation points.
1) Suvorovskaya, 2) MAS, 3) Pamir.
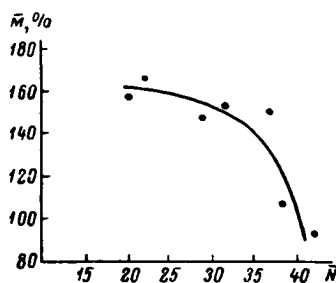
FIGURE 9.

The foregoing results bring out the large differences in the dependence of M on z for areas differing in elevation above sea level and in topographic and climatic conditions.

The author wishes to extend his thanks to G. I. Bol'shakova, A. Kh. Kurmaeva, and A. F. Sukhonos, who took part in the experimental work connected with scintillation recording.

Bibliography

1. Demidova, A. N. — Trudy soveshchaniya po issledovaniyu mertsaniya zvezd. Moskva — Leningrad. Izdatel'stvo AN SSSR. 1959.

2. Zhukova, L. N. — Trudy soveshchaniya po issledovaniyu mertsaniya zvezd. Moskva — Leningrad. Izdatel'stvo AN SSSR. 1959.

3. Zhukova, L. N. — Izv. GAO, No. 162. 1958.

4. Mel'nikov, O. A., I. G. Kolchinskii, and N. I. Kucherov. — Trudy soveshchaniya po issledovaniyu mertsaniya zvezd. Moskva — Leningrad. Izdatel'stvo AN SSSR. 1959.

5. Demidova, A. N. — Izv. GAO, No. 165. 1960.

6. Tatarskii, V. I. — Trudy soveshchaniya po issledovaniyu mertsaniya zvezd. Moskva — Leningrad. Izdatel'stvo AN SSSR. 1959.

7.   Tatarskii, V. I. and L. N. Zhukova. —DAN SSSR, **124**, No. 3. 1959.

8.   Laikhtman, D. L.   Fizika pogranichnogo sloya atmosfery (Physics of the Boundary Layer of the Atmosphere). —Leningrad, Gidrometeoizdat. 1961.

9.   Darchiya, A. Kh., L. F. Chmil', and Sh. P. Darchiya. —Izv. GAO, No. 165. 1960.

G. V. Akhundova

ASTROCLIMATIC CHARACTERISTICS OF
THE SHEMAKHA OBSERVATORY AREA

The aim of the astroclimatic research at the Shemakha Astrophysical Observatory was to establish the quantitative characteristics of the observatory site (Pirkuli) and to choose a location for the erection of the new 2-m telescope.

In Pirkuli, visual observations were started in May 1958, photographic observations of stellar trails in July 1960. The observations were made with AZT-7 telescope at the 10-m focus.

An expedition dispatched to the Mount Kartdag plateau worked on its program for eight months (from 15 January to 15 September 1961). This observation point is close to Pirkuli (7 km in a straight line), but the two places are located at different elevations (1450 m and 1975 m above sea level, respectively). The difference in elevation and some topographic features suggest that the two places may differ in astroclimatic conditions. The observations in Kartdag and in Pirkuli were made simultaneously, following an identical schedule with identical instruments.

The results for Pirkuli include zenith shimmer disk estimates for 396 nights and 243 photographic plates with 881 trails; for Kartdag, there are 73 zenith shimmer disk estimates and 127 plates with 465 trails.

The photographic trails were generally measured using the MIR-12 instrument. The standard technique /1/ by which the mean square deviation from the mean trail line is determined is highly tedious. We therefore measured the double amplitude of pulsation by training the cross hairs to successive crests and troughs in the trail. The measurements were limited to 25 amplitudes (50 points), and the time required for measurement and treatment was cut to 1/2 or even 1/3. We preferred the simplified technique because in a comparatively short time we had to measure and reduce a large volume of data (370 plates with 1500 trails) and to decide on a site for the erection of the large telescope.

Our procedure gave the mean amplitude of pulsation. By comparing our results with the semiautomatic measurements at Pulkovo, we established that our results were too high by $15-20\%$. This was so because we only measured those amplitudes which were distinguishable as distinct waves, i.e., amplitudes greater than $0''.20-0''.25$. In other words, our procedure gave the upper bound of image pulsations, but this is clearly much better for assessing the relative astroclimatic parameters of two places than the detailed picture. This point, however, must be borne in mind when our results are compared with the data from other areas.

The error in a single amplitude reading at a given zenith distance (A_z'') was estimated as $\pm 0''.05$ by several different techniques (a "standard" plate measured by all the observers, comparison of several zenith amplitudes A_0'' measured on one plate, etc.), which all gave consistent results. Since each plate carried on the average 5 trails, the error in A_0'' was $\pm 0''.03$ /1/. This accuracy is quite sufficient for our purposes.

All eight observers took active part in measurements in order to speed up the procedure. The results of different measurements should of course be reduced to a single system before they can actually be used. Elimination of the luminosity curve errors of individual observers improved the final outcome by as much as 14%.

Reduction to the zenith was made using a relation of the form $A_z = A_0 (\sec z)^a$ /2/. The index a was obtained by inspecting pairs of stars with different z. Exposure time of a single plate, $10-15$ min. During this period, the zenith pulsation amplitude A_0 is approximately constant, and for a pair of stars with different z we have $a = \frac{\Delta \lg A_z}{\Delta \lg \sec z}$. If 5 trails are photographed on one plate, they can be combined into 10 pairs. The index a obtained by this technique is a characteristic of the particular night of observation; it is, however, no more than a statistical datum for the area in general.

The least-square method, as applied by I. G. Kolchinskii, gives a result which is close to that obtained by the method of star pairs only if there are several observations during one night /3/. If one-time observations are used, the night-by-night spread of pulsation amplitudes (which, in general, is fairly substantial) will distort the results, so that almost anything can be obtained, including a decrease in amplitude from zenith to horizon.

Figure 1 plots the zenith pulsation amplitudes A_0'' and the zenith shimmer angles t_0'' for Pirkuli. The results for successive nights are joined with arrows. The direction of each arrow indicates a decrease or an increase in zenith pulsation and shimmer. If no observations are available for successive nights, the results are plotted as discrete points. It is remarkable that the zenith pulsation amplitude and the zenith shimmer angle are equal, although the scatter of amplitude points is greater. A_0'' displays a distinct seasonal variation (the seeing in Pirkuli is better in summer). The minimum values for both A_0'' and t_0'' are $0''.10-0''.20$.

Figure 2 plots the results for Kartdag. The zenith shimmer disk is somewhat smaller than in Pirkuli; this also applies to A_0. The two areas are therefore nearly equivalent astroclimatically.

Various authors tried to detect correlation between the image pulsation amplitude and the shimmer disk in zenith. The two phenomena are known to originate in atmospheric inhomogeneities of different size. If we accept that the inhomogeneities in the atmosphere are independent, i.e., there is absolutely no relation between their frequency and variation, the two phenomena may in fact be uncorrelated.

We now consider Figure 2. The pulsation amplitude and the shimmer disk in zenith generally display the same trend (both either increasing or decreasing). This is particularly evident when observations are available for several nights in succession. If the image pulsation amplitude in zenith increases, the zenith shimmer disk also grows (see the periods

FIGURE 1.

93
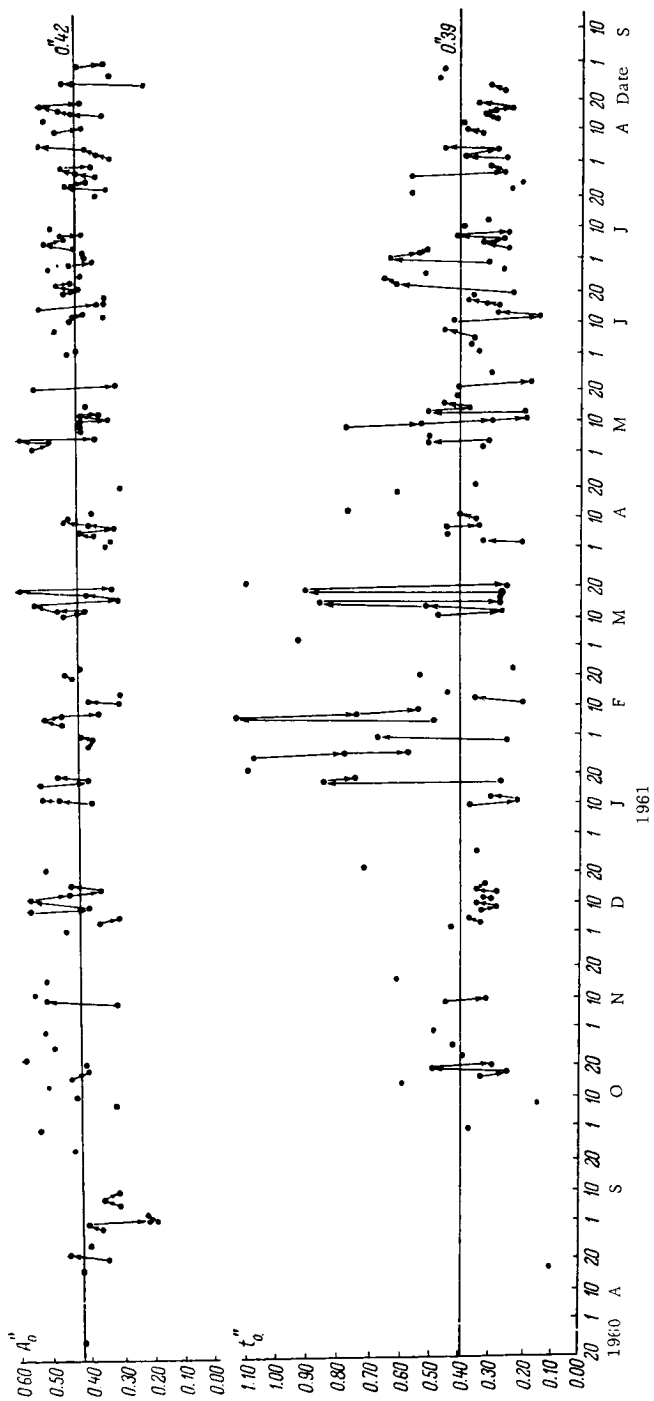
5 — 10 April, 1 — 4 June, 17 — 20 July, 22 — 27 July, 2 — 4 August). This may ·
imply that the two phenomena originate in the same air layer (for Kartdag).
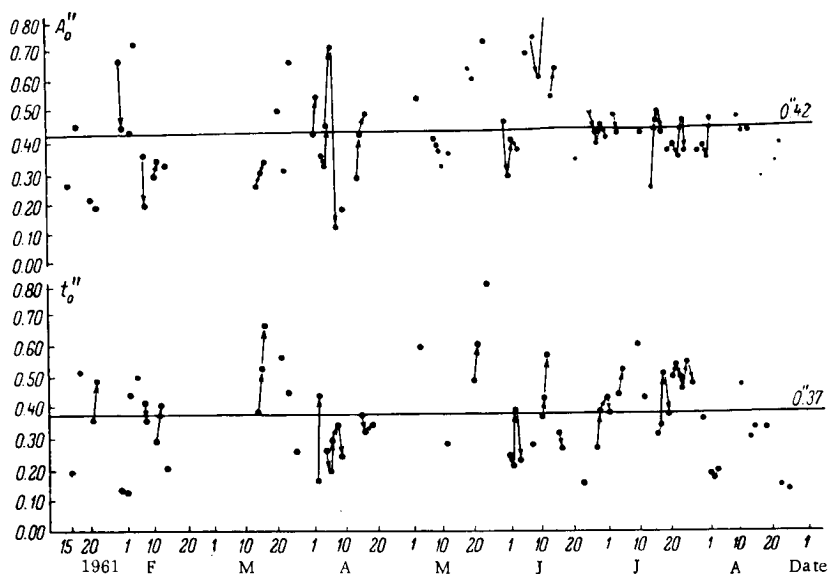
FIGURE 2.

If we now return to Figure 1, which plots the distribution of A_0 and t_0
in Pirkuli, we see that the parallel trend of the two quantities is not so
obvious. For 11 — 18 March, 5 — 9 April, and 4 — 8 July, the two parameters
vary in parallel. But sometimes (2 — 5 May, 8 — 15 May, 21 — 23 June,
26 — 29 July, etc.), the two follow different trends. If we moreover compare
simultaneous observations in Pirkuli and Kartdag, we find that during some
periods (e.g., the end of July) A_0 and t_0 vary in parallel in Kartdag and
follow different trends in Pirkuli. These effects can be explained if we
assume that the image quality is determined by inhomogeneities in a
comparatively thin ground layer, while image pulsation is also influenced
by higher inhomogeneities, i.e., pulsation-producing inhomogeneities are
dispersed in a much thicker air layer, possibly in the entire atmosphere.
This may be the reason for the contradictory results obtained for the
height of pulsation-producing layers.

TABLE 1

		Pirkuli			Kartdag	
	n	n, %	annual expected figure	n	n, %	annual expected figure
Number of clear nights	125	51.2	~185	113	55.1	~200
Among these { perfectly clear	66			42		
more than half-clear	29			41		
less than half-clear	30			30		
Number of overcast nights	119	48.8	~180	92	44.9	~165

It is interesting to compare the meteorological conditions of the two places. Table 1 lists some statistical data for clear and overcast nights in Pirkuli and Kartdag /4/.

We see that in Pirkuli some 180 clear nights can be expected during the year, while in Kartdag the figure is close to 200. However, if we turn to Table 2, which lists some statistical data on wind speeds V in m/sec, we conclude that in Kartdag in 30% of the cases the wind speed is over 5.0 m/sec. These windy nights are inadequate for astronomical observations. The meteorological conditions in Kartdag are therefore in no way superior to those in Pirkuli.

TABLE 2

Place	$V = 0$	$0 < V \leqslant 2.5$	$2.5 < V < 5.0$	$5.0 < V < 10.0$	$10.0 \leqslant V$	n
Pirkuli	64.9	24.5	5.3	5.3	—	208
Kartdag	28.9	15.1	15.1	29.4	11.5	218

The visual method of Danjon and Couder enables us to estimate the effect of atmospheric inhomogeneities which are smaller than the telescope aperture ($< 0.2^m$ for AZT-7). In measuring star trails, we take account of inhomogeneities which are manifested as waves in the photographic recording for the given rate of motion of the star across the plate. The high-frequency pulsation components, however, are neglected: they broaden the trail but produce no waviness. To find the integrated pulsation, which determines the size of the star image in the particular locality, we should allow for all the three factors jointly.

In V. A. Krat's opinion, these three components are independent to first approximation, and the total pulsation amplitude is the square root of their sum. The high-frequency component cannot be determined by direct methods, since the trail thickness is a function of two variables: the high-frequency pulsation and the stellar magnitude, and the contribution from the latter factor is very difficult to isolate. We therefore tried to estimate the size of stellar images for AZT-7 by the following technique.

During 6 nights, 26 plates were taken, each showing five stars near the zenith: α Boo (0^m24); α Oph (2^m13); α CBr (2^m31); β Her (2^m81); γ Her (3^m00). The profiles of the corresponding trails were then measured with the MF-2 microphotometer and the profile halfwidths were determined as distances between half-intensity points. The profile halfwidths $\bar{W}$ averaged over the 26 plates are listed in Table 3 (third column).

TABLE 3

Star	m	$\bar{W}$	$\sigma_{\bar{W}}$	σ_W	$\bar{d}''$	$\sigma_{\bar{d}''}$
α Boo	0.24	0.120	± 0.005	± 0.025	2.5	± 0.1
α Oph	2.13	0.087	0.0032	0.017	1.79	0.07
α CBr	2.31	0.076	0.0026	0.014	1.57	0.05
β Her	2.81	0.084	0.0029	0.015	1.73	0.06
γ Her	3.00	0.086	0.0035	0.017	1.81	0.07

The photographic density of the first star, α Boo, corresponds to the upper "shoulder" of the photographic characteristic, while the densities of the other stars lie along the straight section of the curve. The plates were calibrated with a tube photometer built in our observatory. The fourth column in Table 3 gives the errors in the mean profile values. From these figures we can calculate the standard error for one measured profile (by multiplying by the square root of the number of plates). The standard errors are listed in the fifth column of Table 3 (error in one halfwidth $\bar{W}$). The error in one halfwidth can also be determined by comparing several measurements of one trail. This gives ± 0.005 m ($\pm 0''.1$). The errors in the fifth column of Table 3 are of course higher, which indicates that the size of the image varies from plate to plate, but the variation is small enough to establish a certain mean image size for the 200-mm aperture in Pirkuli. We can therefore say that, within the experimental margin of error, the four stars have approximately the same size (sixth column in Table 3).

The mean size is $1''.72$, and this figure can be adopted as a characteristic image size of a 200-mm telescope for the mean conditions in Pirkuli. There are some indications that this result is close to the maximum, since photographic expansion of the image has inevitably affected our data.

As we have already remarked, this is the integrated effect of three components. We may thus conclude that the amplitude of the high-frequency pulsations is of the same magnitude as the other components (we take $1''.72 = A_{max}$ — the maximum total amplitude — so that the maximum values should be used for the other components also).

The minimum amplitudes of pulsation and shimmer in the zenith in Pirkuli are close to $0''.10$. The minimum image size that can be expected in Pirkuli is close to $0''.5$.

Bibliography

1. Akhundova, G.V. and A.A.Aliev. —Izv. AN AzSSR, phys.-math. and engineering series, No. 6. 1960.

2. Akhundova, G.V., A.A.Aliev, S.G.Zeinalov, and S.K.Kasumov. —Izv. AN AzSSR, phys.-math. and engineering series, No. 6. 1962.

3. Kolchinskii, I.G. —AZh, 34, No. 4. 1957.

4. Akhundova, G.V., A.A.Aliev, S.G.Zeinalov, and S.K.Kasumov. — Izv. AN AzSSR, phys.-math and engineering series, No. 1. 1963.

O. P. Vasil'yanovskaya

THE ASTROCLIMATE OF TADZHIKISTAN   N 67-15474

Investigations of the astroclimate of Tadzhikistan date back to the inauguration of the Dushanbe Observatory (now the Astrophysical Institute of the Tadzhik Academy of Sciences). The observations were carried out according to a conventional visual and instrumental program in the areas of Varzob, Anzob Pass, Ura-Tyube, and Iskander-Kul' Lake. The best results were obtained for the Iskander-Kul' area (the Iskander-Kul' meteorological station and Mount Isterek station), and the stability of the atmospheric transparency in the Iskander-Kul' station was specially commented upon /1/. The only deficiency of this area is the lack of roads for a distance of 8 km.

In 1959, the Astrophysical Institute of the Tadzhik Academy of Sciences appointed a committee to select a site for the Institute's new observatory. The Sanglok area was found to be the most suitable of the various alternatives inspected by the committee. Among the advantages of this site are the small amplitude of diurnal and annual temperature fluctuations, absence of high winds, rarity of sand storms (dust hardly ever reaches that high altitude), completely exposed skyline, and flat ground (without any deep ravines in the area).

In 1960, the Astrophysical Institute, in cooperation with the Pulkovo Observatory, dispatched an expedition to the Sanglok station, and another expedition was organized by the Pulkovo Observatory to the Iskander-Kul' station; a Pamir expedition had been launched by the Pulkovo Observatory in 1959 (Chechekty, Murgab area). The first two expeditions were headed by N. M. Bronnikov, and the third expedition was led by Sh. P. Darchiya. All the three expeditions continued with their work up to October 1960. The results on astronomical seeing collected by the Pulkovo Observatory expeditions were kindly placed at our disposal.

In December 1960, two independent expeditions were dispatched by our Institute to the Iskander-Kul' station and the Khodzha-Obi-Garm resort area. There is a large plateau near that resort, the skyline is fairly exposed, and the place in general is much closer to Dushanbe than the Sanglok station. No previous meteorological data were available for that area. The nearness of deep ravines is among the deficiencies of this place: on one side there is River Varzob (east, approximate depth 1 km), on the other side River Luchob (southwest, approximate depth 0.5 km). There is another ravine of some 0.3 km deep to the north-northeast, in the direction of the resort. Diametrically opposite to the last ravine, there is a fairly high mountain massif.

In October 1961, the Iskander-Kul' expedition was again transferred to Sanglok, since better results had been obtained in the latter area. The Khodzha-Obi-Garm expedition completed its work in May 1962.

The elevations of the relevant stations above sea level are listed below:

Iskander-Kul' . . . . 2260 m
Sanglok . . . . . 2237 "
Chechekty . . . . . 3850 "
Khodzha-Obi-Garm . . ~ 2000 "

The observations in all the expeditions of the Astrophysical Institute and those in Chechekty were made with AZT-7 menisc telescopes ($D = 200$ mm) with a 10-m focus. The observations and the treatment were carried out according to the procedures prescribed by the Pulkovo Main Astronomical Observatory.

I. Seeing was estimated visually according to the five-point Danjon—Couder scale. The observers could assess the blurring of the diffraction disk to within 0.25. In keeping with the Danjon—Couder theory, seeing was characterized by two quantities — the zenith shimmer angle t_0'' and the slope of the straight line plotting the shimmer angle t_z'' vs. the air mass $M(z)$. To permit comparison of different places, the seeing estimates were divided into four groups according to the values of t_0''.

0.00 – 0".20 – excellent seeing
0.21 – 0".30 – good seeing
0.31 – 0".50 – satisfactory seeing
> 0".50 – poor seeing

Statistical data on excellent, good, satisfactory, and poor seeing are listed in Table 1.

TABLE 1

Observation point	Total number of nights (100%)	Percentage of favorable nights	Percentage of nights with			
			excellent seeing	good seeing	satisfactory seeing	poor seeing
Iskander-Kul'	316	82	7	26	43	24
Sanglok	200	72	45	47	8	0
Chechekty	285	84	49	32	17	2
Khodzha-Obi-Garm . .	199	38	0	17	78	5

The dependence of seeing on zenith distance was estimated as follows. The observations in each area were divided into 4 zenith-distance intervals:

0 – 35° – I
36 – 55° – II
56 – 70° – III
71 – 90° – IV

The mean shimmer angle t_z'' was calculated for each group for the entire period of observation. Each mean value was referred to the midpoint of the corresponding interval. The last interval provided the only exception, and the corresponding mean zenith distance was actually calculated. The

. results are arranged in Table 2 and Figure 1. The zenith shimmer angle t_0'' and the slope k of the straight line

$$t_z'' = t_0'' + kM(z)$$

were determined graphically.

TABLE 2

Observation point	t_z''				t_0''	k
	I	II	III	IV		
Iskander-Kul'	0.44 ±0.04	0.52 ±0.04	0.70 ±0.05	1.00 ±0.06	0.43	0.21
Sanglok	0.27 2	0.30 1	0.37 2	0.62 2	0.25	0.11
Chechekty	0.20 2	0.31 2	0.56 3	0.99 10	0.19	0.29
Khodzha-Obi-Garm . .	0.40 1	0.55 1	0.78 2	1.07 3	0.42	0.27

Inspection of Figure 1 reveals that satisfactory seeing is on the average observed up to the following zenith distances:

41° — Iskander-Kul'
72° — Sanglok
62° — Chechekty
40° — Khodzha-Obi-Garm

Statistical calculations were made using individual estimates; these were reduced to the zenith according to the simple formula

$$t_0'' = \frac{t_z''}{M(z)}.$$

The statistical analysis had to provide answers to the following questions:
1) Is there azimuthal march of seeing in the four observation sites?
2) Is there any diurnal march?
3) What is the spread of the individual seeing estimates for each observation site?
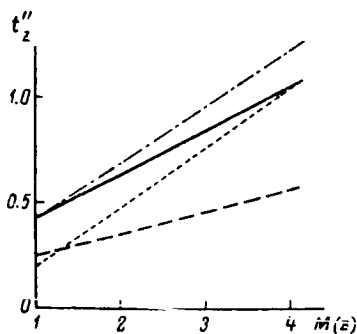

FIGURE 1. t vs. z.
Solid line — Iskander-Kul', dash–dotted line — Khodzha-Obi-Garm, dotted line — Sanglok, dashed line — Chechekty.
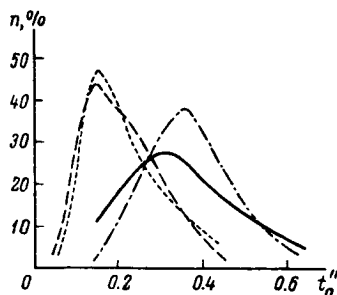
FIGURE 2. Percentage distribution of seeing.
Legend as in Figure 1.

The entire t_0'' range was divided into $0''.1$ intervals. The sum total of estimates in all the intervals was reckoned as 100%. The corresponding distribution graphs were plotted month by month, as well as integrated for the entire period of observation.

The azimuthal march was sought in graphs which gave the distribution of seeing in four azimuths: north, south, east, west. No distinct azimuthal march could be detected in any of the places. No diurnal variation of seeing was detected either. The only exception is the month of October 1960 in Chechekty, where seeing consistently deteriorated by dawn. In other areas, deterioration or improvement of seeing in one of the observation sessions was observed occasionally.

Before the mean zenith shimmer angle is adopted as a seeing characteristic of each area, the spread of individual estimates around the mean must be estimated. Table 3 and Figure 2 plot the percentage distribution of seeing for the entire period of observation, in the four relevant areas.

TABLE 3

Observation point	0.00–0.10	0.11–0.20	0.21–0.30	0.31–0.40	0.41–0.50	> 0.50	Total number of observations (100%)
Iskander-Kul'	0	11	24	26	16	23	18191
Sanglok	5	44	32	14	2	3	10848
Chechekty	4	47	24	17	6	2	8546
Khodzha-Obi-Garm .	0	3	22	38	24	13	9139

We see from the graph that Sanglok and Chechekty are by far superior to other sites. To sum up, the seeing in Sanglok is the best of the four areas under consideration. Chechekty is not far from Sanglok in this respect.

II. Image pulsation was observed by photographing star trails with the clock mechanism stopped. The trails were photographed on unsensitized Agfa Astro-Platten at the telescope focus. Instrumental vibrations, however, could not be avoided in these observations, and several precautions were undertaken in measurements and treatment: a) the photographs were taken with the clock mechanism stopped, b) the shutter had been opened some time before the star actually reached the plate field, c) the trails were photographed when the wind speeds did not exceed 5 m/sec, d) the trail edges were ignored.

The observations were made far from highways, so that no vibrations could conceivably be caused by road traffic in the area. The instrumental vibration was therefore reduced to an insignificant level.

The trails were photographed three times during the night. The photographed stars were all close to the meridian, at four different zenith distances. The trails were measured with the universal micrometric microscope UIM-21. In most cases, the trails could be measured over lengths of $25-30$ mm, which corresponded to $34-41^s$. The measurements were made at one millimeter intervals. If a substantial extremum occurred between the marked points, it was measured separately. The treatment

of each trail gave the maximum pulsation amplitude A_{max}, the mean pulsation amplitude $\bar{A}$, and the rms amplitude σ. The rms pulsation amplitude was adopted as the principal trail characteristic. The dependence between this parameter and the maximum pulsation amplitude was investigated for Iskander-Kul', Sanglok, and Khodzha-obi-garm. The results obtained for the different observation sites were found to be fairly close to one another, so that the entire volume of data could be analyzed statistically as one batch. A total of 2898 estimates were reduced.

A correlation coefficient of 0.89 with a standard deviation of 0.004 was obtained.

The mean amplitude $\bar{A}$ is related to the rms amplitude σ by the simple expression $\sigma = \sqrt{\dfrac{\pi}{2}} \, \bar{A}$. This relation was verified using the 434 trails from the Khodzha-Obi-Garm area.

The following dependence was assumed for the pulsation amplitude as a function of zenith distance:

$$\sigma_z = \sigma_0 + k \, \mathrm{tg} \, z,$$

where σ_z is the rms pulsation amplitude at the zenith distance z, σ_0 the rms pulsation amplitude in zenith. The parameters σ_0 and k were determined graphically for each session.

The accuracy of the measurements was estimated by M. Usmanova who used two plates of high quality. Each plate was measured 10 times over a few days' period. The mean square errors in a single determination of σ'', σ''_0, and k were found to be as follows:

$$\varepsilon_\sigma = \pm \, 0''.05,$$
$$\varepsilon_{\sigma_0} = \pm \, 0''.04,$$
$$\varepsilon_k = \pm \, 0''.02.$$

The mean square error in a single measurement of A_{max} grows with increasing maximum amplitude; the relative error is 17%. The reliability of different observers was evaluated by letting them measure identical trails on plates which differed in focusing precision and in image pulsation amplitude. The measurements were shown to be consistent for accurately focused plates. If the trail is slightly out of focus, there is a systematic divergence in the results of different observers. We generally tried to avoid these extrafocal trails.

As with shimmer disks, the image pulsation estimates were divided into groups according to the values of σ_0:

$$0.00 - 0''.20 - \text{excellent}$$
$$0.21 - 0''.30 - \text{good}$$
$$0.31 - 0''.50 - \text{satisfactory}$$
$$> 0''.50 - \text{poor}$$

The distribution of images in these pulsation groups is listed in Table 4. The dependence of the rms amplitude on tg z was obtained as follows.

The observations in each place were divided into four groups according to their zenith distances:

$$0 - 20° - \text{I}$$
$$21 - 40° - \text{II}$$
$$41 - 55° - \text{III}$$
$$56 - 70° - \text{IV}$$
$$71 - 90° - \text{V}$$

The values of σ_z and z in each group were averaged over the entire period of observation. The results are given in Table 5 and Figure 3.

TABLE 4

Observation point	Total number of observations (100%)	Percentage of observations with			
		excellent seeing	good seeing	satisfactory seeing	poor seeing
Iskander–Kul' . . .	174	4	19	64	13
Sanglok	92	81	17	2	0
Khodzha–Obi–Garm .	168	17	33	42	8

TABLE 5

Observation point	σ_z''				
	I	II	III	IV	V
Iskander–Kul' . . .	0.46 ± 0.01	0.52 ± 0.01	0.58 ± 0.02	0.75 ± 0.03	0.95 ± 0.05
Sanglok	0.17 ± 0.01	0.20 ± 0.01	0.24 ± 0.01	0.32 ± 0.02	0.37 ± 0.02
Khodzha–Obi–Garm .	0.45 ± 0.05	0.47 ± 0.04	0.56 ± 0.06	0.76 ± 0.08	0.99 ± 0.10

Satisfactory pulsation amplitudes on the whole were observed up to the following zenith distances:

$$28° - \text{Iskander–Kul'}$$
$$79° - \text{Sanglok}$$
$$35° - \text{Khodzha–Obi–Garm}$$

The σ_0'' and k calculated graphically from the data for the entire period of observation were as follows:

	σ_0''	k
Iskander–Kul'	0.42	0.15
Sanglok	0.16	0.07
Khodzha–Obi–Garm	0.38	0.18

As with shimmer disks, we plotted the distribution of the zenith rms pulsation amplitudes σ_0'' and the distribution of the angular coefficients k. The distribution was not affected by the time of observation.

The distribution of the rms pulsation amplitudes (in percent) for the entire period of observation is shown for the different places in Figure 4 (Table 6), and the distribution of the angular coefficient k is given in Figure 5 (Table 7).
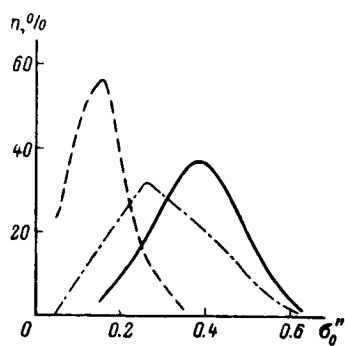
FIGURE 3. σ_z vs. tg z.
Legend as in Figure 1.
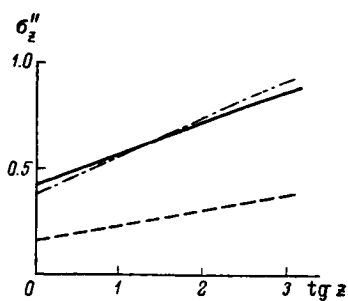
FIGURE 4. Percentage distribution of σ_0.
Legend as in Figure 1.
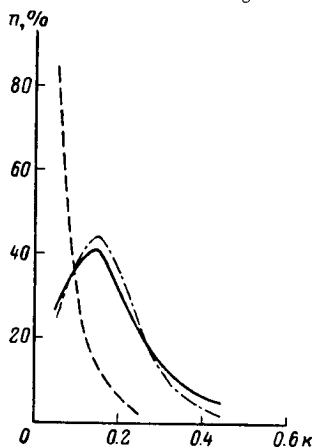
FIGURE 5. Percentage distribution of k.
Legend as in Figure 1.

TABLE 6

Observation point	0.00–0.10	0.11–0.20	0.21–0.30	0.31–0.40	0.41–0.50	>0.50	Total number of observations (100%)
Iskander-Kul'	0	4	17	36	32	11	307
Sanglok	24	57	17	2	0	0	103
Khodzha-Obi-Garm . .	1	16	32	24	18	9	173

TABLE 7

Observation point	0.00–0.10	0.11–0.20	0.21–0.30	0.31–0.40	0.41–0.50	>0.50	Total number of observations (100%)
Iskander-Kul'	26	41	21	6	5	1	307
Sanglok	85	13	2	0	0	0	99
Khodzha-Obi-Garm . .	25	44	21	6	2	2	171

103

It follows from the preceding that the stellar image pulsation in Sanglok
is substantially less than in the other two areas.

III. According to the Pulkovo Observatory requirements, scintillation
of stars should be observed visually. In our expeditions, however, visual
estimates of scintillation were more or less regularly recorded only in
Iskander-Kul', and there are consequently inadequate data for a comparative
evaluation of the different areas as regards scintillation. Scintillation was
therefore assessed by measuring trail beading /2/. Visual estimates of
scintillation from star trails were obtained by N. N. Suslova for all the
areas. A comparison of 100 scintillation estimates obtained in this way
with the visual estimates of scintillation in Iskander-Kul' gave satisfactory
agreement.

The scintillation of stars in Sanglok was less than in the other two areas.

IV. The atmospheric transparency was estimated by photographing
Polaris at the 10-cm focus of the AZT-7 telescope, at the center of the
plate. The photographs were taken simultaneously by two expeditions at
0100 hours Dushanbe standard time with a special 1×1 cm insert, so
that the photometric wedge standard appeared outside the normally exposed
area of the plate. Exposure time 10 sec. Unsensitized Agfa Astro-Platten
were used. On 1 Aug. 1961, Polaris was replaced with the star NPS 5
($m_{ph} = 6.^m46$), and exposure time was raised to 1 min. It was suggested
that the plates with the imprint of the standard wedge taken simultaneously
in two areas should be developed in the same developing bath. Unfortunately,
there were only few simultaneous pairs of plates, and the constancy of the
developing conditions was maintained by always using a fresh developer
from a batch prepared separately for each series of plates from the two
observation sites. The negatives were measured with the MF-2 micro-
photometer. The photometric wedge was calibrated in stellar magnitudes
using NPS stars, and the difference of the light attenuation factors could
thus be obtained directly in stellar magnitudes. The results indicate that
the higher atmospheric extinction in Khodzha-Obi-Garm than in Iskander-
Kul' produces an additional attenuation of 0.^{m}3 per unit air mass.
Comparing these results with observations of atmospheric transparency
published by various observers for Iskander-Kul' and Dushanbe, we reach
the conclusion that the atmospheric transparency in Khodzha-Obi-Garm
is approximately the same as in Dushanbe, i.e., the photographic extinction
factor is nearly 0.^{m}6. No analogous conclusions could be reached for the
Sanglok atmosphere, since no parallel observations were available.

The daytime atmospheric transparency can be quantitatively estimated
by examining the solar aureole and the blue of the sky. In our expeditions,
these quantities were estimated three times daily (9^h, 13^h, and 17^h Dushanbe
standard time) using Tikhov's scale. Sanglok and Khodzha-Obi-Garm
give very close results; the results for Iskander-Kul' are somewhat
superior. The winter months in Sanglok are an exception: the corresponding
parameters are distinctly superior to those for Khodzha-Obi-Garm and
Iskander-Kul'. In summer, the atmospheric transparency in Sanglok is
apparently close to that in Dushanbe, while in winter it is much higher.
We must stress that this estimate of atmospheric transparency is
insufficiently reliable.

V. When looking for observatory site, we must know the proportion
of favorable nights and days in each area. The nights and the days were

divided into four groups: clear — no cloudiness at any time; adequate — transient cloudiness not greater than 3; interrupted — only some of the nighttime observations were completed satisfactorily, inadequate — constant cloudiness greater than 3. The cloudiness was estimated according to a 10-point scale. The data on cloudiness are listed in Table 8 (nights) and Table 9 (days).

Examination of Tables 8 and 9 shows that the favorable nights are most numerous in Iskander-Kul', reaching a low for Khodzha-Obi-Garm. Clear days are much rarer than clear nights. Khodzha-Obi-Garm is again characterized by the fewest clear days of the three.

TABLE 8

Observation point	Total number of nights (100%)	Clear nights, %	Adequate nights, %	Interrupted nights, %	Inadequate nights, %
Iskander-Kul'	302	57	6	14	28
Sanglok	338	37	6	22	35
Khodzha-Obi-Garm . .	365	22	8	17	53

TABLE 9

Observation point	Total number of days (100%)	Clear days, %	Adequate days, %	Interrupted days, %	Inadequate days, %
Iskander-Kul'	301	20	2	47	31
Sanglok	327	20	2	36	42
Khodzha-Obi-Garm . .	365	10	5	43	42

Recordings of other meteorological data lead to the following conclusions.

(a) The winds are low at all the three observation sites, mostly not exceeding 4 m/sec. The highest proportion of completely calm nights is recorded for Iskander-Kul'.

(b) The amplitude of temperature fluctuations is the least in Sanglok, with a diurnal mean of 7°C, and the greatest at the Murgab meteorological station, with a mean of 17°C.

(c) The humidity in all the observation areas is small, mostly less than 50%.

Sanglok is thus the best of the considered sites in Tadzhikistan, and its advantages can be summarized as follows.

1) Seeing approximately as in Chechekty, but in Sanglok the reduction in seeing toward the horizon is much slower (Figure 1). Excellent and good zenith seeing $(t''_0 \leqslant 0''.30)$ is observed in the following proportion of the cases:

Iskander-Kul' . . . . . 33 %
Sanglok 92
Chechekty 81
Khodzha-Obi-Garm . . 17

105

2) Star image pulsation is the least in Sanglok (Figure 3, Table 5); the proportions of observations with excellent and good rms zenith pulsation amplitudes ($\sigma_0^* \leqslant 0''.30$) are the following:

Iskander-Kul' . . . . . 23 %
Sanglok 98
Khodzha-Obi-Garm . . 50

The pulsation amplitude in Sanglok increases very slowly toward the horizon, so that on the average, up to zenith distances of $z = 79°$, the rms pulsation amplitude does not exceed $0''.50$.

3) The least scintillation is recorded for Sanglok.

4) Small amplitude of temperature fluctuations.

5) Exposed hirozon.

6) Favorable topography.

As regards other characteristics — the proportion of favorable nights and days, winds, humidity — the areas considered are fairly close to one another. Khodzha-Obi-Garm is the only exception: here the number of favorable nights is much less than in other places. The atmospheric transparency in Sanglok has been studied inadequately, and no definite conclusions can be reached in this respect. However, even if the transparency is somewhat poorer than in Iskander-Kul' and in Chechekty, this cannot influence the main decision that Sanglok is obviously the most suitable site.

The observations were carried out with the participation of the following fellows of the Astrophysical Institute of the Tadzhik Academy of Sciences: A. Ya. Filin, K. A. Nikitin, A. P. Klyukina, Yu. I. Cherepanov, N. N. Suslova, V. Satyvaldiev, D. S. Yunusova. The bulk of trail measurements were made by N. I. Vorob'eva, L. A. Pakhomova, V. N. Trofimenko, and M. Usmanova. All the fellows of the Institute's Department of Variable Stars and Stellar Astronomy, and also some workers from other departments took part in calculations.

In conclusion it is my pleasant duty to extend sincere thanks to the Astroclimate Group of the Pulkovo Observatory who kindly placed at our disposal the data collected by their expeditions in Tadzhikistan and who took active interest in the discussion of our results.

Bibliography

1. Vasil'yanovskaya, O. P. —Byuleten' SAO, No. 22 — 23 : 65. 1957.

2. Bugoslavskaya, E. Ya. —Trudy soveshchaniya po mertsaniyu zvezd, p. 173. Moskva — Leningrad. Izdatel'stvo AN SSSR. 1959.

A. Kh. Kurmaeva and Sh. P. Darchiya

ASTROCLIMATIC CHARACTERISTICS OF THE CHECHEKTY SITE IN EASTERN PAMIR

N 67-15475

1. Pamir is the highest mountain area in the USSR. The mountains here run in latitudinal direction in a system of large parallel ranges, the eastern half of which, as if welded at an altitude of 4000 m by the floors of broad valleys and depressions, constitutes the Eastern Pamir /1/. Eastern Pamir is crossed by broad valleys with calm rivers tracing their course along the valley floor or with dry river channels extending in the depressions. The valleys occur at altitudes of 3700—4200 m, with rounded, gently sloping, snowless ranges, often crowned with cliffy crests, rising further to a height of 800—1000 m above the valley floor. Stone and sand flats, almost devoid of any vegetation, extend over tens of kilometers.

The climatic conditions in Eastern Pamir are very rigorous, atmospheric precipitation is negligible (60 mm annually), the landscape arid and desert-like. The alpine desert of Eastern Pamir is apparently the most arid territory in the Soviet Union. High elevation and low air temperature are responsible for the low moisture content of the air throughout the year.

A study of the astroclimatic characteristics of Eastern Pamir was first begun in November 1959 and continued for nearly a year (until 18 November 1960). The observations were carried out within the Chechekty natural boundary, at a height of 3860 m, near Murgab. The observation site was near the local biological station of the Tadzhik Academy of Sciences.

The Chechekty site is characterized by frequent winds, with speeds rising to 5—6 m/sec. The winds subside or cease altogehter by nighttime. The sand dust raised by the wind concentrates in the lowermost atmospheric layers, rapidly settling to the ground as soon as the winds stop. The high ranges surrounding the Chechekty natural area provide effective protection against the sand raised by dust storms in the Taklamakan desert. Table 1 lists some nighttime meteorological data for the Chechekty site.

TABLE 1

	Cloudiness 0–2	Cloudiness 8–10	$v \leqslant 1$ m/sec	B		Nocturnal variation $\Delta T \leqslant 5°$	Diurnal variation	
				$\beta \leqslant 6\%$	$\beta > 10\%$		$\Delta T \leqslant 5°$	$\Delta T > 15°$
Percentage of nights	67.2	7.4	46.2	79.8	1.6	16.0	4.5	39.6
Number of nights	223	223	235	180	180	322	265	265

We see that the nocturnal and the diurnal temperature variation is fairly large. This is attributed to the marked continental climate of Eastern Pamir.

It is remarkable that only one night (out of 62) in July and August 1960 was clouded and that during the entire stay in Chechekty (343 nights) observations were made during 292 nights, which constitutes 85% of the observation period. The scheduled number of observation sessions in Chechekty was 1029, and 742 observations were actually carried out (i.e., 72% of the scheduled total).

Eastern Pamir thus appears to be a fairly distinctive area in astro-climatic respect. Its characteristics should be determined and further compared with analogous data from other areas with radically different climatic and geographical conditions.

2. The observations at Chechekty were made with TM-140 telescopes (during three months), and then with AZT-7 telescopes, three times a night. Seeing was determined according to the Danjon-Couder scale at four azimuths and star trails were photographed to estimate image pulsation. It should be noted that the seeing in Chechekty, unlike that in other areas /2, 3/, is independent of the direction in which the observations are made; the yearly shimmer angle averaged over all the azimuths is $t_0 = 0''.24$ (Table 2). Seeing does not change much from month to month, and considerable deterioration is apparent only in November 1959 and February 1960 (Figure 1, Table 2), the shimmer angle rising to a high of $0''.38$ in November.

TABLE 2

Year, month	South	East	North	West	Monthly average t_0
1959 Nov.	0.37	0.34	0.35	0.36	0.36
Dec.	0.20	0.21	0.20	0.21	0.20
1960 Jan.	0.18	0.17	0.16	0.18	0.18
Feb.	0.29	0.30	0.29	0.30	0.30
March	0.23	0.23	0.24	0.23	0.23
Apr.	0.24	0.20	0.21	0.22	0.22
May	0.23	0.22	0.21	0.23	0.22
June	0.22	0.21	0.21	0.21	0.21
July	0.21	0.20	0.21	0.21	0.21
Aug.	0.20	0.25	0.21	0.19	0.21
Sept.	0.28	0.26	0.28	0.26	0.27
Oct.	0.26	0.27	0.28	0.27	0.27
Average .	0.24	0.24	0.24	0.24	0.25

In winter, seeing somewhat deteriorated over night (the average shimmer rising from $0''.21$ to $0''.26$ to $0''.28$; see Table 3). In summer (April—August), seeing hardly changed in nighttime ($0''.22$, $0''.20$, $0''.21$).

If the image quality is classified as excellent, good, and poor, the percentage distribution for Chechekty is as listed in Table 4. We see from the table that nearly half the estimates are under "excellent". There are virtually no "poor seeing" cases.
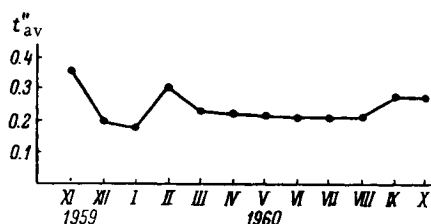

FIGURE 1. Annual variation of seeing in Chechekty.

As regards image pulsation σ'' (the rms trail deviation), measurements of 461 star trails show that near the zenith ($z = 0 - 20°$), $\sigma \leq 0''.20$ in 39% of the cases. We made use of σ'' measured directly for zenith stars: no attempts were made to derive zenith-reduced amplitudes σ_0'' with the aid of the $\sigma = f(\lg z)$ curve, since not all the cases follow the tangent curve and σ_0'' is not equal to the actually measured values. A correlation between seeing and pulsation amplitude has been established for Chechekty*.

TABLE 3

Year, month	Observation sessions			t_0'' mean
	1	2	3	
1959 Nov.	0.29	0.36	0.38	0.34
Dec.	0.16	0.18	0.25	0.20
1960 Jan.	0.15	0.19	0.17	0.17
Feb.	0.24	0.29	0.33	0.29
March	0.20	0.26	0.25	0.24
Apr.	0.22	0.22	0.21	0.22
May	0.24	0.23	0.20	0.22
June	0.22	0.20	0.22	0.21
July	0.21	0.20	0.21	0.20
Aug.	0.21	0.18	0.20	0.20
Sept.	0.22	0.27	0.30	0.26
Oct.	0.23	0.26	0.31	0.27
Average .	0.21	0.24	0.25	
Winter .	0.21	0.26	0.28	
Summer .	0.22	0.20	0.21	

* This problem is discussed in detail in Sh. P. Darchiya's paper in this volume.

The correlation coefficient of 0.69 corresponds to a significant correlation with a variance of $0''.06$ in t'' and $0''.03$ in σ''. The percentage of $\sigma \leq 0''.20$ recovered from the correlation relation is 35% for stars near the zenith, while actual measurements give 39%. We see that the correlation is fairly reliable.

TABLE 4

Number of observations	$t_0 \leq 0''.20$	$t_0 \leq 0''.30$	$0''.30 < t_0 \leq 0''.40$	$t_0 > 0''.40$
284 nights . . .	48.5	31.0	13.4	5.6
685 sessions . .	46.7	32.6	13.0	6.0

It follows from our analysis that in Chechekty at zenith distance of 45°, $\sigma_{45} \leq 0''.40$ in 88% of the cases. This is highly significant for planetary observations, since on account of the low geographic latitude of the site planets are frequently observed for fairly lengthy periods at $z \approx 45°$. Moreover, as in other mountain areas, the image quality is very good up to large zenith distances. In Chechekty, perfect images of the Moon, Jupiter, and Saturn are often obtained very close to the horizon (nearly at 70°). Various lunar features and the Cassini division in Saturn's rings appear very sharp and distinct under $\times 500$ magnification at the 10-m equivalent focus of the AZT-7 telescope ($D = 200$ mm). As many as seven zones could be often observed on Jupiter.

All the preceding points not only to a very calm atmosphere, but also to exceptional transparency of the air. Unfortunately, no special transparency determinations were made at Chechekty. The daytime transparency was estimated from the appearance of the solar aureole according to Tikhov's scale $(0-6)$. During the entire period of daytime observations (359 sessions), the Sun appeared without any aureole in 208 cases, i.e., 58%. An aureole ≤ 1 (the sky around the Sun was still blue) was observed in 294 cases (82%). These estimates indicate that the atmospheric transparency in Chechekty is indeed high.
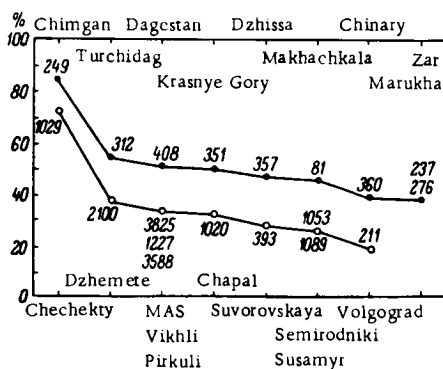

FIGURE 2. Distribution of clear observation sessions for various places.

3. As we have already mentioned, 85% of the 343 nights in Chechekty were favorable for observation. In terms of observation sessions (some times not all the three sessions could be completed during the night), the favorable percentage was 72% (742 out of 1029 sessions). This is an exceptionally high percentage, as we see from the curve of comparison w th other sites plotted in Figure 2. Two groups of observation points are given. In the first group (circles) we have those places where consecutive observations have been made for a long period, covering all the times of year (the only exceptions are Suvorovskaya — autumn and early spring, and Volgograd — autumn, winter, spring); the second group (dots) comprise short-period observations (mainly in the summer). The number of observation sessions in each area is marked along the curves. The ordinate gives the corresponding percentage of clear sessions.

The above percentage of excellent seeing cases was based on the number of nights or sessions favorable for astronomic observations, and not on the total number of nights spent in the area. This being so, the results of observations in different places may prove to lack a common denominator for comparison. Consider the following example. The observers stayed for 343 days in Chechekty; 292 nights were favorable for observation and 186 nights were classified under "excellent". The number of "excellent
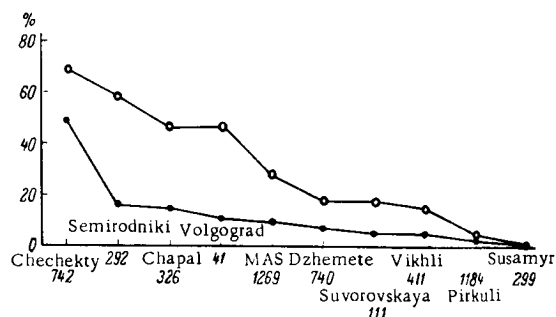

FIGURE 3. Distribution of excellent seeing sessions for various places.

seeing" nights is thus 54% of the total period spent in Chechekty (343 nights) and 64% of the number of favorable nights (292). The former figure (54%) implies that 54 excellent seeing nights can be expected for each 100 nights spent in Chechekty. The latter figure (64%) indicates that 64 out of every 100 clear nights in Chechekty are characterized by excellent seeing, but it is not certain how long one should remain in Chechekty to achieve this result. Furthermore, the former percentage of excellent seeing nights is 10% less than the latter percentage. If this difference were constant for all observation points, we could proceed with a more or less reliable comparison on the basis of the number of favorable nights (sessions). But this is not so. The curves in Figure 3 plot the percentage of excellent seeing nights in relation to the number of favorable sessions (top curve) and in relation to the total number of sessions (bottom curve). We see that the difference is not constant. Chechekty and Semirodniki are close to each other (69 and 59%) on the upper curve, while on the lower curve the

readings for these two observation sites are markedly different (50 and 16%). Simple calculation shows that to reach, say, 50 excellent seeing nights, one should spend 100 nights in Chechekty and 312 nights in Semirodniki. *

The comparison of Chechekty with other places is therefore based on the total number of days (sessions) spent in the area, and not on the number of favorable sessions.

The bottom curve in Figure 3 shows that Chechekty is distinctly superior to all other observation sites in this respect. Figure 4 plots similar graphs for the second group of observation points. The upper curve is based on the number of favorable nights. In Figure 4, as well as in Figure 3, the corresponding number of favorable sessions is marked for each locality.

4. All the foregoing applies to excellent seeing ($t_0 \leq 0''.20$, $\sigma \leq 0''.20$). It is, however, no less interesting to establish the percentage of good and satisfactory seeing. In this case, by applying the method of Boyer /4/, we shall be able to compare our data with the results for some observation points in France, in particular for Pic du Midi. Boyer plotted curves of the shimmer angle vs. the number of observations reduced to 1000 (Figure 5).
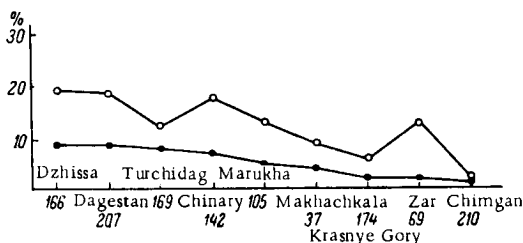
FIGURE 4. Distribution of excellent seeing sessions for various places.
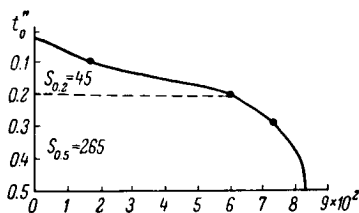
FIGURE 5. Boyer's curve for Pic du Midi.

Shimmer angles $t_0 > 0''.5$ were classified as "unacceptable", and the 0.5 ordinate was therefore regarded as the null point. The calculations, on the other hand, were based on the entire number of observations (including those with $t_0 > 0''.5$). The evaluation criterion for good seeing is provided by the sum

$$S_{0.5} = \int_0^{0.5} \varphi(t)\, dt,$$

which is in fact the area under the t_0 distribution curve. A partial sum

$$S_{0.2} = \int_0^{0.2} \varphi(t)\, dt,$$

can be adopted as a characteristic of excellent seeing. In Boyer's graph, $S_{0.5} = 500$ is the maximum figure characteristic of an ideal shimmer-free site. Of the six observatories examined by Boyer, Pic du Midi was found

---

* Similar calculations were carried out by Sh. P. Darchiya for a greater volume of observational material (AZh, 41(1):147–155. 1964).

FIGURE 6. Distribution of the "good seeing" criterion of $S_{0.5}$ for various places.

FIGURE 7. Distribution of the "good seeing" criterion of $S_{0.5}$ for various places.

113

FIGURE 8. Distribution of the "excellent seeing" criterion $S_{0.2}$
for various places.

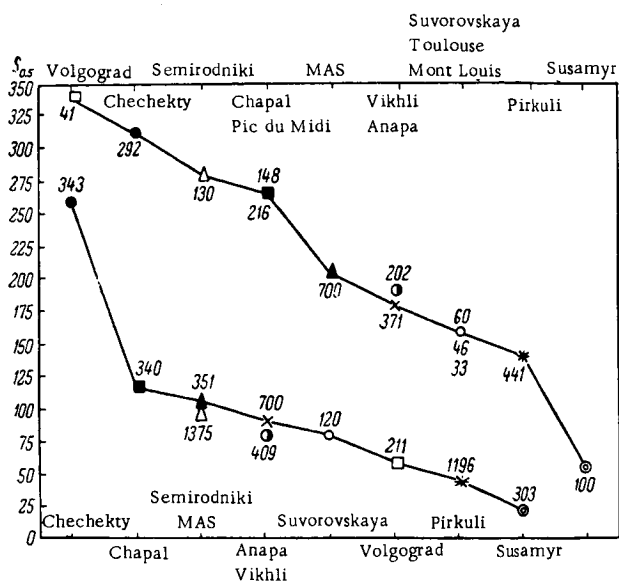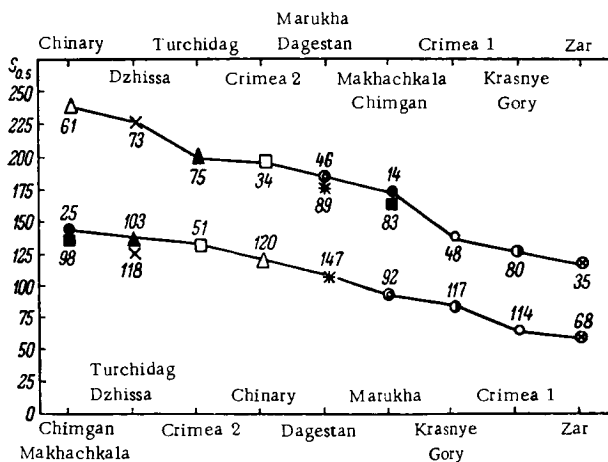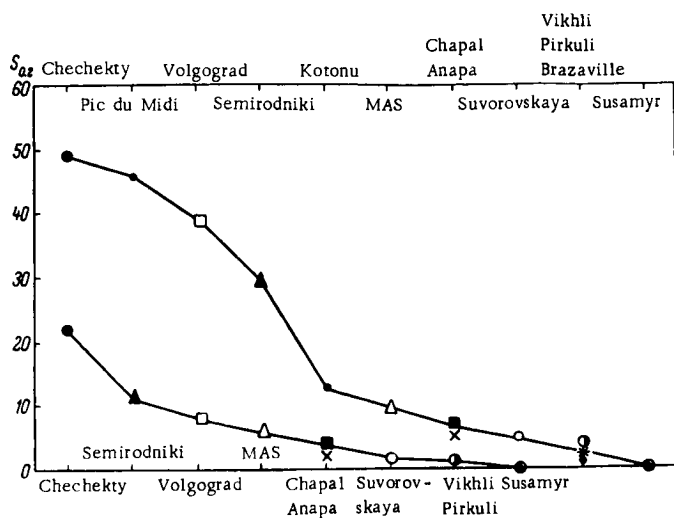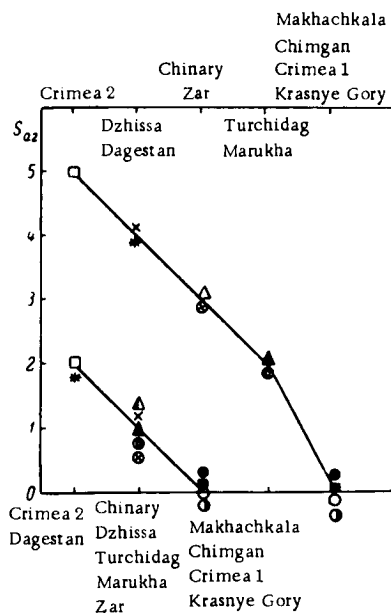FIGURE 9. Distribution of the "excellent
seeing" criterion $S_{0.2}$ for various places.

.to have the highest $S_{0.2}$, as well as $S_{0.5}$. We carried out similar calculations for Chechekty and other places. Figure 6 plots the distribution of $S_{0.5}$ for various sites: the upper graph is based on the number of favorable nights, and the lower on the total number of nights spent in the area. The numbers attached to each point represent, respectively, the number of observations and the number of nights spent in the area. We see from the graphs that the $S_{0.5}$ for Chechekty (particularly on the bottom curve) is higher than for other sites. The $S_{0.5}$ of Chapal is equal to that of Pic du Midi. The $S_{0.5}$ of Semirodniki is somewhat higher than that of Pic du Midi. According to the lower curve (which is the more reliable in our opinion), the $S_{0.5}$ for Semirodniki, Chapal, and the Mountain Astronomical Station are of the same order (on the upper graph, however, the results for MAS are much poorer). In Figure 7, analogous graphs are plotted for the second group of observation sites.

If the discussion is confined to excellent seeing (i.e., $S_{0.2}$, and not $S_{0.5}$ — the "good seeing" criterion), Chechekty again gives the best results (Figure 8). Pic du Midi is second in the order of favorable nights. If, however, we consider the curve of total time spent in the area, Chechekty is seen to be much superior to other places as regards $S_{0.2}$. For Pic du Midi the corresponding data unfortunately are not available. Figure 9 plots the distribution of $S_{0.2}$ for the second group of observation points.

It follows from the preceding that Chechekty has obvious advantages in comparison to other places as regards image quality and image pulsation. (The observations available for different sites were treated and reduced according to a single procedure.)

TABLE 5

Observation point	Total number of observations	$v_0 \leq 1$ m/sec	$B \leq 60\%$	$B > 80\%$
Chechekty	706	41	79	1.6
MAS	624	50	8	43
Semirodniki	1056	30	32	35
Chapal	1053	60	26	42

In conclusion we give Table 5 which lists some nighttime meteorological data for the four best observation sites. We see that the parameters for Chechekty are again the best.

The Chechekty site in Eastern Pamir is thus highly favorable for various astronomical observations.

Bibliography

1. Veremeichikova, E.I. —Geofizicheskii Byulleten', No.11. 1962.

2. Darchiya, A.Kh. and Sh.P.Darchiya. —Trudy soveshchaniya po issledovaniyu mertsaniya zvezd. Moskva—Leningrad, Izdatel'stvo AN SSSR. 1959.

3. Darchiya, A.Kh, L.F.Chmil', and Sh.P.Darchiya. —Izv. GAO, No.165. 1960.

4. Boyer, Ch. —L'Astronomie, Sept. issue, p.379.1958.

N. M. Bronnikova

OBSERVATION OF IMAGE PULSATION IN THE
SANGLOK AREA (TADZHIKISTAN) IN SUMMER 1960

Sanglok, an area to the south of the Tadzhik capital Dushanbe, is one of the sites included in the 1960 astroclimatic research program of the USSR Academy of Sciences' Main Astronomical Observatory (Pulkovo). Astro-climatic observations were carried out in the area between the months of July and October 1960.

Star trails were photographed for various zenith distances at the 10-m focus of the AZT-7 telescope, with its driving mechanism stopped. Thirty-one negatives with 157 star trails were taken during the entire observation period. Seeing (image quality) was estimated according to the Danjon-Couder scale in parallel with the photographic observations. The work was carried out with the participation of O. P. Vasil'yanovskaya, A. Ya. Filin, and K. A. Nikitin from the Astrophysical Institute of the Tadzhik Academy of Sciences. Star trails were measured at Pulkovo with the semiautomatic device developed by O. B. Vasil'ev and V. S. Sumin.

TABLE 1

Measurements of σ_0'', K, t_0''

Date	Session	σ_0''	K	t_0''	Date	Session	σ_0''	K	t_0''
			July				August		
22/23	morning	0".09	0.030	0".29	18/19	evening	(0".04)	(0.030)	0".22
26/27	night	0.26	0.004	0.28		morning	(0.10)	(0.012)	0.25
	morning	0.09	0.022	0.26	19/20	evening	(0.20)	0.003	0.22
27/28	morning	0.07	0.024	0.27		morning	0.09	0.012	0.22
28/29	morning	0.10	0.026	0.18	20/21	evening	0.20	0.010	0.25
29/30	night	0.04	0.022	0.25		night	0.14	0.014	0.28
					21/22	night	0.08	0.008	0.21
		August				morning	0.05	0.010	0.24
					22/23	morning	0.10	0.010	0.35
1/2	morning	(0.12)	(0.016)	0.22	24/25	night	(0.07)	(0.024)	0.28
2/3	morning	0.09	0.020	0.20		morning	(0.04)	(0.055)	0.35
3/4	evening	0.13	0.015	0.21	25/26	evening	0.07	0.010	0.26
	morning	(0.18)	(0.022)	0.24		morning	0.16	0.012	0.22
4/5	night	0.13	0.009	0.18	26/27	evening	0.13	0.006	0.22
	morning	0.17	0.001	0.25		night	(0.06)	0.020	0.26
15/16	night	(0.05)	(0.022)	0.22	31/1	evening	0.20	0.006	0.19
17/18	evening	(0.09)	(0.022)	0.24		morning	0.27	0.008	0.18
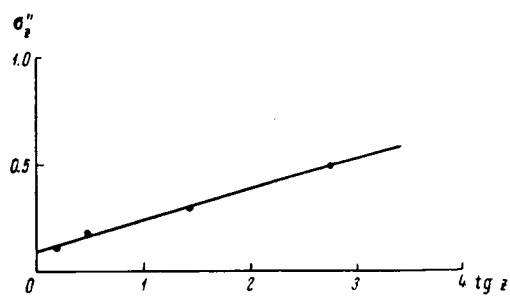
FIGURE 1. σ_z distribution of the first kind.

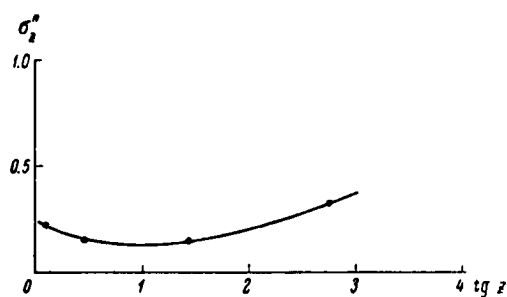FIGURE 2. σ_z distribution of the second kind.
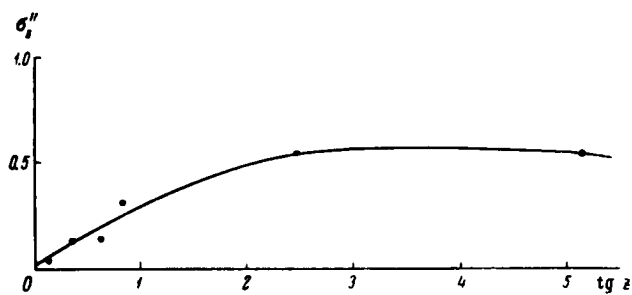

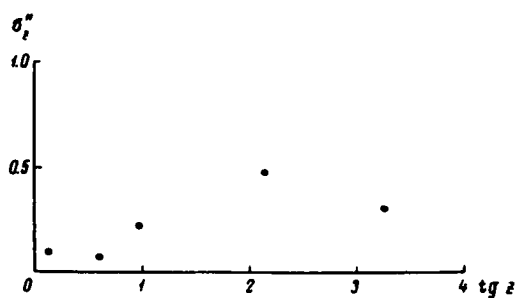FIGURE 3. σ_z distribution of the third kind.

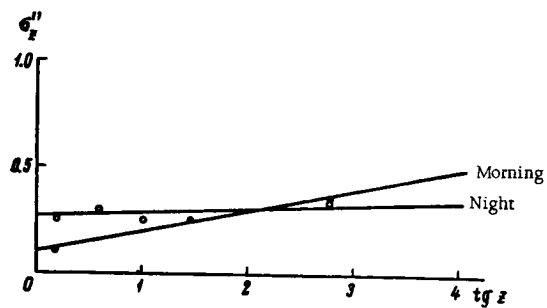FIGURE 4. σ_z distribution of the fourth kind.

118

FIGURE 5. σ_z distribution for different observation sessions (26/27 July).
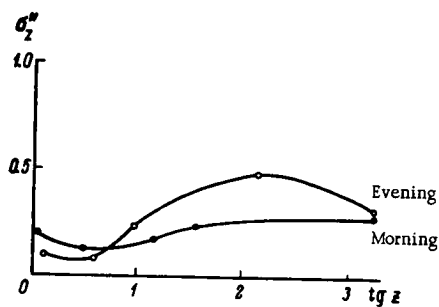

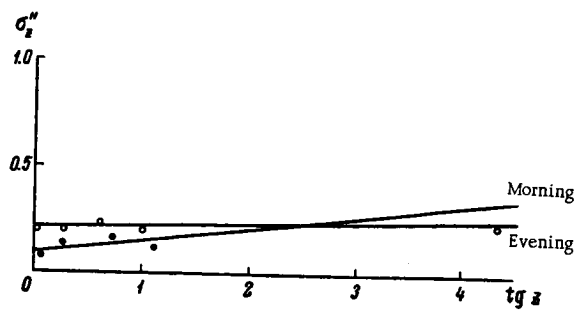FIGURE 6. σ_z distribution for different sessions (18/19 Aug.).

FIGURE 7. σ_z distribution for different sessions (19/20 Aug.).

Trail measurements give the rms pulsation amplitude γ''_z for each trail. Assuming a tangent-law distribution of σ''_z in zenith distance $(\sigma''_z = \sigma''_0 + K \operatorname{tg} z)$, we plotted σ''_z as a function of tg z. σ''_0 — the rms pulsation amplitude reduced to the zenith — was read off these graphs; the slope K of the lines was also measured (Table 1).

By comparing $\sigma''_z = \sigma''_0 + K \operatorname{tg} z$ lines for all the negatives, we have established that σ''_z is not always a linear function of tg z, or in other words σ''_z depends on the state of the atmosphere. Perturbing layers with different characteristics may occur at different zenith distances, and these layers distort the regular distribution of σ''_z.

All the curves can be divided into four groups.

(1) Direct proportionality. The points closely fit a straight line (Figure 1).

(2) The points fit a straight line from large z to z ~ 45°; as z decreases further, the curve displays an upward trend, i.e., σ''_z increases toward the zenith (Figure 2).

(3) σ''_z remains nearly constant from the horizon to z ~ 50 — 55°, dropping steeply at smaller zenith distances, i.e., σ''_z decreases rapidly toward the zenith (Figure 3).

(4) The dependence is very complex — probably a superposition of the three curves above (Figure 4).

Of the total of 31 curves, 15 were of the first kind, 7 of the second kind, 6 of the third kind, and 3 of the fourth kind.

During some of the nights, two observation sessions were held. Figures 5 — 7 plot the distribution of σ''_z for three nights (18/19 Aug., 19/20 Aug., and 26/27 July) showing each of the two sessions separately. The curves for different sessions in one night are nearly identical. This implies that the particular σ''_z distribution is by no means random.

In analyzing these curves we noticed a certain systematic variation of slope from evening to morning, and also a regular variation in σ''_0. σ''_0 decreases toward the morning, while K increases. In the morning, the rate of change of σ''_z at high zenith distances is faster, i.e., the difference between zenith and horizon pulsation amplitudes in the morning is considerably greater than that difference in the evening. Table 2 lists σ''_0 and K and the probable errors for different observation sessions, as calculated from the entire volume of observations. The errors represent the deviation of the individual readings from the arithmetic average.

Unlike σ''_0 and K, σ''_{01} and K_1 were calculated ignoring those dates when the zenith-distance variation of amplitude was not linear and σ''_0 and K could not be found with complete certainty (the values in parentheses in Table 1).

TABLE 2

Distribution of σ''_0 and K for different sessions

	Evening	Night	Morning
σ''_0	0″.13 ± 0″.02	0″.12 ± 0″.02	0″.11 ± 0″.01
σ''_{01}	0″.15 ± 0″.01	0″.13 ± 0″.02	0″.12 ± 0″.01
K	0.013 ± 0.002	0.015 ± 0.002	0.019 ± 0.002
K_1	0.009 ± 0.001	0.011 ± 0.002	0.016 ± 0.002
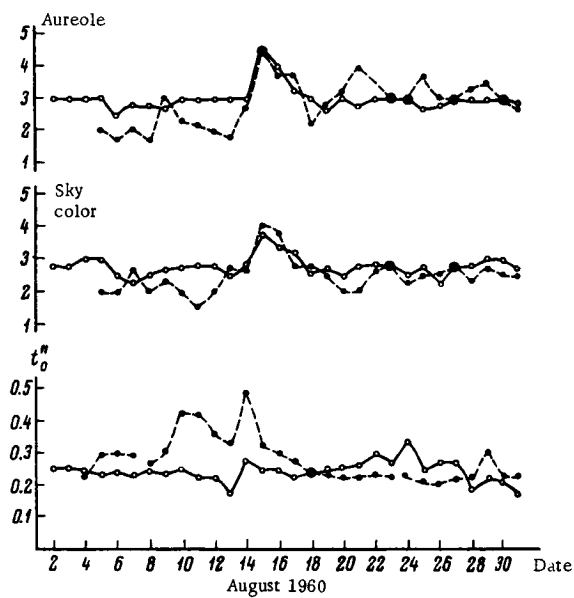
FIGURE 8. Distribution of t_0'' solar aureole, and sky color for Sanglok (—◯—◯—) and Iskander-Kul' (—●—●—) in August 1960.
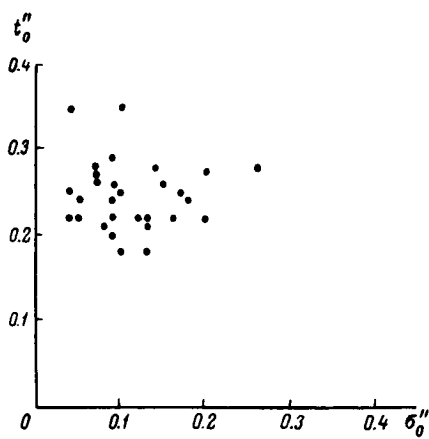
FIGURE 9. σ_0'' vs. t_0''.

More extensive material should be analyzed if we are to reach a reliable conclusion concerning the variation of σ_0'' and K.

It is remarkable that nearly always when the distribution of σ_z'' was not linear, the atmospheric transparency was seen to deteriorate. In summer, intense dust haze may cover almost the entire territory of Tadzhikistan. Strong winds in Afghanistan deserts raise dust clouds which are transported northward by air currents, and Tadzhikistan is not exempt from this optical hazard. For example, in 14, 15 August, intense dust haze penetrated as far as Iskander-Kul' Lake, where the second group of the Pulkovo expedition was making its observations. Iskander-Kul' is located some 100 km to the north from Sanglok, behind two mountain ranges. In hazy periods, t_0'' — the shimmer angle reduced to the zenith — was also seen to increase. Figure 8 plots the time variation of t_0'' in Sanglok and Iskander-Kul'. The same figure also gives for comparison the size of the aureole and the color of the sky, both estimated according to Tikhov's scale. These estimates, however, only characterize the qualitative state of the atmosphere. Inspection of Figure 8 shows that the large jump in t_0'' in the night of 14/15 August was a forewarning of the dust storm which raged during the day on 15 August, when at both points the solar aureole number was 4.5 and the sky color number 4.

In conclusion we plot σ_0'' against t_0'' (Figure 9) and σ_z'' against t_z'' (Figure 10). There is absolutely no correlation between σ_0'' and t_0'', whereas σ_z'' and t_z'' appear to be correlated to a certain extent. This indicates that the zenith values of the shimmer disk and of image pulsation should be measured directly for stars at the zenith: "reduced" values present a false picture on the state of the atmosphere.

FIGURE 10. σ_z'' vs. t_z''.

A. D. Skoropupov

THE ASTROCLIMATE OF NOVOSIBIRSK

Astroclimatic observations in Novosibirsk were organized following the suggestion of Academician S. L. Sobolev, and the project was supported at all stages by the Pulkovo Observatory, in the person of the late N. I. Kucherov, then a senior research fellow at Pulkovo. The aim of these observations was to select a site for the erection of the Novosibirsk Astronomical Observatory.
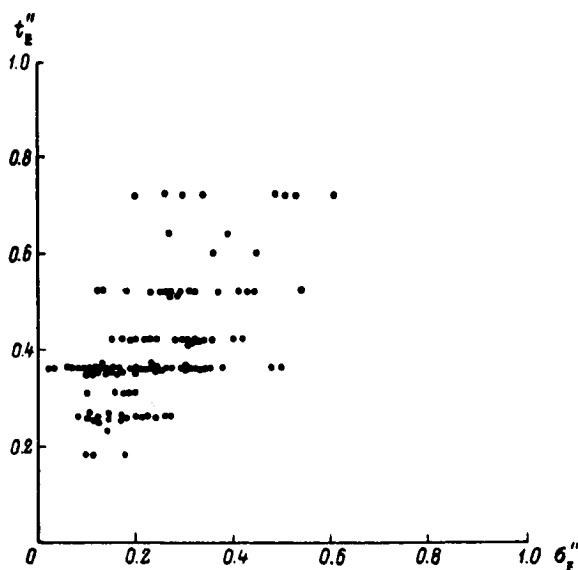
Astroclimatic characteristics are generally determined by the combined photographic and visual techniques recommended by the Pulkovo Observatory.

Visual observations of seeing (image quality) are made with the AZT-7 telescope ($D = 200$ mm). In July-February, observations were made with $\times 500$ magnification (focal distance 2 m, relative aperture 1 : 10). In March, to improve the photographic trails, the telescope was extended to an equivalent focal distance of 10 m and a relative aperture of 1 : 50 ($\times 2000$ magnification).

Three observation sessions were held daily: an evening session up to 2400 P. M. local time, a night session from 2400 P. M. to 0200 A. M., and a morning session terminating an hour or an hour and a half before sunrise. Visual scans comprised observations of stars in four azimuths (east, south, west, north); in each azimuth, we observed from 6 to 12 stars at zenith distances from $5 - 10°$ to $70 - 80°$.

Seeing was estimated using the 5-point Danjon-Couder scale /1/; estimates were made to within 0.5 of scale point.

The observations were reduced following the theory of Danjon and Couder, according to the procedure accepted by the Pulkovo Observatory expeditions and previously published in /2 — 4/.

The astronomical observations were accompanied by regular meteorological observations, made day and night at 4 hours intervals. The meteorological conditions were also reviewed at night before and after each astronomical session. Various meteorological instruments available at our station recorded wind velocities, humidity, air temperature, soil temperature, atmospheric pressure, precipitation, atmospheric transparency, fogs, etc. Synoptic charts, aerological data, and solar radiation readings were available for each and every astronomical session. Comparative meteorological data were provided by Meteorological Service stations within a 120 km circle, where a physicogeographical survey of the area is now under way. Collation of all these data with astronomical observations established various remarkable correlations, which are discussed in the following.

TABLE 1

Percentage of nights with excellent, good, fair, and poor seeing (July 1961 – June 1962)

Seeing		t_z''	Number of nights	Percentage
		$z = 20°$		
Excellent	. . . .	≤ 0.15	15	8
Good	. . . .	≤ 0.30	92	46
Fair	. . . .	≤ 0.55	76	37
Poor	. . . .	> 0.55	19	9
		$z = 45°$		
Excellent .	. . . .	≤ 0.20	16	8
Good	. . . .	≤ 0.35	54	27
Fair	. . . .	≤ 0.75	106	53
Poor	. . . .	> 0.75	26	12
		$z = 70°$		
Excellent .	. . . .	≤ 0.20	4	2
Good .	. . . .	≤ 0.70	63	31
Fair	. . . .	≤ 1.00	56	28
Poor	. . . .	> 1.00	78	39

TABLE 2

The percentage of excellent, good, fair, and poor seeing for the first, second, and third observation sessions (July 1961 – 1962)

t_z''	1st session		2nd session		3rd session	
	n	$n, \%$	n	$n, \%$	n	$n, \%$
			$z = 20°$			
≤ 0.15	13	9	8	7	4	4
≤ 0.30	65	46	57	44	29	31
≤ 0.55	57	39	53	40	53	56
> 0.55	8	6	11	9	8	9
			$z = 45°$			
≤ 0.20	16	11	11	9	4	4
≤ 0.35	44	31	38	30	17	18
≤ 0.75	72	51	68	52	53	56
> 0.75	11	7	12	9	20	22
			$z = 70°$			
≤ 0.20	3	2	3	3	0	0
≤ 0.70	48	34	45	35	23	25
≤ 1.00	34	24	29	22	21	23
> 1.00	57	40	52	40	49	52

CHARACTERIZATION OF THE OBSERVATION SITE

The fundamental characteristic derived from visual observations is the percentage of good seeing at zenith distances of 20°, 45° and 70°. Seeing is described as good if the seeing at the zenith is ≤ 2.5, i.e., if $t_0'' \leq 0''.25$ and correspondingly $t_{20}'' \leq 0''.30$, $t_{45}'' \leq 0''.35$ and $t_{70}'' \leq 0''.70$.

We see from Table 1 that in our observation area the percentage of good seeing (excellent seeing included: its percentage is fairly low) is more than 50% for zenith distances up to 20° and more than 30% for zenith distances of 45° and 70°, i.e., one third of all the nights is characterized by good seeing conditions up to large zenith distances.

The percentage of poor seeing for zenith distances of up to 45° is low (nearly 10%); for $z = 70°$, poor seeing is more frequent than fair seeing.

The distribution of seeing over the night (Table 2) shows that the morning values are much lower that the readings obtained in the evening and at night. This actually lowers the average percentage of seeing as calculated for all the three sessions.

We also see from Table 2 that the percentage of good seeing at each zenith distance is nearly the same in the evening and at night, i.e., seeing remains stable up to 1 or 2 A.M., deterioration mostly setting in during the second half of the night.

Another important characteristic of the observation site is the height (zenith distance) of transition from one Danjon-Couder number to the next. The transition heights were read off the $\delta = f(z)$ curves for each observation session, and the monthly averages (in degrees) are listed in Table 3.

TABLE 3

Month	Transition height			
	from 1 to 2	from 2 to 3	from 3 to 4	from 4 to 5
1961 July	42°	50°	69°	68°
August	28	51	64	68
September	37	49	58	64
October	40	38	59	67
November	–	38	52	63
December	31	41	56	68
1962 January	–	38	50	62
February	34	40	48	60
March	–	31	47	64
April	–	34	52	68
May	–	32	43	59
June	22	35	53	64
Average	33°	40°	54°	65°

We see from the data in Table 3 that during 12 months seeing changed from 2 to 3 and from 3 to 4 (the good seeing range) between 40° and 50°. In July, August, and September 1961, the transition height was greatest, nearly 60°; the transition height did not change much during the rest of the year.

TABLE 4

Percentage of nights with excellent, good, fair, and poor seeing with one, two, and three observation sessions (July 1961 – June 1962)

t_0''	July			August			September			October			November			December			January			February			March			April			May			June			Total		
	N	n	n%	N	n	n%	N	n	n%	N	n	n%	N	n	n%	N	n	n%	N	n	n%	N	n	n%	N	n	n%	N	n	n%	N	n	n%	N	n	n%	N	n	n%
One session																																							
≤ 0″.10	16	0	0	7	0	0	8	1	12	4	1	25	6	1	17	7	0	0	4	0	0	6	0	0	6	0	0	3	0	0	10	0	0	16	0	0	93	3	3
≤ 0.25		10	63		7	100		4	50		1	25		4	66		3	43		1	25		2	33		0	0		0	0		0	0		5	31		37	41
≤ 0.40		6	37		0	0		3	38		2	50		0	0		3	43		1	25		3	50		3	50		2	67		5	50		6	38		34	36
> 0.40		0	0		0	0		0	0		0	0		1	17		1	14		2	50		1	17		3	50		1	33		5	50		5	31		19	20
Two sessions																																							
≤ 0″.10	4	0	0	6	0	0	5	0	0		–		4	0	0	8	0	0	4	0	0	5	0	0	7	0	0	4	0	0	7	0	0		–		54	0	0
≤ 0.25		4	100		5	83		4	80		–			0	0		4	50		1	25		1	20		2	29		0	0		1	14		–			22	41
≤ 0.40		0	0		1	17		1	20		–			3	75		2	25		2	50		3	60		2	29		3	75		2	29		–			19	35
> 0.40		0	0		0	0		0	0		–			1	25		2	25		1	25		1	20		3	42		1	25		4	57		–			13	24
Three sessions																																							
≤ 0″.10		–		3	0	0	6	0	0	6	0	0	3	0	0	5	0	0	8	0	0	7	0	0	10	0	0	7	0	0		–			–		55	0	0
≤ 0.25		–			3	100		4	66		2	33		0	0		1	20		0	0		0	0		1	10		1	14		–			–			12	22
≤ 0.40		–			0	0		1	17		4	67		3	100		3	60		4	50		2	29		4	40		5	72		–			–			26	47
> 0.40		–			0	0		1	17		0	0		0	0		1	20		4	50		5	71		5	50		1	14		–			–			17	31

Note. N the number of nights with one, two, and three observation sessions; n the number of nights with excellent, good, fair, and poor seeing.

126

The nighttime conditions in the Novosibirsk — Akademgorodok area are also characterized by the percentage of nights with a varying number of observation sessions and different zenith image qualities (Table 4).

Nearly half of the 202 nights were single-session nights; nights with two and three observation sessions were equally numerous, the number of nights in each group equal to approximately one half of the number of single-session nights. The number of nighttime sessions is reduced not only by weather conditions but also by the time of year, i.e., the length of the night (in May and June no more than two observation sessions can be fitted into one night, and in July the night in Novosibirsk is so short that only one session can be held).

Excellent zenith seeing is comparatively rare (in September, October, and November only); good seeing occurs on the average in 41% of the cases, with a peak frequency in July and August and a low in spring (March, April, May). The percentage of poor seeing was the highest in spring, particularly in May, i.e., May is the month of worst astronomical seeing.

TABLE 5

Month	Total number for treatment		Number of clear nights
	nights	sessions	
1961 July	20	24	4
Aug.	16	28	7
Sept.	19	36	7
Oct.	10	22	6
Nov.	13	23	4
Dec.	20	38	7
1962 Jan.	16	36	10
Feb.	18	37	10
March	23	50	13
Apr.	14	32	13
May	17	24	14
June	16	16	10
Total	202	366	105

The number of nights and observation sessions, as well as the number of clear nights in the area, are listed in Table 5. A clear night is such that the cloudiness does not exceed 2 — 3 during the entire night or a certain part of it. The highest number of observation-worthy nights occurred in March, July, and December; fewest favorable nights were recorded in October. The number of clear nights reached a high in May and April (nearly every night during these months), and also in March; 10 clear nights were recorded in January, February, and June (more than half of the observation nights during each month).

RESULTS OF OBSERVATIONS

Six different kinds of functional dependence between seeing and zenith distance $\delta = f(z)$ emerged during the treatment of the observational material /2, 3/ (Figure 1).

The vertical variation of atmospheric density in our area was regularly measured with radio sondes, and we therefore proceeded to establish a correlation, if any, between the different seeing curves (so-called image types) and atmospheric density.
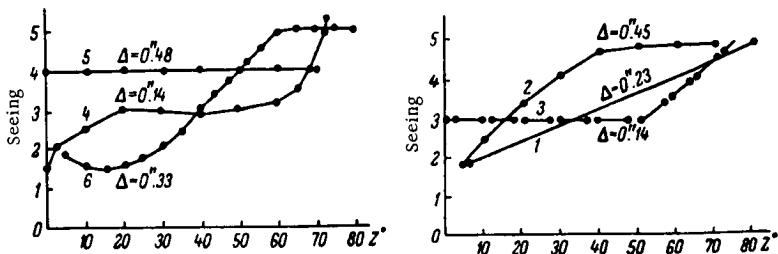

FIGURE 1.

Inspection of the $\delta = f(z)$ curves for each observation session led to the conclusion that types 3, 4 were the most common in our area, types 1 and 5 occurring seldom. For most of the "atypical" curves, however, the parameter Δ (the difference between the minimum and the maximum t_0'') characterizing the spread of the experimental points is small, i.e., in these cases t_z is proportional to sec z and the corresponding curve can be applied for the reduction of t_z'' to the zenith.

TABLE 6

Month	Number of sessions	$\Delta = t_0'' \max - t_0'' \min$				Image types				
		< 0.15	0".16 — 0".25	0".26 — 0".35	> 0".35	1	3	4	5	atypical
1961 July	24	17	7	0	0	2	2	2	0	18
Aug.	28	23	3	2	0	0	8	0	0	20
Sept.	36	18	12	4	2	0	5	0	0	31
Oct.	22	10	12	0	0	0	5	0	0	17
Nov.	23	6	12	4	1	0	4	0	0	19
Dec.	38	9	21	6	2	0	11	0	0	27
1962 Jan.	36	8	12	8	8	0	12	0	0	24
Feb.	37	8	8	10	11	0	11	0	0	26
March	50	26	17	4	3	4	27	4	6	9
Apr.	32	18	12	1	1	2	23	2	0	5
May	24	8	7	4	5	0	16	0	1	7
June	16	7	8	1	0	2	11	0	0	3
Total	366	158	131	44	33	10	135	8	7	206

Table 6 lists the distribution of the various $\delta = f(z)$ curves in terms of the parameter Δ for each of the 12 months and gives the number of cases that can be definitely classified as types 1, 3, 4 and 5. The number of "atypical" images is also listed in the table.

TABLE 7

Variation of shimmer angle at various zenith distances

	July	August	Sept.	October	Nov.	Dec.	January	February	March	April	May	June	Yearly average
			1961			t''_{av}			1962				
t''_0	0.18	0.21	0.25	0.28	0.34	0.32	0.41	0.41	0.44	0.35	0.43	0.34	0.33
t_{20}	0.20	0.21	0.25	0.29	0.41	0.34	0.42	0.41	0.46	0.33	0.35	0.30	0.33
t_{45}	0.26	0.29	0.35	0.39	0.51	0.49	0.60	0.61	0.64	0.47	0.68	0.46	0.48
t_{70}	0.46	0.57	0.63	0.76	0.75	0.83	0.96	0.99	1.22	1.05	1.30	1.16	0.89
						t''_{min}							t''_{min} yearly
t''_0	0.09	0.14	0.10	0.10	0.09	0.12	0.16	0.12	0.19	0.20	0.25	0.19	0.09
t_{20}	0.09	0.14	0.13	0.13	0.10	0.14	0.18	0.13	0.18	0.18	0.18	0.15	0.09
t_{45}	0.14	0.18	0.14	0.15	0.14	0.15	0.22	0.17	0.27	0.24	0.27	0.32	0.14
t_{70}	0.18	0.20	0.20	0.17	0.18	0.22	0.39	0.34	0.48	0.63	0.59	0.63	0.17
						t''_{max}							t''_{max} yearly
t''_0	0.32	0.43	0.62	0.40	0.54	0.68	0.85	0.41	1.05	0.63	0.82	0.53	1.05
t_{20}	0.52	0.36	0.48	0.39	0.72	0.72	0.83	0.41	1.17	0.63	0.89	0.48	1.17
t_{45}	0.52	0.77	1.04	0.55	0.89	1.04	1.25	0.61	1.44	0.95	1.25	0.72	1.44
t_{70}	0.52	1.25	1.44	1.09	1.25	1.44	1.44	0.99	1.44	1.44	1.44	1.44	1.44

TABLE 8

Variation of shimmer angle t''_0 for various observation sessions

Session	July	August	September	October	November	December	January	February	March	April	May	June	Yearly average
			1961						1962				
I	—	0.21	0.22	0.22	0.33	0.26	0.37	0.31	0.41	0.31	0.31	0.31	0.30
II	0.21	0.18	0.23	0.31	0.30	0.37	0.43	0.40	0.49	0.35	—	0.34	0.33
III	0.14	0.24	0.29	0.30	0.38	0.34	0.42	0.53	0.48	0.35	0.46	—	0.36

TABLE 9

Variation of shimmer angle t''_0 for various azimuths

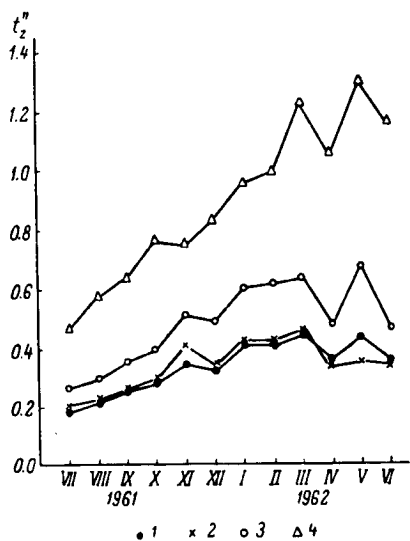| Azimuth	July	August	September	October	November	December	January	February	March	April	May	June	Yearly average
			1961						1962				
East . .	0.23	0.22	0.27	0.27	0.38	0.36	0.43	0.41	0.43	0.36	0.41	0.33	0.34
South . .	0.16	0.16	0.21	0.23	0.31	0.30	0.36	0.37	0.43	0.38	0.42	0.33	0.30
West . .	0.19	0.17	0.20	0.23	0.26	0.27	0.33	0.33	0.46	0.36	0.42	0.33	0.30
North . .	0.23	0.26	0.33	0.32	0.39	0.36	0.47	0.49	0.45	0.36	0.44	0.35	0.34

FIGURE 2. Variation of shimmer angle at various zenith distances.

1) t_0'' 2) t_{20}'' 3) t_{45}'' 4) t_{70}''.
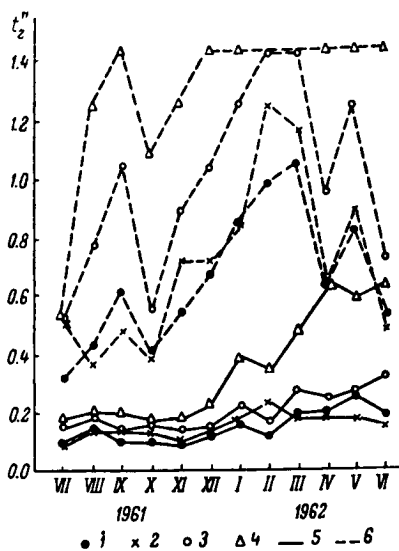
FIGURE 3. Minimum and maximum shimmer angles for zenith distances of 0°, 20°, 45°, 70°.

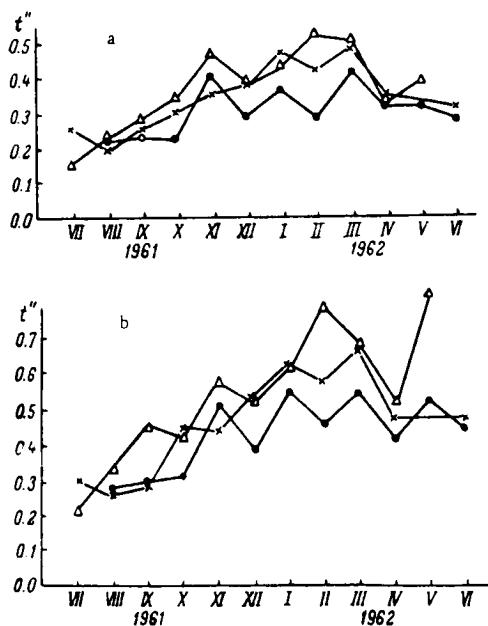1) t_0'' 2) t_{20}'' 3) t_{45}'' 4) t_{70}''.

FIGURE 4. Variation of t_{20}'' (a) and t_{45}'' (b) for various observation sessions.
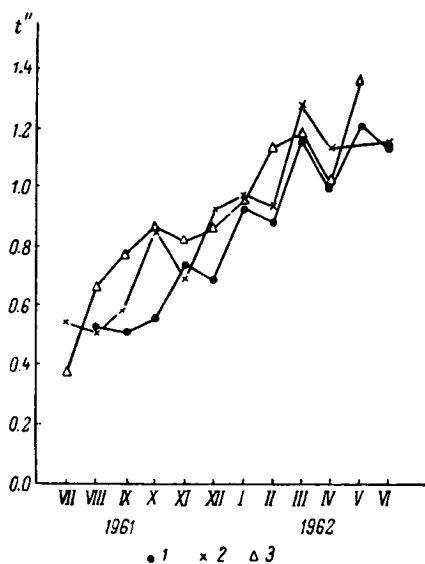● evening session; ✕ nighttime session; △ morning session.

FIGURE 5. Variation of t''_{q0} for various observation sessions.
1) evening session; 2) nighttime session; 3) morning session.
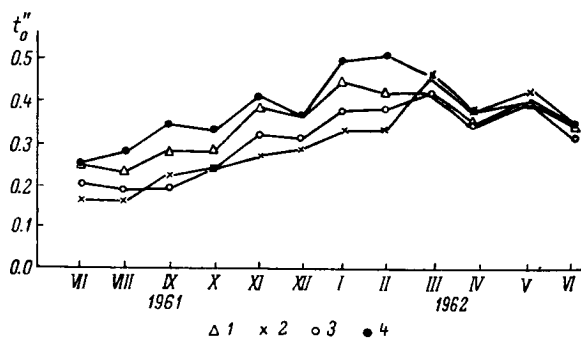

FIGURE 6. Variation of t''_0 for different azimuths.
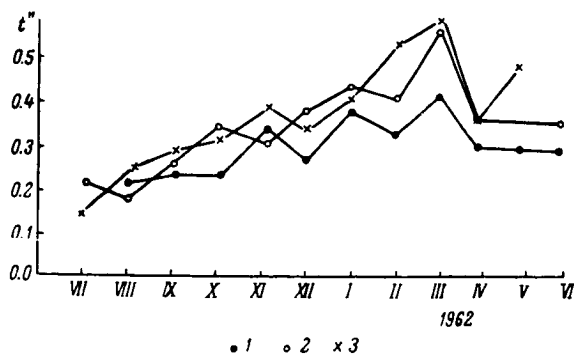1) east; 2) south; 3) west; 4) north.

FIGURE 7. Variation of t''_0 for various observation sessions.
1) evening; 2) night; 3) morning.

131

In July-November, types 3 and 4 are comparatively few; in December, January, and February (winter), these image types occur in one third of the observation sessions, while in March, May, June, and especially April type 3 and 4 curves are even more numerous (up to 90%). In some cases the curves actually coincide with the standards plotted in Figure 1 or they are displaced by no more than 0.5 or 1 in either direction (in these cases $\Delta \leq 0''.2$).

A characteristic curve for the July-November period is an extended polygonal line in the vertical range between 1.5, $2.0 - 4.0$ (July-October), and $3.0 - 5.0$ (November).

In July, August, September, and also in February the seeing in the north and the east azimuths was considerably poorer than in the south and the west: the "north" and "east" $\delta = f(z)$ curves are markedly displaced relative to the "west" and "south" curves. In other months, and particularly in March, April, May, and June, the curves of different azimuths show a much better fit.

We could not find any apparent reason for the deterioration of seeing in northerly and easterly directions.

Tables 7, 8, 9, 10 and the curves in Figures $2 - 7$ give the monthly and the yearly average shimmer angle. From these data we can trace the variation of shimmer angle at various zenith distances, and also as a function of observation session and azimuth.

TABLE 10

Variation of shimmer angle t''_z for various azimuths

Azimuth	July	Aug.	Sept.	Oct.	Nov.	Dec.	Jan.	Feb.	Mar.	April	May	June	Yearly average
	1961 г.						1962 г.						
$z = 20°$													
East . . .	0''28	0''21	0''23	0''26	0''37	0''33	0''42	0''36	0''47	0''32	0''41	0''30	0''33
South . . .	0.20	0.18	0.25	0.26	0.35	0.35	0.37	0.32	0.47	0.33	0.42	0.30	0.32
West . . .	0.18	0.22	0.35	0.25	0.32	0.33	0.42	0.35	0.47	0.33	0.45	0.31	0.33
North . . .	0.22	0.20	0.23	0.27	0.42	0.33	0.44	0.40	0.49	0.31	0.47	0.32	0.34
$z = 45°$													
East . . .	0.37	0.31	0.36	0.42	0.54	0.53	0.65	0.62	0.64	0.52	0.61	0.47	0.50
South . . .	0.26	0.24	0.26	0.34	0.44	0.41	0.52	0.45	0.63	0.54	0.61	0.45	0.43
West . . .	0.24	0.24	0.27	0.34	0.38	0.39	0.49	0.43	0.65	0.47	0.63	0.48	0.42
North . . .	0.32	0.37	0.41	0.36	0.49	0.47	0.71	0.59	0.70	0.51	0.62	0.51	0.50
$z = 70°$													
East . . .	0.51	1.14	1.44	—	1.23	1.20	1.57	1.12	1.15	1.02	1.23	1.22	1.07
South . . .	0.41	0.40	0.47	0.54	0.68	0.70	0.84	0.98	1.14	1.04	1.37	1.02	0.80
West . . .	0.47	0.45	0.56	0.54	0.59	0.65	0.75	0.79	1.16	1.04	1.28	1.13	0.79
North . . .	0.90	0.97	1.09	0.96	0.96	0.95	1.20	1.30	1.23	1.06	1.31	1.18	1.09

Inspection of the numerical and the graphical representations of t''_z leads to the following conclusions.

1) The shimmer angle regularly increases from month to month during the July-March period at all zenith distances; in April the shimmer disk

is smaller, in May it again increases reaching the annual high at $z = 45°$
and $z = 70°$; in June a downward trend in t''_z is recorded.

2) The monthly shimmer angles in the zenith and at $z = 20°$ are nearly
equal; a difference of $0''.1$ is recorded in October and May only. The
yearly averages at these zenith distances are also equal $(0''.33)$.

3) At $z = 45°$, the shimmer disk differs by $0''.1$ from its zenith value
in July-November; the difference in December-March and in May is $0''.2$.
The yearly average is $0''.5$, which is a satisfactory result.

4) At $z = 70°$, the shimmer disk increases steeply, and the yearly
average t''_{70} is nearly a second.

5) The minimum shimmer disks in the zenith and at zenith distances of
$20°$ and $45°$ do not change much from month to month during the entire
year, fluctuating by no more than $0''.15$; this also applies to $z = 70°$ during
the period from July to December.

6) The month-by-month variation of the maximum values is closely
correlated at all z, and it is only at $z = 70°$ during the months of December —
June that t''_{max} remains constant, despite the fluctuations in this parameter
at other z.

7) In the northerly and the easterly directions, the seeing conditions
are poorer than in the southerly and the westerly directions: during
most of the months and particularly from July to February, t''_z in the
north and the east azimuths are higher than in the west and the south
azimuths.

8) The zenith seeing during any month is higher in the evening and at
night, but this dependence is not as pronounced as that at $z = 20°$, $45°$,
and $70°$.

9) The yearly averages of the shimmer disk for various observation
sessions and azimuths, and for zenith distances of up to $20°$, are close
to $0''.3$, which is a satisfactory result.

COMPARISON OF OBSERVATION SITES

The data published in /3, 4/ and excerpts made by the author from the
reports of Pulkovo Observatory expeditions, now in Pulkovo archives,
served as a basis for comparison with the results of astroclimatic
observations in the Novosibirsk-Akademgorodok area. All the observation
sites available for comparison were located in Caucasus and the data were
collected by the Pulkovo Observatory expeditions in the years 1956 — 1961.
The relevant information and the seeing data (the blurring of the diffraction
disk) for the various observation sites are listed in Tables 11 — 19.

The observation time in most of the areas was unfortunately short
(4 — 6 months), reaching one year for the Mountain Astronomical Station in
the Kislovodsk area and somewhat more than a year in Pirkuli (the Shemakha
Observatory). Full-scale comparison with our data is therefore possible
for the last two sites only. It should be noted that the observations in
these areas were not simultaneous — they were made in different years
(see Table 11).

The results for the 1961 observation sites could in principle be compared
with the corresponding period of observations in the Novosibirsk area, but
since the duration of observations at these sites was small (4 — 5 months),

TABLE 11

No.	Observation site	Elevation H, m	Period of observation	No. of days spent in area	Observation nights		sessions	Number of star observations
					num-ber	%		
1	Village Suvorovskaya, Essentuki District, Stavropol Territory	300	7 Aug. – 10 Oct. 1956 and 5 Feb. – 11 Apr. 1957	130	70	54		2016
2	Turchidag, Dagestan	2281	24 June – 4 Oct. 1957	102	73	72		4380
3	MAS, Kislovodsk area	2100	13 Dec. 1957 – 11 Dec. 1958	363	180	52		12960
4	Pirkuli, Shemakha Observatory	1400	11 May 1958 – 30 Sept. 1959	497	135	27		
	Caucasus 1961							
5	Krasnye Gory		May – August	118	80	68	175	
6	Chinari		June – September	123	58	47	144	
7	MAS		May – September	153	72	47	165	
8	Dzhissa		May – August	118	72	61	172	
9	Chapal		May – September	129	74	57	164	
10	Semirodniki		May – September	133	56	42	117	
11	Marukha		May – August	102	101	99	180	
12	Novosibirsk – Akademgorodok		July 1961 – June 1962	365	202	55	366	11580
			May – Sept. 1961 – 1962	153	88	58	128	

TABLE 12

Percentage of high seeing nights

No.	Observation site	$t_{20}'' \leqslant 0''30$ (%)	$t_{45}'' \leqslant 0''35$ (%)	$t_{70}'' \leqslant 0''70$ (%)
1	Suvorovskaya	23		
2	Turchidag.	38	34	42
3	MAS	69	75	58
4	Pirkuli	42	34	49
5	Krasnye Gory	20	12	6
6	Chinari	82	56	42
7	MAS	29	12	16
8	Dzhissa	80	47	29
9	Chapal	86	45	48
10	Semirodniki	97	80	69
11	Marukha	45	29	18
12	Novosibirsk	53	35	33

TABLE 13

No.	Observation site	Transition height		
		from 2 to 3	from 3 to 4	from 4 to 5
1	Suvorovskaya	5°	29°	58°
2	Turchidag.	4	33	62
3	MAS	21	54	69
4	Pirkuli	8	31	57
5	Novosibirsk . . .	40	54	65

TABLE 14

Percentage of type 3 and 4 images

No.	Observation site	Types 3 and 4 (%)
1	Suvorovskaya	48
2	Turchidag	61
3	MAS	44
4	Novosibirsk	39
5	Pirkuli	60

TABLE 15

Percentage of high seeing nights for the three observation sessions

No.	Observation site	Evening	Night	Morning
		$t''_{20} \leqslant 0''.30$		
1	Suvorovskaya	44%	28%	27%
2	Turchidag. . . .	36	46	33
3	MAS	67	64	76
4	Pirkuli . . .	41	47	32
5	Krasnye Gory .	18	22	22
6	Chapal . .	77	75	97
7	Marukha . .	39	36	48
8	Novosibirsk . .	55	51	35
		$t''_{45} \leqslant 0''35$		
1	Suvorovskaya	37	21	34
2	Turchidag. . . .	32	40	32
3	MAS	76	70	78
4	Pirkuli . . .	33	46	21
5	Krasnye Gory .	6	13	11
6	Chapal . .	64	76	43
7	Marukha . .	26	22	23
8	Novosibirsk . .	42	39	22
		$t''_{70} \leqslant 0''70$		
1	Suvorovskaya	35	20	40
2	Turchidag. . . .	41	43	42
3	MAS	63	51	60
4	Pirkuli . . .	42	54	41
5	Krasnye Gory .	4	8	9
6	Chapal . .	71	51	60
7	Marukha . .	37	38	57
8	Novosibirsk . .	36	38	25

TABLE 16

Percentage of nights with high seeing at $z = 20°$, $45°$, $70°$ for the four azimuths

No.	Observation site	Azimuths			
		east	south	west	north
	$t_{20}'' \leqslant 0.''30$				
1	Suvorovskaya	29	33	32	30
2	Turchidag	44	32	34	44
3	MAS	66	68	74	68
4	Pirkuli	39	35	45	50
5	Novosibirsk	54	50	39	47
	$t_{45}'' \leqslant 0.''35$				
1	Suvorovskaya	24	33	40	39
2	Turchidag	44	27	31	35
3	MAS	70	77	78	74
4	Pirkuli	36	27	42	31
5	Novosibirsk	26	40	36	27
	$t_{70}'' \leqslant 0.''70$				
1	Suvorovskya	27	37	43	28
2	Turchidag	49	31	43	44
3	MAS	59	57	61	54
4	Pirkuli	40	50	56	49
5	Novosibirsk	11	45	43	13

TABLE 17

Shimmer angle t_0'' for various observation sessions

No.	Observation site	Observation sessions		
		evening	night	morning
1	Krasnye Gory	0".42	0".41	0".39
2	Chinari	0.26	0.26	0.26
3	Semirodniki	0.18	0.20	0.18
4	Marukha	0.30	0.33	0.30
5	Novosibirsk	0.30	0.33	0.36

TABLE 18

Shimmer angle t_0'' for various azimuths

No.	Observation site	Azimuth			
		east	south	west	north
1	Krasnye Gory	0".40	0".41	0".41	0".40
2	Chinari	0.27	0.26	0.25	0.26
3	Semirodniki	0.20	0.20	0.18	0.18
4	Marukha	0.31	0.33	0.31	0.30
5	Novosibirsk	0.34	0.30	0.30	0.34

covering summer and early autumn only, there was not much to be gained by this comparison, and we therefore ignored the possibility. Sites 1, 2, 5 — 11 are listed in Table 11 for purposes of comparison between themselves and also in order to present a true picture of the astroclimatic coverage of the USSR territory.

TABLE 19

Zenith shimmer angle

No.	Observation site	$t''_{0_{min}}$	$t''_{0_{max}}$	$t''_{0\,av}$
1	Suvorovskaya	0".17	0".66	0".35
2	Turchidag	0.18	0.54	0.33
3	MAS	0.10	1.44	0.28
4	Pirkuli	0.16	1.44	0.40
5	Krasnye Gory			0.40
6	Chinari			0.26
7	Semirodniki			0.19
8	Marukha			0.31
9	Novosibirsk	0.09	1.05	0.33

In /3/ and /4/ a detailed comparison is made of the shimmer disk (the blurring of the diffraction pattern) as measured mainly at four sites: Suvorovskaya, Turchidag, Mountain Astronomical Station (MAS), and Pirkuli. Matching observation periods were picked out to permit comparison of the Mountain Astronomical Station data with other sites.

The MAS proved to be the best of the four sites as regards the following fundamental criteria: (1) image quality (at all zenith distances and in all observation sessions, the percentage of high seeing at MAS was nearly 70%, while for other sites it ranged from 30 to 50%); (2) the height of transition from one seeing number to the next; (3) the percentage of nights with excellent zenith seeing; (4) the values of t''_{0av} and $t''_{0\,min}$.

We now proceed with a comparison between Novosibirsk — Akademgorodok, on the one hand, and MAS and Pirkuli, on the other.

1) The percentage of favorable nights (Table 11) in Novosibirsk (55%) is somewhat higher than at MAS (52%), and considerably higher than in Pirkuli (27%).

2) The percentage of nights with high seeing up to zenith distances of 20° is 69% at MAS, 42% in Pirkuli, and 53% in Novosibirsk; at zenith distances of 45° and 70°, however, Novosibirsk is considerably inferior to MAS and inferior to Pirkuli in this respect (Table 12).

3) Novosibirsk leads in heights of transition from one seeing number to the next (Table 13): here high seeing persists up to greater zenith distances.

4) The percentage of type 3 and 4 images at MAS and in Novosibirsk is nearly the same (44% and 39%); in Pirkuli, these image types are much more frequent (60%; see Table 14).

5) Nights with consistently good seeing at zenith distances of 45° and 70° are considerably fewer in Novosibirsk than at MAS; the percentage is the same as in Pirkuli up to $z = 45°$, and only for 70° the Pirkuli figures are higher (Table 15). At MAS the seeing deteriorates at night, while in Pirkuli and Novosibirsk it decreases by sunrise; nighttime seeing is highest in Pirkuli.

6) Seeing is azimuth-dependent for all the observation sites, but MAS leads in the percentage of high seeing in all directions (Table 16).

7) $t''_{0\,av}$ (Table 19) is 0".28 at MAS, 0".40 in Pirkuli, and 0".33 in Novosibirsk, i.e., Novosibirsk occupies the second place; the minimum and the maximum values of t''_0 are the most favorable in Novosibirsk.

Without going into the possible reasons for the particular configuration of astroclimatic factors for the different observation sites, we may state that the Novosibirsk — Akademgorodok area possesses a favorable astroclimate: at least it is no less favorable than in some places in Caucasus.

Further astroclimatic observations in Novosibirsk, it is hoped, will confirm this preliminary conclusion.

Bibliography

1. Danjon, A. and A. Couder. —AZh, **17** : 1. 1940.

2. Akhundova, G. V. and Sh. P. Darchiya. —Izv. AN AzSSR, phys.-math. series, No. 3. 1960.

3. Darchiya, Sh. P. —Izv. GAO, No. 169. 1961.

4. Akhundova, G. V. and Sh. P. Darchiya. —Izv. AN AzSSR, phys.-math. series, No. 1. 1961.

5. Darchiya, A. Kh. and Sh. P. Darchiya. — Trudy soveshchaniya po issledovaniyu mertsaniya zvezd. Moskva — Leningrad, Izdatel'stvo AN SSSR. 1959.

6. Kucherov, N. I. —Trudy soveshchaniya po issledovaniyu mertsaniya zvezd. Moskva — Leningrad, Izdatel'stvo AN SSSR. 1959.

7. Kolchinskii, I. G. —AZh, **34** : 638. 1957.

I. P. Rozhnova

A PHOTOELECTRIC METHOD OF IMAGE PULSATION
RECORDING AND SOME RESULTS OF OBSERVATIONS

Photoelectric recording of image pulsation provides the relevant
information immediately in the course of observation. This constitutes
the main advantage of the photoelectric techniques as compared to
conventional "trail" measurements /1/.

Figure 1 is a block diagram illustrating the photoelectric method
developed at the Institute of Electrical Engineering. The star image
is focused on the edge of a right-angled prism. The light reflected from
the two adjoining faces of the prism strikes the photomultipliers 1, 2
which are coupled through cathode followers 3, 4 into the bridge network
5. The edge of the prism is aligned with the optical axis of the telescope.
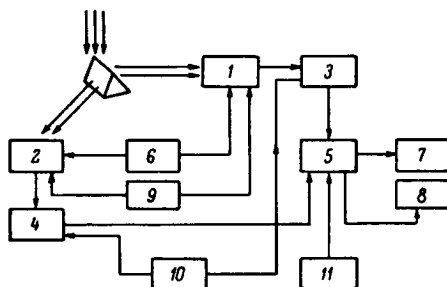
FIGURE 1.

If the star lies precisely on the optical axis, equal luminous fluxes are
reflected from the two faces, and the bridge is balanced. A shift of star
image in either direction from the telescope's optical axis due to atmospheric
turbulence produces bridge imbalance which is proportional to the displace-
ment of the star image relative to the prism edge. An a.c. voltage from
an 8 kc/s audio generator 6 is applied between the cathode and the first
dynode in the photomultiplier. This voltage provides the carrier frequency,
which is modulated by the pulsation of the star image. Photomultipliers
are supplied in parallel from a common high-voltage source 9. In Figure 1,
blocks 10 and 11 are the supplies of the cathode followers and of the bridge
network.

The imbalance voltage is a function of image pulsation. This voltage is fed into a measuring device 7 (frequency spectrum analyzer, correlator, quadratic integrator, etc.), which can be replaced depending on the particular problem under investigation. In principle, the assembly will measure image pulsation in a very wide range of frequencies. The upper limit is set by the photomultiplier time constant ($f \simeq 10^9$ c/s). In practice, however, the response region is further restricted by the inertia of the recording devices. A more detailed description of the method is given in /2/.

If the star image is shifted completely to one of the prismatic faces, the same equipment can be used in brightness scintillation measurements.

Trial tests were carried out at the Crimea Astrophysical Observatory in summer 1961, with an AZT-7 telescope. The equivalent focus of the optical system was 10 m. Considerable efforts were devoted to the exact alignment of the prism edge relative to the axis t and the precision of the driving mechanism. A special electric clock was built for the driving mechanism of the telescope /3/.
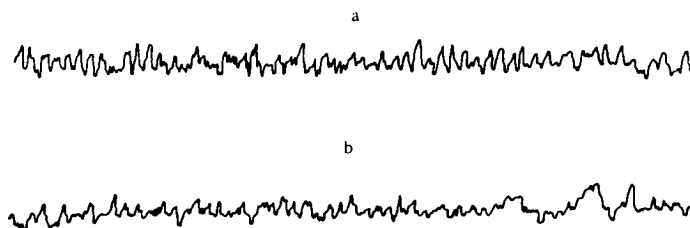
FIGURE 2. Pulsation oscillograms of Polaris with the driving mechanism stopped (a) and running (b); taken on 2 September 1962, $z = 45°$.

To avoid instrumental errors, image pulsations are generally recorded with the driving mechanism stopped /4/. A study of the instrumental vibrations in a driven telescope is no less complex than the investigation of image pulsation proper /5, 6, 7/. We nevertheless tried to estimate the contribution from the instrumental vibrations with the driving mechanism running. The telescope was carefully pointed to Jupiter and proper alignment of the prism edge with the axis t was ensured. Pointing errors were eliminated by checking the electric balance visually on the screen of the EO-7 oscilloscope /7/, with the driving mechanism stopped. The star image could move along the prism edge without causing imbalance of a previously balanced circuit. The pulsation of Polaris was then observed with the driving mechanism stopped and running. In fixed-telescope observations, Polaris drifted along the prism edge remaining in the field of vision for nearly 10 min. This was quite sufficient for taking the oscillograms. Figure 2 is a pulsation recording of Polaris with the driving mechanism stopped (a) and running (b). The oscillograms do not reveal any inherent differences between the two modes of recording. A tube potentiometer with 40 kohm input resistance was used as the recorder in our experiments. This instrument is very useful for field work, since the recordings are traced on a chalk-surfaced paper tape, which does not

require further treatment. The deficiency of the technique is the low transport speed of the tape, 50 mm/sec. The tape speed in the oscillograms in Figure 2 was 10 mm/sec.

Image pulsation is a composite phenomenon. It is inseparable from the blurring of the diffraction pattern and the displacement of the "shimmer disk" due to atmospheric turbulence. The so-called "star trails" in fact trace the displacement of the entire shimmer disk. The photoelectric method of course records also those components which are responsible for the irregularities of the diffraction pattern within the shimmer disk.

The photoelectric method is adapted for pulsation measurements of symmetric planets. We have obtained several pulsation oscillograms for Jupiter. As we all know, planets do not scintillate. The recording of the pulsation of planets by the photoelectric method is therefore of considerable significance, since brightness scintillation is automatically eliminated. Figure 3 shows an oscillogram which traces the pulsation (a)
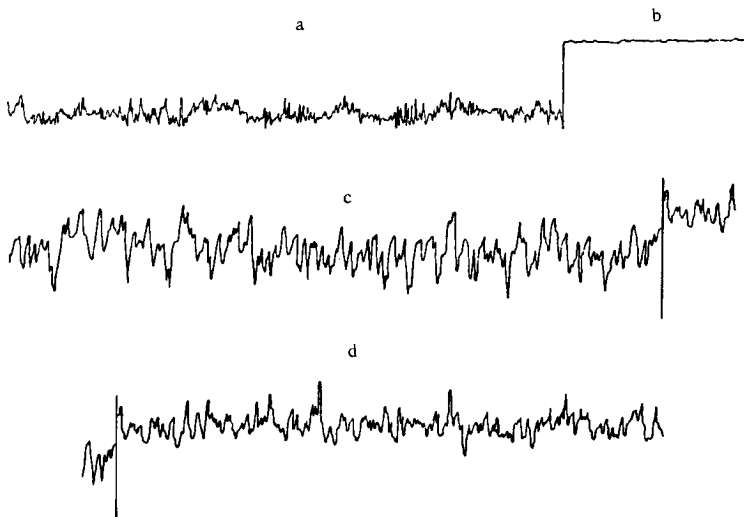
FIGURE 3. Pulsation (a) and scintillation (b) of Jupiter for 8 August 1961 ($z = 80°$); pulsation (c) and scintillation (d) of α Bootis for 30 August 1961 ($z = 67°$).

and the scintillation (b) of Jupiter. The recording demonstrates the fact that planets pulsate without scintillating. For the sake of comparison, the same figure gives the pulsation (c) and scintillation (d) oscillograms for α Bootis.

The spectral densities of planetary and stellar pulsation recorded by the photoelectric method should be expected to differ. The point is, that the pulsation of planets is produced by the displacement of the entire diffraction disk, and the oscillogram is free from components which distort the diffraction pattern. Jupiter was seen to pulsate only in poorseeing nights at large zenith distances. Our instrument detected no pulsation in high seeing nights.

The spectral density calculated from planetary pulsation oscillograms is plotted in Figure 4. The autocorrelation function

$$B(\tau) = \lim_{\Delta T \to \infty} \frac{1}{2T} \int_{-T}^{+T} y(t) y(t + \tau)\, dt$$

was found by the conventional method, and the spectral density

$$P(\omega) = \frac{2}{\pi} \int_{0}^{\infty} B(\tau) \cos \omega \tau\, d\tau$$

was then determined.

The planetary spectral density should be compared with the spectral density of stellar image pulsation. The spectral density curve of α Bootis is plotted in Figure 5. We see that the stellar curve contains components of higher frequencies. A comparison of the pulsation spectral densities of planets and stars (Figures 4, 5) supports the suggestion that stellar image pulsation is made up from two components: the displacement of the
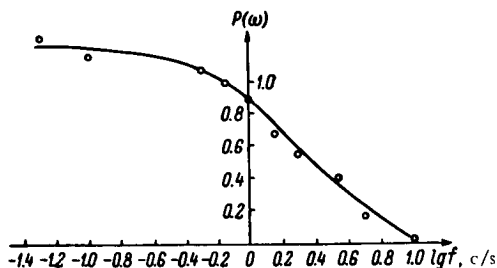
FIGURE 4. Spectral density of image pulsation of Jupiter for 8 August 1961, $z = 80°$.
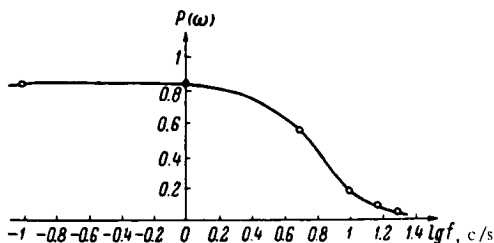
FIGURE 5. Spectral density of image pulsation of α Bootis for 22 August 1961, $z = 70°$.

entire "shimmer disk" and migration of the photometric center of gravity within the disk. The latter phenomenon is responsible for the high frequency components which appear in the pulsation spectra of stars, while being absent from the planetary pulsation spectra. This also distorts the diffraction disk of the star image. It is significant that the spectral

densities of planetary and stellar pulsation reveal a pronounced saturation plateau in the low frequency region. Spectral densities of brightness scintillation also approach a certain saturation level in the low frequency region: this has been proved theoretically by V. I. Tatarskii /8/ and is confirmed by numerous observations. Furthermore, the general tendencies of stellar scintillation and pulsation have much in common. But in our particular case there is a possibility that saturation is produced by instrumental factors. The maximum pulsation amplitude should not exceed half the diameter of the star's shimmer disk. This corresponds to a case when the entire star image lies on one of the prism faces, and further displacement away from the prism edge does not increase the photocurrent. The minimum pulsation amplitude is of course determined by the actual width of the edge, which in our experiments did not exceed 5μ. Therefore, the larger the image, the smaller the pulsation amplitudes that can be detected.

It is remarkable that the amplitude spectrum of star image pulsation derived by U. Mayer /9/ from "trails" is similar to a certain extent to the spectral density of planetary pulsation (Figure 4) in the region of the "higher" frequencies. In both cases, the pulsation amplitude steeply falls off near $1-2$ c/s. In our opinion, this is a trivial effect, since the pulsation in either case is produced by the displacement of the entire shimmer disk. At lower frequencies, the curves trace separate courses. Mayer's amplitude spectrum reveals no saturation.

The rms pulsation amplitude σ calculated for Jupiter from the corresponding oscillograms is approximately equal to 6.00% of the image diameter. At the time of observation, the diameter of Jupiter was 45" (according to cataloged data). Hence, $\sigma = 2".70$. The rms pulsation amplitude of α Bootis was nearly 50.0% of the image diameter. If the diameter of star image is taken equal to the diameter of the central diffraction disk, then for our telescope it is 1".4. Then $\sigma = 0".700$. The star image is seldom equal to the diffraction disk, however: the actual diameters of star images commonly exceed the expected diffraction disk by a considerable factor (sometimes by as much as one order of magnitude). The actual σ for α Bootis is therefore higher than the above figure in seconds of arc.

The errors of the photoelectric technique are mainly conditioned by the ratio of the star's brightness scintillation amplitude to the total luminous flux at the time of observation, since no special measures were taken to compensate the brightness scintillation. The rms brightness scintillation of stars is mostly $5-15\%$ of the mean luminous flux /10/. If the star is precisely aligned with the optical axis, the scintillation effects are cancelled. As the star shifts from the prism edge, imbalance sets in, which is proportional to the pulsation amplitude, and a certain imbalance-proportional component is therefore introduced by brightness scintillation. There is some evidence that scintillation and pulsation of stars are uncorrelated effects /9/. Pulsation and scintillation are random phenomena. The probability that the maximum of brightness scintillation should coincide with a pulsation maximum is therefore low. The characteristic error of the method is thus estimated at $5-15\%$.

Brightness scintillation can be compensated without making the technique much more complex. Part of the luminous flux (20 — 30%) should be deflected through a semitransparent mirror and another photomultiplier should be provided. Once the scintillation amplitude and the imbalance current are known, a feedback loop can be employed to compensate the brightness scintillation picked up by differentially coupled photomultipliers.

Bibliography

1. Trudy soveshchaniya po mertsaniyu zvezd (Transactions of the Committee on the Scintillation of Stars). — Moskva — Leningrad, Izdatel'stvo AN SSSR. 1959.

2. R o z h n o v a , I. P. and Yu. A. S a b i n i n . Novaya tekhnika v astronomii (Modern Techniques in Astronomy). — Moskva — Leningrad, Izdatel'stvo AN SSSR. 1963.

3. R o z h n o v a , I. P. and Yu. A. S a b i n i n . — Sbornik rabot po voprosam elektromekhaniki, No. 9. Izdatel'stvo AN SSSR. 1963.

4. K o l c h i n s k i i , I. G. — AZh, 34, No. 4. 1957.

5. C o n d e r , A. CR, 203 : 609. 1936.

6. S t r ö m g r e m , B. — Matematisk Tidsskrift, Første Del., 15. 1945.

7. B u g o s l a v s k a y a , E. Ya. — Trudy soveshchaniya po mertsaniyu zvezd. Moskva — Leningrad, Izdatel'stvo AN SSSR. 1959.

8. T a t a r s k i i , V. I. Teoriya flyuktuatsionnykh yavlenii pri rasprostranenii voln v turbulentnoi atmosfere (Theory of Fluctuational Phenomena for the Propagation of Waves in a Turbulent Atmosphere). Moskva. 1959.

9. M a y e r , U. — Z. f. Aph., 49 : 161 — 167. 1960.

10. Z h u k o v a , L. N. Dissertation. — Pulkovo Observatory. 1959.

Z. N. Kuteva and Yu. A. Sabinin

A PROGRAMMED TELESCOPE DRIVING SYSTEM

As astronomy develops and man advances into space, astronomical instruments are expected to meet constantly increasing standards. Automation provides one of the most effective means for the improvement of telescopic observations. Manual manipulations of large telescopes constitute a formidable task, and it is therefore highly desirable to build special systems for automatic pointing and guiding. Telescopes engaged on comparatively narrow, topical research programs can even be guided by preprogrammed systems. In particular, a need was felt in programmed automatic guiding of specialized telescopes used in measurements of atmospheric transparency. Atmospheric transparency is determined by measuring the luminous flux reaching an automatic photometer from certain bright stars. Nightly observation schedules are drawn up for 4 — 5 stars which are comparatively far from other bright objects. During the night, the observer should point the telescope to each of the selected stars in succession and, having pointed the telescope, he is expected to track the star for as long as needed to complete the measurements. The observational data in atmospheric transparency survey are recorded by automatic photometers. A possibility therefore exists of freeing the observer from the tedious telescope guiding operations, i. e., the telescope can be guided without human intervention by a preprogrammed device.

A programmed automatic guiding system for transparency survey telescopes was built and tested at the Institute of Electrical Engineering pursuant to an agreement with the Crimea Astrophysical Observatory. Transparency survey telescopes are used in observations of a limited number of stars, and automatic pointing and guiding can therefore be achieved with continuous operation elements. The accuracy attainable with these systems depends on the complexity of the electronic circuitry employed. Let us consider some programmed guiding systems using rotating transformers (RT).

We first describe the simplest system designed for programmed pointing and guiding of an equatorial telescope.

The setup unit for the input of the equatorial coordinates α and δ into the computer comprises the following components (Figure 1) : 1) storage devices which store the constant coordinates α and δ of a limited number of stars selected for observation; 2) α and δ switches which connect the computer to each pair of coordinates in succession; 3) a programmed device which controls the coordinate switches, setting the star selection sequence in accordance with the specifications included in the program.

We now consider in some detail the main components of the setup unit.

Since all the arithmetic and logic operations are carried out by RT, the star coordinates in the storage device are conveniently represented by a. c. voltage which is proportional to the sine or the cosine of the corresponding angle u_i or δ_i. The number of rotating transformers in the storage device is then equal to twice the number of stars to be scanned. Since even the observation schedules of highly specialized telescopes include several stars (5 — 6 stars for transparency survey telescopes), the storage may prove to be quite bulky. To make the memory more compact, most of the rotating transformers can be replaced with program transformers PT_a and PT_δ. The number of lead pairs in these transformers should be equal to the number of stars selected by each. The voltage obtained from each pair of leads is proportional to the sines and cosines of u_i and δ_i. The phase of the voltage specifies the sign of the corresponding trigonometric function. Since the power requirements of PT are small, a small-sized transformer can be used to store a large number of stars. PT should preferably be designed as autotransformers, with a transformer ratio of nearly 1.
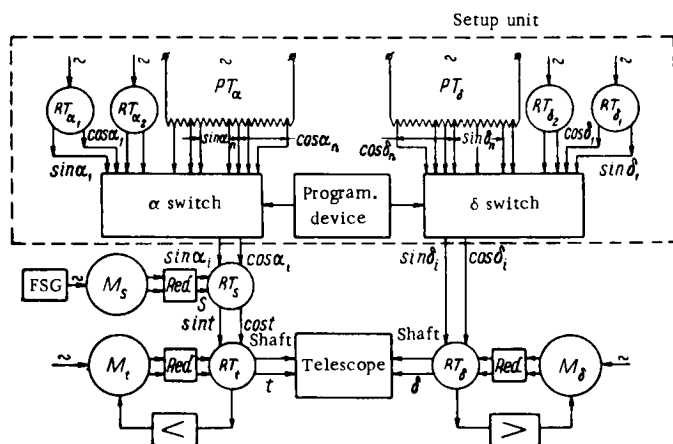
FIGURE 1. A programmed automatic guiding system.

Two-three pairs of rotating transformers should be provided in addition to the program transformers in the storage device: these transformers will permit extension of the original observation schedule stored in the program transformers.

The programmed device and the switches can be built from simple and sturdy elements, since transparency survey telescopes are trained on a limited number of stars.

A program loading unit with a capacity of up to 30 stars is shown in Figure 2.

The connection with voltages which are proportional to the sine and the cosine of the angles a_i and δ_i is made when two relays are tripped: one of the three relays R_{1-3} and one of the ten relays RP_{1-10}. The relays R and RP are controlled by a paper tape on which the observation program has been punched.

146

The paper tape is wound on a drum which turns uniformly, completing one revolution during the program running time T. The holes punched in the tape each intercept one of the sliding contacts. When a contact reaches a hole, it makes connection with the metallic drum, which is connected to the plus of the power source, and the relay is tripped. The holes for the R contacts are punched so that at any given time one of the relays is connected to the power supply. Similarly, in the RP group there is a single worling relay at any time. When the relays R and RP are tripped simultaneously, a voltage specifying the program selected angle develops at the output. By altering the position and the length of the holes in the paper tape, we may change the programmed sequence and the observation time. The output voltages proportional to $\sin \alpha_i$, $\cos \alpha_i$ and $\sin \delta_i$, $\cos \delta_i$ are fed into the respective channels which turn the telescope in hour angle and in declination.
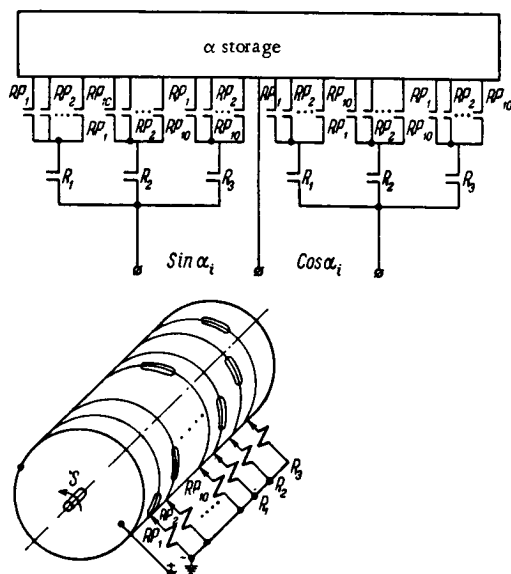
FIGURE 2. Program loading device.

A sidereal clock permits the constant star coordinate α to be added to the current sidereal time S. The sidereal clock uses a synchronous motor which turns the RT_S shaft at a uniform speed of 1 revolution per sidereal day. The motor is supplied by a frequency-stabilized generator. When the RT_S shaft whose stator windings are fed by voltage proportional to the sine and the cosine of the angle α_i turns through an angle S, the rotor windings develop voltages which are proportional to the sine and the cosine of the angle $t = S - \alpha$. RT thus performs addition of sidereal time with right ascension.

Voltages proportional to $\sin t$ and $\cos t$ move the telescope to position specified by the hour angle t. A rotating transformer RT is provided on the telescope's hour axis, and its stator windings are supplied by the

rotor windings of RT_S. The voltage developed by the sine winding of RT_t is fed through an amplifier to the driving motor M_t, which initially points the telescope at the specified angle t and then guides the telescope after the star. Once the telescope has been pointed and automatic guiding has been turned on, the automatic photometer is actuated by a relay which is fed by the input voltage of the t and δ trackers.

The telescope follows the star since the sidereal time changes continually and the voltage of the RT_t sine winding varies correspondingly.

The declination guiding system is somewhat simpler than the hour angle system, since it does not contain any clocks. In other respects, the two systems are analogous.

The described system can be used both in programmed and in automatic guiding. In the latter case it is of course much simpler: the setup device includes only two rotating transformers RT_α and RT_δ which are set on mounts with high-precision scales; the programmed device and the switches are omitted. RT_α and RT_δ scales are set to the coordinates of some particular star and the t and δ axes of the telescope are pointed as required with the aid of a tracking system; subsequent guiding is provided as before.
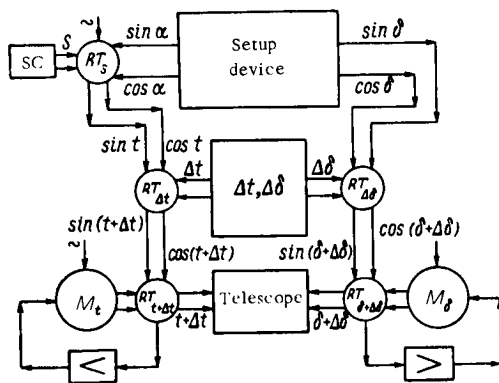
FIGURE 3. Programmed guiding in the coordinates $t + \Delta t$ and $\delta + \Delta \delta$.

If the system described in this paper is used in atmospheric transparency surveys, the observer should only prepare the observation schedule, punch it on paper tape, load it into the programmed device, and later reduce the data recorded by the automatic photometer.

If refraction errors should be taken into consideration in telescope guiding, a somewhat more complex system is used which, in addition to the above described components, also contains a device that computes the mean refraction and corrects the positions of the hour axis and the declination axis accordingly (Figure 3). Refraction corrections are computed by a circuit which is also built using RT. This circuit, however, is fairly simple, since the corrections are functions of sines and cosines of the angles t and δ:

$$\Delta t = -\rho_0 \frac{\cos \varphi \sin t}{\cos \delta \, (\sin \varphi \sin \delta + \cos \varphi \cos \delta \cos t)} , \quad \Delta \delta = \rho_0 \frac{\sin \varphi \cos \delta - \cos \varphi \sin \delta \cos t}{\sin \varphi \sin \delta + \cos \varphi \cos \delta \cos t} .$$

. Here Δt, $\Delta\delta$ are the mean refraction corrections in the hour axis and the declination axis settings. The arithmetic-logic unit using RT is so built that the output shafts of the system are continually set to angles Δt and $\Delta\delta$ by a tracking system /1/.

The refraction corrections are added to the current coordinates t and δ by the rotating transformers $RT_{\Delta t}$ and $RT_{\Delta\delta}$. Tracking systems then point the telescope to the coordinates $t+\Delta t$ and $\delta+\Delta\delta$.

The system was experimentally tested at the Crimea Astrophysical Observatory. It was applied to achieve programmed pointing to 4 bright stars in different parts of the celestial sphere. Measurements have shown that pointing errors did not exceed 2'.5 of arc.
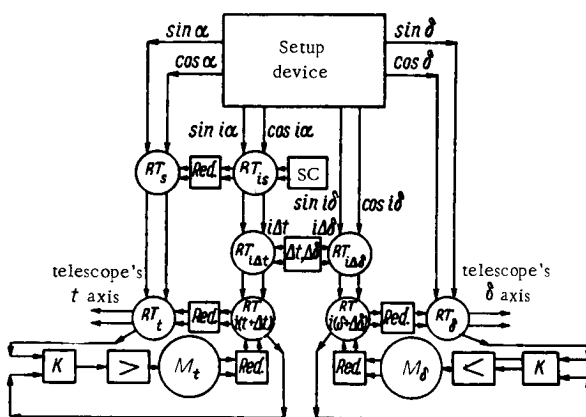
FIGURE 4. An improved programmed guiding system.

Automatic pointing errors can be further reduced by introducing more sophisticated circuitry. The additional features of high-precision systems include 1) computation of current coordinates by two sets of coarse and fine adjustment rotating transformers; 2) highly accurate determination of refraction errors taking account of temperature and pressure and correction for instrumental errors introduced by the telescope (Figure 4).

Δ	t	δ for t = 0	15°	30°	40°	45°	50°	55°	60°	75°	80°	85°
30"	t_1	18°25' 71°35'		27° 50'		37° 50'			37°			
15"	t_2	31° 59°			17° 40'	19° 50'	19° 15'	15° 10'				
45"	t_3	8°10' 81°50'		43° 16'		53° 20'			58° 10'	50° 40'	33° 10'	
1'	t_4	0 90°	39° 50'	54° 45'		65° 30'			74° 30'	82° 25'	85°	87° 30'

If high-precision RT are employed, the guiding errors will correspondingly drop. Preliminary calculations indicate that the errors in this case need not exceed $20-30''$.

In conclusion we should note that the pointing and guiding accuracy can be increased considerably by resorting to special-purpose programming techniques: observation programs can be prepared for stars in particular areas of the sky, where refraction errors are negligible. To estimate the refraction errors Δ in telescope pointing and guiding, we calculated (see table) and plotted in t, δ coordinates the boundaries of regions where the errors did not exceed $15''$, $30''$, $45''$, and $1'$ (Figure 5).
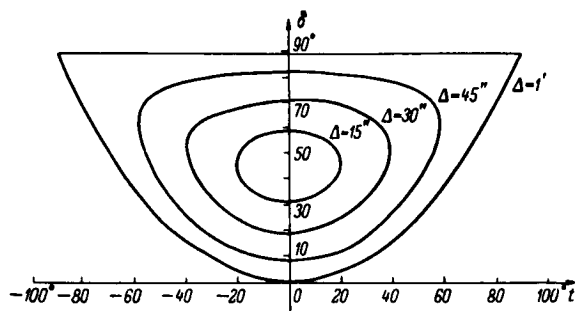
FIGURE 5. An auxiliary graph for preparation of observation programs.

The graph in Figure 5 is very helpful in the preparation of programs with refraction errors not exceeding a predetermined value. In this case, refraction errors need not be computed or corrected for, and the guiding system is considerably simplified.

If no attempt is made to develop general-purpose, universal guiding programs, automatic pointing and guiding systems can be built which ensure high accuracy and reliability even with comparatively simple circuitry using rotating transformers.

Bibliography

1. Mamedova, Z.N. —In: "Sbornik rabot po elektromekhanike", Vol. 5. 1961.

P. V. Nikolaev

FLUCTUATION OF STAR IMAGES AND
AUTOMATIC TELESCOPE GUIDING

The prevalent trend in astronomical instrumentation during the last decade is toward the construction of large and medium-sized telescopes with complex automatic guiding systems. Examples of this trend are provided by the ZTSh telescope of the Crimea Astrophysical Observatory with a 2.6 m mirror and the Lick Observatory telescope (USA) with a 3 m mirror. Automatic driving of large, all-purpose telescopes of this category is achieved in several complementary stages: automatic pointing systems direct the telescope tube to the desired object, high-precision electro-mechanical clocks time the driving mechanism, special automatic systems ensure that the abservatory dome and the telescope tube turn in unison, auxiliary operations and recording devices are automated, and, finally, automatic guiding is set up. Automatic guiding systems are photoelectric trackers which keep the star image stationary relative to the photographic plate, the spectrograph slit (with automatic spectrum broadening), the photometer aperture, or any other pickup device. Tracking corrections may be applied to the main leads, and then the entire telescope is turned through the required additional angle (whole telescope guiding); another possibility is that the recording device is displaced (e. g., the film holder) or a plane-parallel optical glass plate provided in front of the inlet element of the recorder is rotated (local guiding). Photoelectric trackers respond directly to the star image. The sensors of these tracking systems are provided either in the optical guider or at the edge of the optical field of the main telescope (depending on the mode of guiding and on the particular problem under investigation), in which case they respond to star images at the outskirts of the field in the focal plane of the main telescope. The trackers can also be made to respond to the light of a star reflected from spectrograph cheeks.

To ensure high-quality guiding, the automatic guider should compensate not only biased errors, but also random shifts of the image from the sighting axis due to anomalous refraction and pulsation, whose amplitude is by no means negligible. The automatic guiders should therefore be virtually free from fluctuational input errors due to sensor noise (a photomultiplier is generally used) and brightness scintillation of the guiding object.

The designer of photoelectric trackers for automatic guiding systems therefore must cope with a difficult problem: he is required to build a tracking system which meets the above standards and which moreover cancels initial deviations and inaccuracies (pointing errors) in a reasonable

time, the transient process being nearly aperiodic. We should note that ·
the maximum initial deviation is equal to half the optical field of the photo-
guider and may sometimes be as high as tens of seconds of arc.

Let us briefly consider the biased errors in telescope driving and their
general variation. The biased errors in the driving of an equatorial
telescope by a clock mechanism are mainly attributable to atmospheric
refraction and bending (deformation) of the telescope tube. Because of
these errors the telescope is initially pointed somewhat below the apparent
direction to the object, i.e., an error in zenith distance creeps in,

$$\Delta z = \Delta z_1 + \Delta z_2, \tag{1}$$

where Δz_1 is the error due to atmospheric refraction, Δz_2 the error due to
deformation of the telescope tube. The components of Δz along the declination
axis δ and the hour axis t are respectively

$$\Delta\delta = -(\Delta z_1 + \Delta z_2)\cos q, \\ \Delta t = (\Delta z_1 + \Delta z_2)\sin q \sec \delta, \tag{2}$$

where q is the parallax angle for the given coordinates of the object.

As the telescope follows the star, the hour angle t changes continually,
and the zenith distance z therefore also varies. The error Δz does not
remain constant, since its components Δz_1 and Δz_2 are functions of z. To
first approximation, the refraction error is given by

$$\Delta z_1 = r_0\,\mathrm{tg}\,z, \tag{3}$$

and the bending error by

$$\Delta z_2 = B\sin z, \tag{4}$$

where r_0 is the mean refraction constant at the telescope site, B a constant
coefficient which characterizes the stiffness of the telescope tube.

Substituting Δz_1 and Δz_2 from (3) and (4) into (2) and expressing z and q in
terms of the equatorial coordinates t and δ of the object, we obtain

$$\Delta\delta = -\left(\frac{r_0}{\sin\varphi\sin\delta + \cos\delta\cos\varphi\cos t} + B\right)\times \\ \times(\sin\varphi\cos\delta - \cos\varphi\sin\delta\cos t), \tag{5}$$
$$\Delta t = \left(\frac{r_0}{\sin\varphi\sin\delta + \cos\varphi\cos\delta\cos t} + B\right)\cos\varphi\sin t\sec\delta.$$

Differentiating with respect to t, we obtain expressions for the rate of
growth of the biased errors in t and δ at the time of observation and for
the "acceleration" in their rate of growth:

$$\left. \begin{array}{l} \Delta\dot\delta = -\left[\dfrac{r_0\sin\varphi}{(\sin\varphi\sin\delta + \cos\varphi\cos\delta\cos t)^2} + B\sin\delta\right]\cos\varphi\cdot\sin t, \\[4mm] \Delta\dot t = \left[\dfrac{r_0\,(\sin\varphi\sin\delta\cos t + \cos\varphi\cos\delta)}{(\sin\varphi\sin\delta + \cos\varphi\cos\delta\cos t)^2} + B\cos t\right]\cos\varphi\sec\delta, \end{array} \right\} \tag{6}$$

$$\Delta \ddot{\delta} = - \left[r_0 \sin \varphi \, \frac{\sin \varphi \sin \delta \cos t + \cos \varphi \cos \delta \, (1 + \sin^2 t)}{(\sin \varphi \sin \delta + \cos \varphi \cos \delta \cos t)^3} + \right.$$

$$\left. + B \sin \delta \cos t \right] \cos \varphi,$$

$$\Delta \ddot{t} = \left\{ r_0 \, \frac{\sin \varphi \sin \delta \cos \delta \cos t + 2 \, (\cos \varphi \cos \delta)^2 - (\sin \varphi \sin \delta)^2}{(\sin \varphi \sin \delta + \cos \varphi \cos \delta \cos t)^3} - \right.$$

$$\left. - B \right\} \cos \varphi \sin t \sec \delta. \tag{7}$$

As an illustration, Figures 1 — 6 plot the corrections for biased errors, and the corresponding speeds and accelerations of compensating telescope driving in hour angle and in declination, as a function of the hour angle. The curves in Figures 1 — 6 correspond to $\varphi = 44°.5$, $r_0 = 60''$, $B = 300''$; they cover the entire working range of telescopes, with $z \leqslant 75°$. The geographical latitude $\varphi = 44°.5$ is the latitude of the Crimea Astrophysical
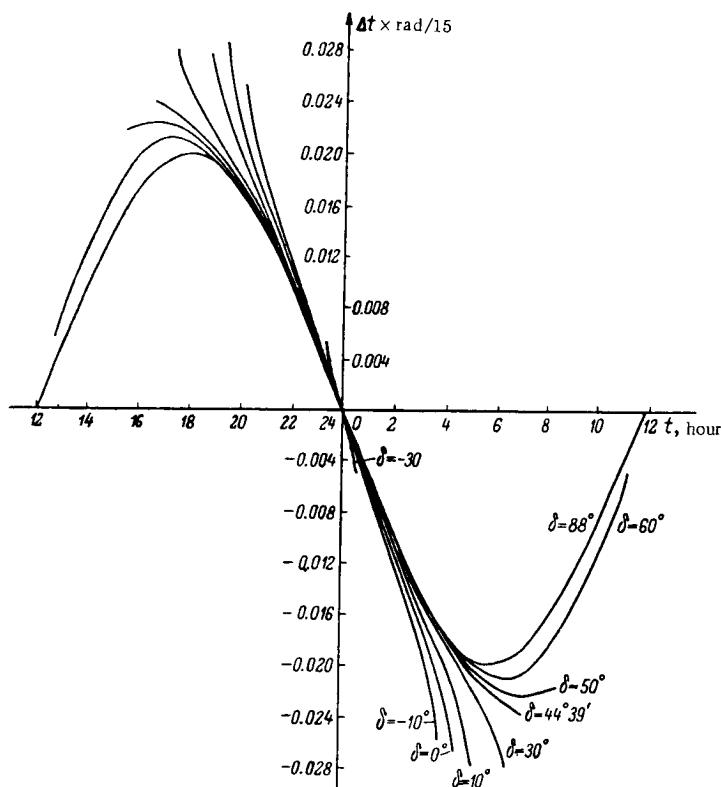
FIGURE 1. Biased error Δt vs. hour angle t.

Observatory. From Figures 1 — 6 we see that even if the coefficient B is too high, the maximum correction speeds and accelerations of the guiding system are very low:

$$\Delta \ddot{t}_M = 0.05 \sec \delta \, ''/\sec, \quad \Delta \ddot{t}_M = 1.5 \cdot 10^{-5} \sec \delta \, ''/\sec^2,$$
$$\Delta \ddot{\delta}_M = 0.05 \, ''/\sec, \quad \Delta \ddot{\delta}_M = 1.5 \cdot 10^{-5} \, ''/\sec^2. \tag{8}$$

To simplify the discussion, the factor sec δ in the expressions for Δt, $\Delta^{.}t$, $\Delta^{..}t$ is henceforth taken equal to unity: this corresponds to the case of local guiding, when the errors t are equal over the optical field and angle. This simplifying assumption was adopted in the construction of the curves in Figures 1, 3, and 5.

A guiding error of two tenths of the image diameter is quite satisfactory for most astronomical observations. The permissible error of automatic guiding systems is therefore taken as

$$\varepsilon = 0.2d, \tag{9}$$

where d is the diameter of the star image in the focal plane of the main telescope. The total error ε of any tracking system is a sum of a static error ε_s attributable to the static moment on the drive shaft and a dynamic error ε_d, i.e.,

$$\varepsilon = \varepsilon_s + \varepsilon_d. \tag{10}$$

The dynamic error ε_d is in turn a sum of errors contributed by the steady-state motion ε_g and the transient process (free mode) ε_f.
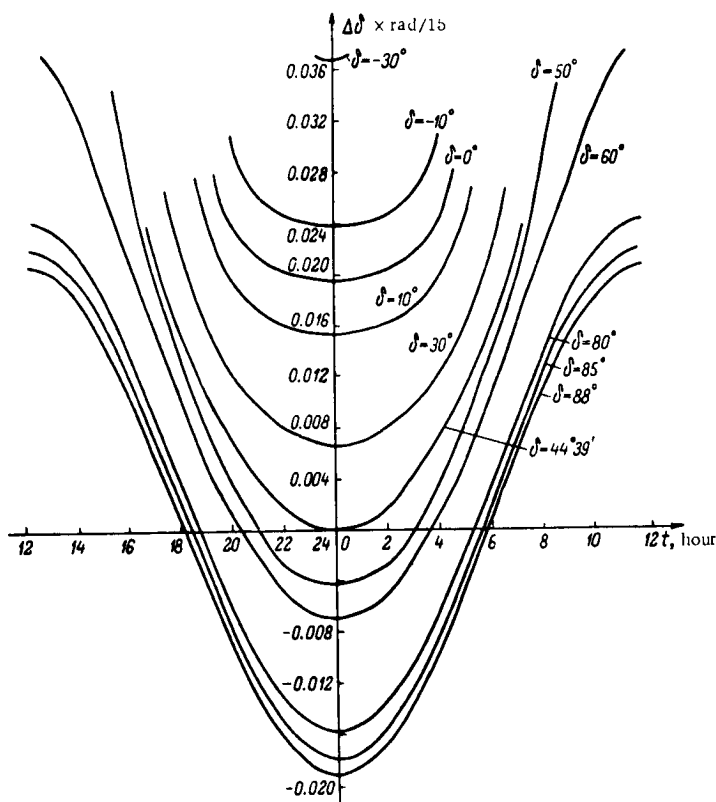
FIGURE 2. Biased error $\Delta\delta$ vs. hour angle t.

If in calculations of photoelectric trackers we take account of biased disturbances at the input and neglect the dry friction of the drive shaft, the static gain (the quality factor) D of the system can be adopted as its basic parameter; the quality factor is defined by

$$D = \frac{1.3\Delta \dot t_M}{\varepsilon_g} \qquad (11)$$

and this definition is in force for any of the telescope axes, since $\Delta \dot t_M = \Delta \dot \delta_M$.
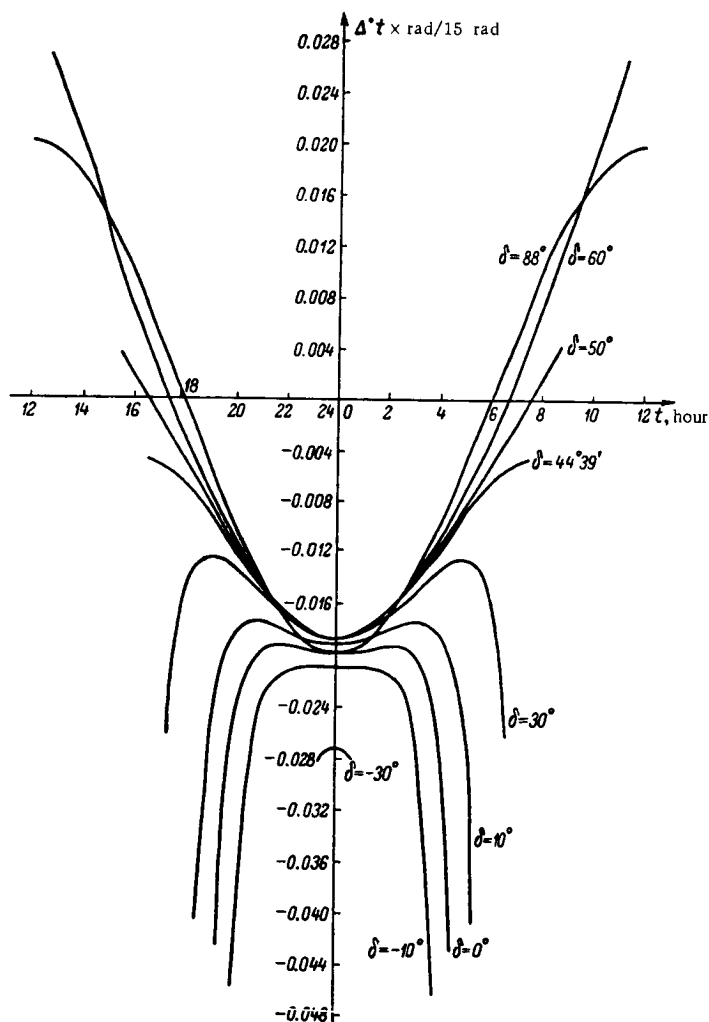
FIGURE 3. Rate of growth of the biased error in t.

The introduction of the quality factor as the main parameter is justified in this case, since the input error grows almost uniformly due to the vanishingly small accelerations (see (8)). If we take $\varepsilon_g = 0.1 d$, the quality factor is
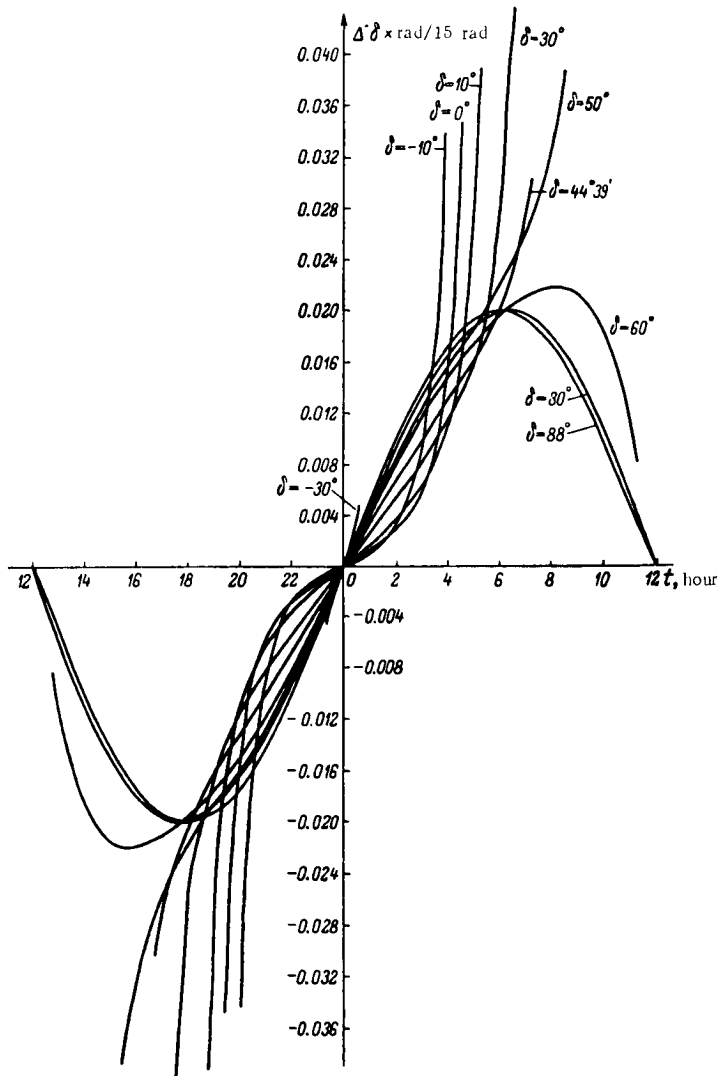
FIGURE 4. Rate of growth of the biased error in δ.
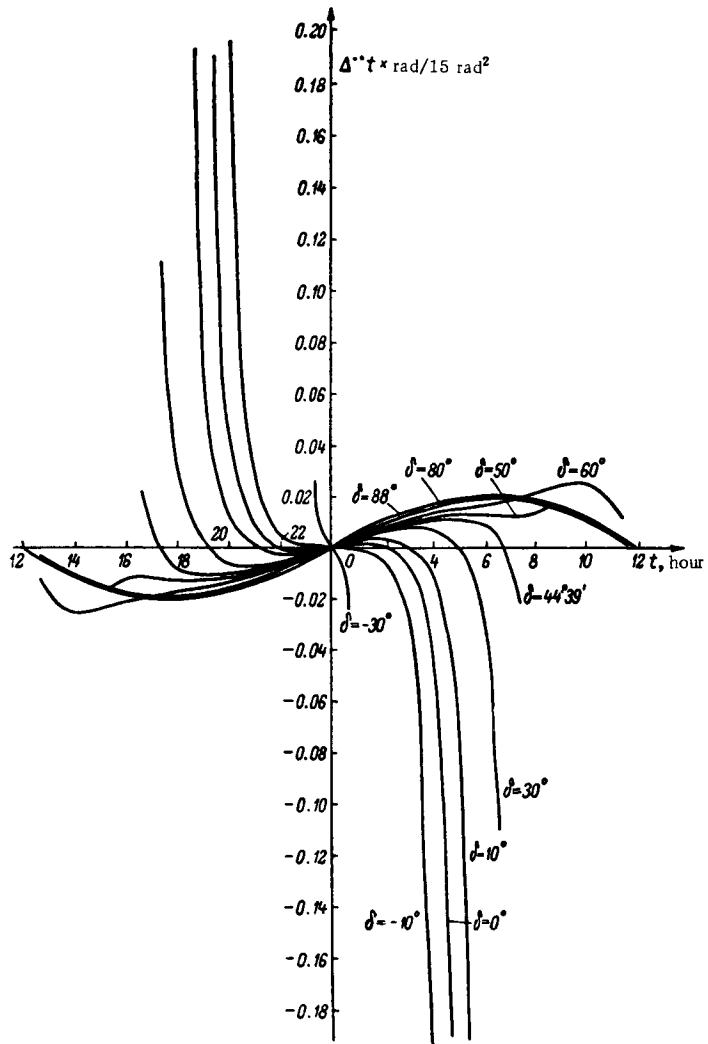
FIGURE 5. Time change in the rate of growth of the biased error in t.
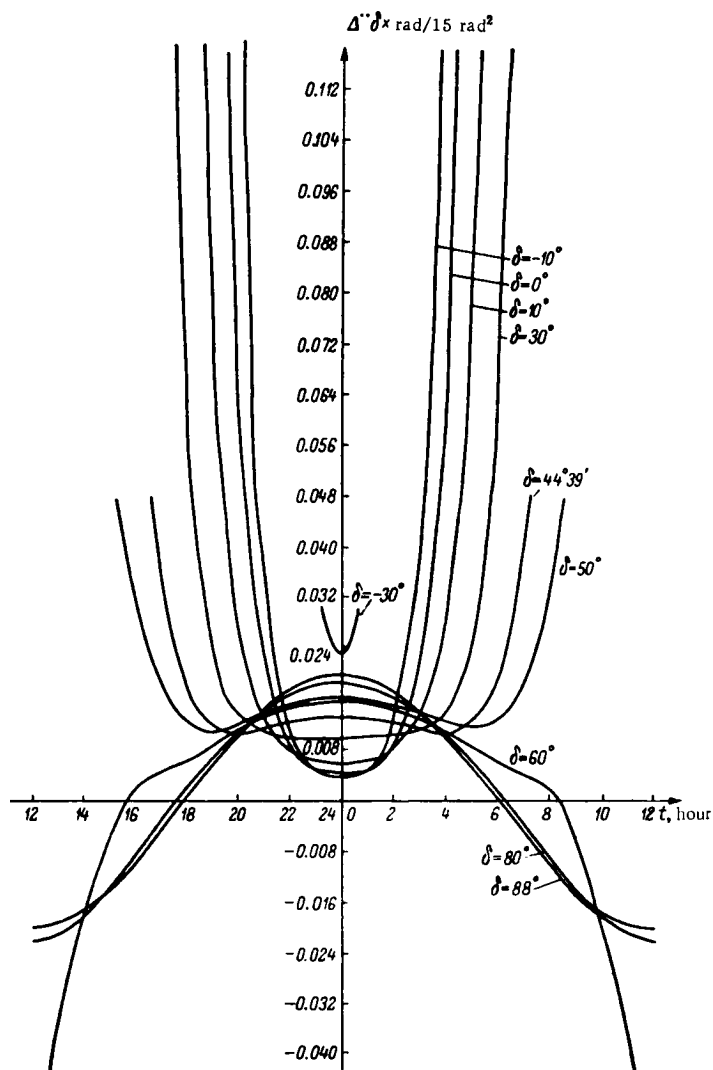
FIGURE 6. Time change in the rate of growth of the biased error in δ.

numerically obtained from (8) and (11): $D = 1.3 \cdot 0.05/0.1\, d'' = 0.65/d''$ sec^{-1};
for $d = 1''$ this gives $0.65\, sec^{-1}$. Since the quality factor is fairly low, the
designer can easily ensure aperiodic transients, despite the very narrow
linear zone of phototracker response, which is equal to $0.5\, d/1/$. However,
a maximum correction speed of $1.3 \cdot \Delta' t_{M}$ does not meet the requirement
of fairly rapid compensation of the initial discrepancy. The maximum
acceptable speed in this respect is $5 - 7''/sec$, which corresponds to a
quality factor of $D = 5/0''.5 = 10/d''$ sec^{-1}; for $d = 1''$, this gives $10\, sec^{-1}$.
With this quality factor, the total error of the photoelectric tracker caused
by biased disturbances is much less than the permissible value under
steady-state conditions. However, the above applies only in the ideal
case, when no position and brightness fluctuations are observed and the
amplifier channel is noiseless. In practice, both these factors have a
finite significance. The system originally designed for the ideal case
of pure biased perturbations should therefore be modified so that the
errors from image scintillation and amplifier noises, together with position
fluctuation errors, do not exceed the permissible value of ε. This problem
can be tackled in several different ways, but we shall only consider two
principal techniques.

The first technique represents the fluctuations at the tracker input as
a sum of several sinusoidal input functions with constant amplitudes and
known frequencies, while the phase relationships are random. The second
approach is based entirely on the statistical characteristics of the fluctuations
of the input signal. We know from the theory of trackers /2/ that the
maximum error ε_i with sinusoidal input perturbations of frequency ω_i and
amplitude Θ_i is given by

$$\varepsilon_i = \left| \frac{1}{1 + K\,(j\omega_i)} \right| \Theta_i = |\Phi_\varepsilon\,(j\omega_i)|\,\Theta_i, \tag{12}$$

where $K\,(j\omega)$ is the phase-amplitude characteristic of the open tracking
system.

The fluctuation amplitude at the tracker output is similarly derived from
input sinusoidal noise:

$$\Theta_{i\ n\ out} = |\Phi\,(j\omega_i)|\,\Theta_{i\ n\ in} = \left| \frac{K\,(j\omega_i)}{1 + K\,(j\omega_i)} \right| \Theta_{i\ n\ in}, \tag{13}$$

where $\Phi(j\omega)$ is the phase-amplitude characteristic of the closed system.
Expressions (12) and (13) are both valid for a linear tracking system.
They can be applied to the case of automatic telescope guiding, since,
on the one hand, the random shifts of the star image from the sighting axis
do not exceed 0.5 and, on the other, the input noise amplitude (brightness
scintillation and photomultiplier noise) is generally less than the saturation
signal: automatic guiding is thus regarded as a linear process.

If amplitude-frequency characteristics of the random noises at the
tracker input, $\Theta_{i\ n\ in} = f\,(\omega)$, are known with fair accuracy, the amplitudes
$\Theta_{i\ n\ out}$ can be computed from (12) and (13) for several ω corresponding to
significant amplitudes $\Theta_{i\ n\ in}$ Since the input noise is uncorrelated, the
resultant output noise can be represented as a square root of the sum of
the squares of the input noise components:

$$\Theta_n = \sqrt{\Theta_{i\ n\ out1}^2 + \Theta_{i\ n\ out2}^2 + \cdots + \Theta_{i\ n\ out\ n}^2}. \tag{14}$$

159

Similarly, if the function $\theta_i = f(\omega)$ is known for each of the guiding axes (t and δ), we may write from (12)

$$\varepsilon_0 = \sqrt{\varepsilon_{i1}^2 + \varepsilon_{i2}^2 + \cdots + \varepsilon_{in}^2}. \tag{15}$$

The overall input error is therefore given by

$$\varepsilon_n = \sqrt{\varepsilon^2 + \theta_n^2}. \tag{16}$$

By adjusting the phase-amplitude characteristic, we can always satisfy the necessary condition $\varepsilon_n < \varepsilon$.

The mathematical tools of the theory of tracking systems are fairly primitive, and we can only analyze the operation of the system in the time-independent case.

Time-independent random processes can be characterized for our purpose by the distribution function $W(x)\,dx$ and the correlation function or the spectral density function /3/. The correlation function $R(\tau)$ indicates to what extent the successive signal values depend on the preceding values. Mathematically, it is a time-average of the product $x(t)\,x(t+\tau)$, specifically

$$R(\tau) = \lim_{T \to \infty} \frac{1}{2T} \int_{-T}^{+T} x(t)\,x(t+\tau)\,dt. \tag{17}$$

The initial value $R(0)$ of the correlation function is the mean square of the random function, x^2. Therefore, if the correlation function $R(\tau)$ of the random output signal is known, we can immediately find the mean square tracking error due to random noise at the input or at any point of the amplifier channel.

The spectral density $S(\omega)$ is the density of the mean power transmitted by the signal during a certain period in the frequency interval between ω and $\omega + \Delta\omega$. The spectral density of a time-independent random process is a Fourier transform of its correlation function, and vice versa:

$$S(\omega) = \int_{-\infty}^{+\infty} R(\tau)\, e^{-j\omega\tau}\,d\tau, \tag{18}$$

$$R(\tau) = \frac{1}{2\pi} \int_{-\infty}^{+\infty} S(\omega)\, e^{-j\omega\tau}\,d\omega. \tag{19}$$

From (19) we have

$$R(0) = x^2 = \frac{1}{2\pi} \int_{-\infty}^{+\infty} S(\omega)\,d\omega. \tag{20}$$

Substituting the spectral density of the output signal $S(\omega)_{\text{out}}$ in relation (20) and integrating, we find the mean square tracking error due to random time-independent noise. We see that the correlation function of output error $R(\tau)_{\text{out}}$ or its spectral density $S(\omega)_{\text{out}}$ are required for the determination of the mean square of the random output error. In general, with two time-independent random inputs — the driving error with a spectral density $S_g(\omega)$

• and a noise error with a spectral density $S_n(\omega)$, the spectral densities of signal reproduction and of reproduction errors at the output of a linear tracking system are respectively given by /4/

$$
\left.
\begin{aligned}
S_1(\omega) &= |\Phi(j\omega)|^2 S_g(\omega) + |\gamma(j\omega)|^2 S_n(\omega) + \Phi^*(j\omega) S_{gn}(\omega) \gamma(j\omega) + \\
&\quad + \Phi(j\omega) S_{ng}(\omega) \gamma^*(j\omega), \\
S_2(\omega) &= |\Phi_\varepsilon(j\omega)|^2 S_g(\omega) + |\gamma(j\omega)|^2 S_n(\omega) + \Phi_\varepsilon^*(j\omega) S_{gn}(\omega) \times \\
&\quad \times \gamma(j\omega) + \Phi_\varepsilon(j\omega) S_{ng}(\omega) \gamma^*(j\omega).
\end{aligned}
\right\}
\qquad (21)
$$

In the particular case $S_{gn}(\omega) = S_{ng}(\omega) = 0$ (which is often encountered in practice), i.e., when the driving signal and the noise are uncorrelated, expressions (21) take the simple form

$$
\begin{aligned}
S_1(\omega) &= |\Phi(j\omega)|^2 S_g(\omega) + |\gamma(j\omega)|^2 S_n(\omega), \\
S_2(\omega) &= |\Phi_\varepsilon(j\omega)|^2 S_g(\omega) + |\gamma(j\omega)|^2 S_n(\omega).
\end{aligned}
\qquad (22)
$$

In (21) and (22), $\Phi_\varepsilon(j\omega)$ and $\gamma(j\omega)$ are the transfer functions of the error and the noise signal, $S_{ng}(\omega)$ and $S_{gn}(\omega)$ the spectral densities which correspond to cross-correlation between the driving signal and the noise, $\Phi^*(j\omega)$, $\gamma^*(j\omega)$, $\Phi_\varepsilon^*(j\omega)$ the conjugate transfer functions of $\Phi(j\omega)$, $\gamma(j\omega)$, $\Phi_\varepsilon(j\omega)$.

In the particular case of the noise signal applied at the input of the tracking system (this case is characteristic of automatic guiding systems, e.g., brightness scintillation of the star), the spectral density of reproduction error is given by

$$
S_2(\omega) = |\Phi_\varepsilon(j\omega)|^2 S_g(\omega) + |\Phi(j\omega)|^2 S_n(\omega). \qquad (23)
$$

If the spectral densities of the control signal (in automatic guiding, the spectral density of position fluctuations of the object star) and of noise (brightness scintillation of the star) are known, the internal characteristics of the photoelectric tracker (i.e., the transfer function $K(j\omega)$) should be modified so as to satisfy the inequality

$$
\bar\varepsilon = \sqrt{\varepsilon_g^2 + \varepsilon_n^2} < \varepsilon_{add}, \qquad (24)
$$

where

$$
\varepsilon_g^2 = \frac{1}{\pi} \int_0^\infty |\Phi_\varepsilon(j\omega)|^2 S_g(\omega)\, d\omega,
$$

$$
\varepsilon_n^2 = \frac{1}{\pi} \int_0^\infty |\Phi(j\omega)|^2 S_n(\omega)\, d\omega.
$$

If the precision of the automatic guiding system is specified in terms of the maximum error ε, and not the rms error $\bar\varepsilon_{add}$, the computations should be continued until the maximum error of the photoguider is determined. For a normally distributed random process, the error probability density distribution is /3/

$$
W(\varepsilon) = \frac{1}{\sigma_\varepsilon \sqrt{2\pi}}\, e^{-\frac{\varepsilon^2}{2\sigma_\varepsilon^2}}, \qquad (25)
$$

where $\sigma_\epsilon = \sqrt{\overline{\epsilon^2}}$. We thus see that the rms error is a parameter of the normal distribution. In probability theory it is generally assumed that a random event cannot occur for all practical purposes if its probability is less than 0.007. In normal distribution the corresponding maximum error is $\epsilon_{max} = 2.7\sigma_\epsilon = 2.7\epsilon$, and the condition to be satisfied by the photoguider is

$$2.7\epsilon < \epsilon. \tag{26}$$

It follows from the preceding that effective automatic guiding systems cannot be designed unless we know the amplitude-frequency characteristics of brightness and position fluctuations or the statistical characteristics of these fluctuations (spectral densities and correlation functions) expressed in absolute magnitudes. Position fluctuations should be known for each of the two control axes (t and δ) separately. The question of correlation between position and brightness fluctuations should be considered, and if the two phenomena are correlated, the cross-correlation functions and the corresponding spectral densities should be determined.

Because of space limitations, we could not consider the question of photomultiplier noise and its effect on the design of photoguiders. It seems clear, however, that reliable data should be available on correlation, or otherwise, between photomultiplier noise and star image fluctuations. Position fluctuation is a particularly important factor in calculations of automatic guiding by local means. In this case the system may be fairly fast, since the output force elements move small masses with small moments of inertia, and a low-inertia a. c. electric motor with a hollow rotor can be used as a driving element. Calculations of automatic guiding systems should be made using averaged modal fluctuation characteristics, in order to make the results applicable to telescopes of any aperture for arbitrary zenith distances. The determination of these characteristics is a lengthy experimental procedure which should be carried out according to a standard program specially devised for this purpose. An alternative approach calls for detailed measurements of the fluctuation characteristics at each projected erection site separately.

In conclusion, we consider another aspect of image fluctuation — the variation of the stellar shimmer disk. At the beginning of this paper we have mentioned that one of the basic photoguider parameters is the quality factor D, defined as the ratio of the velocity of the drive shaft under steady-state conditions to the input error. We have further established that the minimum quality factor for any guiding system, derived assuming only biased input errors, is given by

$$D = \frac{10}{d''} \ \sec^{-1}.$$

The diameter of the apparent image d, however, may change from night to night; this clearly leads to a change in the quality factor D and the stability of the tracking system may deteriorate. Photoguiders should therefore be calculated for the modal image diameter in each particular observation site, and a sufficient stability tolerance should be provided for the eventuality of images much smaller than the assumed size.

The Pulkovo Observatory has launched an ambitious project concerned with the determination of astronomical seeing in various places in the USSR.

This project should be further continued in order to accumulate statistical data for new observation sites and to determine the influence of various external factors on image quality.

Bibliography

1. Sabinin, Yu. A. and P. V. Nikolaev. — Izv. KAO AN SSSR, No. 24. Moskva, Izdatel'stvo AN SSSR. 1960.

2. Vasil'ev, D. V. and G. S. Filippov. Osnovy teorii i rascheta sledyashchikh sistem (Fundamentals of the Theory and Calculation of Tracking Systems). — Moskva, Gosenergoizdat. 1959.

3. Vasil'ev, D. V., B. A. Mitrofanov, G. L. Rabkin, G. N. Samokhvalov, A. L. Semenkovich, A. V. Fateev, and N. P. Checherin. Raschet sledyashchego privoda (Tracker Calculations). — Leningrad, Sudpromgiz. 1958.

4. Solodovnikov, V. V. Statisticheskaya dinamika lineinykh sistem avtomaticheskogo upravleniya (Statistical Dynamics of Linear Automatic Control Systems). — Moskva, Fizmatgiz. 1960.

5. Chestnut, G. and R. Mayer. Design and Calculation of Tracking Systems and Control Systems. — [Russian translation. 1959.]

O. B. Vasil'ev and V. S. Sumin

AUTOMATIC AND SEMIAUTOMATIC INSTRUMENTS FOR IMAGE PULSATION MEASUREMENTS FROM PHOTOGRAPHIC STAR TRAILS

One of the main astroclimatic characteristics is the pulsation of star images due to atmospheric instability. Image pulsation is commonly measured from photographic star trails. A star is photographed with the driving mechanism of the telescope stopped. On account of the Earth's diurnal rotation, the star image is stretched into a thin streak—trail, which displays a certain waviness due to the pulsation of the star. The pulsation amplitude is determined by calculating the rms deviations of the individual trail points from the mean trail line.

These measurements are generally carried out with a MIR-12 microscope: the coordinates of trail points are successively measured at fairly small intervals, and the results are reduced mathematically. This is obviously a time-consuming procedure (the reduction of a single trail occupying a few hours), so that a considerable quantity of the data collected by various expeditions is doomed to remain untreated. A need was felt in fully or partially automatic techniques, combining trail measurements with rapid reduction of the numerical data.

A semiautomatic instrument for trail measurements was first proposed by V. B. Sukhov. Unfortunately, he did not see his idea carried to completion, but his pickup (Figure 1) features in the semiautomatic instruments built by the authors.

The optical system of the MIR-12 microscope is driven at a constant speed of 9 mm/sec by an electric motor. The negative is set so that the cross hairs of the eyepiece micrometer travel approximately along the trail, as is schematically shown in Figure 2. The observer continually adjusts the eyepiece micrometric screw, so that the cross hairs are guided along the trail midline, retracing all its convolutions. A linear potentiometer is mechanically coupled with the micrometric screw: the slide-wire voltage is proportional to the angle of the screw and therefore to the ordinate of the current trail point. By scanning the entire trail and letting the cross hairs repeat all the ups and downs, we recover a potentiometer voltage which is an exact reproduction of the trail topology.

The instrument built in 1960 by one of the authors (V. S. Sumin) employed a paired potentiometer (Figure 3). The slide-wire voltage of potentiometer R_1
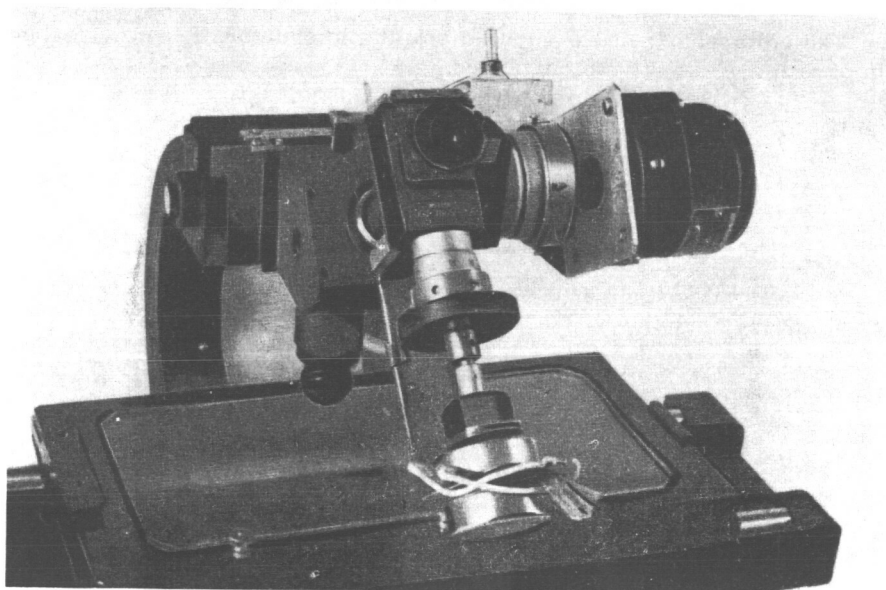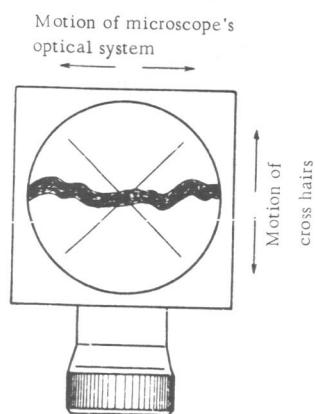
$$U_1 = E_0 y \tag{1}$$

FIGURE 1.

Motion of microscope's
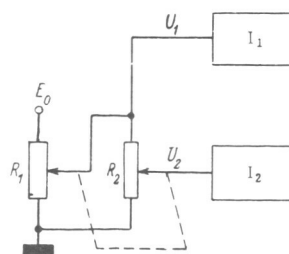optical system

Motion of cross hairs

FIGURE 2.

FIGURE 3.

is impressed on the potentiometer R_2. If $R_2 \gg R_1$, the slide-wire voltage of R_2 is

$$U_2 = E_0 y^2. \tag{2}$$

The voltages U_1 and U_2 are fed into the integrators I_1 and I_2, respectively. Integration gives the two quantities

$$I_1^* = \int_{t_1}^{t_2} U_1 dt = \frac{E_0}{v} \int_{x_1}^{x_2} y\, dx, \tag{3}$$

$$I_2^* = \int_{t_1}^{t_2} U_2 dt = \frac{E_0}{v} \int_{x_1}^{x_2} y^2 dx, \tag{3'}$$

and, scaling, we find

$$I_1 = \frac{v}{E_0} I_1^* = \int_{x_1}^{x_2} y\, dx, \tag{4}$$

$$I_2 = \frac{v}{E_0} I_2^* = \int_{x_1}^{x_2} y^2 dx. \tag{4'}$$

Hence the variance

$$\sigma^2 = \frac{1}{x_1 - x_1} \int_{x_1}^{x_2} y^2 dx - \left(\frac{1}{x_2 - x_1} \int_{x_1}^{x_2} y\, dx \right)^2. \tag{5}$$

Here x_1 and x_2 are the end points of the measured trail section. If $x_2 - x_1 = \text{const} = 1$, equation (5) takes the form

$$\sigma^2 = \int_{x_1}^{x_2} y^2 dx - \left(\int_{x_1}^{x_2} y\, dx \right)^2 = I_2 - I_1^2. \tag{6}$$

The variance is determined in relative units which can be easily converted into seconds of arc if we know the magnification of the microscope, the voltage E_0, the length of the measured section $x_2 - x_1$, and the gain of the integrators.

In practice, however, the potentiometers R_1 and R_2 are nonlinear, and the variance σ should be tabulated for various combinations of I_1 and I_2 (such tables were computed by Yu. I. Beruchka). The reference to tables of course causes a certain inconvenience when working with the semi-automatic instrument. Another deficiency is that for small σ and large I_1, the relative error in σ, though small for I_1 and I_2 separately, becomes fairly large. For these reasons the original semiautomatic model was discontinued, although it had been successfully used in the reduction of the findings of the 1960 expeditions, which later had served as a basis for the preliminary choice of the 1961 survey area for the final selection of the erection site for the BTA telescope.

From the foregoing we see that the accuracy of σ can be increased by putting $I_1 = 0$, i.e., the constant component of the signal fed into the analog computer should be filtered off. In this case, the voltage should not be

squared at the input (as in the previous model), since the potentiometer R_2 multiplies the voltage U_1 by the screw angle y, and the constant component, which is easily eliminated by a dividing capacitance, is very difficult to separate from the screw angle. For this reason, in all subsequent models of the instrument we either omitted voltage squaring altogether, or provided a special electronic voltage squarer.

In 1960, simultaneously with the development of the first semiautomatic model, O. B. Vasil'ev built an integrator without squaring. This simplification is justified since the deviations of the star image from the mean line constitute a normally distributed random variable. The mean pulsation amplitude measured with the instrument is therefore multiplied by a constant factor of 1.25 to obtain the mean square amplitude. This second model was used in the reduction of the findings of the 1961 Zelenchuki expedition of the Pulkovo Observatory and thus directly assisted in the final selection of the site for the erection of the BTA telescope.
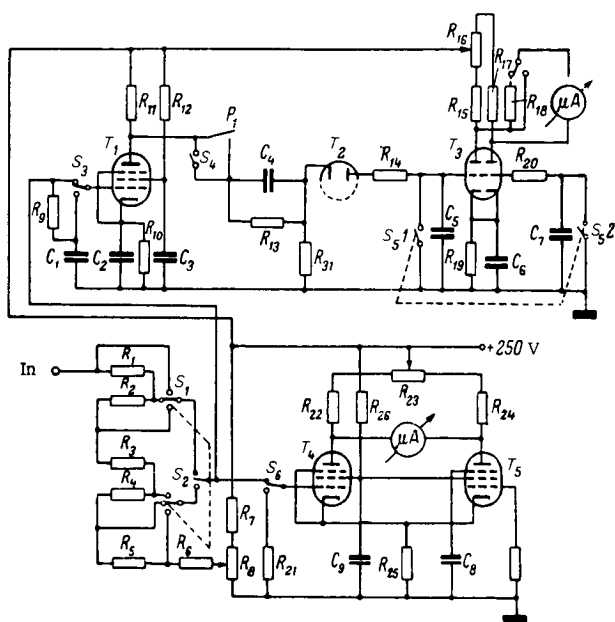

FIGURE 4.

Sukhov's pickup was incorporated in the instrument, and the pickup voltage was fed to the integrator. A circuit diagram of the integrator is shown in Figure 4. The input voltage is delivered through a divider which reduces the signal to 1/2, 1/5, 1/10, 1/20, or 1/50 of the initial value. The input filter truncates all frequencies higher than 5 c/s, so that the interference from the a.c. mains is effectively eliminated. The integrator is provided with a single amplifier stage (6Zh8 tube). The signal from the anode load of the amplifier tube is fed through the condenser C_4 and the diode 6Kh6S into the integrating circuit $R_{14}C_5$. In this particular circuit arrangement, the diode is so connected that the integrating capacitance receives only the negative fluctuations of the signal. The

capacitance C_4 is adjusted to cut off all fluctuations with frequencies less
than 0.05 c/s. This eliminates the constant component of the signal, as
well as the low frequency oscillations due to the inclination and the
curvature of the trail. The voltage of the integrating capacitance is
impressed on the grid of one of the two halves of the 6N8S tube (a bridge
amplifier). A microammeter displays the integrator readings.

The divider signal is fed into another bridge amplifier (two 6Zh8
tubes), as well as into the integrator. A microammeter displays the
fluctuations at integrator input. The potentiometer nearly compensates
the constant component of the signal, and this is actually reflected in
the microammeter readings. The integration time is set by a mechanical
timer comprising a SD-2 synchronous motor and a set of reduction gears.

A calibration curve should should be plotted for each individual observer
working with the instrument, since the accuracy with which the cross
hairs are guided along the trail depends on the observer's experience
and on his emotional makeup. This is of course true for any semiautomatic
instrument. Because of the particular choice of the integrator (the RC
circuit strictly speaking is an inertial link, and not an integrator), linear
integration is ensured only if the time constant is substantially greater
than the integration time. Since the integration time is 2 min (this
corresponds to a trail section 18 mm long), the time constant of the RC
circuit should be fairly high. The capacitance charging currents are
therefore comparable with the grid currents of the respective amplifiers,
as well as with the leakage currents from the capacitance and with the
currents set up by the e.m.f. of the 6Kh6S diode. Furthermore, the gain
factor of the amplifiers used in this model may change in time. All these
deficiencies can be avoided to a considerable degree by using low-drift
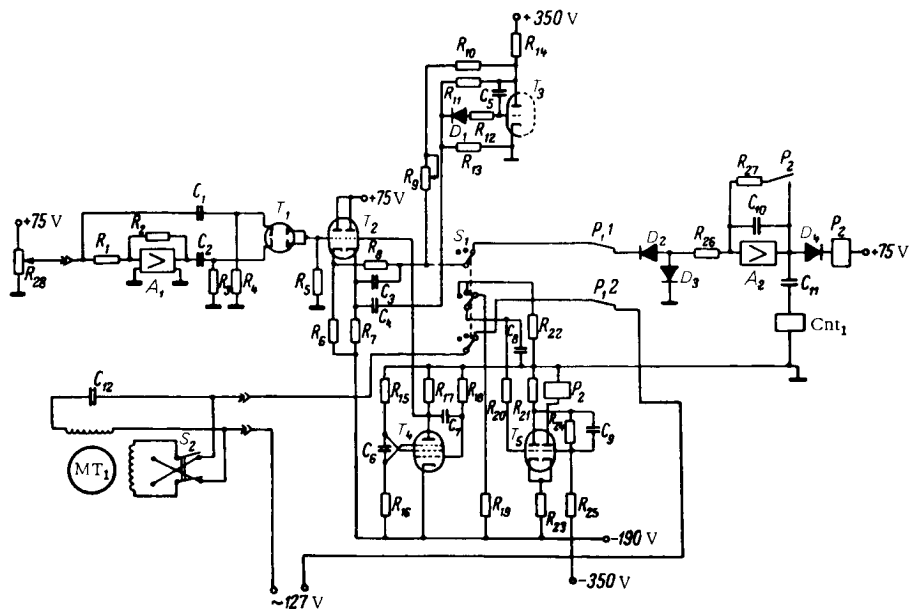operational amplifiers.

FIGURE 5.

1822

Figure 5 is a circuit diagram of the SIGMA-1 model built by V.S. Sumin in 1961 using UPT-4 operational amplifiers. As we have previously observed, high accuracy is ensured only if I_1 is constantly kept equal to zero, which corresponds to elimination of the constant component from the input of the analog device. Expression (6) then takes the form

$$\sigma^2 = \int_{x_1}^{x_2} y^2 dx. \tag{7}$$

The instrument described in the following has been designed to solve this equation.

Voltage U is impressed on the input from the potentiometer R_{28} attached to the microscope. This voltage is fed into a phase inverter — operational amplifier A_1. The amplifier comprises three amplifying stages, each reversing the sign of the input voltage, so that the voltage will have its original sign reversed at the output. Without additional feedback loops, the UPT-4 amplifier has an exceptionally high gain (of the order of $5 \cdot 10^4$). These amplifiers are therefore never used without deep negative feedback. In the general case, the transfer function of the amplifier loop (regulated by feedback) is given with fair precision by the expression

$$K(p) = -\frac{Z_2(p)}{Z_1(p)}. \tag{8}$$

Here $Z_1(p)$ and $Z_2(p)$ are the additional impedances coupled into the loop (Figure 6). In our case, these impedances are active resistances R_1 and R_2, such that

$$R_1 = R_2. \tag{9}$$

The transfer function of the amplifier loop is thus written as

$$K(p) = -\frac{Z_2(p)}{Z_1(p)} = -\frac{R_2}{R_1} = -1, \tag{10}$$

i.e., the amplifier is in fact an inverter. The inverter output is the quantity $-y$. The C_1R_4 and C_2R_3 links filter off the constant component of both the direct and the "inverted" signals. Note that the constant component produced by the inaccurate setting of the null point or its drift is also eliminated, so that the amplifier A_1 cannot conceivable cause any trouble in actual operation.
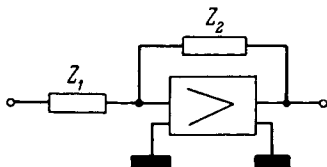

FIGURE 6.

Two voltages $U_\sim$ and $-U_\sim$ are impressed on the cathodes of the diode T_1. Since in the following we shall only deal with these alternating signal components, the subscript $\sim$ is henceforth omitted. The diodes transmit only negative voltage, and the anode potential is therefore invariably equal to the potential of the cathode on which the negative voltage is impressed at the particular instant, i.e., the anodes reproduce the absolute value of the voltage with a minus sign, $-|y|$. The absolute value is essential if we are to use

a squarer: its characteristic curve is a single branch of a parabola. The minus sign is a feature of the particular squarer used.

The principle on which the squarer functions is illustrated in Figure 7. The voltage $-|y|$ is added to a sawtooth voltage, whose frequency is much higher than that of the measured voltage, and to a constant voltage, whose magnitude is such that with a zero input signal the bottom peaks of the sawtooth voltage are on zero level. When an input signal is picked up, the
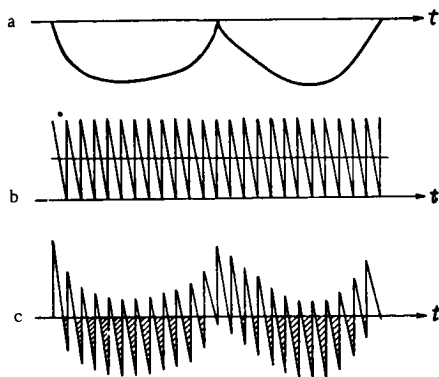

FIGURE 7.

"saw" is displaced down by the amount y. The limiter diodes D_2 and D_3 (Figure 5) transmit negative voltage only. The mean current through the load R_{26} during one period of the "saw" is determined by the area of the cross hatched triangle in Figure 7: it is therefore proportional to the square of the triangle height. The height of the triangle is y, and thus

$$i_{av} = ky^2. \tag{11}$$

This is a fairly simple squarer which has proved itself time and again in experimental work. It is particularly convenient in analog computers where squaring is repeated several times, since a single sawtooth generator can supply several squarers or multipliers.

The sawtooth generator is a transitron using the tube T_4 (6P9). The sawtooth voltage from the tube anode is fed through a cathode follower (the right half of T_2), the condenser C_3, the switch S_1, and the contacts of the time relay $P_1 1$, finally reaching the limiter diodes D_2 and D_3. This is also the destination of the voltage $-|y|$ obtained from the left half of T_2 and fed through the resistance R_8.

The limiting value is set by the tube T_3. The sawtooth voltage and the feedback voltage from the tube anode (through the resistance R_{11}) are impressed on the grid. The diode D_1 transmits only negative voltage. A feedback condenser C_5 is coupled between the anode and the grid, so that an inertial circuit is obtained. Under steady running conditions, the tube anode is maintained at a constant voltage. The potentiometer R_9 selects the bias of the diode D_2, which ensures normal operation of the squarer. If for some reason the amplitude of the sawtooth voltage decreases, the diode D_1 will transmit a smaller portion of one period, the positive

grid-cathode voltage of T_3 will increase, and the anode potential will fall. The positive bias of the diode D_2 will therefore also decrease. If the "saw" amplitude increases, the potential of the T_3 grid decreases and the D_2 bias increases.

The squarer output voltage (triangular pulses) is fed into the integrator (operational amplifier A_2). If in Figure 6 a capacitance is substituted for Z_2 and a resistance for Z_1, we must put in (8)

$$Z_2(p) = \frac{1}{pC}, \quad Z_1(p) = R. \tag{12}$$

Hence,

$$K(p) = -\frac{1}{pRC} \tag{13}$$

The circuit is indeed an integrator. The integrator gain is

$$\xi = -\frac{1}{RC}. \tag{14}$$

A so-called "hybrid circuitry" (combination of analog and digital devices) was employed to reduce integration errors. The armature of a polarized relay P_2 is connected with the A_2 output through the diode D_4. The other end of the armature is connected to the positive terminal of a 75 V rectifier. As soon as the condenser C_{10} is charged to $+75$ V, the diode D_4 starts conducting current. Relay P_2 is tripped and its contacts discharge the capacitances C_{10} and C_{11} through the resistance R_{27}. The C_{11} discharge current trips an electromechanical pulse counter Cnt_1, and the capacitance C_{10} is again charged from zero.

The integration time is 2 min: it is set automatically by a timer (T_5 tube). When the switch S_1 is held in the extreme left and central positions, the capacitance C_8 is discharged through R_{22}. The integrator input in this case is disconnected and the supply of the pickup motor MT_1 is turned off. If the switch S_1 is moved to the extreme right, the motor circuit is made, the squarer output is coupled into the integrator input, and the capacitance C_8 is discharged through R_{19}, which is connected to a -190 V supply. Initially, the left half of T_5 conducts, and the right half is cut off, so that no current flows through the armature of the relay P_1. As soon as the negative voltage across C_8 is sufficient to pass current through the tube, the circuit (a Schmidt trigger) is "flipped" and the relay P_1 is triggered: it turns off the motor supply and disconnects the integrator input. The measurements are completed. The operator writes down the count and resets the counter to zero. Before the instrument can be used again, the switch S_1 should be moved all the way to the left (to discharge the capacitance C_8) and then returned to the extreme right.

The integrator gain is such that σ, in seconds of arc, is calculated from the equality $\sigma'' = \sqrt{\frac{N}{1000}}$, where N is the count.

The switch S_2 reverses the motor. A single trail section can be measured more than once by traveling back and forth along the trail; the final result is calculated as the average of the successive measurements.
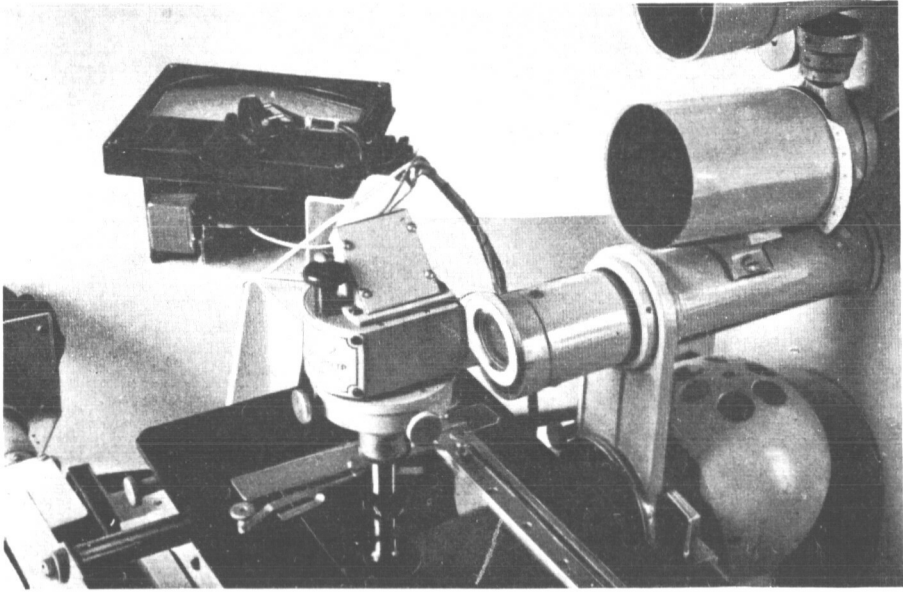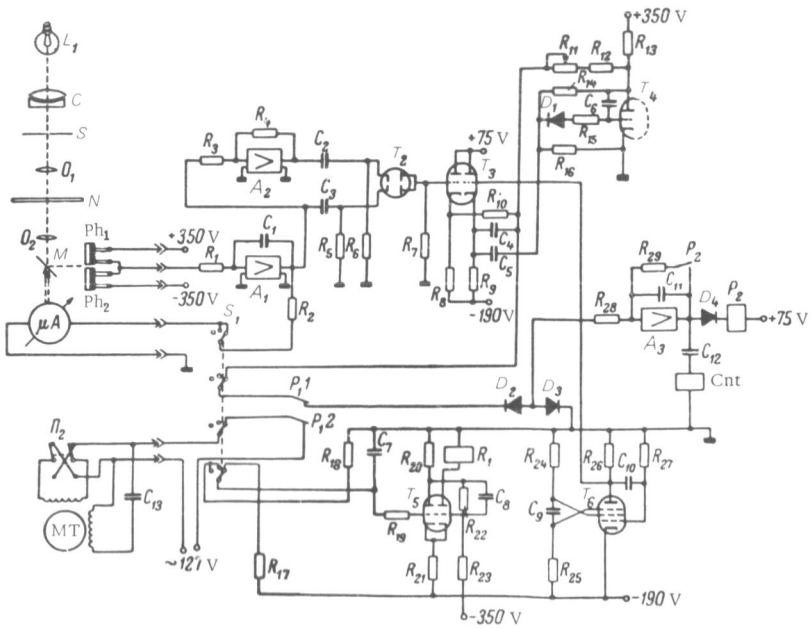
FIGURE 8.

FIGURE 9.

The model which we have just described is free from most of the shortcomings inherent in the earlier models, and yet it is fairly simple. But even this improved instrument is not free from the main deficiency of semiautomatic devices: the results depend on the experience of the individual operator, his emotional makeup, attitude, etc. The results of measurements are thus not free from subjective errors, which can be eliminated only by comparing the data with results obtained by conventional techniques. In practice, this means that calibration curves should be plotted for each individual observer. The instrument is thus not absolute. Absolute instruments run without human intervention, i.e., they are fully automatic.

In 1962, O. B. Vasil'ev proposed a pickup for a fully automatic instrument (see photograph in Figure 8). The pickup comprises an MF-2 micro-photometer, and its circuit diagram is shown in Figure 9. The light from the lamp L_1 passes through the condenser C and strikes the slit S. The image of the slit is projected by the objective O_1 on the negative N. The second objective O_2 projects a blown up image of the trail section to be measured on two joined photoelectric cells Ph_1 and Ph_2. A mobile mirror M attached to the axis of the microammeter μA is provided between the objective O_2 and the photocells. The photographic plate is so aligned that the projected slit image crosses the trail at right angles. The trail is in turn parallel to the direction of motion of the microphotometer carriage.
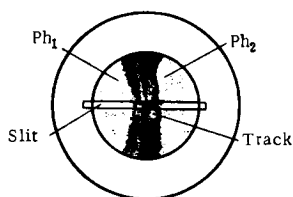

FIGURE 10.

The micrometric screw of the carriage is rotated by a reversible motor, so that the carriage moves with a constant speed of 9 mm/sec, and the slit image covers successively all the points of the measured trail section. The arrangement is schematically shown in Figure 10. The slit "defines" a fairly short trail section, whose image is then projected on the photocells. The photocells are coupled into a bridge circuit. The bridge is balanced if the trail image is photometrically bisected by the thin boundary line between the two joined photocells. The amplifier A_1 is coupled into the bridge diagonal (Figure 9). The microammeter μA, with the mirror M attached to its axis, is connected with the amplifier output by the resistance R_2 and the switch S_1. If the image of the measured trail segment is displaced relatively to the boundary line, the bridge is unbalanced: the A_1 output voltage deflects the microammeter pointer with the mirror M. By turning around the microammeter axis, the mirror will shift the trail image across the photocells until the bridge is again balanced. As the trail is scanned, the mirror continuously tracks its deflections from the mean line, and the A_1 output voltage reproduces the exact shape of the trail.

The amplifier output voltage is then treated as described above: it is integrated as in the SIGMA-1 model. Comparison of the circuit diagrams in Figures 5 and 9 easily shows that the circuitry of SIGMA-2 can be readily adapted to run with a semiautomatic pickup. This is highly important, since the automatic model will only measure negatives of high photometric quality (without spots, scratches, and other defects, which may affect the photometry), and this requirement can be seldom

met in the field. Negatives which are judged to be defective for automatic reduction are treated on the semiautomatic device. This does not mean, however, that two separate instruments must be purchased: it is sufficient to provide a semiautomatic pickup for the fully automatic SIGMA-2 model, which can be plugged in for the reduction of slightly defective negatives.
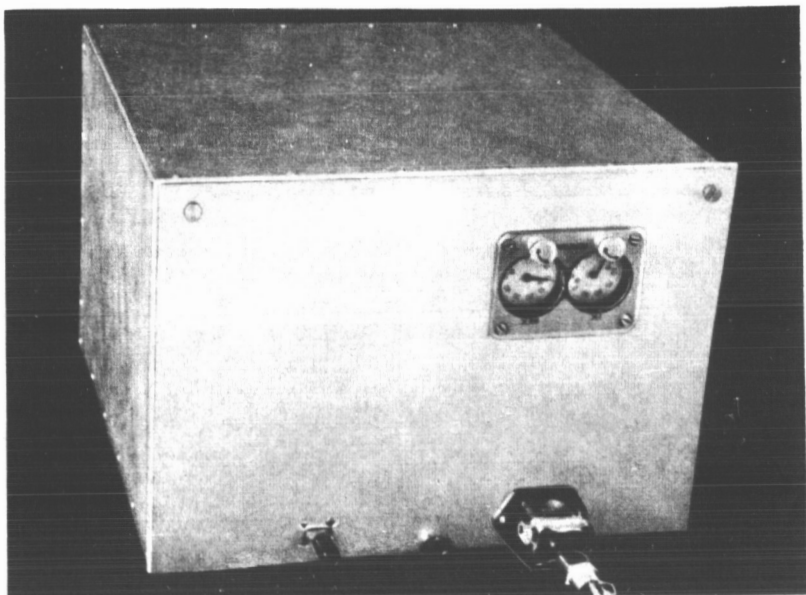

FIGURE 11.

SIGMA-1 and SIGMA-2 models look the same from outside (see photograph in Figure 11). They are supplied by a stabilized ESV-3 rectifier which generates four stabilized voltages: $+350$, -190, and -350 V.

Further improvement of the SIGMA-1 and SIGMA-2 models is only a matter of time.

Bibliography

1. Vasil'ev, O.B. —Izv. GAO, No. 170 : 144 — 154. 1962.

2. Fel'dbaum, A.A. Vychislitel'nye ustroistva v avtomaticheskikh sistemakh (Analog Devices in Automatic Systems). —Fizmatgiz. 1959.

3. Fitsner, L.N. and L.I.Shevchenko. —Priborostroenie, No. 8:7 — 9. 1957.